ORNL/TM-2021/2312

High Flux Isotope Reactor Low-Enriched Uranium U-10Mo Fuel Design Parameters

Benjamin R. Betzler
David Chandler
Jin Whan Bae
Eva E. Davidson
Germina Ilas
Jennifer L. Meszaros

Approved for public release.
Distribution is unlimited.

March 18, 2022

ORNL/TM-2021/2312

Nuclear Energy and Fuel Cycle Division

HIGH FLUX ISOTOPE REACTOR LOW ENRICHED URANIUM U-10MO FUEL DESIGN PARAMETERS

Benjamin R. Betzler
David Chandler
Jin Whan Bae
Eva E. Davidson
Germina Ilas
Jennifer L. Meszaros

March 18, 2022

Prepared by
OAK RIDGE NATIONAL LABORATORY
Oak Ridge, TN 37831-6283
managed by
UT-Battelle, LLC
for the
US DEPARTMENT OF ENERGY
under contract DE-AC05-00OR22725

CONTENTS

LIST OF FIGURES

LIST OF TABLES

ABBREVIATIONS

3M Material Management and Minimization

BOC beginning-of-cycle

CE control element

DOE US Department of Energy

DOTRSM Design Optimization Tool - Response Surface Methodology

EOC end-of-cycle

HEU highly enriched uranium

HFIR High Flux Isotope Reactor

HPC high-performance computing

HSSHTC HFIR Steady State Heat Transfer Code

IFE inner fuel element

LEU low-enriched uranium

MCNP Monte Carlo N-Particle code

MOC middle-of-cycle

NNSA National Nuclear Security Administration

OFE outer fuel element

ORNL Oak Ridge National Laboratory

PHAME Python HFIR Analysis and Measurement Engine

SL safety limit

TSR technical safety requirement

U-10Mo uranium-molybdenum

USHPRR US High Performance Research Reactor

ACKNOWLEDGMENTS

This work is supported by the National Nuclear Security Administration Office of Material Management and Minimization (3M), US Department of Energy. The authors thank the reviewers of the manuscript Emilian Popov and Kara Godsey at Oak Ridge National Laboratory.

ABSTRACT

Activities to convert the HFIR from HEU to LEU are ongoing as part of the US Department of Energy (DOE) National Nuclear Security Administration (NNSA) nuclear nonproliferation mission. Design activities to study the conversion of HFIR from HEU to LEU fuel explored different fuel design features and shapes with a uranium-molybdenum (U-10Mo) monolithic alloy fuel. This high-density alloy contains 90 wt % uranium and 10 wt % molybdenum and has a uranium density of 15.318gU/cm^3. The goal of these studies is to generate several candidate HFIR LEU fuel designs of varying fuel fabrication complexity that meet the current HEU performance metrics and safety requirements.

Recent advancements in modeling and simulation tools and design methods enabled a thorough analysis of the available design space with U-10Mo fuel. A surrogate model used this analysis as training data to quickly determine the performance of a design given specific design parameters. An optimization module used this surrogate model to quickly search this multidimensional search space given specific desired performance characteristics. This approach was made possible by the large available design space with U-10Mo fuel. Shift, a Monte Carlo tool optimized for high-performance computing (HPC) architectures, was used for faster calculation and better data management for reactor physics simulations. Once most of these design studies were complete, a new suite called the Python HFIR Analysis and Measurement Engine (PHAME) was developed to connect all fuel design analysis steps, making design studies more efficient and reproducible. The post-processing capabilities of these new tools are leveraged for the information provided herein. Leveraging these tools, several candidate fuel designs were selected with varying levels of feature complexity and reactor performance.

This report provides design feature details for four selected HFIR LEU U-10Mo fuel designs and their corresponding performance and safety metrics. Nominal best-estimate design parameters and irradiation conditions, including fission rate densities, power densities, heat fluxes, and cumulative fission densities, are provided. Simulations show that the high uranium density of U-10Mo fuel provides a large potential design space that enables various LEU designs to meet HEU core performance metrics and safety requirements with a power increase from 85 MW (HEU) to 95 MW or 100 MW (LEU).

1. INTRODUCTION

The High Flux Isotope Reactor (HFIR) is a US Department of Energy (DOE) Office of Science User Facility that is operated at the Oak Ridge National Laboratory (ORNL). HFIR is a versatile research reactor providing one of the highest steady-state neutron fluxes of any reactor in the world for neutron scattering experiments. HFIR is focused on fundamental and applied research on the structure and dynamics of matter, as well as materials irradiation studies and production of medical, industrial, and research isotopes.

ORNL is funded by the DOE NNSA Office of Material Management and Minimization (M^3) to perform HFIR conversion activities such as the design studies presented herein. US High Performance Research Reactor (USHPRR), including HFIR, the Advanced Test Reactor, the National Institute of Standards and Technology Research Reactor, the Massachusetts Institute of Technology Research Reactor, and the University of Missouri Research Reactor, are providing research on potential low-enriched uranium (LEU) alternatives in support of NNSA's nonproliferation mission.

Initial studies to convert HFIR from its current highly enriched uranium (HEU) dispersion fuel to LEU fuel explored uranium-molybdenum (U-10Mo) monolithic alloy fuel because of its high uranium density [1, 2]. HFIR's interim U-10Mo fuel design [2] consists of both radially and axially contoured fuel profiles. These fuel contours are fabrication complexities not associated with the other USHPRR fuel designs. The resulting HFIR-specific U-10Mo fuel manufacturing R&D process was anticipated to be long and expensive, and it was uncertain whether the manufacturing process would result in adequate yields to maintain an economically viable fuel. To mitigate this high project risk, HFIR initiated fuel design studies with LEU uranium-silicide dispersion (U_3Si_2 -Al) fuel in 2017. The manufacturing R&D effort for U_3Si_2 -Al fuel is anticipated to be more streamlined and less costly, and the resulting process is expected to be capable of higher yields at a lower cost than U-10Mo monolithic fuel. HFIR officially rebaselined to U_3Si_2 -Al fuel in 2019.

It is still important to fully document the candidate U-10Mo monolithic alloy fuel designs, despite the fact that current studies are focused on U_3Si_2 -Al dispersion fuels with different uranium metal densities [3, 4, 5, 6]. The U_3Si_2 -Al dispersion fuels are still under development, and many of the design processes developed for the U-10Mo fuel design studies were adopted for the U_3Si_2 -Al fuel designs. The goal of the HFIR conversion efforts is to design, qualify, fabricate, and deploy LEU HFIR fuel that will maintain or exceed current reactor performance metrics and safety requirements at an affordable cost [7]. Following the conversion of HFIR from HEU to LEU fuel, (1) the ability of HFIR to perform its scientific missions must be maintained or enhanced, (2) all safety requirements must be met, and (3) annual operating costs must not increase.

This report presents design characteristics and performance parameters for candidate U-10Mo fuel designs. Similar design reports detail the performance of the low-density U_3Si_2 -Al [8] and high-density U_3Si_2 -Al [9] fuel designs, which are the focus of current conversion design efforts. An optimization approach leveraging reactor physics and steady-state thermal hydraulics simulations yields optimal designs using this alloy fuel [10, 11, 12, 13, 14] and predefined conversion assumptions [7]. Four fuel designs are presented herein, representing designs with varying fabrication complexity and reactor performance. These designs demonstrate the large design space available as a result of the high density of the fuel. Designs presented in this report meet or exceed most HFIR HEU core performance metrics and safety requirements [15].

The design parameters highlighted in this report are as follows:

1. fuel element and fuel plate geometry and features,
2. temporal fission rate density distributions,
3. temporal power density distributions,
4. temporal heat flux distributions, and
5. discharge cumulative fission density distributions.

2. FUEL ELEMENT GEOMETRY

The HFIR core consists of concentric annular regions: a central flux trap containing vertical experimental targets; two fuel elements — inner fuel element (IFE) and outer fuel element (OFE) — separated by a thin water labyrinth region; a region containing two control elements (CEs); a beryllium reflector; and a water region up to the edge of the pressure vessel, which is located in a pool of water [16].

The fuel assembly consists of an integral two-element configuration; the IFE is designed to be seated within the OFE. The IFE and OFE are composed of numerous 1.27 mm thick involute-shaped fuel plates separated by 1.27 mm thick coolant channels (Fig. 1). The fuel plates are composed of a fuel region (also known as *fuel meat*) and a filler region enclosed by aluminum cladding. In the current HEU design, the fuel meat is a mixture of aluminum powder and U_3O_8 with 93 wt % ^{235}U. The fuel meat is contoured along the arc of the involute plate to reduce edge power peaking. The IFE contains B_4C for reactivity hold-down and to control power distribution during operation. The fuel plates are inserted into slots located in the cylindrical aluminum side plates, and they extend into machine grooves, where they are attached to the side plates via circumferential welds. Key geometry and operational parameters are provided in Table 1. More details of the fuel element geometry can be found in the work by Ilas et al. [17].

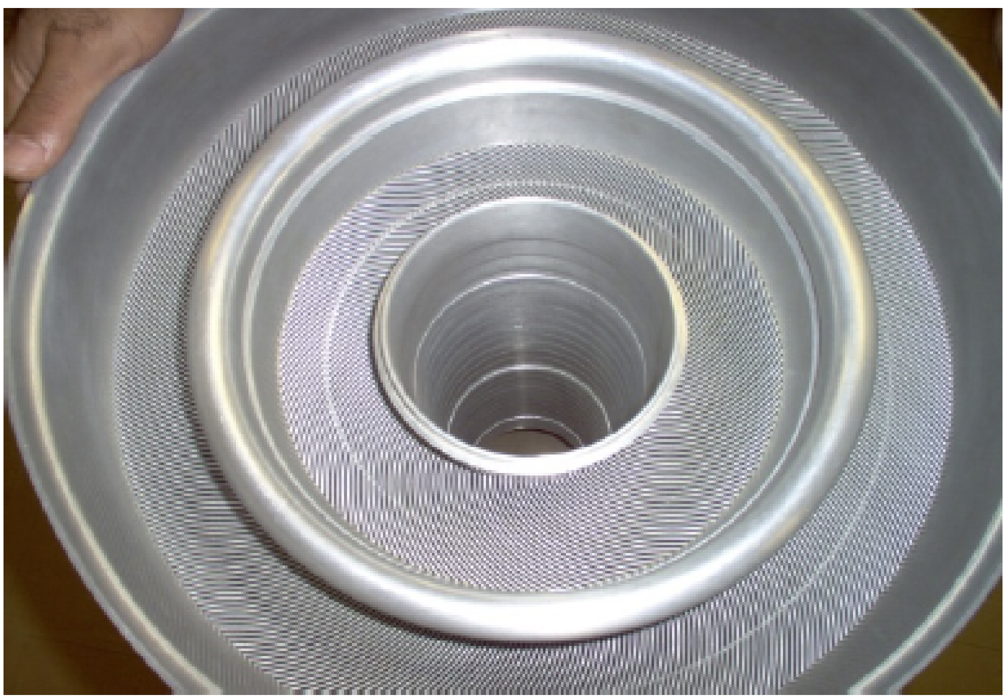

Figure 1. HFIR inner and outer fuel elements.

Table 1. Key HFIR HEU geometry and operational parameters

Parameter	Units	Value	
Power	MW	85	
Cycle length	days	24–26	
Coolant	-	light water	
Inlet coolant temperature	°C	48.89	
Inlet coolant pressure	MPa	3.33	
Primary flow rate	m^3/s	1.01	
Number of fuel elements	-	2	
Fuel plate cladding	-	Al	
Cladding thickness	μm	254	
Fuel meat	-	U_3O_8-Al	
Fuel plate filler	-	Al (+B_4C in IFE)	
Fuel meat + filler thickness	μm	762	
Fuel plate thickness	μm	1,270	
Coolant channel thickness	μm	1,270	
Metal-to-water ratio	-	1	
^{235}U enrichment	wt % ^{235}U /U	93	
^{235}U loading	kg	9.40	
U loading	kg	10.11	
U_3O_8density	g/cm^3	8.22	
^{235}U density	$g^{235}U/cm^3$ U_3O_8	6.47	
Active fuel meat length	cm	50.80	
Fuel plate length	cm	60.96	
Active fuel zone volume	L	50.03	
Average power density	MW/L	1.70	
Fuel meat heat transfer area	m^2	39.84	
		IFE	**OFE**
Number of fuel plates	-	171	369
^{235}U loading	kg	2.60	6.80
^{235}U loading	g/plate	15.18	18.44
U_3O_8-to-Al mass split	wt % U_3O_8	30	40
Burnable poison	-	^{10}B in B_4C	-
^{10}B loading	g	2.70	-
^{10}B density	mg/cm^3	1.752	-
Involute radius	cm	6.91261	14.91742
Fuel plate width	cm	9.21004	8.09752
Distance from inner plate edge to involute origin	cm	0.29718	0.29464
Distance along involute to fuel meat start	cm	0.23241	0.21336
Distance along involute to fuel meat end	cm	8.02259	7.22884
Fuel meat width	cm	7.79018	7.01548
Fuel meat heat transfer area	m^2	13.53435	26.30132
Inner radius of fuel meat	cm	7.11950	15.11586
Outer radius of fuel meat	cm	12.53239	20.87073
Active fuel zone volume	L	16.97643	33.05139

3. URANIUM-MOLYBDENUM MONOLITHIC ALLOY FUEL

The study described in this report considered the 17.02 g/cm^3 , U-10Mo monolithic alloy fuel with an enrichment of 19.75 wt % ^{235}U/U. The fuel foil is coated with a 25.4 micron (1 mil) zirconium barrier layer and then cladded with aluminum. A summary of the U-10Mo material composition, including mass fractions and densities assumed for this study, is provided in Table 2. With an assumed enrichment of 19.75 wt % ^{235}U , the ^{235}U density in the U-10Mo fuel foil is 3.025 g/cm^3. For simplicity, the thin zirconium barrier layer is not modeled; this has a negligible impact on results [10].

Table 2. U-10Mo material composition data

Parameter	Unit	Symbol	Value	Source
Mo density in U-10Mo	g/cm^3	$\rho_{Mo,M}$	1.702	
U density in U-10Mo	g/cm^3	$\rho_{U,M}$	15.318	
U-10Mo density	g/cm^3	ρ_M	17.02	[18, 19]
^{235}U enrichment	g^{235}U/gU	e	0.1975	assumed based on LEU enrichment
^{235}U density in U-10Mo	g/cm^3	$\rho_{U5,M}$	3.025	$\rho_{U,M}(e)$

An enrichment of 19.75 wt % ^{235}U/U is assumed for these studies because this is the established enrichment for the LEU conversion studies. The assumed weight percent for ^{234}U, ^{236}U, and ^{238}U in U are 0.18, 0.09, and 79.78, respectively. The isotopic composition used in the neutron transport calculations is listed in Table 3.

Table 3. U-10Mo material atom fraction data

Isotope	Atom fraction
^{92}Mo^{42}	1.57798E-03
^{94}Mo^{42}	9.86106E-04
^{95}Mo^{42}	1.69871E-03
^{96}Mo^{42}	1.78204E-03
^{97}Mo^{42}	1.02136E-03
^{98}Mo^{42}	2.58439E-03
^{100}Mo^{42}	1.03311E-03
^{234}U^{92}	6.92817E-05
^{235}U^{92}	7.75124E-03
^{236}U^{92}	3.55044E-05
^{238}U^{92}	3.09944E-02

During operation, the accumulation of solid and gaseous fission products that occupy a greater volume than the fissioning uranium will induce swelling of the fuel material. Relative to the current lower density dispersion fuel, which has some accommodating porosity, the high density of the U-10Mo monolithic alloy will cause the fuel plates to swell more. Fuel meat swelling causes the plate thickness to increase, resulting in a reduced in-core coolant-to-metal ratio. The reduction in the volume of water adjacent to the fuel plates degrades reactor performance by introducing negative reactivity and therefore reducing cycle length. It also adversely affects the thermal safety margin by thinning the coolant channel.

The swelling rate of the U-10Mo alloy is functionalized in terms of cumulative fission density, increasing with burnup. In a detailed fuel swelling study, this volumetric swelling was calculated, and the thickness of adjacent coolant channel regions was effectively decreased [13]. The impact of fuel swelling on cycle length was shown to be significant, primarily in terms of shortening the cycle length by approximately 1.5 days due to water displacement and its negative effect on reactivity. Because of the computational expense in explicit modeling, fuel swelling is not specifically modeled in the design study simulations, but fuel cycle metrics are adjusted according to an applied cycle length reduction of 1.5 days. In addition, in the HFIR Steady State Heat Transfer Code (HSSHTC) calculations, fuel swelling is taken into consideration by decreasing the coolant channel thickness to assess the impact on steady state thermal safety margins.

4. COMPUTATIONAL METHODS

A systematic approach for design optimization was developed and deployed [13, 12, 14] to leverage high-fidelity modeling and simulation in determining candidate designs with U-10Mo fuel. This method was first implemented and demonstrated with a 50.8 cm (20 inch) long active fuel region, showing flexibility within the design space to be optimized for different performance metrics. This resulted in two candidate designs with borated side plates: one optimized for uranium utilization with a relatively long cycle length, and one optimized for cold source flux with a cycle length more similar to that of the current HEU fuel design. These two designs demonstrate the flexibility that the U-10Mo fuel form provides, presenting a shorter cycle length option to address potential unknowns in extending the oxide cladding growth correlation beyond the current cycle length for the HEU fuel. An additional design was generated in which boron was moved from the side plate to within the fuel plate cladding, providing another fabrication option for locating burnable poison.

Because the low-density U_3Si_2 fuel designs require elongated fuel regions to generate designs that have adequate cycle lengths, an additional U-10Mo design was generated with a 55.88 cm (22 inch) long active fuel region. The systematic design optimization approach was repeated with elongated fuel with no axial contouring.

The computational tools used in this work are shown in Table 4. Additional design and analysis methods were used to generate response surfaces and to search for optimized designs among the available design space.

Table 4. Analysis codes used for this work

Name	Description	Reference
Shift	Monte Carlo radiation transport code that simulates neutron transport in HFIR, as well as depletion of fuel and target isotopes	[20]
HSSHTC	Reads processed output from Shift to calculate steady-state thermal hydraulic metrics such as heat flux and steady-state temperature	[3, 21]
Design Optimization Tool - Response Surface Methodology (DOTRSM)	Reads design parameter–dependent performance metrics, generates response surfaces, builds surrogate models, and generates optimized designs	[12]
PHAME	Driver for the entire analysis process; organizes and passes data between tools; also contains a visualization suite	[10, 22]

The analysis process is as follows:

1. Define the design space using prior knowledge obtained from previous design work (e.g., reactor power and fuel foil radial shape).
2. Generate Monte Carlo N-Particle code (MCNP) [23] geometry from analyst input (Fig. 2).
3. Generate corresponding Shift input files.

4. Run Shift with critical CE position search to determine critical CE position.
5. Parse Shift outputs to produce reactor physics performance metrics.
6. Create HSSHTC input files from the metric database.
7. Run HSSHTC.
8. Parse HSSHTC output files to store thermal hydraulics metrics.
9. Determine the acceptability of neutronic and thermal hydraulic metrics of the defined design space.
10. Use the optimization suite Design Optimization Tool - Response Surface Methodology (DOTRSM) to functionalize analysis results in terms of design parameters.
11. Use DOTRSM to determine optimized design given some preferred weights.
12. Repeat process to generate neutronics and thermal hydraulic metrics for the optimized design.

While significant portions of this optimization procedure was automated, several disjointed scripts were used to generate metrics and run inputs. A full HFIR Monte Carlo N-Particle code (MCNP) model with a representative experimental loading was used to generate these metrics [24].

Following these design studies, several improvements were made to (1) decrease time of analysis, (2) decrease inconsistencies in the analysis, and (3) increase reproducibility [25, 22]. This analysis suite was used to postprocess some of the design metrics presented herein.

4.1 NEUTRONICS MESH

The involute fuel plates within the fuel elements are explicitly modeled using a set of hexahedra to approximately define the fuel foil, Al fuel plate cladding, and the water coolant between the plates. The radial meshes radii used to define the hexahedra approximating the fuel meat shape are listed in Tables 5 and 6, respectively. A total of 21 radial mesh cells were used to define the IFE, primarily because it has a smaller involute radius and therefore has more curvature than the OFE. The IFE and OFE axial meshes for the 50.8 cm (20 inch) length fuel foil designs consist of 19 cells, as described in Table 7. The elongated fuel design with a 55.88 cm (22 inch) long fuel foil has 21 axial cells, as described in Table 8. Nonuniform radial and axial mesh cells are defined to accurately capture the fuel shape and the flux gradients that occur at the axial and radial extremes of the fuel meat.

4.2 THERMAL-HYDRAULICS MESH

The HSSHTC is a 2D R-Z steady-state heat transfer code with a mesh represented as (i,j) nodes. The IFE and OFE radial meshes defining the fuel meat consist of 11 nodes each, as shown in Table 9. For the 50.8 cm (20 inch) active fuel length designs, the IFE and OFE axial meshes consist of 40 nodes, as shown in Table 10, to align with the current mesh used for the HEU fuel plates. For the 55.88 cm (22 inch) active fuel length designs, the IFE and OFE axial meshes were regenerated to consist of 23 nodes, as shown in Table 11. The HSSHTC node locations were selected based on the following guidelines: (1) ~0.4 cm Δs (Δ distance along arc length s) at radial edges, (2) 0.5 cm Δz at axial edges, (3) internal fuel meat nodes approximately at neutronic s midpoints, (4) internal fuel nodes approximately at neutronic z midpoints, and (5) nodes at location optimized for energy conservation based on the power distribution. Very fine axial and radial meshes at the radial and axial extremes were not desired because HSSHTC does not conduct heat into the unfueled regions and a very fine mesh around the frame of the fuel meat would result in additional over-conservatism. Figure 3 illustrates the HSSHTC nodes superimposed onto the neutronics mesh.

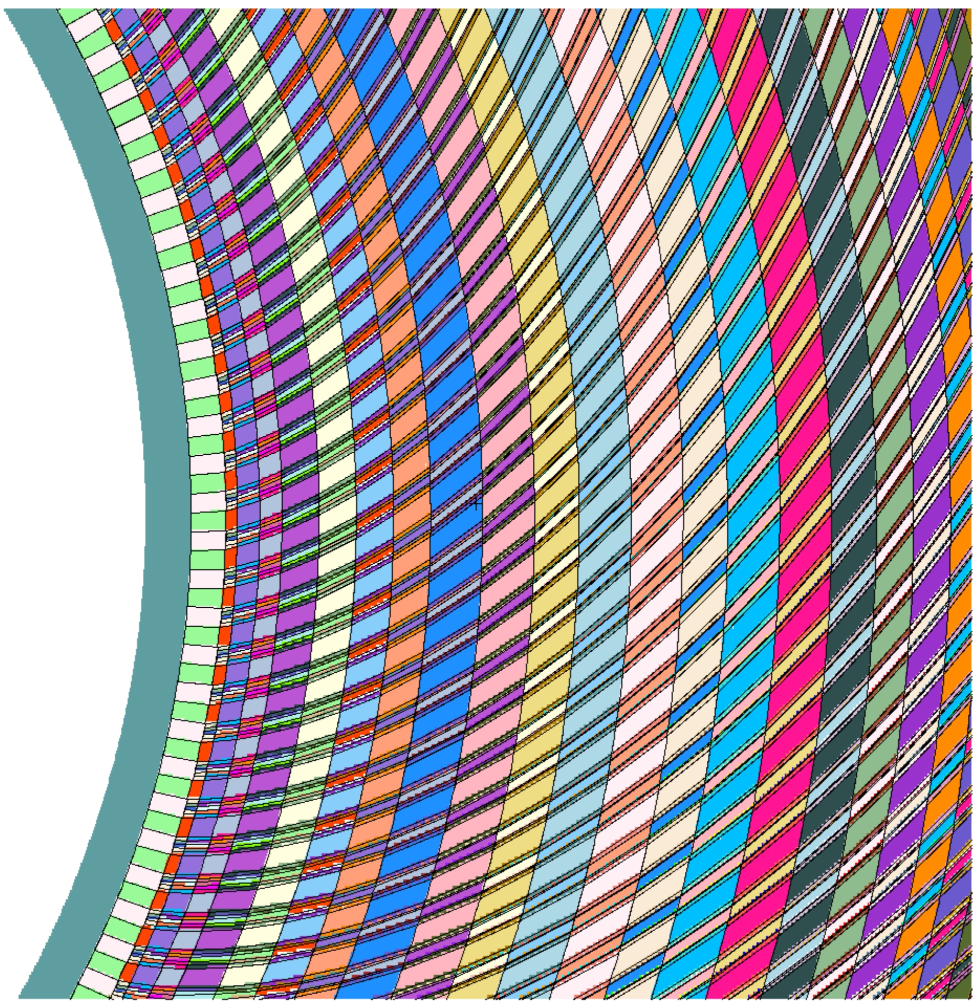

Figure 2. This figure displays the PHAME-generated MCNP file geometry.

Table 5. Radii of the IFE fuel regions in the neutronics model

No.	r_i(cm) *	r_o(cm)	Δr(cm)
1	7.124 378	7.20	0.08
2	7.20	7.35	0.15
3	7.35	7.50	0.15
4	7.50	7.75	0.25
5	7.75	8.00	0.25
6	8.00	8.25	0.25
7	8.25	8.50	0.25
8	8.50	8.85	0.35
9	8.85	9.20	0.35
10	9.20	9.50	0.30
11	9.50	9.85	0.35
12	9.85	10.20	0.35
13	10.20	10.50	0.30
14	10.50	10.85	0.35
15	10.85	11.20	0.35
16	11.20	11.50	0.30
17	11.50	11.75	0.25
18	11.75	12.00	0.25
19	12.00	12.20	0.20
20	12.20	12.40	0.20
21	12.40	12.546 96	0.15

* r_i and r_o are inner and outer radii; $\Delta r = r_o - r_i$

Table 6. Radii of the OFE fuel regions in the neutronics model

No.	r_i(cm) *	r_o(cm)	Δr(cm)
1	15.139 05	15.30	0.16
2	15.30	15.50	0.20
3	15.50	16.00	0.50
4	16.00	16.50	0.50
5	16.50	17.00	0.50
6	17.00	17.50	0.50
7	17.50	18.00	0.50
8	18.00	18.50	0.50
9	18.50	19.00	0.50
10	19.00	19.50	0.50
11	19.50	20.00	0.50
12	20.00	20.50	0.50
13	20.50	20.75	0.25
14	20.75	20.955 36	0.21

* r_i and r_o are inner and outer radii; $\Delta r = r_o - r_i$

Table 7. Axial mesh for fuel regions in the neutronics model with a 50.8 cm (20 inch) active fuel length

No.	z_{upper}(cm) *	z_{lower}(cm)	Δz (cm)
1	25.4	24.9	0.50
2	24.9	24.4	0.50
3	24.4	23.4	1.00
4	23.4	22.4	1.00
5	22.4	21.0	1.40
6	21.0	16.0	5.00
7	16.0	11.0	5.00
8	11.0	6.0	5.00
9	6.0	1.0	5.00
10	1.0	−1.0	2.00
11	−1.0	−6.0	5.00
12	−6.0	−11.0	5.00
13	−11.0	−16.0	5.00
14	−16.0	−21.0	5.00
15	−21.0	−22.4	1.40
16	−22.4	−23.4	1.00
17	−23.4	−24.4	1.00
18	−24.4	−24.9	0.50
19	−24.9	−25.4	0.50

* Location is with respect to the core midplane (at axial location 0.0 cm).

Table 8. Axial mesh for fuel regions in the neutronics model with a 55.88 cm (22 inch) active fuel length

No.	z_{upper}(cm) *	z_{lower}(cm)	Δz (cm)
1	27.94	27.44	0.50
2	27.44	26.94	0.50
3	26.94	25.94	1.00
4	25.94	24.94	1.00
5	24.94	23.00	1.94
6	23.00	18.00	5.00
7	18.00	13.00	5.00
8	13.00	8.00	5.00
9	8.00	3.00	5.00
10	3.00	1.00	2.00
11	1.00	−1.00	2.00
12	−1.00	−3.00	2.00
13	−3.00	−8.00	5.00
14	−8.00	−13.00	5.00
15	−13.00	−18.00	5.00
16	−18.00	−23.00	5.00
17	−23.00	−24.94	1.94
18	−24.94	−25.94	1.00
19	−25.94	−26.94	1.00
20	−26.94	−27.44	0.50
21	−27.44	−27.94	0.50

* Location is with respect to the core midplane (at axial location 0.0 cm).

Table 9. Radii of the fuel nodes in the HSSHTC model

i	IFE r (cm)	OFE r (cm)
3	7.124	15.139
4	7.493	15.521
5	7.820	15.837
6	8.254	16.252
7	9.014	17.007
8	10.012	18.007
9	11.011	19.007
10	11.753	19.752
11	12.119	20.279
12	12.326	20.67
13	12.547	20.955

Table 10. Axial mesh for fuel nodes in the HSSHTC model with a 50.8 cm (20 inch) active fuel length

i	z (cm) *	i	z (cm)
3	25.40	22	−1.13
4	24.90	23	−3.50
5	24.50	24	−6.00
6	24.10	25	−8.50
7	23.70	26	−11.00
8	23.30	27	−13.50
9	22.88	28	−16.00
10	22.40	29	−18.15
11	21.80	30	−19.80
12	21.00	31	−21.00
13	19.80	32	−21.80
14	18.15	33	−22.40
15	16.00	34	−22.88
16	13.50	35	−23.30
17	11.00	36	−23.70
18	8.50	37	−24.10
19	6.00	38	−24.50
20	3.50	39	−24.90
21	1.13	40	−25.40

*Location is with respect to the core midplane at axial location 0.0 cm.

Table 11. Axial mesh for fuel nodes in the HSSHTC model with a 55.88 cm (22 inch) active fuel length

i	z (cm) *	i	z (cm)
3	27.94	15	−2.00
4	27.44	16	−5.50
5	26.94	17	−10.50
6	26.32	18	−15.50
7	25.44	19	−20.50
8	23.97	20	−23.97
9	20.50	21	−25.44
10	15.50	22	−26.32
11	10.50	23	−26.94
12	5.50	24	−27.44
13	2.00	25	−27.94
14	0.00		

*Location is with respect to the core midplane at axial location 0.0 cm.

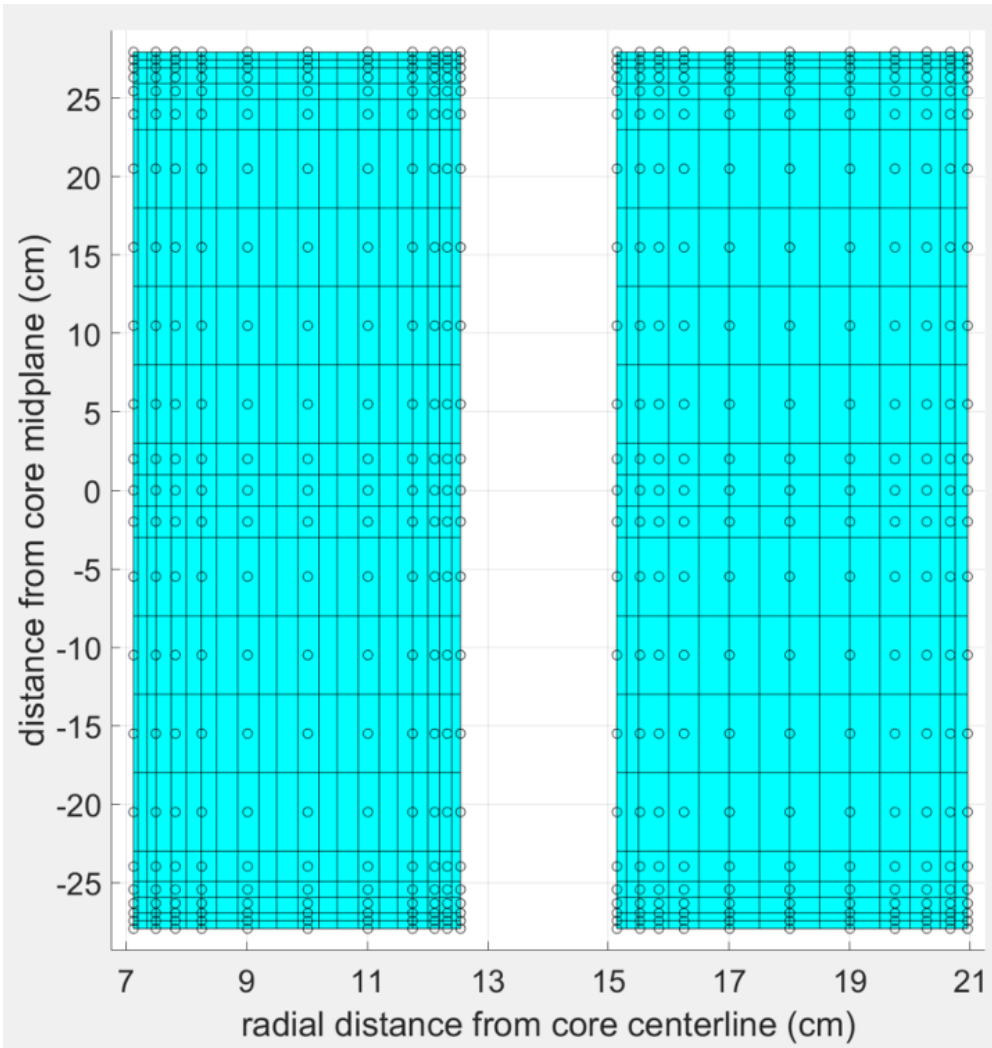

Figure 3. Fuel element HSSHTC nodes (black circles) superimposed on neutronics mesh (black lines) for the 55.88 cm (22 inch) fuel design.

4.3 DESIGN PARAMETER CALCULATION METHODS

4.3.1 Fission Rate Density

The fission rate density f_d in a given fuel region is

$$f_d = \frac{1}{V_{\text{fuel}}} \sum_{i}^{M} \int_{0}^{\infty} dE \int_{\partial V \in V_{\text{fuel}}} dV N_i(\mathbf{r}) \sigma_{i,f}(\mathbf{r}, E) \phi(\mathbf{r}, E), \tag{1}$$

where V_{fuel} is the volume of the given fuel region, N_i is the number density of isotope i, $\sigma_{i,f}$ is the fission cross section of isotope i, ϕ is the scalar flux, and the sum is over the M fissionable isotopes within the fuel region. The unit of f_d is fissions per second per cubic cm of fuel particle.

4.3.2 Cumulative Fission Density

Cumulative fission density is calculated by taking the time integral of the fission rate density values:

$$F_d(t_f) = \frac{1}{V_{\text{fuel}}} \sum_{i}^{M} \sum_{t}^{T} \int_{0}^{\infty} dE \int_{\partial V \in V_{\text{fuel}}} dV N_{i,t}(\mathbf{r}) \sigma_{i,f}(\mathbf{r}, E) \phi_t(\mathbf{r}, E) \Delta t. \tag{2}$$

The unit of F_d is fissions per cubic cm of fuel particle. The maximum cumulative fission density in this report is an interpolated value between the last full cycle day and the next day. For example, if the cycle length is 26.7 days, then the maximum cumulative fission density is at:

$$F_d(26.7) = F_d(26) + [F_d(27) - F_d(26)] \times 0.7. \tag{3}$$

4.3.3 Power Density

Power density is calculated by multiplying the fission rate density by the average energy generated per fission (200.7 MeV *). A conservative assumption is made that all energy generated by fission is deposited locally in the fuel meat:

$$P_d = f_d * 200.7 \frac{MeV}{fission} * \frac{1.60218 * 10^{-16}\,\text{kJ}}{1\text{MeV}}. \tag{4}$$

The unit of P_d is kW per cubic cm of fuel particle.

4.3.4 Heat Flux

Nominal heat fluxes are estimated using the following expression:

$$q''_{(r,z)}(\frac{W}{cm^2}) = \overline{q''}(\frac{W}{cm^2})\phi_{(r,z)} = \frac{P_{tot}(W) f_{FE}}{A(cm^2)} \phi_{(r,z)}, \tag{5}$$

*This Q value of 200.7 Mev/fission is a ‘typical’ Q value used in HFIR analyses close to the approximate cycle-averaged value that was recently calculated for the optimized silicide design. The BOC and EOC Q values were estimated to be 200.49 and 201.46 MeV/fission, respectively, givin the average Q value of 200.98 MeV/fission [6].

where $q''_{(r,z)}$ is the nominal heat flux at (r, z), $\overline{q''}$ is the core average heat flux, $\phi_{(r,z)}$ is the relative fission density at (r, z), P_{tot} is the total reactor power, f_{FE} is the fraction of total heat deposited in the fuel element, and A is the heat transfer area. A f_{FE} value of 0.965 is used from [26], and a heat transfer area of $4.3820e^5 cm^2$ is used for 22-inch fuel, as shown below in Eq. (6):

$$A_{FE} = (\Delta s_{IFE} \times N_{IFE} + \Delta s_{OFE} \times N_{OFE}) \times (H \times 2), \tag{6}$$

where Δs = length of fuel meat along involute,
N = number of fuel plates in fuel element, and
H = height of fuel plate.

4.4 DESIGN OPTIMIZATION METHODS

A design optimization approach was developed to systematically explore the available design space with U-10Mo fuels and to quickly generate optimized designs given desired metrics and design parameters [12, 14]. The first step in the process was to determine the possible design parameter ranges defining the U-10Mo designs: reactor power, total fuel mass, mass split betweeen the IFE and OFE, fuel radial contour shape, and boron loading. Then, a surrogate model was built using the results from several high-fidelity simulations to quickly generate key metrics given specific design parameters. A search algorithm then used results from this surrogate model to search the design space and determine an optimized design given a specified weighting for the performance metrics. More detail on this optimization approach is provided in the literature [12, 14].

This systematic design process was first completed for 50.8 cm (20 inch) long active fuel designs. The large available design space allowed for selection of two feasible optimized designs: one optimized for cold source flux, and one optimized for uranium utilization (Table 12). An additional version relocating the boron from the side plate to the fuel plate cladding was also generated.

Table 12. Comparison of weights used to generate candidate designs

Parameter	Cold weight	Utilization weight
Cf production	0.5	1.0
Cycle length	-	-
Cold source moderator vessel cold flux	10.0	1.0
Cold source cold flux ratio	1.0	1.0
Reflector fast flux	0.1	1.0
Reflector fast flux ratio	0.1	1.0
Flux trap fast flux	0.1	1.0
Flux trap flux ratio	0.1	1.0
Cm target flux	0.5	1.0
Uranium utilization	-	10.0

After this design study was complete, this systematic design process was repeated for 55.88 cm (22 inch) long active fuel designs without an axial contour. The longer designs allowed for the thinning of the fuel foil shape such that an axial flat shape met all metrics, but only at powers lower than 100 MW. The longer fuel zone also results in effectively spreading out the power, reducing the power per unit length. Therefore, the available design space for these longer fuel designs was significantly reduced.

5. CANDIDATE FUEL DESIGN PARAMETERS

All four U-10Mo fuel designs share some key geometric and operational characteristics (Table 13). All fuel designs have centered and symmetric fuel zones, meaning that the fuel foil is centered within the thickness of the fuel plate to provide equal heat conduction on each side of the plate. The designs have different features that impact manufacturing processes and resulting design parameters (Table 14). Table 15 shows the design features selected for these fuel design options. The fuel axial length may either be 50.8 cm (20 inches) as in the current HEU fuel design, or it may be lengthened to 55.88 cm (22 inches), as in most of the U_3Si_2 fuel designs. Two candidate designs have similar characteristics, but they are optimized for different performance metrics—cold source flux and uranium utilization (description of the metrics are shown in Table 16).

Table 13. Key HFIR LEU geometry and operational parameters common to all presented designs

Parameter	Units	Value	
Power	MW	100, 95	
Coolant	-	light water	
Inlet coolant temperature	°C	48.89	
Inlet coolant pressure	MPa	3.33	
Primary flow rate	m^3/s	1.01	
Number of fuel elements	-	2	
Zr thickness	μm	25.4	
Fuel plate thickness	μm	1270	
Coolant channel thickness	μm	1270	
Metal-to-water ratio	-	1	
Active fuel meat length	cm	50.8, 55.88	
Fuel plate length	cm	60.96	
Active fuel zone volume	L	50.53, 55.58	
Average power density	MW/L	1.98, 1.71	
Fuel meat heat transfer area	m^2	40.12, 44.13	
		IFE	**OFE**
Number of fuel plates	-	171	369
Involute radius	cm	6.91261	14.91742
Fuel plate width	cm	9.21004	8.09752
Distance from inner plate edge to involute origin	cm	0.29718	0.29464
Distance along involute to fuel meat start	cm	0.23114	0.23439
Distance along involute to fuel meat end	cm	8.02706	7.32267
Fuel meat width	cm	7.79592	7.08828
Fuel meat heat transfer area	m^2	13.54432, 14.89875	26.57425, 29.23167
Inner radius of fuel meat	cm	7.12438	15.13905
Outer radius of fuel meat	cm	12.54696	20.95536
Active fuel zone volume	L	17.02368, 18.72606	33.50434, 36.85477

The input generation script allows the user to specify different combinations of design features. Figure 4 shows the MCNP geometry representation of these design features.

Table 14. Fuel design features and benefits

Design option	Description	Benefit
Axial contour (i.e., toe)	The lowest 3 cm of the fuel is linearly interpolated from the top shape to a radially flat fuel profile with reduced thickness.	Because the coolant flows from top to bottom in HFIR, the location of the limiting thermal margin is at the bottom (i.e., the outlet). By reducing fuel mass on the bottom, outlet power peaking is reduced.
Center and symmetric fuel zone	The fuel meat is centered and symmetric within the fuel plate thickness and is surrounded by an equal amount of cladding on each side (plates consist of cladding, fuel, and cladding, instead of cladding, fuel, and cladding).	Enhances heat transfer path from fuel meat to coolant. The amount of heat dissipated from the convex and concave sides of the involute are equal.
Reactor power	Thermal power output of the HFIR reactor	Increasing the power increases flux in the core, but it tends to reduce cycle length and minimum burnout margins.
Long fuel	Axial length of the fuel is increased from 20 inches to 22 inches.	Longer fuel means more fissile material can be loaded, but it also will decrease the minimum burnout margin at the bottom of the fuel.
Boron placement	Boron is placed on either the side plate or the fuel plate.	Placement of boron mitigates local power peaking.

Table 15. Currently analyzed U-10Mo designs that meet the performance and safety metrics

Name	Axial contour	Reactor power [MWt]	Long fuel	Boron location
22-inch	N	95	Y	Side plate
Utilization	Y	100	N	Side plate
Cold	Y	100	N	Side plate
Bclad	Y	100	N	Fuel plate

*All designs have center-symmetric fuel.

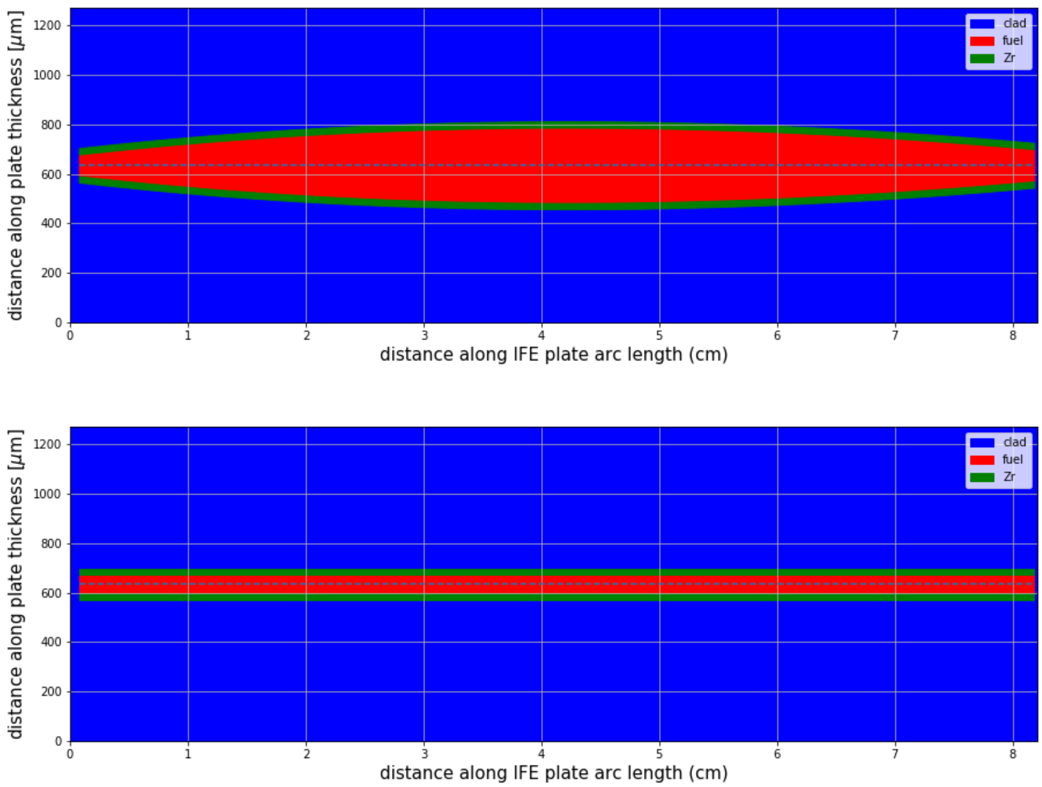

Figure 4. The top image shows the center and symmetric fuel. The bottom image shows the center and symmetric fuel shape at the bottom of the axial fuel zone. The axial contour interpolates between these two shapes, reducing the fuel thickness to 75 μm over the bottom 3 cm of the active fuel zone.

6. OVERVIEW OF METRICS

The metrics used to measure the LEU core performance and safety are shown in Table 16. A more detailed explanation is provided in Ilas et al. [15].

All the designs meet or exceed HEU metrics (Table 17). The most variation in performance between designs is seen in cycle length and Cf production rate.

6.1 DESCRIPTION OF METRICS

This section presents a brief description and the calculation method for each metric. All flux metrics are spatially and temporally averaged, so the single value denotes the average value across all radial, axial, and temporal (day) meshes.

6.1.1 Cf Production Rate

One of the primary missions of HFIR is isotope production, including the production of ^{252}Cf , which is created within the curium-oxide targets inside the flux trap region through a complex absorption and decay chain. This metric is calculated by obtaining the mass of ^{252}Cf at the end of the cycle and dividing by the cycle length.

Table 16. Metrics used to measure the performance and safety of the LEU core

Metric	Type	Units	Description
Cf production rate	Performance	mg/day	Time-averaged mass of Cf produced from the Cm targets
Cm target thermal flux	Performance	$\frac{\text{neutrons}}{\text{cm}^2\cdot\text{s}}$	Thermal flux (E < 0.625 eV) in the Cm target
Cold source moderator vessel cold flux ratio	Performance	-	Ratio of cold flux (E < 0.103978 eV) to total flux in cold source
Cold source moderator vessel cold flux	Performance	$\frac{\text{neutrons}}{\text{cm}^2\cdot\text{s}}$	Cold flux (E < 0.103978 eV) in the moderator vessel
Cycle length	Performance	days	Number of days the LEU core can maintain criticality
Flux trap fast flux	Performance	$\frac{\text{neutrons}}{\text{cm}^2\cdot\text{s}}$	Fast flux (E > 0.1 MeV) in flux trap
Flux trap fast flux ratio	Performance	-	Ratio of fast flux (E > 0.1 MeV) to total flux in flux trap
Reflector fast flux	Performance	$\frac{\text{neutrons}}{\text{cm}^2\cdot\text{s}}$	Fast flux (E > 0.1 MeV) in reflector
Reflector fast flux ratio	Performance	-	Ratio of fast flux (E > 0.1 MeV) to total flux in reflector
^{235}U loading	Design	kg	Mass of ^{235}U in the fuel
^{235}U utilization	Performance	day/kg	Cycle length divided by loaded ^{235}U
Minimum burnout margin	Safety	-	Thermal safety margin

6.1.2 Cycle Length

Cycle length denotes the number of days the core can maintain criticality. The critical element position search module determines positions throughout operation, ending when the core is subcritical, with the control elements fully withdrawn. From the control element position curve, an interpolation is made to estimate the cycle length. For example, if a core is subcritical with fully withdrawn control elements starting on day 27, then the cycle length would be 26.N days, where N is interpolated from the control element position curve.

6.1.3 Cold Source Flux and Ratio

The cold source flux magnitude and cold-to-total flux ratio indicate the quality of the flux for cold neutron science. Increased brightness (i.e., greater magnitude) and reduced noise (i.e., higher cold-to-total flux ratio) are desired. Because LEU fuel has a more hardened spectrum than HEU, the cold-to-total flux ratios of these designs do not meet HEU metrics.

Because the cold source neutron source region is radially external to the control elements, the cold source region flux is highly affected by the control element location. Therefore, designs with longer cycle lengths and associated slower control element withdrawals have a relatively lower average cold source flux.

6.1.4 Flux Trap Fast Flux and Ratio

The flux trap is the center region in HFIR that experiences the highest flux ($\sim 10^{15}\,\frac{\text{neutrons}}{cm^2\cdot\text{s}}$). The flux trap region is used for isotope production and materials irradiation testing. Fast flux in the flux trap is used for materials irradiation studies to accelerate damage testing. The fast flux and fast-to-total flux ratio metrics are calculated by spatially averaging the fast fluxes in the material irradiation targets located in the flux trap. This results in a time-resolved quantity that is then averaged over the cycle.

Table 17. Performance and safety metrics for the U-10Mo LEU silicide designs meet or exceed HEU metrics except for the cold source cold flux ratio, minimum burnout margin, and uranium utilization.

Metrics	HEU	22-inch	utilization	cold	boron-clad
Cf production rate	1.388	1.461	1.627	1.511	1.596
Cycle length	26.2	31.789	34.321	26.602	31.953
Cm target flux	>1.00E+15	1.56E+15	1.63E+15	1.66E+15	1.64E+15
Flux trap fast flux	1.07E+15	1.10E+15	1.25E+15	1.25E+15	1.24E+15
Flux trap fast flux ratio	0.29	0.308	0.32	0.316	0.316
Reflector fast flux	2.89E+14	3.14E+14	3.24E+14	3.34E+14	3.24E+14
Reflector fast flux ratio	0.192	0.2	0.202	0.198	0.201
Cold source cold flux ratio	0.736	0.721	0.717	0.72	0.718
Cold source flux	4.48E+14	4.47E+14	4.67E+14	4.85E+14	4.67E+14
Minimum burnout	1.61	1.536	1.53	1.592	1.542
^{235}U loading	9.4	19.713	23.989	19.486	23.805
^{235}U utilization	2.78	1.613	1.431	1.365	1.342

6.1.5 Minimum Burnout Margin

Safety limit (SL) calculations must show that for cases in which a given process variable is at its SL, all other variables are at their limiting control settings (LCSs), and all uncertainties in the technical knowledge of the process are resolved unfavorably. If these conditions are met, then no hot spot burnout can occur. At each time step, HSSHTC determines the average temperatures and heat fluxes at the given power and then calculates the effects of uncertainties in reactor process conditions, tolerances and uncertainties in fuel manufacturing, and analysis/correlation uncertainties. At the last time step specified in the input, the reactor power is increased until the hot spot surface heat flux is equal to the surface heat flux predicted by the Gambill burnout heat flux correlation [27]. The burnout margin metric is defined as the burnout-to-nominal power ratio, and the minimum burnout margin is the smallest ratio calculated over the cycle.

For the 95 MW or 100 MW LEU core, a minimum burnout power of 129.2 MW or 136 MW is required to meet the current 1.36 flux-to-flow SL; however, a greater margin is required to render an LEU design option feasible, because the minimum predicted HEU margin is 1.61, and the assumptions made for the LEU fuel uncertainty factors associated with manufacturing tolerances and physics correlations may need to be refined. This makes it prudent to favor a more conservative calculation at this stage in the analysis. It is ideal to maintain the HEU-calculated margin (1.61), but a margin of 1.51 has been defined by the HFIR conversion team as the minimum margin to declare a LEU design feasible. This margin has been somewhat arbitrarily selected based on a previous SL and the difference between the SL and the calculated limit being ≈0.15. The difference of 0.15 is then added to the current SL of 1.36 to arrive at 1.51.

A design that meets the HEU calculated 1.61 is preferred, but given the tight restraints on the design space, the 1.51 margin is adequate as long as it notably passes the technical safety requirement (TSR) SL of 1.36 and the reduced margin is offset by performance and fabrication improvements.

6.1.6 Reflector Fast Flux and Ratio

The removable beryllium reflector has eight large aluminum-lined irradiation positions, and one of these facilities is often used for materials irradiation purposes when large targets are to be irradiated. For the reflector flux, these metrics are calculated by spatially averaging the fluxes in the 8 irradiation facilities (1A, 1B, 3A, 3B, 5A, 5B, 7A, 7B) within the removable beryllium reflector region. This results in a time-resolved quantity that is then averaged over the cycle.

6.1.7 ^{235}U Loading and Utilization

The ^{235}U loading metric denotes a total mass of ^{235}U in the fuel elements. The mass of fissile material is roughly proportional to the cycle length. The utilization metric is the cycle length divided by the initial ^{235}U mass loading. The HEU core has a lower ^{235}U loading and a higher utilization because it has a substantially lower amount of ^{238}U, so it is less impacted by fuel parasitic neutron absorption.

7. DESIGN SPECIFICATIONS AND PARAMETERS

This section presents the four candidate designs and their time-dependent, nominal maximum detailed design parameters (i.e., fission rate density, power density, heat flux, and cumulative fission density.). The larger plots that show the spatially dependent values are provided in the appendices for readability. The reference numbers in each section are links to the plots in the document. The plots only show the beginning-of-cycle (BOC), first day, middle-of-cycle (MOC), and end-of-cycle (EOC) values. The BOC and EOC state points are provided because they bound the cycle operations. Results at the first day into the cycle are provided because at that stage, fission product poisons have approximately reached their equilibrium conditions, the control elements have rapidly withdrawn with respect to BOC, and the peak parameters at the outer radial edge of the OFE on the core midplane can be observed. MOC conditions are provided because they approximately represent cycle average results.

The fuel plate geometry for each design is discussed in the following subsections for the four designs. As an example, interpretation of the 22-inch design's IFE fuel plate is illustrated in Figure 5. The fuel meat thickness (t) profiles are defined as polynomial curves, $f(x)$, where x is the arc distance from the origin of the involute-generating radius. Thus, $x = 0$ is the origin of the involute-generating radius, which is 2.7215 inches (6.91261 cm) from the reactor core centerline for the IFE. The distance from the inner edge of the IFE plate to the origin of the involute is 0.117 inches (0.29718 cm). The distances from the origin of the involute to the fuel meat start and stop edges are taken as 0.091 inches (0.23114 cm) and 3.16026 inches (8.02706 cm). The nominal fuel plate arc length is 3.626 inches (9.21004 cm).

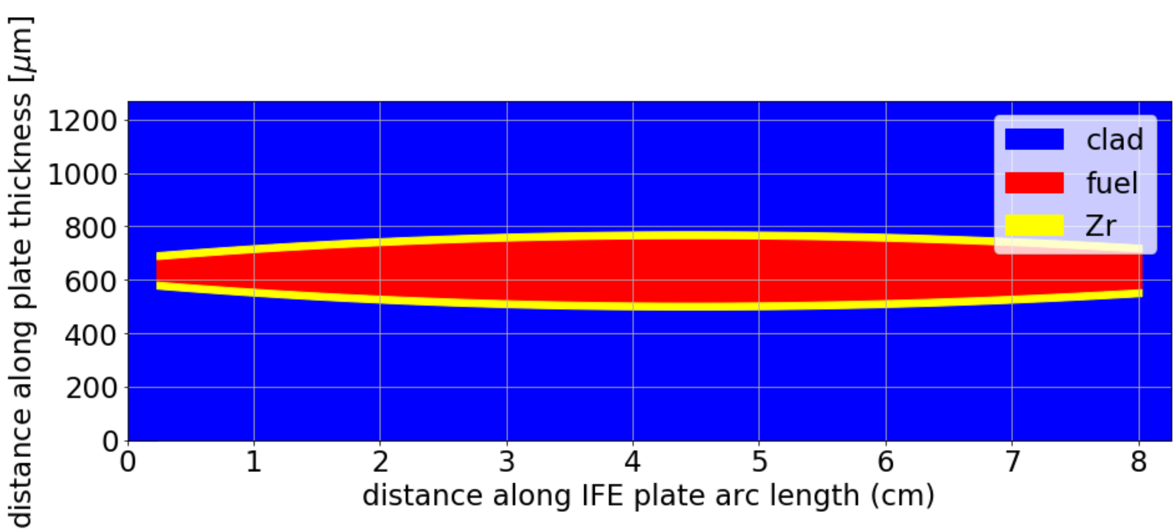

Figure 5. Interpretation of fuel plate plots with 22-inch design IFE illustrated.

7.1 22-INCH DESIGN

The 22-inch design is generated by elongated fuel zone, borated side plates, no axial contour, and performance metrics weighted favoring uranium utilization. The cycle length of this design is 31.79 days. The 22-inch fuel design specifications are presented in Table 18.

Table 18. Key 22-inch design geometry and operational parameters

Parameter	Units	Value	
Center-symmetric fuel zone	–	yes	
Axial contour	–	no	
U loading	kg	99.813	
^{235}U loading	kg	19.7131	
^{10}B loading	g	3.56	
		IFE	OFE
^{235}U loading	kg	4 4727	15 2404
^{235}U loading per plate	g/plate	26 15614	41 3019
Active fuel length	cm	55.88	
Reactor power	MW	95	

7.1.1 Fuel Meat Shape

The fuel meat thickness profile of the 22-inch design is described in Table 19, where the thickness of the fuel meat (μm) is represented by a polynomial function of the distance from the origin of the involute-generating radius (cm). Illustrations of the IFE and OFE fuel meat shapes are shown in Figure 6.

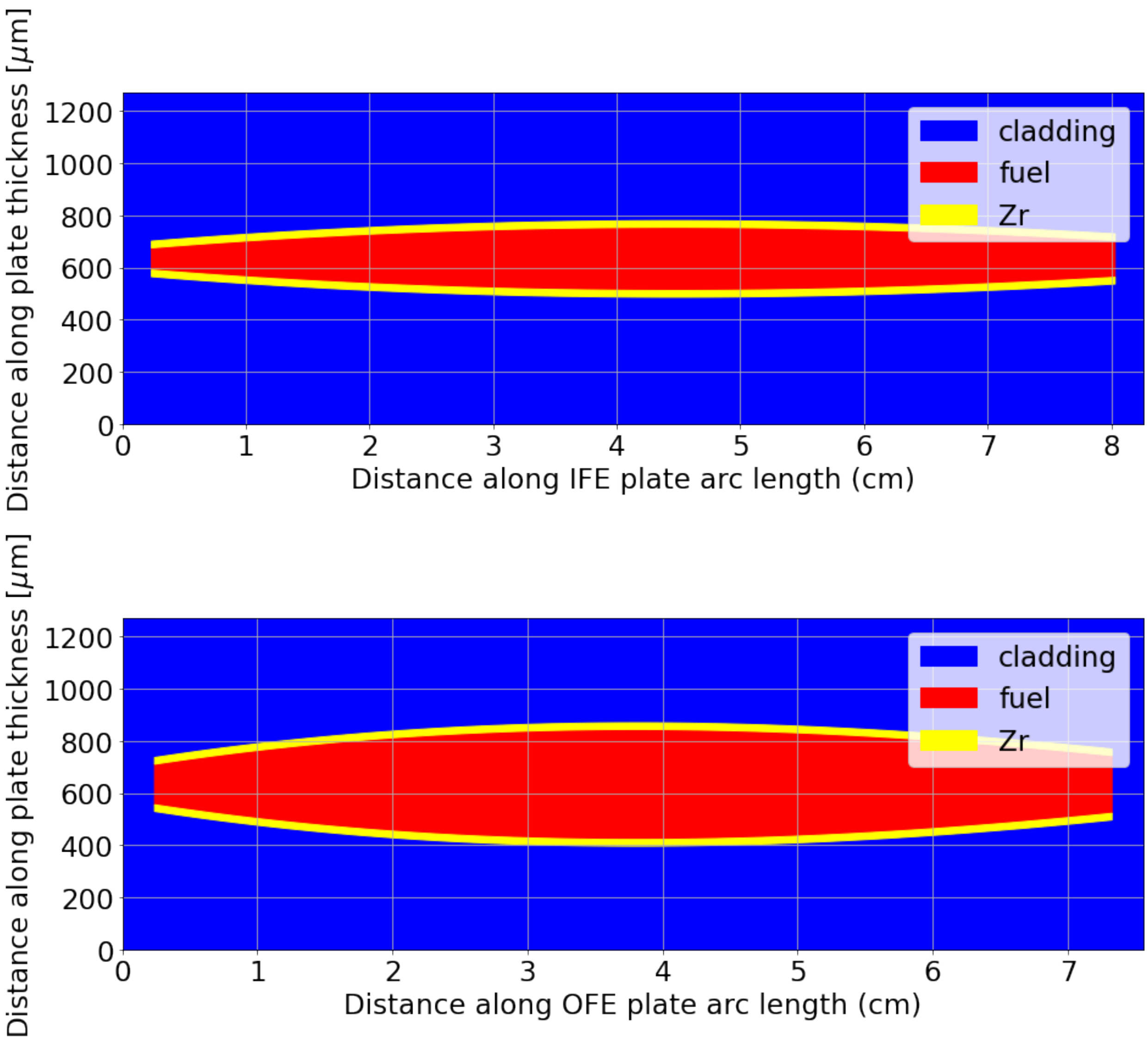

Figure 6. IFE (top) and OFE (bottom) fuel meat shapes for the 22-inch design.

Table 19. Fuel shape polynomial coefficients for the inch 22 design

Order	3	2	1	0
IFE	0.0954	-9.6307	80.3829	66.9045
OFE	0.6856	-26.3541	170.4414	116.8665

7.1.2 Fission Rate Density

Figure 7 shows the maximum fission rate density during operation for each fuel element. Table 20 lists the peak fission rate results and provides references to the figures in the appendices that illustrate the spatial fission rate density values for the four selected state points for each fuel element.

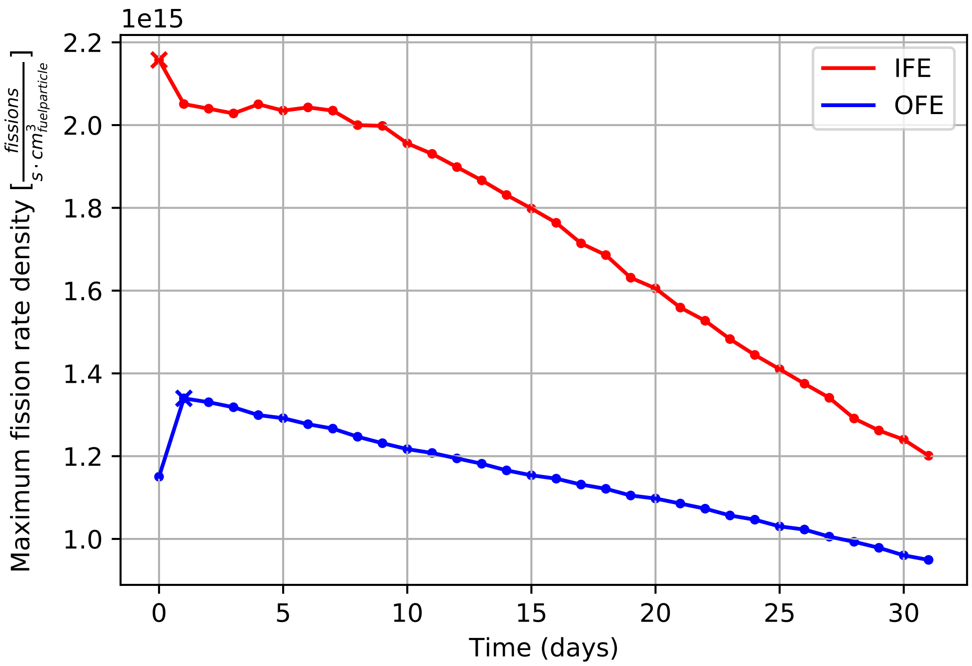

Figure 7. 22-inch design maximum fission density during operation.

Table 20. Minimum and maximum fission rate densities in the 22-inch design.

Day	Region	Minimum	Maximum	Unit	Ref.
0	IFE	3.54	21.57	$10^{14}\ \frac{\text{fissions}}{\text{s}\cdot\text{cm}^3_{fuelparticle}}$	Fig. 33
1	IFE	3.4	20.51		Fig. 34
15	IFE	3.52	17.98		Fig. 35
31	IFE	3.7	12.01		Fig. 36
0	OFE	1.24	11.5		Fig. 37
1	OFE	1.25	13.4		Fig. 38
15	OFE	1.41	11.54		Fig. 39
31	OFE	1.65	9.49		Fig. 40

7.1.3 Power Density

The power density values are the fission rate density values multiplied by the average energy generated per fission. It is conservatively assumed that all energy generated by fission is deposited locally in the fuel meat. Therefore, the power density and fission rate density results have identical trends, and only the magnitudes of the results are different. Figure 8 shows the maximum local power density during operation for each fuel element. Table 21 lists the maximum power density results and provides references to the figures in the appendices. Plots in the appendices show the spatial power density values for each of the four selected state points for each fuel element.

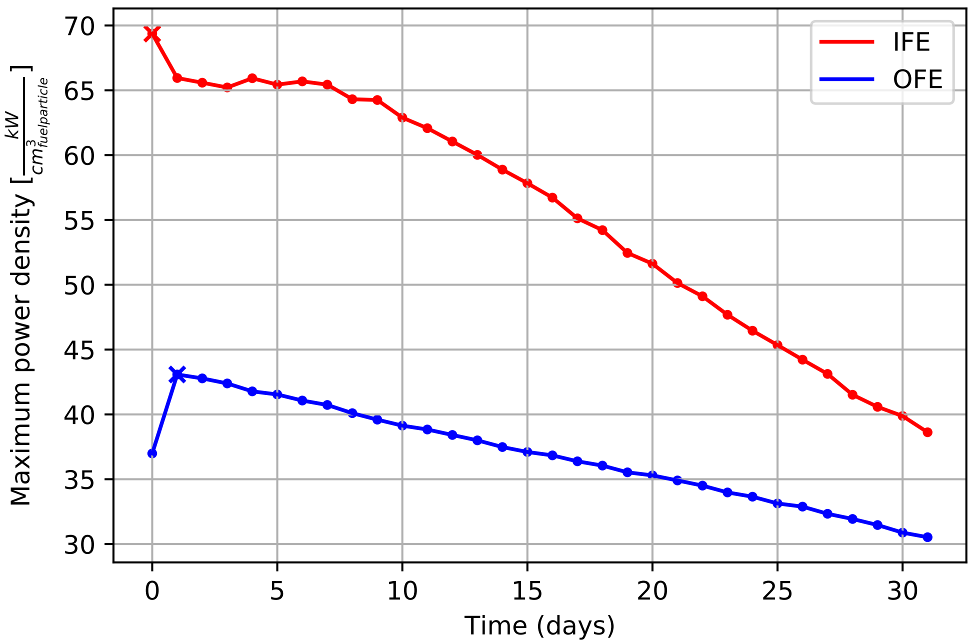

Figure 8. 22-inch design maximum power density during operation.

Table 21. Minimum and maximum power densities in the 22-inch design.

Day	Region	Minimum	Maximum	Unit	Ref.
0	IFE	11.38	69.37	$\frac{kW}{cm^3_{fuelparticle}}$	Fig. 47
1	IFE	10.92	65.95		Fig. 48
15	IFE	11.3	57.83		Fig. 49
31	IFE	11.91	38.62		Fig. 50
0	OFE	3.97	36.99		Fig. 51
1	OFE	4.03	43.08		Fig. 52
15	OFE	4.54	37.1		Fig. 53
31	OFE	5.29	30.53		Fig. 54

7.1.4 Heat Flux

Figure 9 shows the maximum heat flux during operation for each fuel element. Table 22 lists the maximum heat flux results and provides references to the figures in the appendices. Plots in the appendices show the spatial heat flux values for the four selected state points for each fuel element.

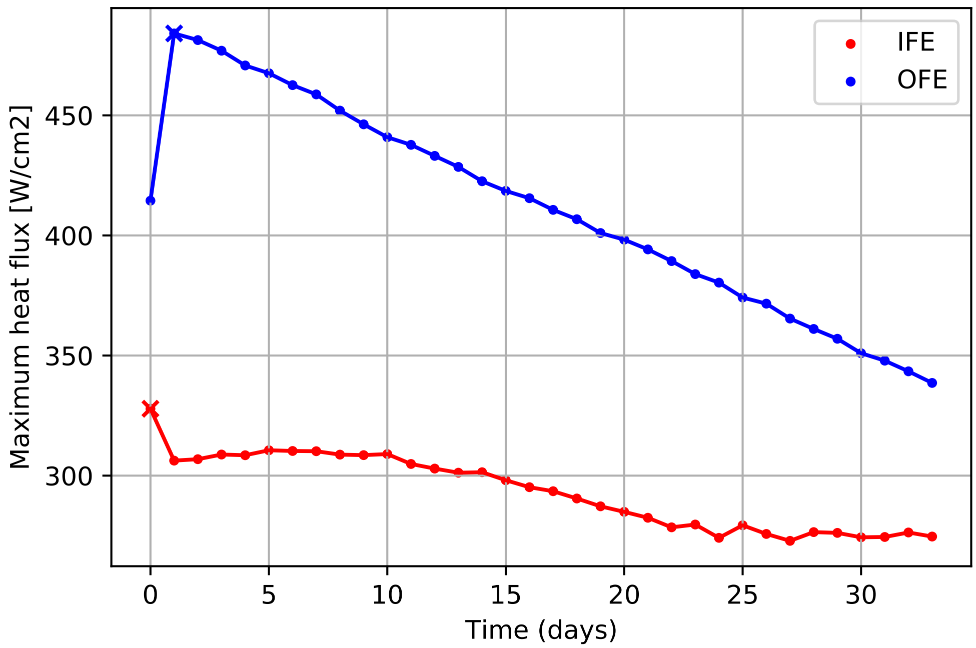

Figure 9. 22-inch design maximum heat flux during operation.

Table 22. Minimum and maximum heat fluxes in the 22-inch design.

Day	Region	Minimum	Maximum	Unit	Ref.
0	IFE	122.4	327.85	$\frac{W}{cm^2}$	Fig. 55
1	IFE	119.84	306.25		Fig. 56
15	IFE	131.9	298.09		Fig. 57
33	IFE	140.93	274.64		Fig. 58
0	OFE	48.28	414.48		Fig. 59
1	OFE	51.37	484.1		Fig. 60
15	OFE	68.82	418.54		Fig. 61
33	OFE	114.52	338.59		Fig. 62

7.1.5 Cumulative Fission Density

Figure 10 shows the maximum local cumulative fission density during operation for each fuel element, and Figure 11 illustrates the fission rate density variation with cumulative fission density for every spatial cell in the neutronics model. Table 23 lists the maximum cumulative fission density results and provides references to the figures in the appendices.

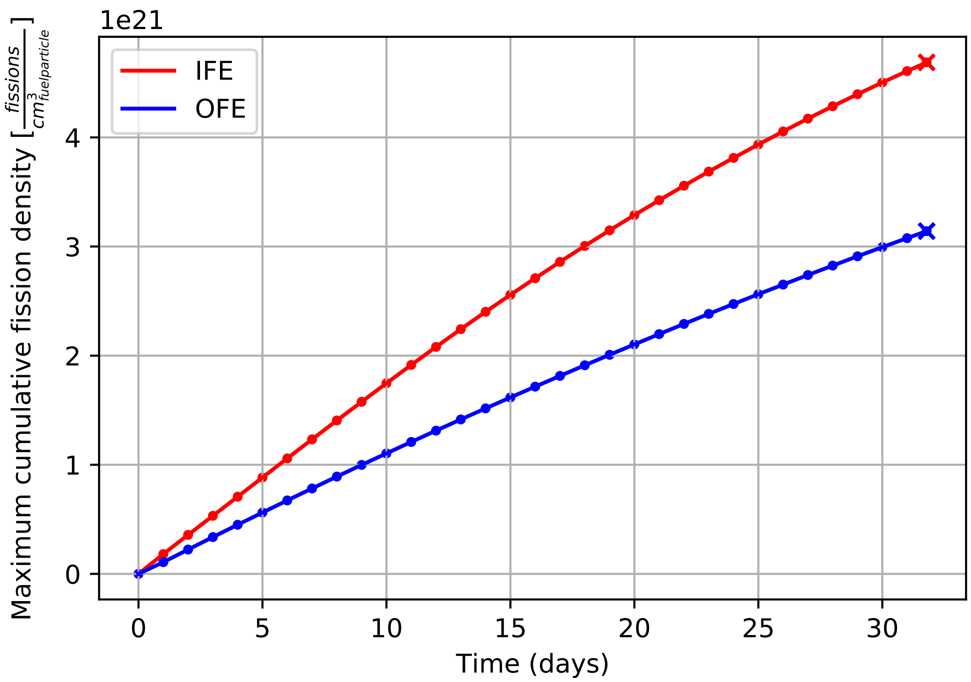

Figure 10. 22-inch design maximum cumulative fission density during operation.

Table 23. Minimum and maximum cumulative fission density values in the 22-inch design.

Day	Region	Minimum	Maximum	Unit	Ref.
1	IFE	0.3	1.82	$10^{20}\ \frac{\text{fissions}}{\text{cm}^3_{fuelparticle}}$	Fig. 41
15	IFE	4.5	25.57		Fig. 42
31	IFE	9.5	46.88		Fig. 43
1	OFE	0.11	1.08		Fig. 44
15	OFE	1.73	16.17		Fig. 45
31	OFE	3.82	31.41		Fig. 46

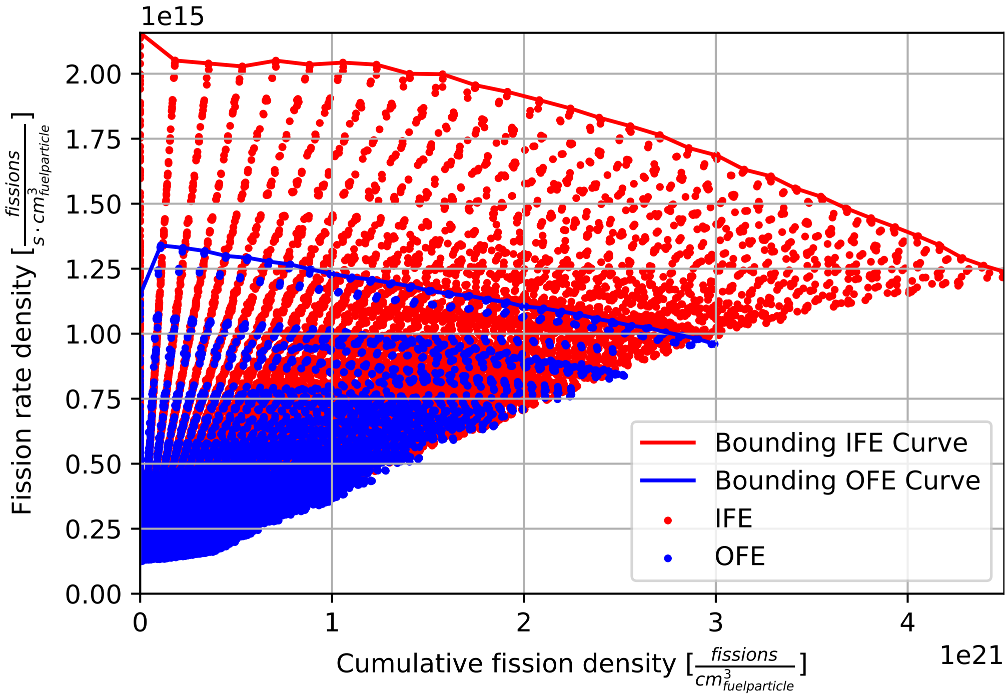

Figure 11. 22-inch design fission rate density variation with cumulative fission density during operation.

7.2 UTILIZATION DESIGN

The utilization design has a 20-inch fuel axial length with borated side plates, axial contour, and performance metrics weighted favoring uranium utilization. The cycle length of this design is 34.32 days. The utilization fuel design specifications are presented in Table 24.

Table 24. Key utilization design geometry and operational parameters

Parameter	Units	Value	
Center-symmetric fuel zone	–	yes	
Axial contour	–	yes	
U loading	kg	121.461	
^{235}U loading	kg	23.9885	
^{10}B loading	g	3.56	
		IFE	OFE
^{235}U loading	kg	6 0647	17 9238
^{235}U loading per plate	g/plate	35 46608	48 57398
Active fuel length	cm	50.8	
Reactor power	MW	100	

7.2.1 Fuel Meat Shape

The fuel meat thickness profile of the utilization design is described in Table 25, where the thickness of the fuel meat (μm) is represented by a polynomial function of the distance from the origin of the involute-generating radius (cm). Illustrations of the IFE and OFE fuel meat shapes are shown in Figures 12 and 13.

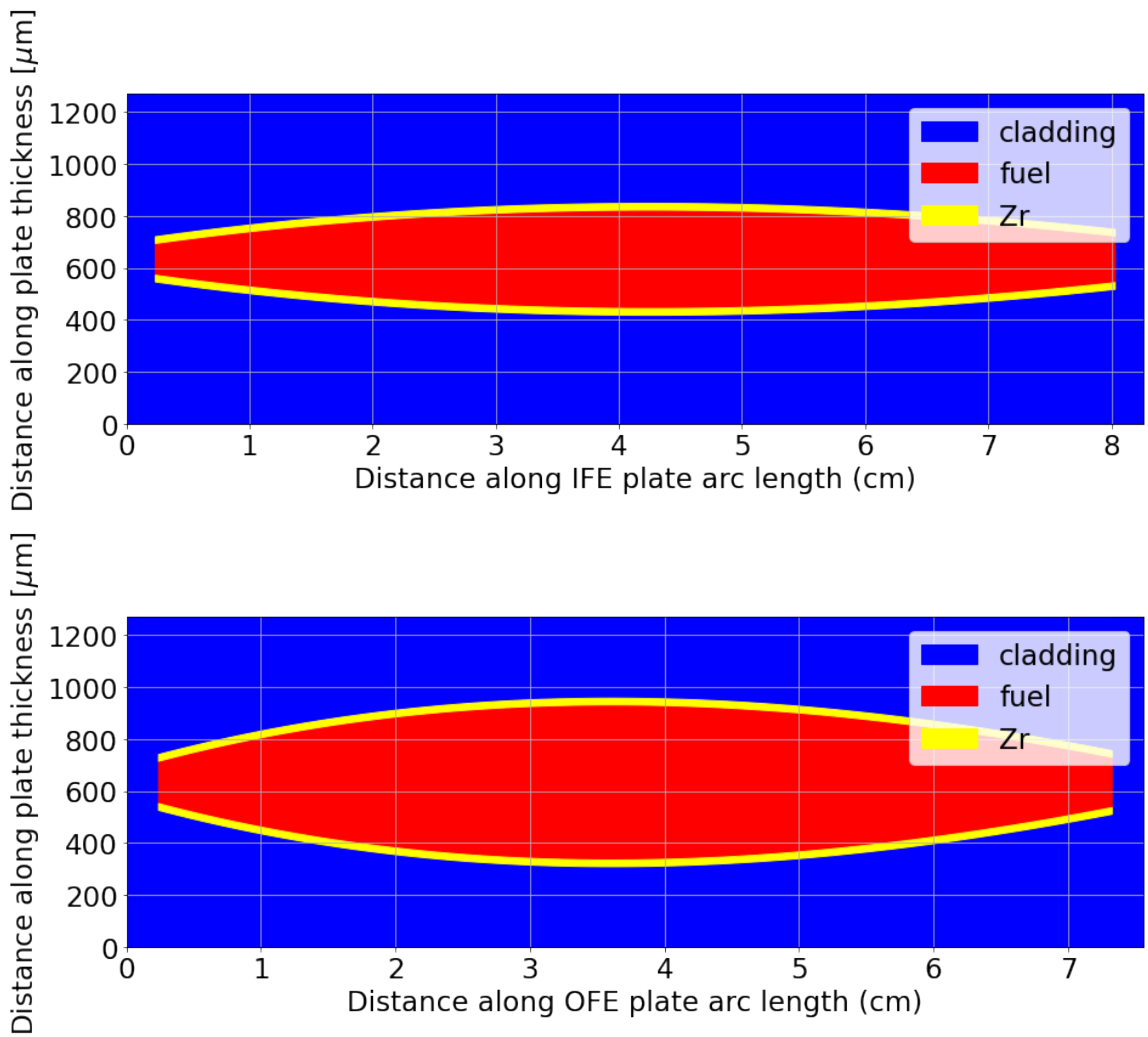

Figure 12. IFE (top) and OFE (bottom) fuel meat shapes for the utilization design.

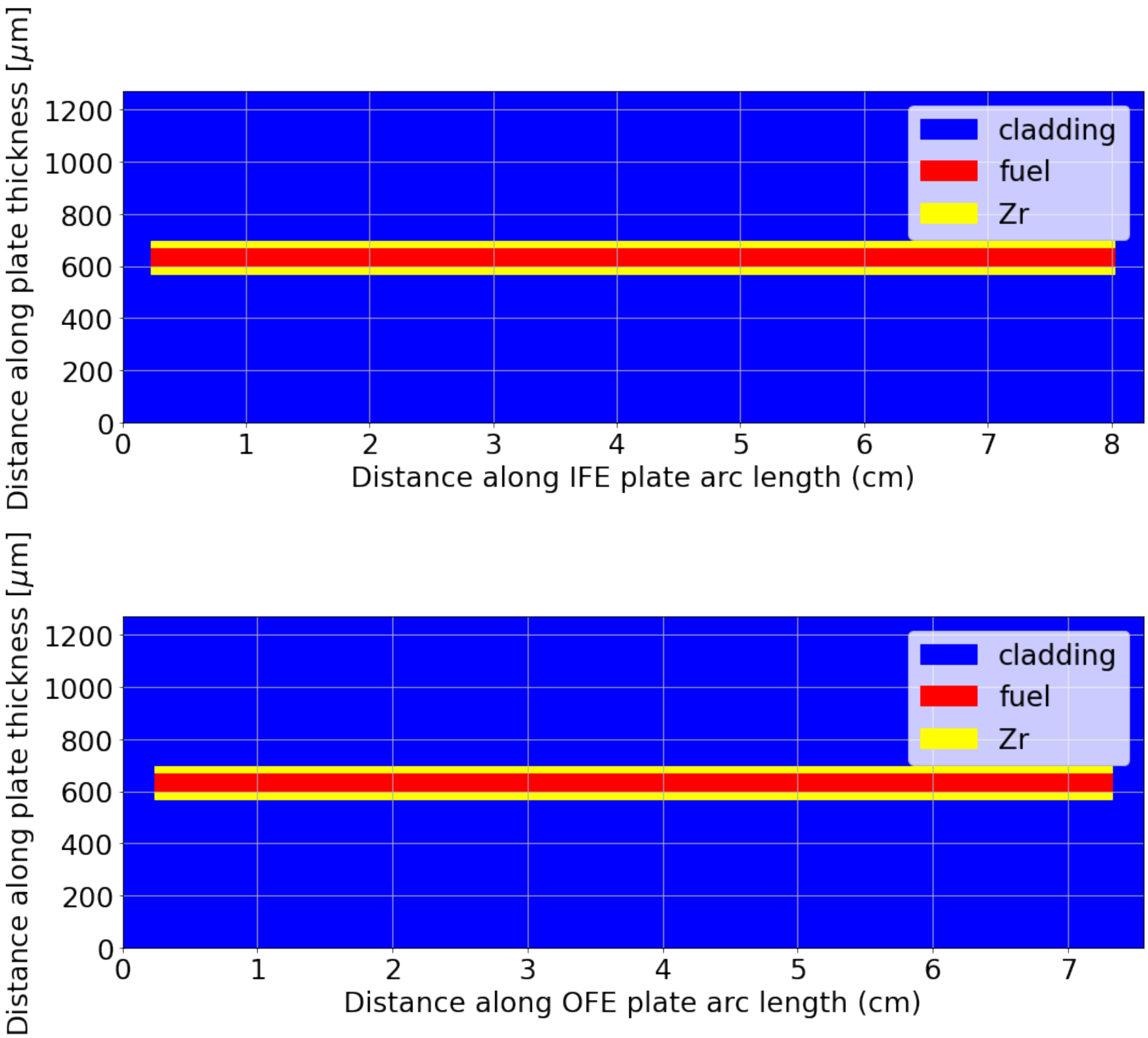

Figure 13. IFE (top) and OFE (bottom) fuel meat shape for the utilization design at the bottom of the axial fuel region. The axial contour increases the minimum safety margin, which usually occurs at the bottom of the core.

Table 25. Fuel shape polynomial coefficients for the utilization design

Order	3	2	1	0
IFE	0.2295	-17.8364	139.3662	91.4586
OFE	1.2813	-47.7629	294.2813	96.8058

7.2.2 Fission Rate Density

Figure 14 shows the maximum fission rate density during operation for each fuel element. Table 26 lists the peak fission rate results and provides references to the figures in the appendices that illustrate the spatial fission rate density values for the four selected state points for each fuel element.

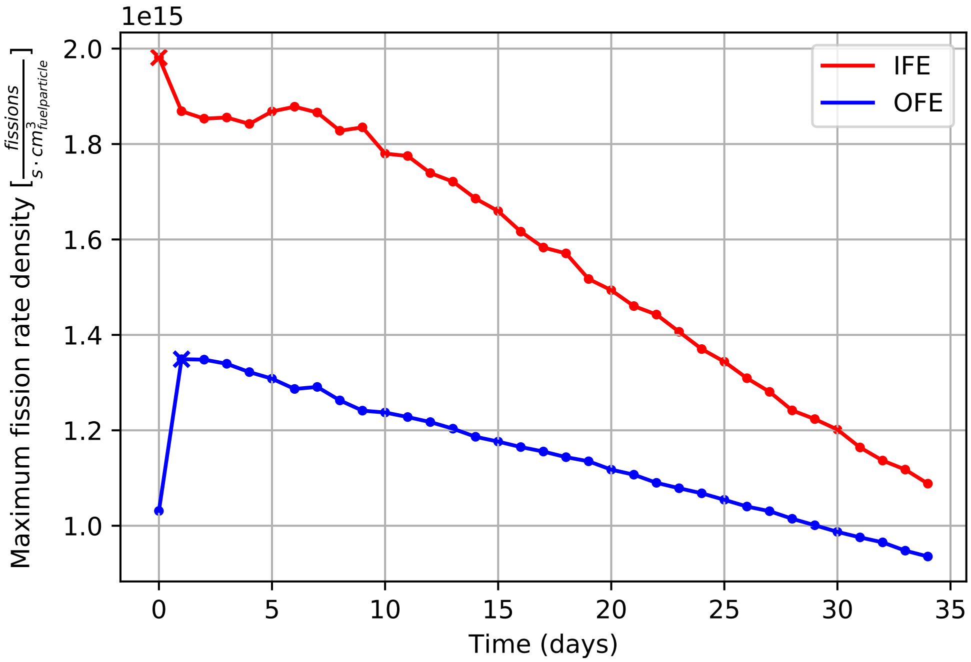

Figure 14. Utilization design maximum fission density during operation.

Table 26. Minimum and maximum fission rate densities in the utilization design.

Day	Region	Minimum	Maximum	Unit	Ref.
0	IFE	2.91	19.81	$10^{14}\ \frac{\text{fissions}}{\text{s}\cdot\text{cm}^3_{fuelparticle}}$	Fig. 63
1	IFE	2.69	18.69		Fig. 64
15	IFE	2.74	16.59		Fig. 65
34	IFE	2.79	10.88		Fig. 66
0	OFE	1.26	10.31		Fig. 67
1	OFE	1.31	13.49		Fig. 68
15	OFE	1.36	11.76		Fig. 69
34	OFE	1.51	9.36		Fig. 70

7.2.3 Power Density

The power density values are the fission rate density values multiplied by the average energy generated per fission. It is conservatively assumed that all energy generated by fission is deposited locally in the fuel meat. Therefore, the power density and fission rate density results have identical trends, and only the magnitudes of the results are different. Figure 15 shows the maximum local power density during operation for each fuel element. Table 27 lists the maximum power density results and provides references to the figures in the appendices. Plots in the appendices show the spatial power density values for each of the four selected state points for each fuel element.

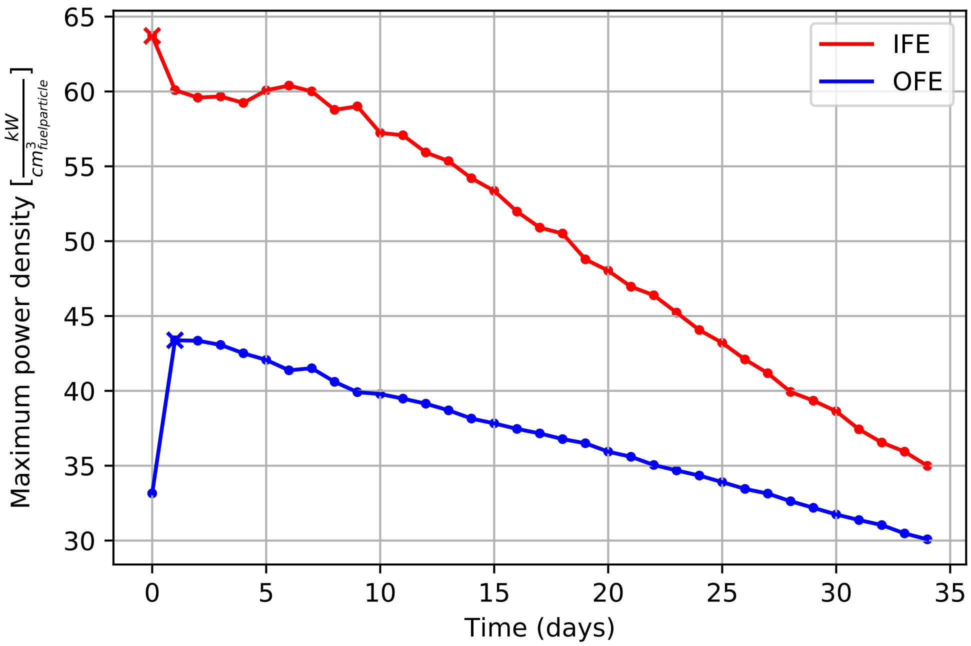

Figure 15. Utilization design maximum power density during operation.

Table 27. Minimum and maximum power densities in the utilization design.

Day	Region	Minimum	Maximum	Unit	Ref.
0	IFE	9.36	63.71	$\frac{kW}{cm^3_{fuelparticle}}$	Fig. 77
1	IFE	8.65	60.09		Fig. 78
15	IFE	8.81	53.36		Fig. 79
34	IFE	8.99	34.99		Fig. 80
0	OFE	4.06	33.15		Fig. 81
1	OFE	4.2	43.38		Fig. 82
15	OFE	4.39	37.83		Fig. 83
34	OFE	4.87	30.08		Fig. 84

7.2.4 Heat Flux

Figure 16 shows the maximum heat flux during operation for each fuel element. Table 28 lists the maximum heat flux results and provides references to the figures in the appendices. Plots in the appendices show the spatial heat flux values for the four selected state points for each fuel element.

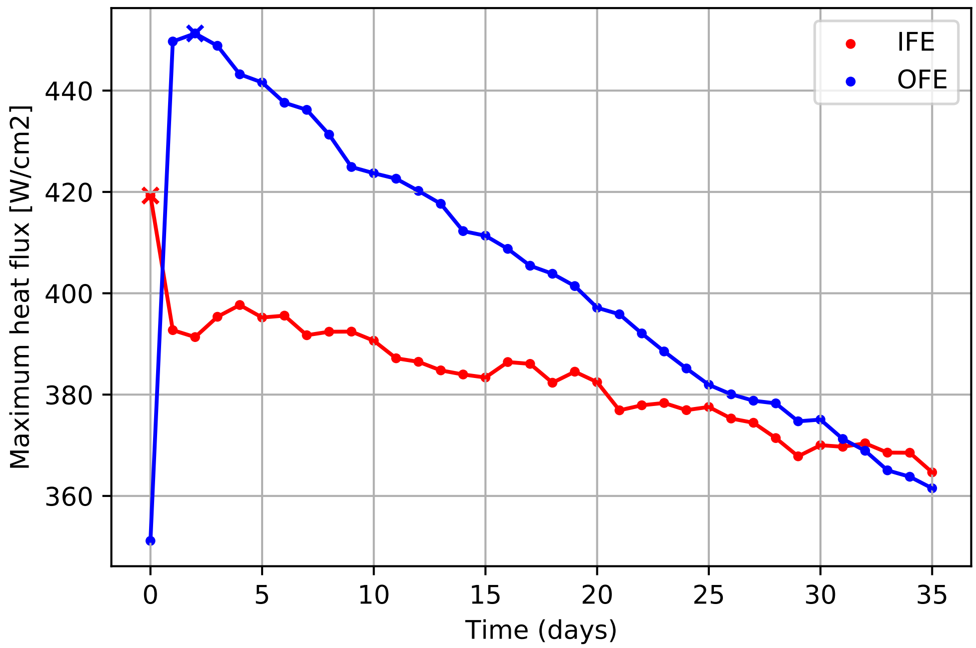

Figure 16. Utilization design maximum heat flux during operation.

Table 28. Minimum and maximum heat fluxes in the utilization design.

Day	Region	Minimum	Maximum	Unit	Ref.
0	IFE	121.87	419.28	$\frac{W}{cm^2}$	Fig. 85
1	IFE	122.82	392.73		Fig. 86
15	IFE	135.47	383.38		Fig. 87
35	IFE	121.64	364.66		Fig. 88
0	OFE	38.44	351.14		Fig. 89
1	OFE	40.21	449.69		Fig. 90
2	OFE	41.4	451.28		Fig. 91
15	OFE	50.07	411.36		Fig. 92
35	OFE	97.82	361.52		Fig. 93

7.2.5 Cumulative Fission Density

Figure 17 shows the maximum local cumulative fission density during operation for each fuel element, and Figure 18 illustrates the fission rate density variation with cumulative fission density for every spatial cell in the neutronics model. Table 29 lists the maximum cumulative fission density results and provides references to the figures in the appendices.

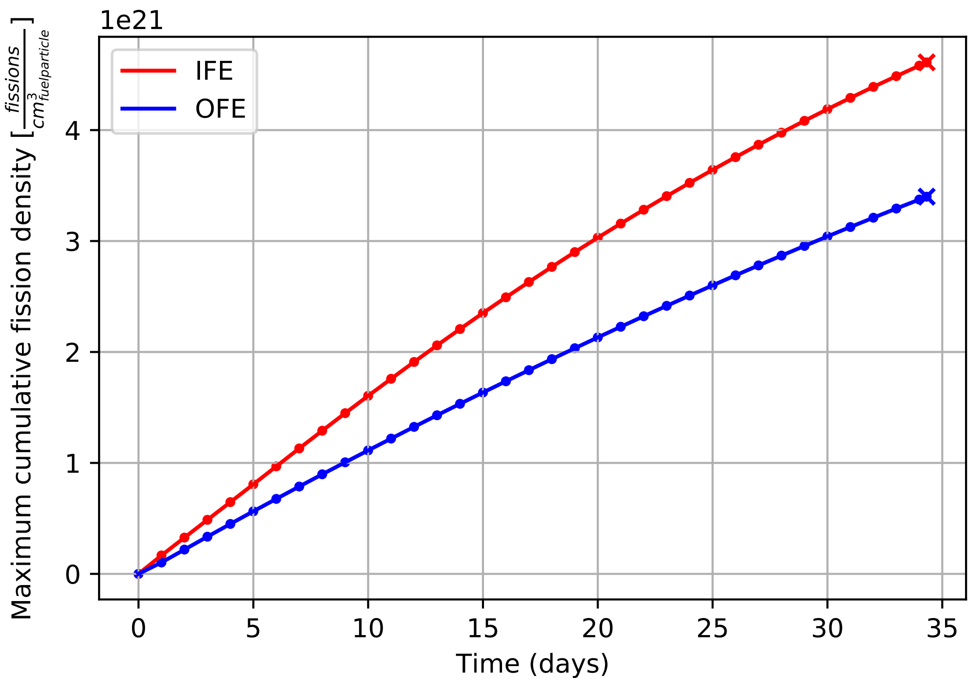

Figure 17. Utilization design maximum cumulative fission density during operation.

Table 29. Minimum and maximum cumulative fission density values in the utilization design.

Day	Region	Minimum	Maximum	Unit	Ref.
1	IFE	0.24	1.66	$10^{20}\ \frac{\text{fissions}}{\text{cm}^3_{fuelparticle}}$	Fig. 71
15	IFE	3.54	23.51		Fig. 72
34	IFE	8.08	46.1		Fig. 73
1	OFE	0.11	1.03		Fig. 74
15	OFE	1.74	16.35		Fig. 75
34	OFE	4.04	34.0		Fig. 76

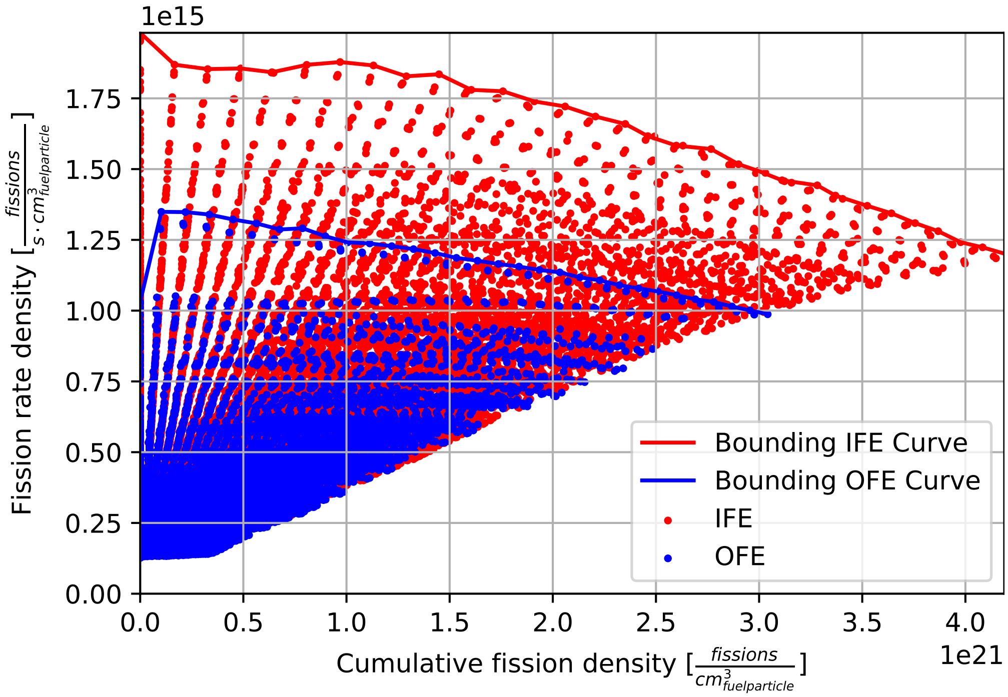

Figure 18. Utilization design fission rate density variation with cumulative fission density during operation.

7.3 COLD DESIGN

The cold design is generated with borated side plates, a fuel axial contour for a better burnout margin, and performance metrics weighted favoring cold source moderator vessel cold flux. The cycle length of this design is 26.6 days. The cold fuel design specifications are presented in Table 30.

Table 30. Key cold design geometry and operational parameters

Parameter	Units	Value	
Center-symmetric fuel zone	–	yes	
Axial contour	–	yes	
U loading	kg	98.6608	
^{235}U loading	kg	19.4855	
^{10}B loading	g	3.56	
		IFE	OFE
^{235}U loading	kg	4 8951	14 5904
^{235}U loading per plate	g/plate	28 62632	39 54038
Active fuel length	cm	50.8	
Reactor power	MW	100	

7.3.1 Fuel Meat Shape

The fuel meat thickness profile of the cold design is described in Table 31, where the thickness of the fuel meat (μm) is represented by a polynomial function of the distance from the origin of the involute-generating radius (cm). Illustrations of the IFE and OFE fuel meat shapes are shown in Figures 19 and 20.

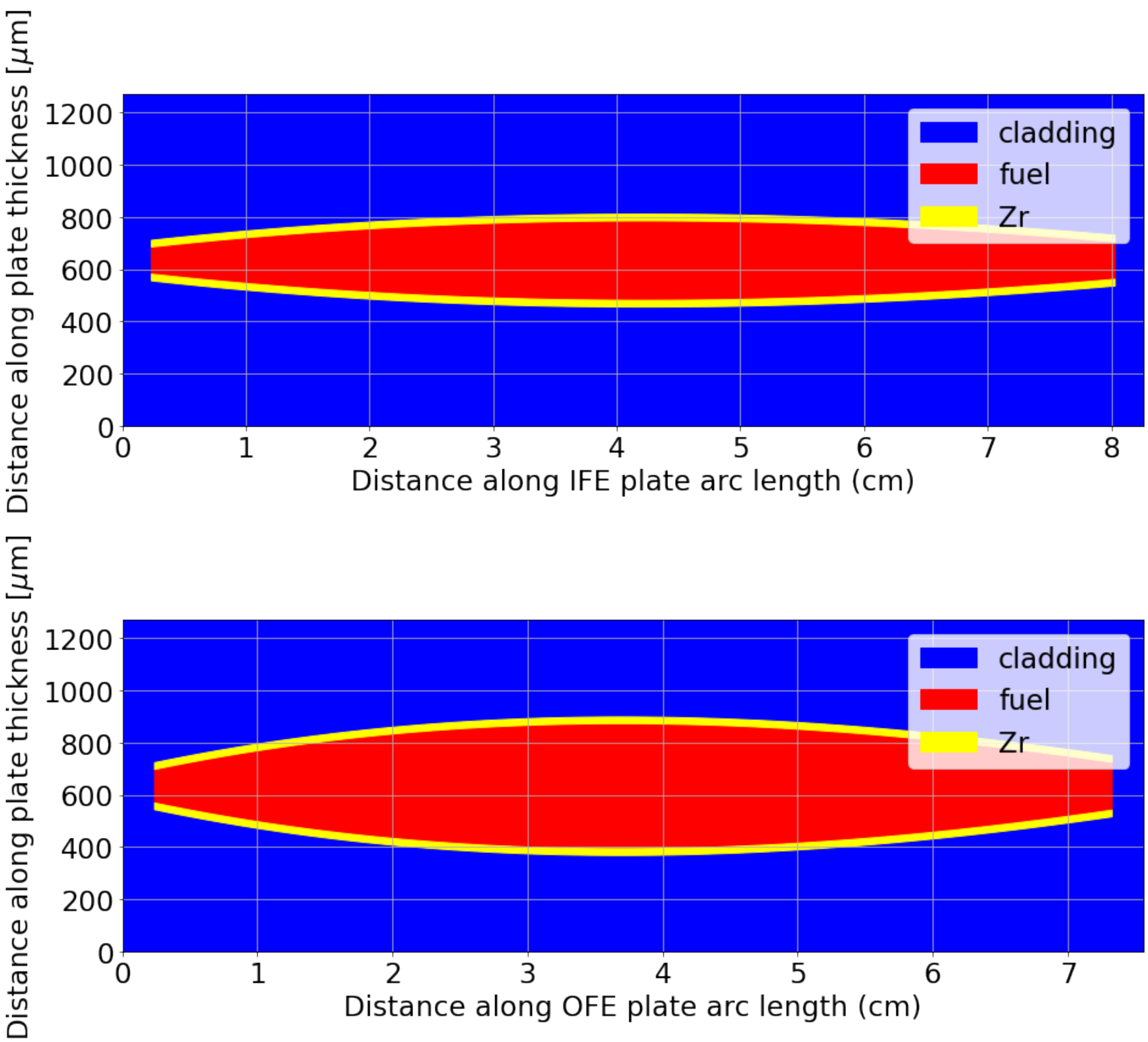

Figure 19. IFE (top) and OFE (bottom) fuel meat shapes for the cold design.

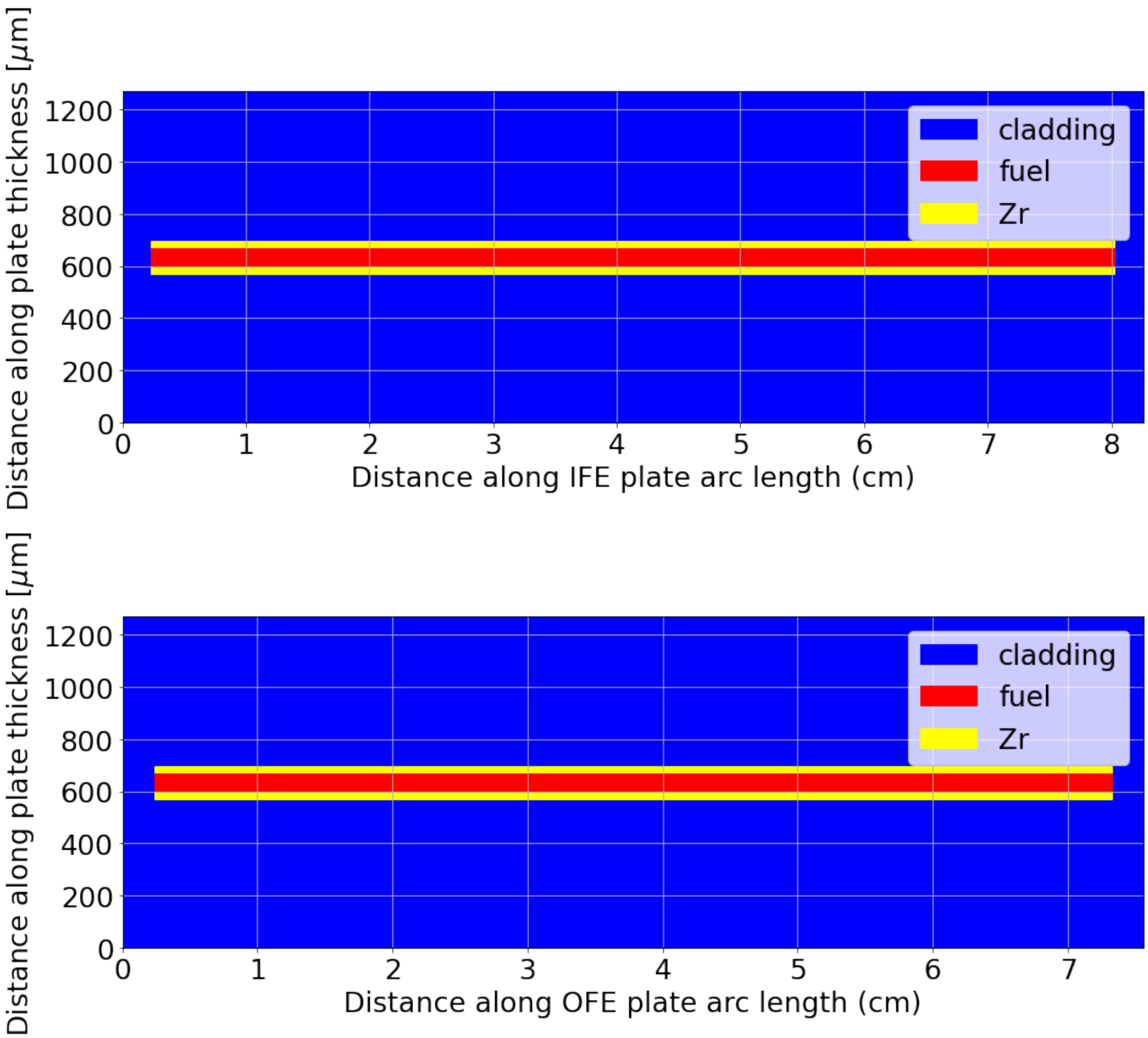

Figure 20. IFE (top) and OFE (bottom) fuel meat shape for the cold design at the bottom of the axial fuel region. The axial contour increases the minimum safety margin, which usually occurs at the bottom of the core.

Table 31. Fuel shape polynomial coefficients for the cold design

Order	3	2	1	0
IFE	0.1823	-14.1554	109.8264	79.47
OFE	0.9832	-36.8403	231.6586	76.389

7.3.2 Fission Rate Density

Figure 21 shows the maximum fission rate density during operation for each fuel element. Table 32 lists the peak fission rate results and provides references to the figures in the appendices that illustrate the spatial fission rate density values for the four selected state points for each fuel element.

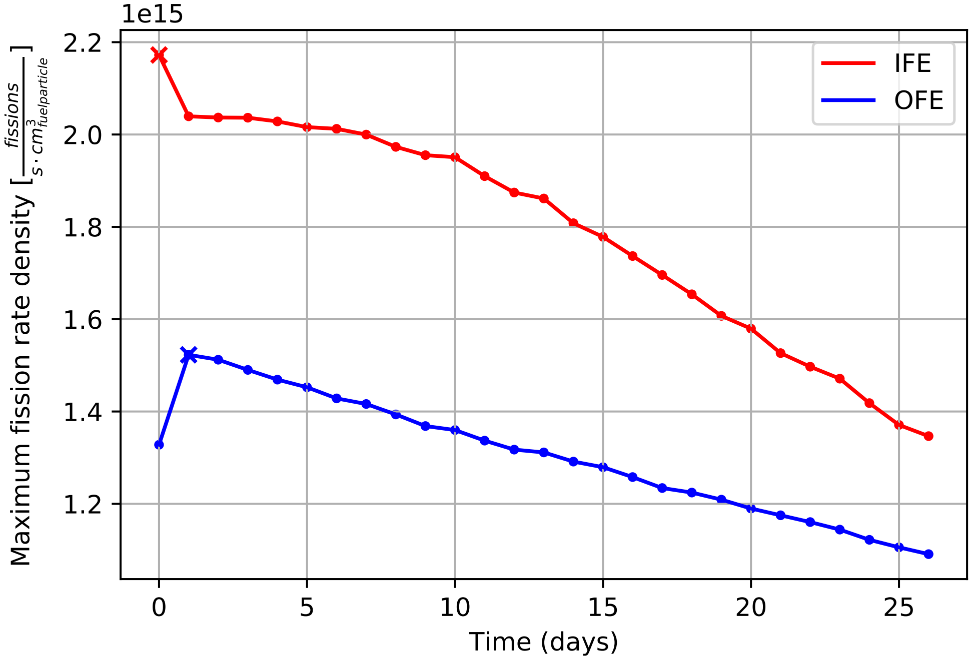

Figure 21. Cold design maximum fission density during operation.

Table 32. Minimum and maximum fission rate densities in the cold design.

Day	Region	Minimum	Maximum	Unit	Ref.
0	IFE	3.66	21.72	$10^{14}\ \frac{\text{fissions}}{\text{s}\cdot\text{cm}^3_{fuelparticle}}$	Fig. 94
1	IFE	3.33	20.39		Fig. 95
15	IFE	3.43	17.78		Fig. 96
26	IFE	3.58	13.47		Fig. 97
0	OFE	1.57	13.28		Fig. 98
1	OFE	1.65	15.23		Fig. 99
15	OFE	1.72	12.79		Fig. 100
26	OFE	1.86	10.91		Fig. 101

7.3.3 Power Density

The power density values are the fission rate density values multiplied by the average energy generated per fission. It is conservatively assumed that all energy generated by fission is deposited locally in the fuel meat. Therefore, the power density and fission rate density results have identical trends, and only the magnitudes of the results are different. Figure 22 shows the maximum local power density during operation for each fuel element. Table 33 lists the maximum power density results and provides references to the figures in the appendices. Plots in the appendices show the spatial power density values for each of the four selected state points for each fuel element.

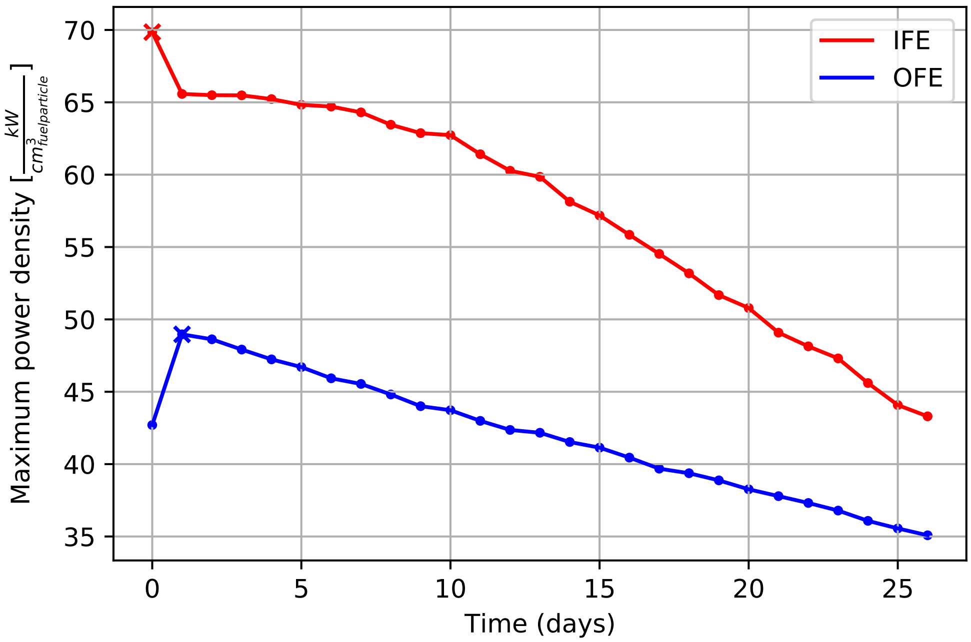

Figure 22. Cold design maximum power density during operation.

Table 33. Minimum and maximum power densities in the cold design.

Day	Region	Minimum	Maximum	Unit	Ref.
0	IFE	11.76	69.85	$\frac{kW}{cm^3_{fuelparticle}}$	Fig. 108
1	IFE	10.71	65.58		Fig. 109
15	IFE	11.04	57.18		Fig. 110
26	IFE	11.53	43.3		Fig. 111
0	OFE	5.04	42.7		Fig. 112
1	OFE	5.32	48.97		Fig. 113
15	OFE	5.51	41.14		Fig. 114
26	OFE	6.0	35.08		Fig. 115

7.3.4 Heat Flux

Figure 23 shows the maximum heat flux during operation for each fuel element. Table 34 lists the maximum heat flux results and provides references to the figures in the appendices. Plots in the appendices show the spatial heat flux values for the four selected state points for each fuel element.

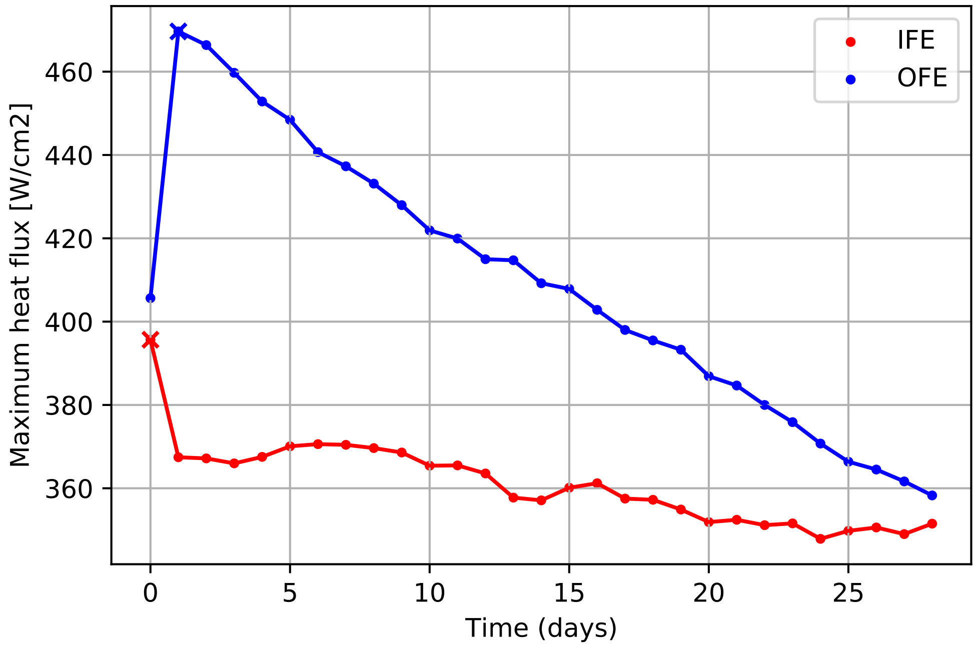

Figure 23. Cold design maximum heat flux during operation.

Table 34. Minimum and maximum heat fluxes in the cold design.

Day	Region	Minimum	Maximum	Unit	Ref.
0	IFE	127.0	395.65	$\frac{\text{W}}{\text{cm}^2}$	Fig. 116
1	IFE	124.12	367.44		Fig. 117
15	IFE	139.99	360.13		Fig. 118
28	IFE	135.84	351.51		Fig. 119
0	OFE	42.37	405.64		Fig. 120
1	OFE	46.18	469.66		Fig. 121
15	OFE	71.69	407.85		Fig. 122
28	OFE	110.41	358.28		Fig. 123

7.3.5 Cumulative Fission Density

Figure 24 shows the maximum local cumulative fission density during operation for each fuel element, and Figure 25 illustrates the fission rate density variation with cumulative fission density for every spatial cell in the neutronics model. Table 35 lists the maximum cumulative fission density results and provides references to the figures in the appendices.

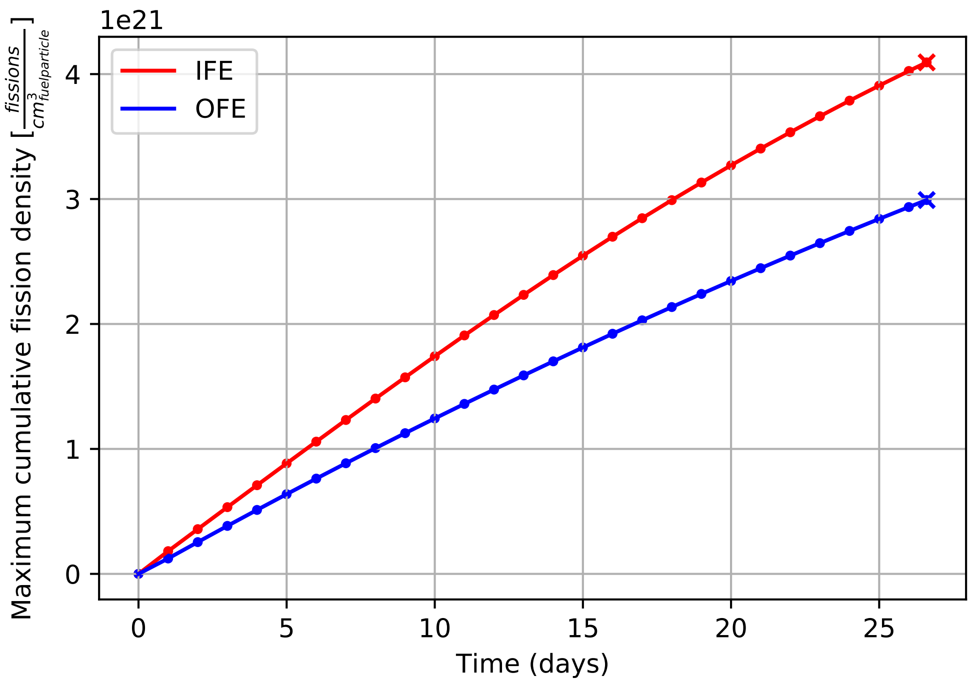

Figure 24. Cold design maximum cumulative fission density during operation.

Table 35. Minimum and maximum cumulative fission density values in the cold design.

Day	Region	Minimum	Maximum	Unit	Ref.
1	IFE	0.3	1.82	$10^{20}\ \frac{\text{fissions}}{\text{cm}^3_{fuelparticle}}$	Fig. 102
15	IFE	4.43	25.46		Fig. 103
26	IFE	7.78	40.94		Fig. 104
1	OFE	0.14	1.23		Fig. 105
15	OFE	2.2	18.12		Fig. 106
26	OFE	3.89	29.92		Fig. 107

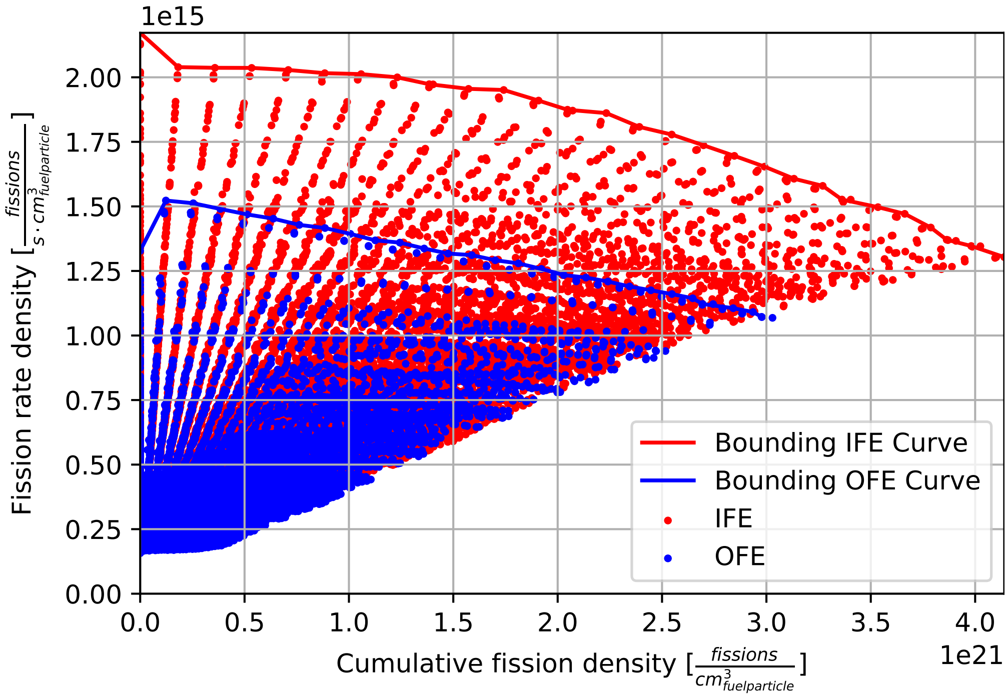

Figure 25. Cold design fission rate density variation with cumulative fission density during operation.

7.4 BORON-CLAD DESIGN

The boron clad design is generated with boron in the IFE fuel plate cladding, a fuel axial contour for a better burnout margin, and performance metrics weighted favoring uranium utilization. The cycle length of this design is 31.95 days. The boron-clad fuel design specifications are presented in Table 36.

Table 36. Key boron -clad design geometry and operational parameters

Parameter	Units	Value	
Center-symmetric fuel zone	–	yes	
Axial contour	–	yes	
U loading	kg	120.5294	
^{235}U loading	kg	23.8046	
^{10}B loading	g	3.56	
		IFE	OFE
^{235}U loading	kg	6 0415	17 763
^{235}U loading per plate	g/plate	35 33041	48 13821
Active fuel length	cm	50.8	
Reactor power	MW	100	

7.4.1 Fuel Meat Shape

The fuel meat thickness profile of the boron-clad design is described in Table 37, where the thickness of the fuel meat (μm) is represented by a polynomial function of the distance from the origin of the involute-generating radius (cm). Illustrations of the IFE and OFE fuel meat shapes are shown in Figures 26 and 27.

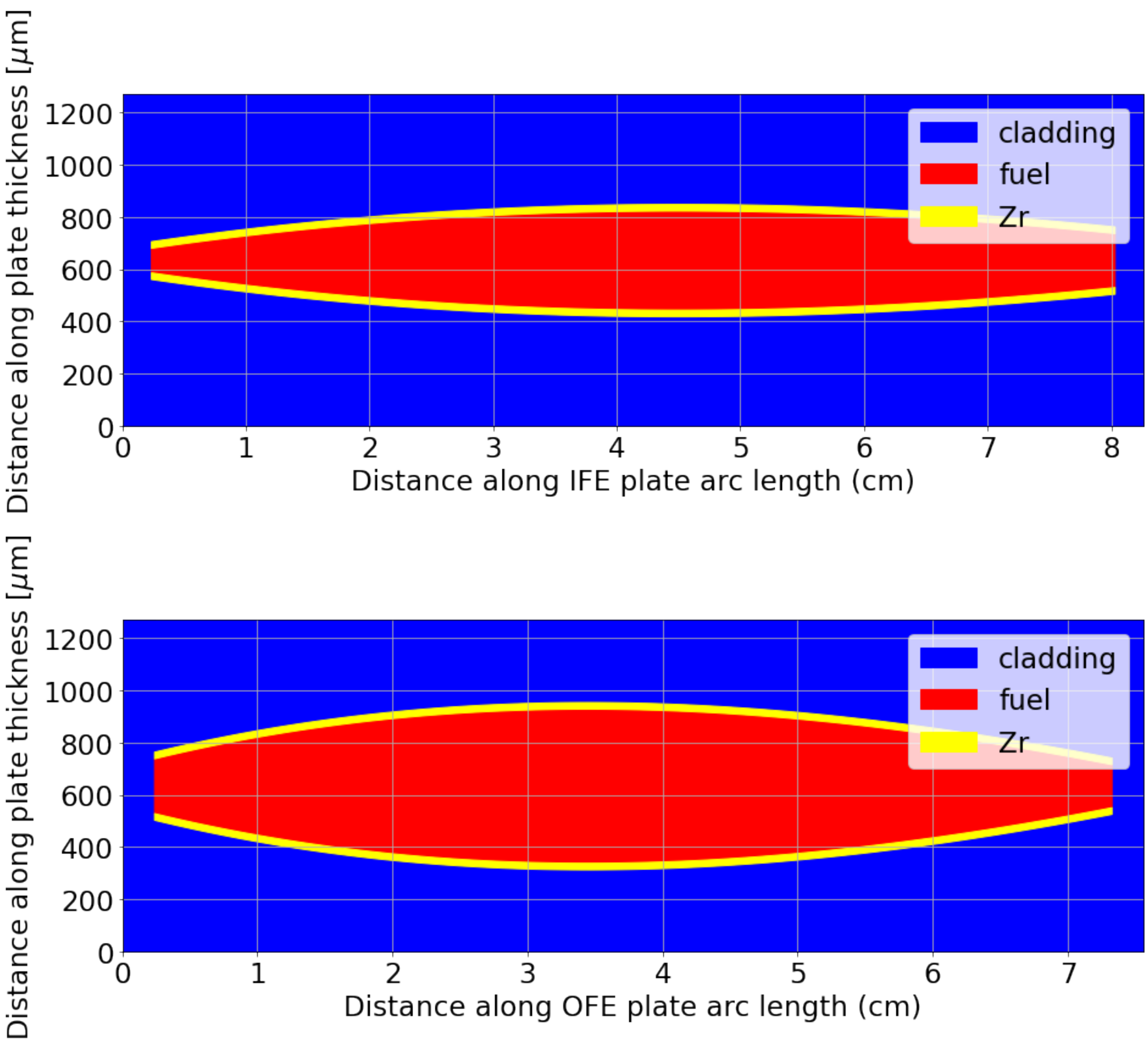

Figure 26. IFE (top) and OFE (bottom) fuel meat shapes for the boron-clad design.

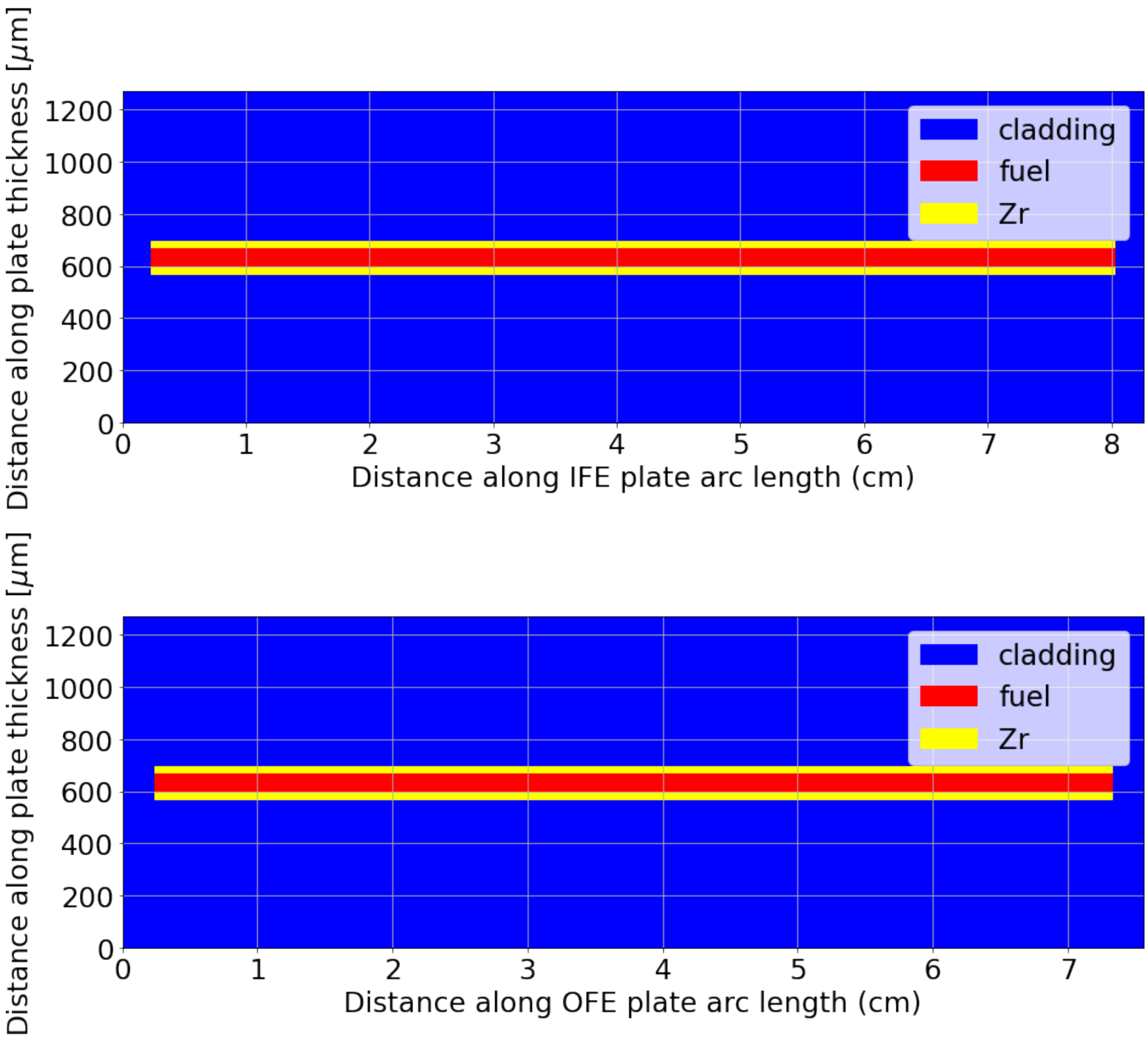

Figure 27. IFE (top) and OFE (bottom) fuel meat shape for the boron-clad design at the bottom of the axial fuel region. The axial contour increases the minimum safety margin, which usually occurs at the bottom of the core.

Table 37. Fuel shape polynomial coefficients for the boronclad design

Order	3	2	1	0
IFE	0.2267	-17.7459	145.9855	61.0276
OFE	1.2411	-45.8107	271.1182	148.5807

7.4.2 Fission Rate Density

Figure 28 shows the maximum fission rate density during operation for each fuel element. Table 38 lists the peak fission rate results and provides references to the figures in the appendices that illustrate the spatial fission rate density values for the four selected state points for each fuel element.

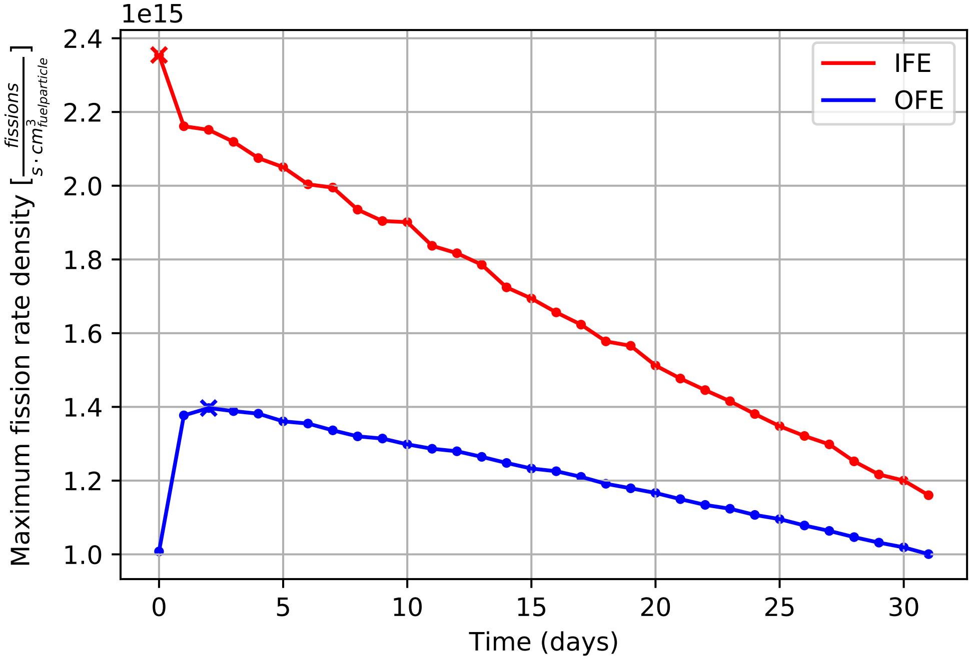

Figure 28. Boron-clad design maximum fission density during operation.

Table 38. Minimum and maximum fission rate densities in the boron-clad design.

Day	Region	Minimum	Maximum	Unit	Ref.
0	IFE	2.85	23.55	$10^{14}\ \frac{\text{fissions}}{\text{s}\cdot\text{cm}^3_{fuelparticle}}$	Fig. 124
1	IFE	2.62	21.61		Fig. 125
15	IFE	2.67	16.94		Fig. 126
31	IFE	2.75	11.6		Fig. 127
0	OFE	1.31	10.08		Fig. 128
1	OFE	1.32	13.77		Fig. 129
2	OFE	1.33	13.97		Fig. 130
15	OFE	1.37	12.33		Fig. 131
31	OFE	1.51	10.01		Fig. 132

7.4.3 Power Density

The power density values are the fission rate density values multiplied by the average energy generated per fission. It is conservatively assumed that all energy generated by fission is deposited locally in the fuel meat. Therefore, the power density and fission rate density results have identical trends, and only the magnitudes of the results are different. Figure 29 shows the maximum local power density during operation for each fuel element. Table 39 lists the maximum power density results and provides references to the figures in the appendices. Plots in the appendices show the spatial power density values for each of the four selected state points for each fuel element.

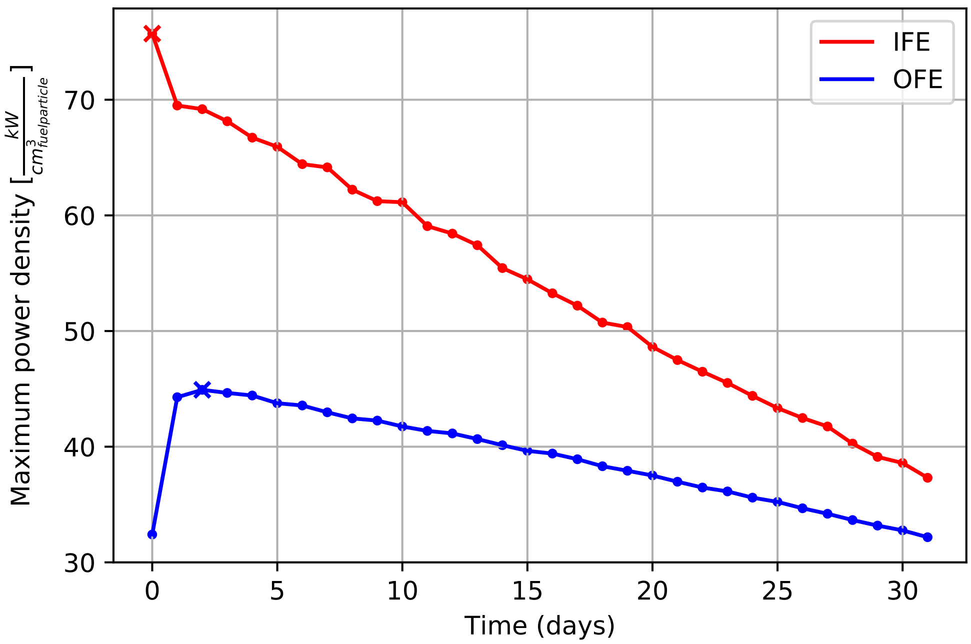

Figure 29. Boron-clad design maximum power density during operation.

Table 39. Minimum and maximum power densities in the boron-clad design.

Day	Region	Minimum	Maximum	Unit	Ref.
0	IFE	9.15	75.72	$\frac{kW}{cm^3_{fuelparticle}}$	Fig. 139
1	IFE	8.42	69.5		Fig. 140
15	IFE	8.57	54.48		Fig. 141
31	IFE	8.86	37.31		Fig. 142
0	OFE	4.22	32.41		Fig. 143
1	OFE	4.24	44.28		Fig. 144
2	OFE	4.29	44.92		Fig. 145
15	OFE	4.42	39.64		Fig. 146
31	OFE	4.85	32.17		Fig. 147

7.4.4 Heat Flux

Figure 30 shows the maximum heat flux during operation for each fuel element. Table 40 lists the maximum heat flux results and provides references to the figures in the appendices. Plots in the appendices show the spatial heat flux values for the four selected state points for each fuel element.

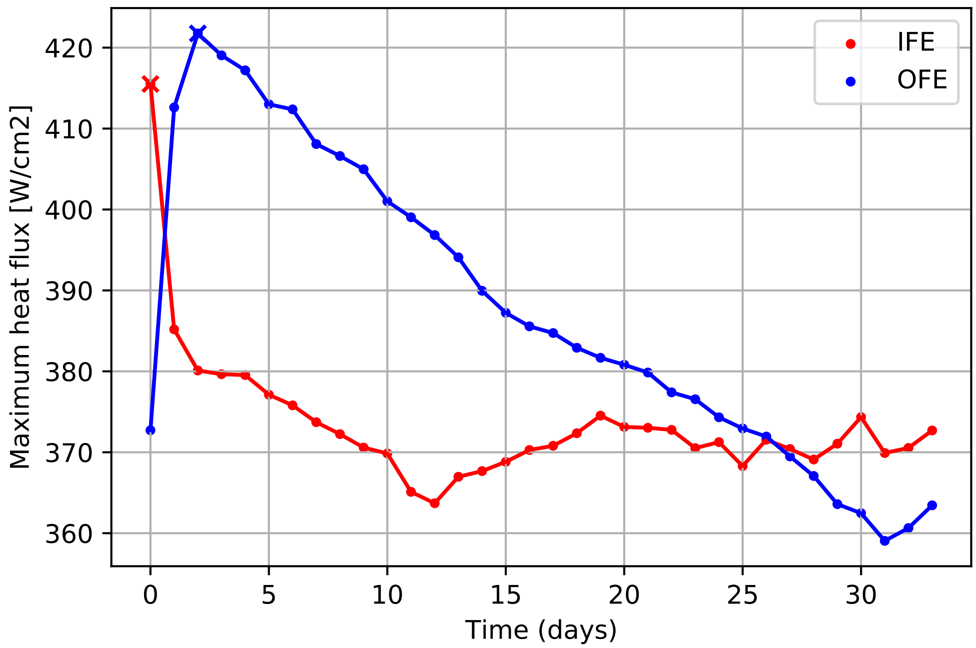

Figure 30. Boron-clad design maximum heat flux during operation.

Table 40. Minimum and maximum heat fluxes in the boron-clad design.

Day	Region	Minimum	Maximum	Unit	Ref.
0	IFE	114.86	415.51	$\frac{W}{cm^2}$	Fig. 148
1	IFE	113.18	385.19		Fig. 149
15	IFE	134.47	368.82		Fig. 150
33	IFE	124.35	372.69		Fig. 151
0	OFE	38.08	372.72		Fig. 152
1	OFE	39.32	412.61		Fig. 153
2	OFE	39.2	421.76		Fig. 154
15	OFE	54.25	387.24		Fig. 155
33	OFE	102.59	363.45		Fig. 156

7.4.5 Cumulative Fission Density

Figure 31 shows the maximum local cumulative fission density during operation for each fuel element, and Figure 32 illustrates the fission rate density variation with cumulative fission density for every spatial cell in the neutronics model. Table 41 lists the maximum cumulative fission density results and provides references to the figures in the appendices.

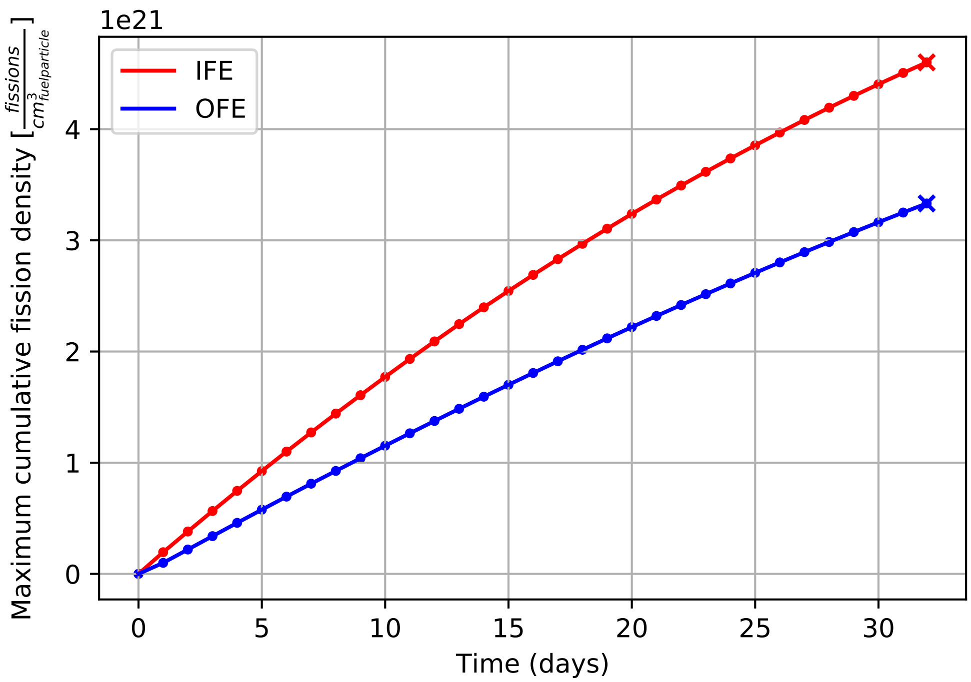

Figure 31. Boron-clad design maximum cumulative fission density during operation.

Table 41. Minimum and maximum cumulative fission density values in the boron-clad design.

Day	Region	Minimum	Maximum	Unit	Ref.
1	IFE	0.24	1.95	$10^{20}\ \frac{\text{fissions}}{\text{cm}^3_{fuelparticle}}$	Fig. 133
15	IFE	3.44	25.45		Fig. 134
31	IFE	7.19	46.01		Fig. 135
1	OFE	0.11	0.99		Fig. 136
15	OFE	1.76	17.01		Fig. 137
31	OFE	3.74	33.32		Fig. 138

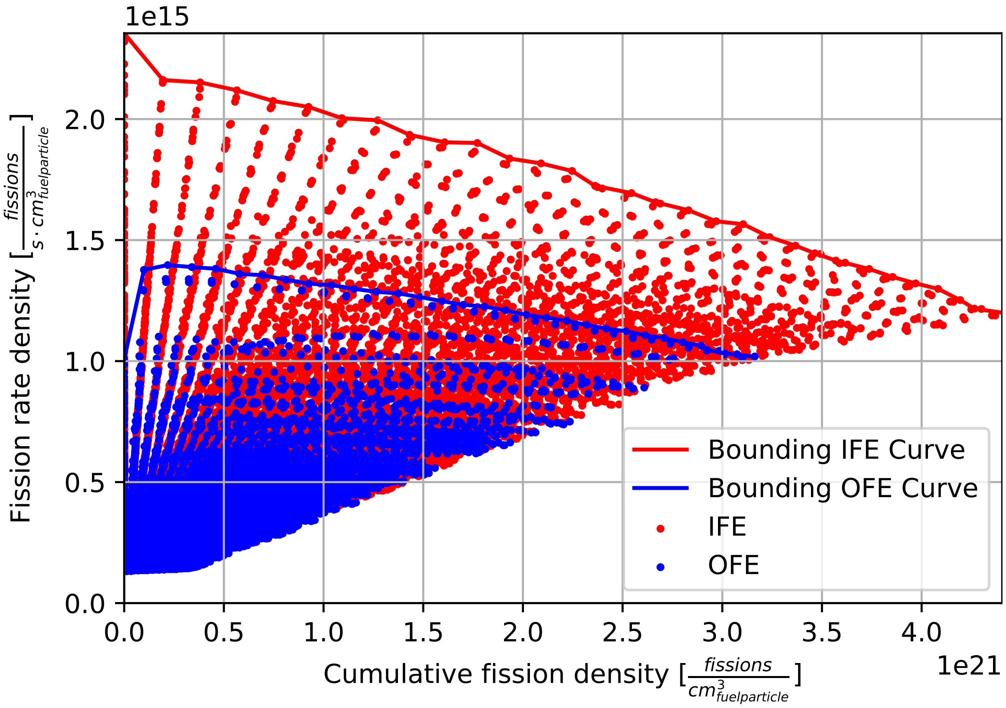

Figure 32. Boron-clad design fission rate density variation with cumulative fission density during operation.

8. DISCUSSION

Core design studies performed by Betzler et al. [14] resulted in four HFIR LEU U-10Mo fuel designs with various performance metrics and design features. The first step in the design approach was to systematically explore the design space to generate metric responses from design parameters. These responses were used to generate candidate designs that emphasize different performance metrics and design features. Compared to the HEU core design, the LEU fuel designs require additional fabrication features, primarily to reduce power peaking and increase thermal safety margin. Introduction of substantial amounts of ^{238}U into the core results in increased self-shielding from the parasitic absorptions in the ^{238}U isotope. The reactor power must therefore be uprated from 85 MW for the HEU core to 95–100 MW for the LEU core to maintain performance. Consequently, additional power peaking mitigation features must be introduced to meet the thermal safety requirements for the compact, high power density core.

This report provides detailed descriptions of these four fuel designs, along with their performance and safety metrics and design parameters. All four fuel designs are presented herein, and all designs meet HEU key performance metrics. However the cold source cold-to-total flux ratio is slightly degraded as a result of the harder LEU fuel spectrum. The slightly increased fast flux down the beamlines, which acts as noise to the neutron scattering instruments, is not anticipated to adversely affect the neutron scattering mission. None of the designs have a greater thermal safety margin than the HEU core; however, they meet the minimum safety limit requirements. Some additional observations from this study are presented below.

- Due to U-10Mo fuel's high density, achieving performance metrics is not a limiting factor.
- An increase in reactor power to at least 100 MW and an axial contour are needed to maintain HEU metrics and the current 50.8 cm (20 inch) fuel length.
- A design feature to suppress power at the bottom of the fuel zone is required.

These four designs are presented to show (1) relevant operating conditions such as fission densities, power densities, and heat fluxes, and (2) design flexibility for fuel fabrication in order to frame irradiation qualification needs and prioritize design feature R&D efforts. The maximum parameters for each fuel element for each of the four presented designs are provided in Table 42.

Table 42. Summary of maximum parameters for each U-10Mo design

		Fission rate density $(\frac{fis}{s \cdot cm^3_{fuelparticle}})$	Power density $(\frac{kW}{cm^3_{fuelparticle}})$	Heat Flux $(\frac{W}{cm^2})$	Cumulative fission density $(\frac{fis}{cm^3_{fuelparticle}})$
22-inch	IFE	2.16E+15	6.94E+01	3.28E+02	4.69E+21
	OFE	1.34E+15	4.31E+01	4.84E+02	3.14E+21
utilization	IFE	1.98E+15	6.37E+01	4.19E+02	4.61E+21
	OFE	1.35E+15	4.34E+01	4.51E+02	3.40E+21
cold	IFE	2.17E+15	6.99E+01	3.96E+02	4.09E+21
	OFE	1.52E+15	4.90E+01	4.70E+02	2.99E+21
boron-clad	IFE	2.35E+15	7.57E+01	4.16E+02	4.60E+21
	OFE	1.40E+15	4.49E+01	4.22E+02	3.33E+21

9. REFERENCES

References

[1] D. Renfro, D. Chandler, D. Cook, G. Ilas, P. Jain, and J. Valentine, *Preliminary Evaluation of Alternate Designs for HFIR Low-Enriched Uranium Fuel*. No. ORNL/TM-2014/154, Oct. 2014.

[2] B. R. Betzler, D. Chandler, E. E. Davidson, and G. Ilas, “High-Fidelity Modeling and Simulation for a High Flux Isotope Reactor Low-Enriched Uranium Core Design,” *Nuclear Science and Engineering*, vol. 187, pp. 81–99, July 2017.

[3] D. Chandler, B. R. Betzler, D. H. Cook, G. Ilas, and D. G. Renfro, “Neutronic and Thermal-Hydraulic Feasibility Studies for High Flux Isotope Reactor Conversion to Low-Enriched Uranium U3Si2-Al Fuel,” in *,Proc. Intl. Conf. PHYSOR 2018*, (Cancun, Mexico), Apr. 2018.

[4] D. Chandler, B. R. Betzler, P. K. Jain, J. W. Bae, D. H. Cook, V. D. Fudurich, T. K. Howard, C. J. Hurt, G. Ilas, J. L. Meszaros, and E. L. Popov, “High Flux Isotope Reactor Conversion from High-Enriched to Low-Enriched Uranium Fuel – a 2019 Progress Update,” in *Proceedings of RERTR 2019*, (Zagreb, Croatia), Oct. 2019.

[5] D. Chandler, B. R. Betzler, D. H. Cook, G. Ilas, and D. G. Renfro, “Neutronic and Thermal-hydraulic Feasibility Studies for High Flux Isotope Reactor Conversion to Low-enriched Uranium Silicide Dispersion Fuel,” *Annals of Nuclear Energy*, vol. 130, pp. 277–292, Aug. 2019.

[6] D. Chandler, B. R. Betzler, J. W. Bae, D. H. Cook, and G. Ilas, “Conceptual Fuel Element Design Candidates for Conversion of High Flux Isotope Reactor with Low-Enriched Uranium Silicide Dispersion Fuel,” in *,Proc. Intl. Conf. PHYSOR 2020*, (Cambridge, UK), 2020.

[7] R. T. Primm, R. J. Ellis, J. C. Gehin, D. L. Moses, J. L. Binder, and N. Xoubi, *Assumptions and Criteria for Performing a Feasability Study of the Conversion of the High Flux Isotope Reactor Core to Use Low-Enriched Uranium Fuel*. No. ORNL/TM-2005/269, Feb. 2006.

[8] B. R. Betzler, D. Chandler, J. Bae, G. Ilas, and J. L. Meszaros, *High Flux Isotope Reactor Low-Enriched Uranium Low Density Silicide Fuel Design Parameters*. No. ORNL/TM-2020/1798, Feb. 2021.

[9] J. Bae, B. R. Betzler, D. Chandler, G. Ilas, and J. L. Meszaros, *High Flux Isotope Reactor Low-Enriched Uranium High Density Silicide Fuel Design Parameters*. No. ORNL/TM-2020-1799, Feb. 2021.

[10] B. R. Betzler, B. J. Ade, D. Chandler, G. Ilas, and E. E. Sunny, “Optimization of Depletion Modeling and Simulation for the High Flux Isotope Reactor,” in *Proceedings of ANS Mathematics and Computational Topical Meeting*, (Nashville, Tennessee, USA), Apr. 2015.

[11] B. R. Betzler, D. Chandler, E. E. Davidson, and G. Ilas, “Design Optimization Studies for a High Flux Isotope Reactor Low-Enriched Uranium Core,” *Trans. Am. Nucl. Soc.*, vol. 117, 2017.

[12] B. R. Betzler, D. Chandler, E. E. Davidson, and G. Ilas, “Optimized Design Performance Analysis Tools for a High Flux Isotope Reactor Low-Enriched Uranium Core,” *Trans. Am. Nucl. Soc.*, vol. 119, 2018.

[13] B. R. Betzler, D. Chandler, D. H. Cook, E. E. Davidson (née Sunny), and G. Ilas, "High Flux Isotope Reactor Low-Enriched Uranium Core Design Optimization Studies," in *,Proc. Intl. Conf. PHYSOR 2018*, (Cancun, Mexico), Apr. 2018.

[14] B. R. Betzler, D. Chandler, D. H. Cook, E. E. Davidson, and G. Ilas, "Design Optimization Methods for High-performance Research Reactor Core Design," *Nuclear Engineering and Design*, vol. 352, Oct. 2019.

[15] G. Ilas, B. R. Betzler, D. Chandler, D. G. Renfro, and E. E. Davidson, *Key Metrics for HFIR HEU and LEU Models*. No. ORNL/TM-2016/581, Oct. 2016.

[16] R. D. Cheverton and T. M. Sims, *HFIR Core Nuclear Design.* No. ORNL-4621, Jan. 1971.

[17] G. Ilas, D. Chandler, B. J. Ade, E. E. Sunny, B. R. Betzler, and D. L. Pinkston, *Modeling and Simulations for the High Flux Isotope Reactor Cycle 400*. No. ORNL/TM-2015/36, Mar. 2015.

[18] SPC-1635, *Specification for Low Enriched Uranium Monolithic Fuel Plates*. Sept. 2015.

[19] TEV-2009, *Supporting Information for the Low Enriched Uranium Monolithic Fuel Design*. Sept. 2015.

[20] T. M. Pandya, S. R. Johnson, T. M. Evans, G. G. Davidson, S. P. Hamilton, and A. T. Godfrey, "Implementation, Capabilities, and Benchmarking of Shift, a Massively Parallel Monte Carlo Radiation Transport Code," *Journal of Computational Physics*, vol. 308, pp. 239–272, Mar. 2016.

[21] T. Cole, L. Parsly, and W. Thomas, *Revisions to the HFIR Steady States Heat Transfer Analysis Code*. No. ORNL/CF-86/68, Apr. 1986.

[22] J. W. Bae, B. R. Betzler, D. Chandler, and G. Ilas, "Automated Fuel Design Optimization for High Flux Isotope Reactor Low Enriched Uranium Neutronic and Thermal Hydraulic Core Design," in *,Proc. Intl. Conf. PHYSOR 2020*, (Cambridge, UK), 2020.

[23] C. Werner, *MCNP6.2 Release Notes*. No. LA-UR-18-20808, 2018.

[24] D. Chandler, B. R. Betzler, E. E. Davidson, and G. Ilas, "Modeling and simulation of a High Flux Isotope Reactor representative core model for updated performance and safety basis assessments," *Nuclear Engineering and Design*, vol. 366, p. 110752, Sept. 2020.

[25] I. Variansyah, J. W. Bae, B. R. Betzler, and G. Ilas, *Metaheuristic Optimization Tool*. No. ORNL/TM-2019/1443, Mar. 2020.

[26] E. E. Davidson (née Sunny), B. R. Betzler, D. Chandler, and G. Ilas, "Heat deposition analysis for the High Flux Isotope Reactor's HEU and LEU core models," *Nuclear Engineering and Design*, vol. 322, pp. 563–576, Oct. 2017.

[27] W. Gambill, *Design Curves for Burnout Heat Flux in Forced-Convection Subcooled Light Water Systems*. No. ORNL-TM-2421, U.S. Atomic Energy Commission, Nov. 1968.

APPENDIX A. DISTRIBUTIONS FOR 22-INCH DESIGN

APPENDIX A-1. FISSION RATE DENSITY DISTRIBUTIONS FOR 22-INCH DESIGN

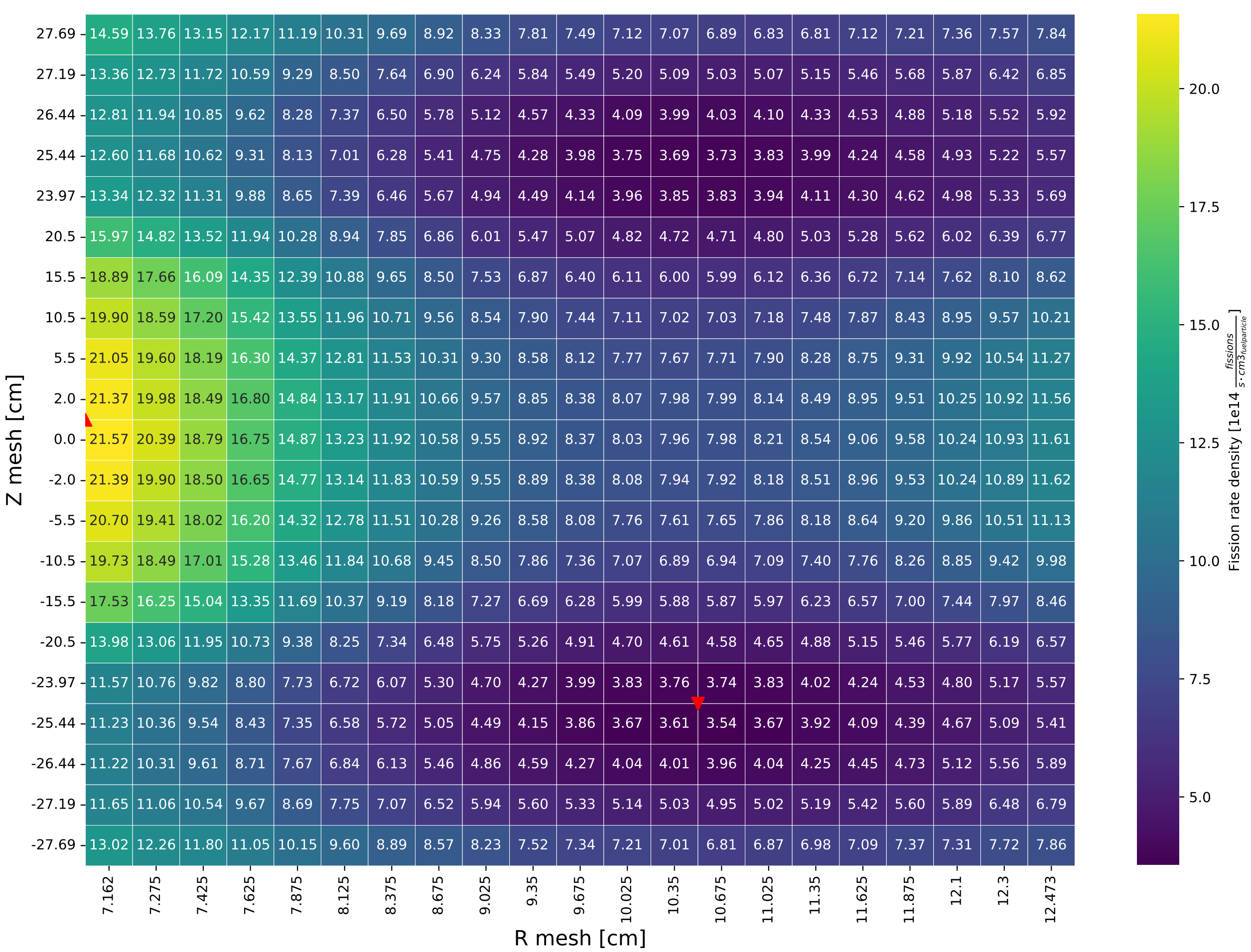

Figure 33. Fission rate density distribution for 22-inch design IFE region on day 0 (see Section 7.1.2).

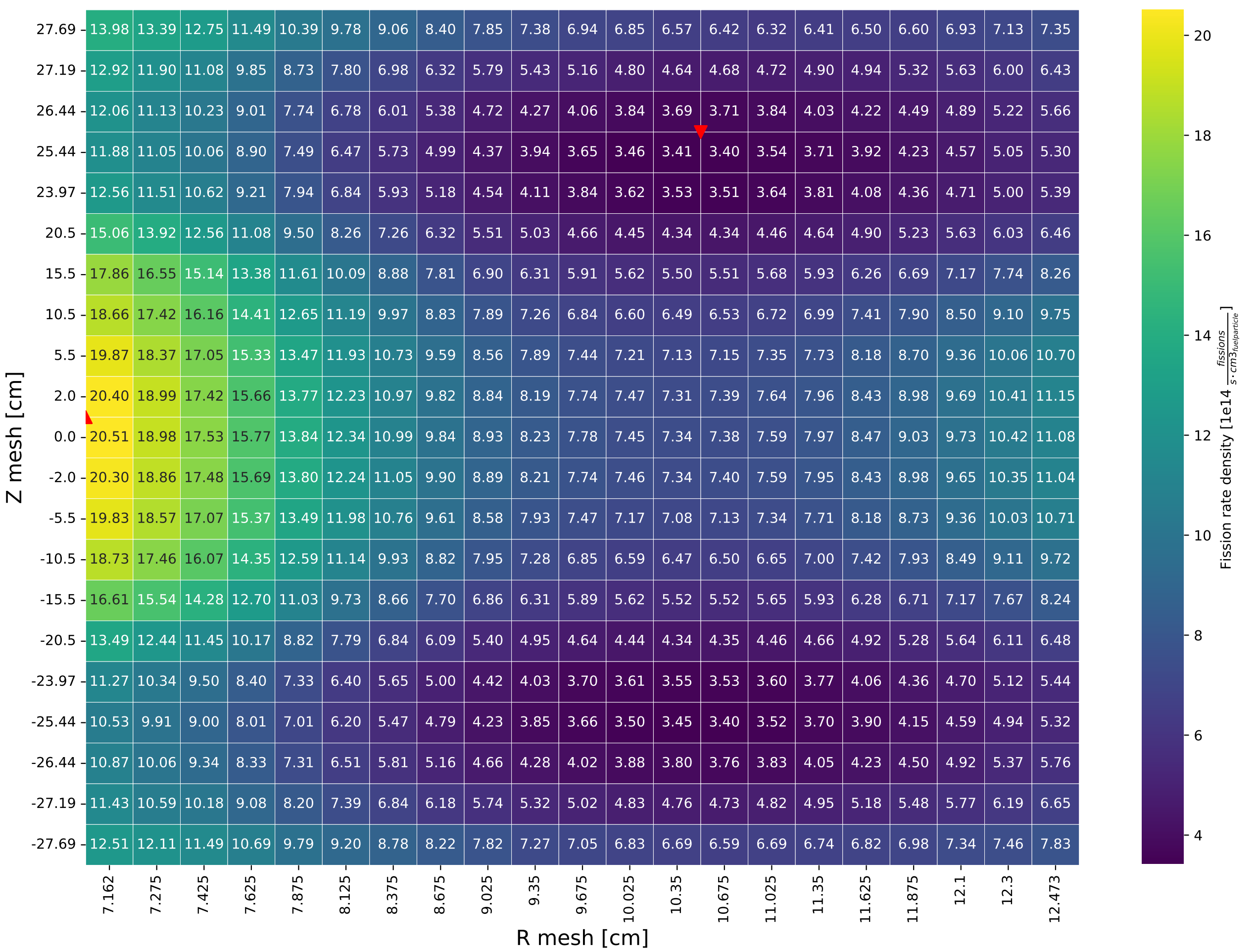

Figure 34. Fission rate density distribution for 22-inch design IFE region on day 1 (see Section 7.1.2).

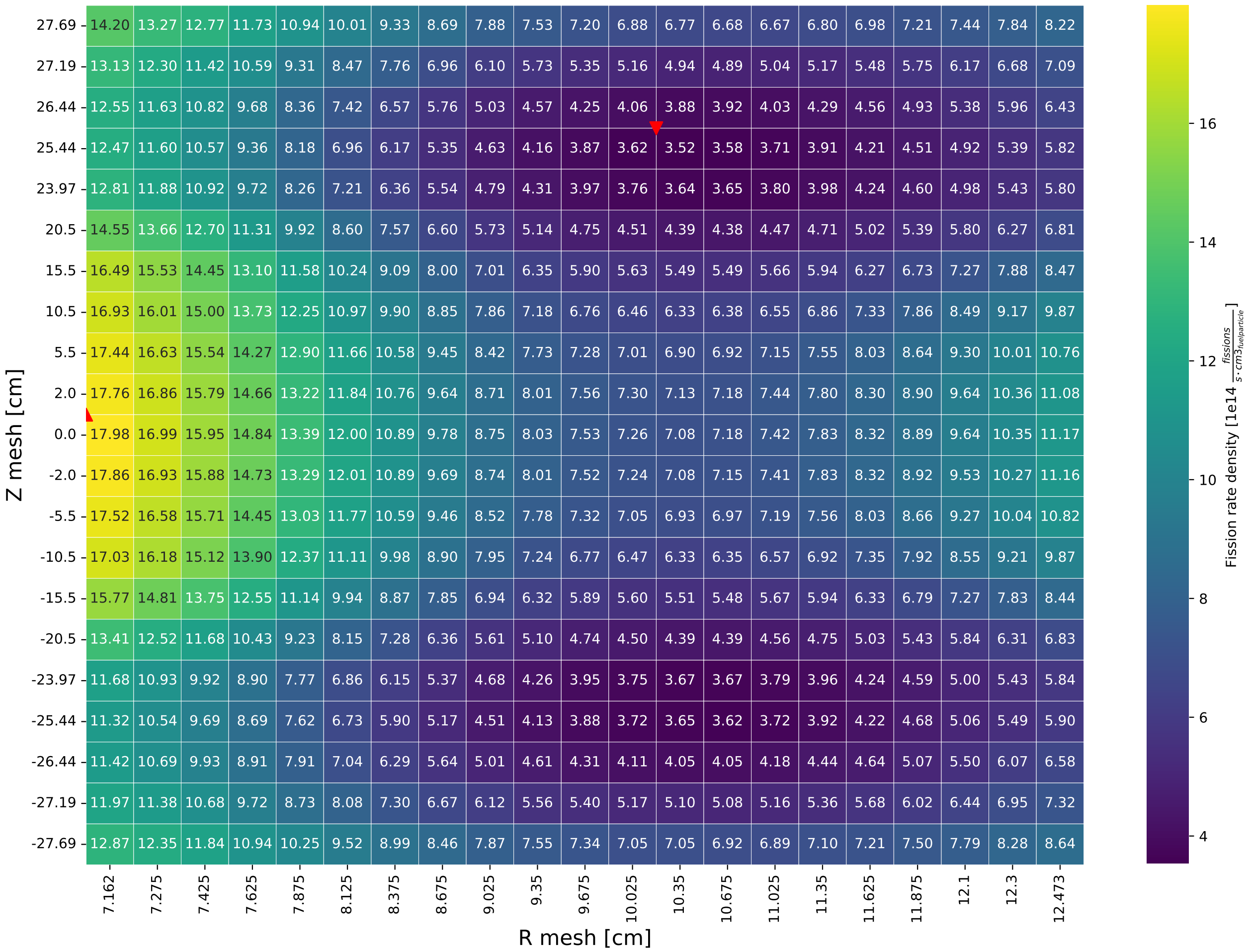

Figure 35. Fission rate density distribution for 22-inch design IFE region on day 15 (see Section 7.1.2).

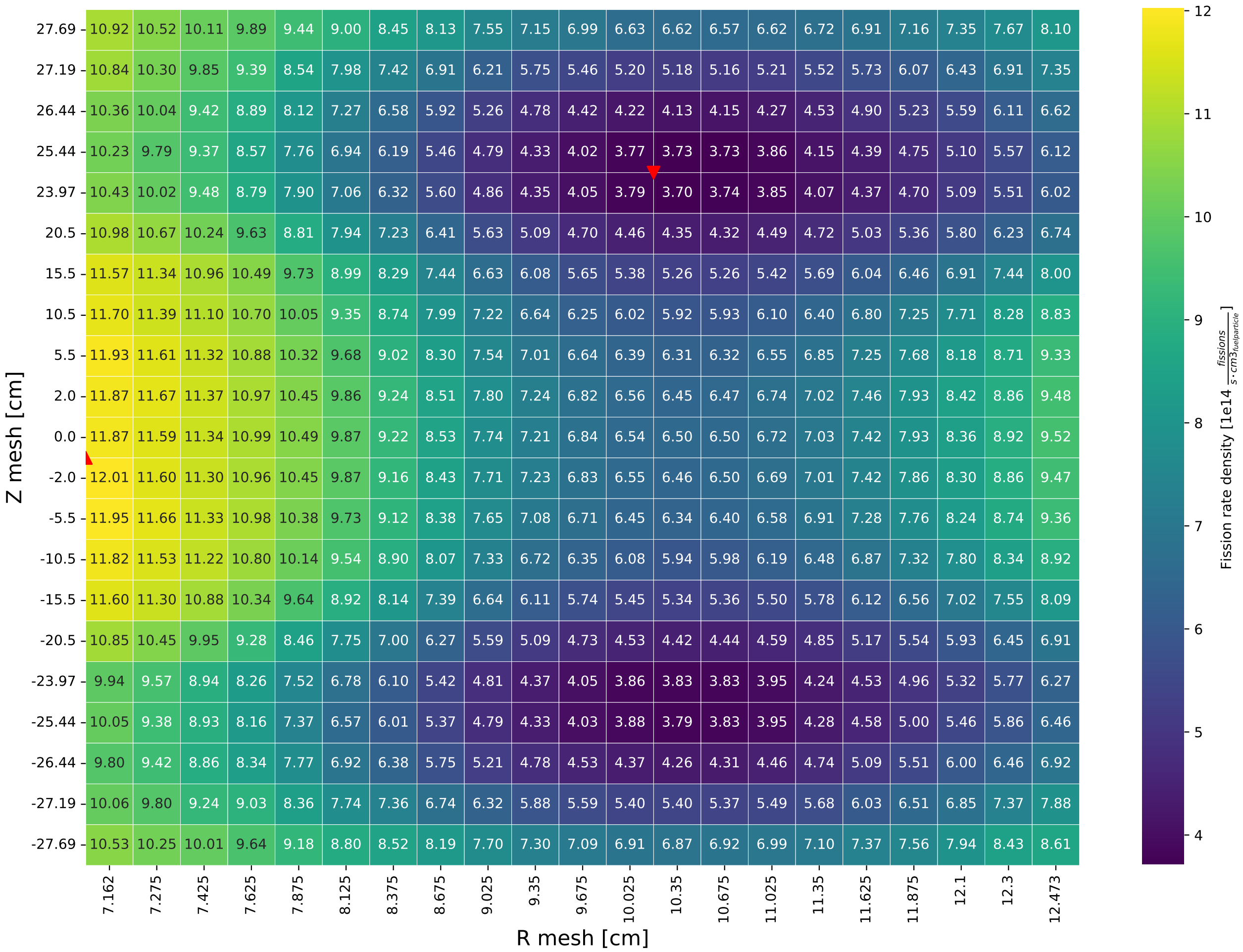

Figure 36. Fission rate density distribution for 22-inch design IFE region on day 31 (see Section 7.1.2).

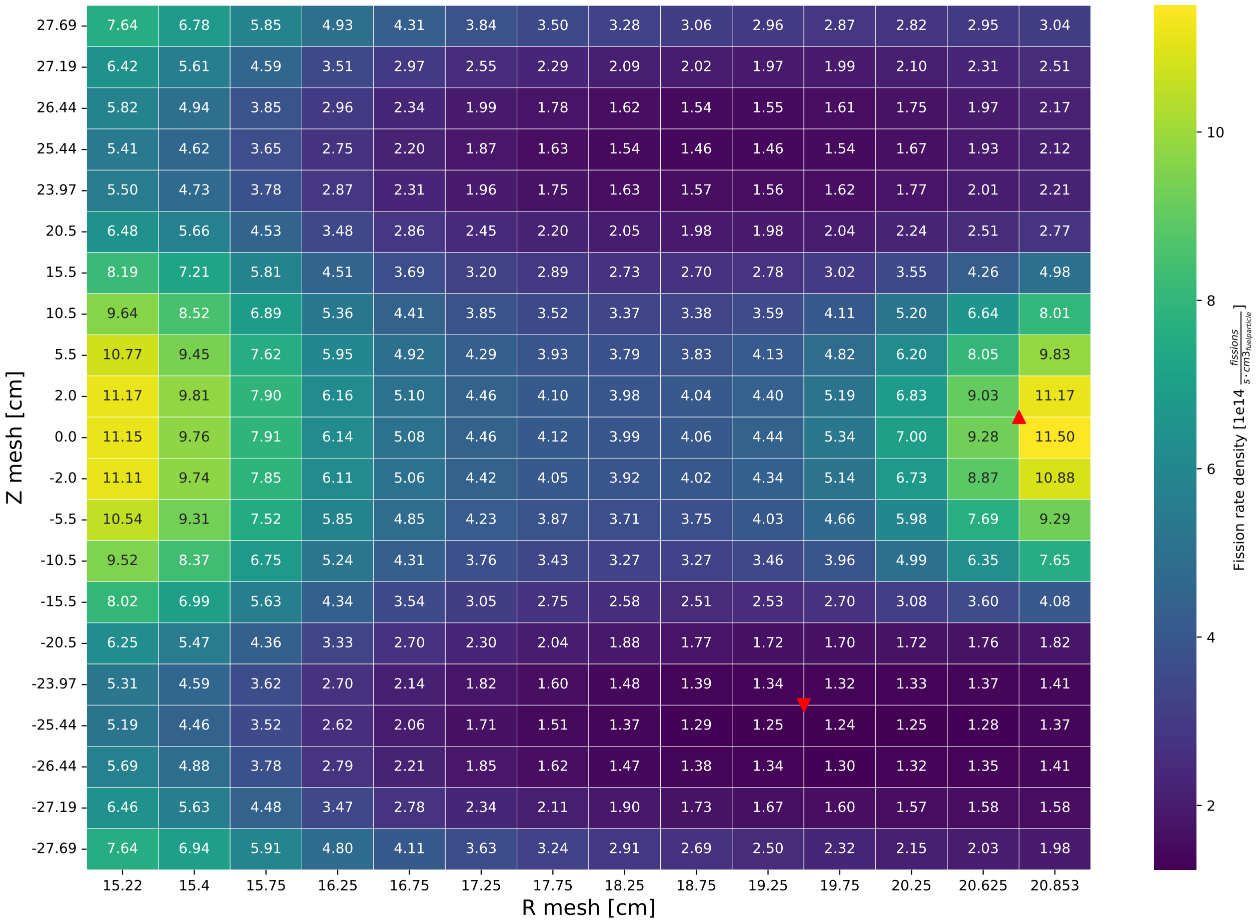

Figure 37. Fission rate density distribution for 22-inch design OFE region on day 0 (see Section 7.1.2).

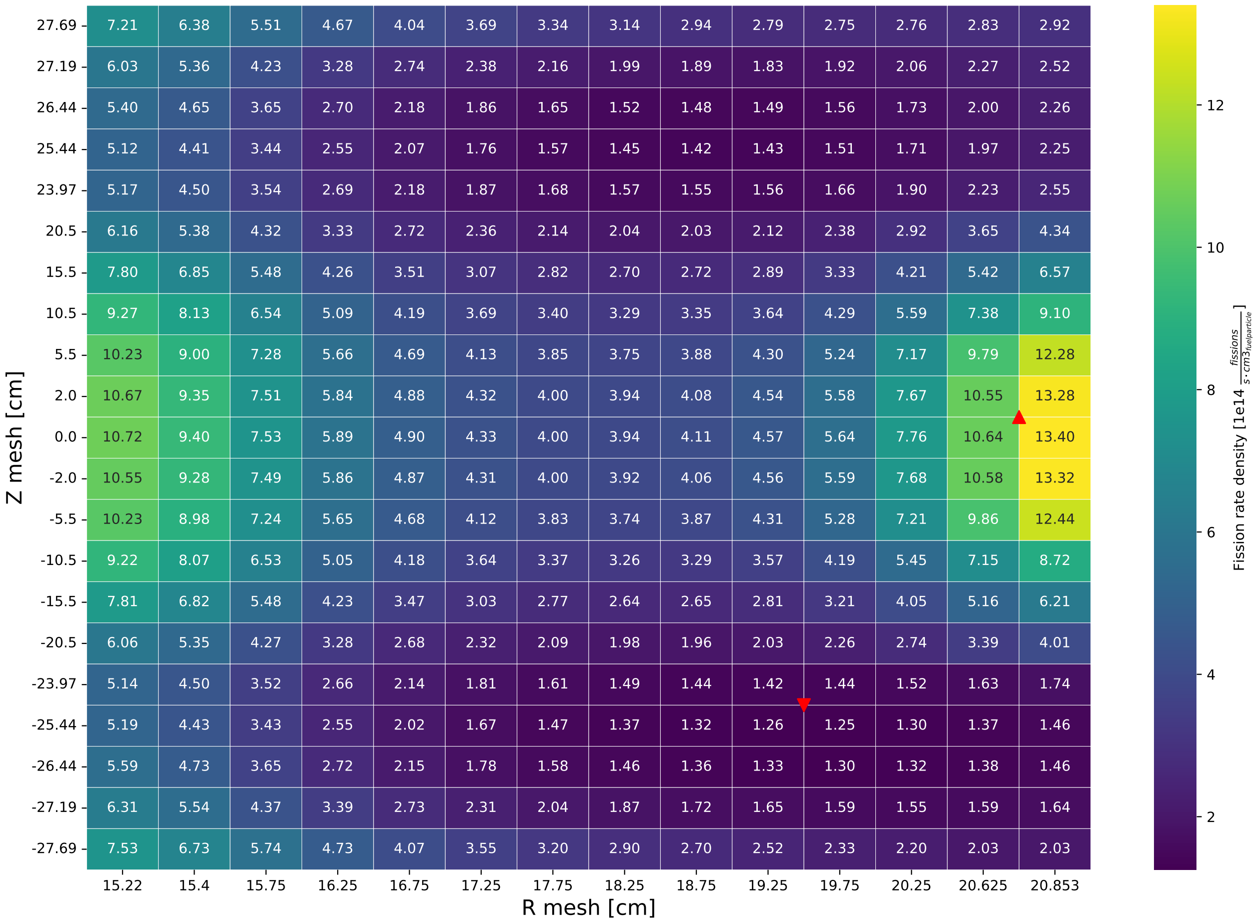

Figure 38. Fission rate density distribution for 22-inch design OFE region on day 1 (see Section 7.1.2).

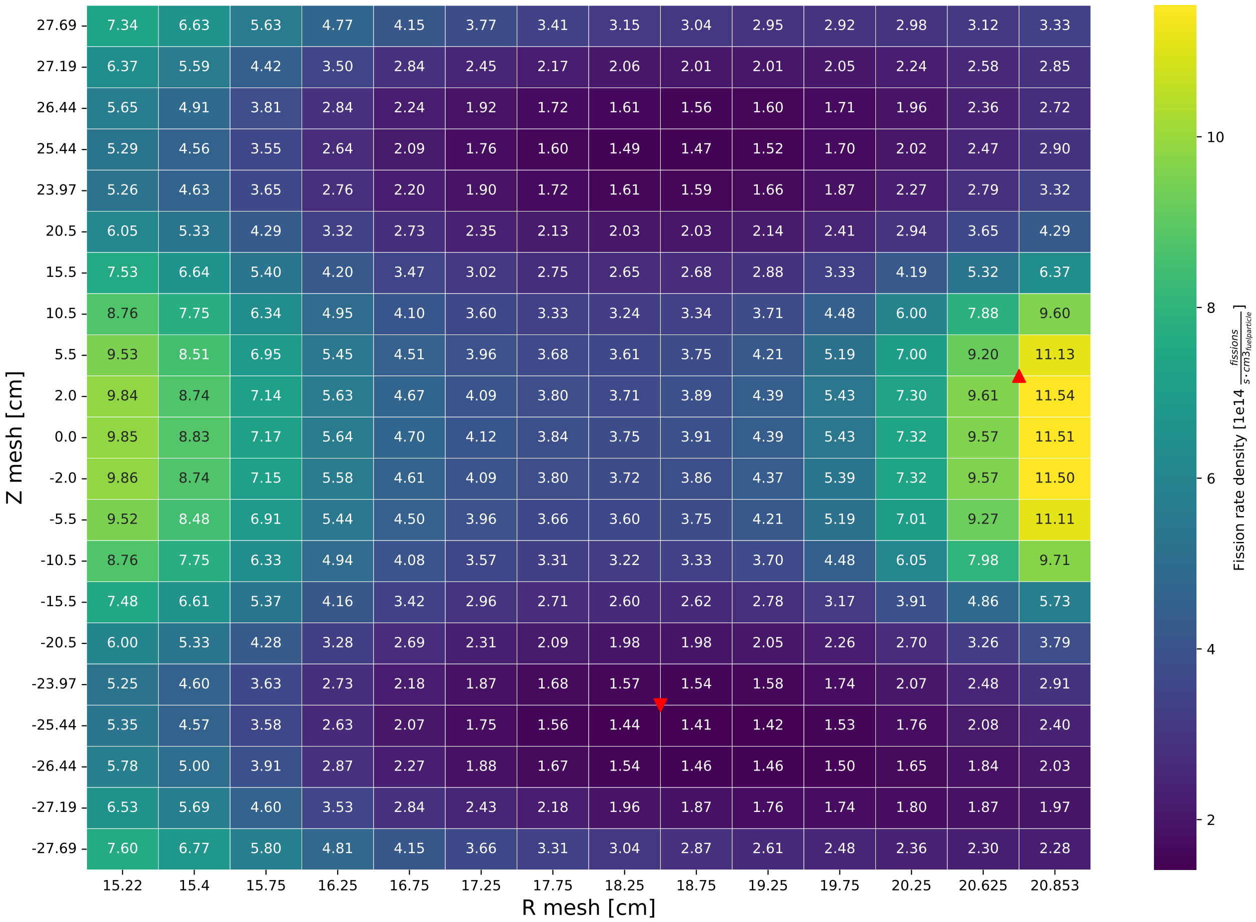

Figure 39. Fission rate density distribution for 22-inch design OFE region on day 15 (see Section 7.1.2).

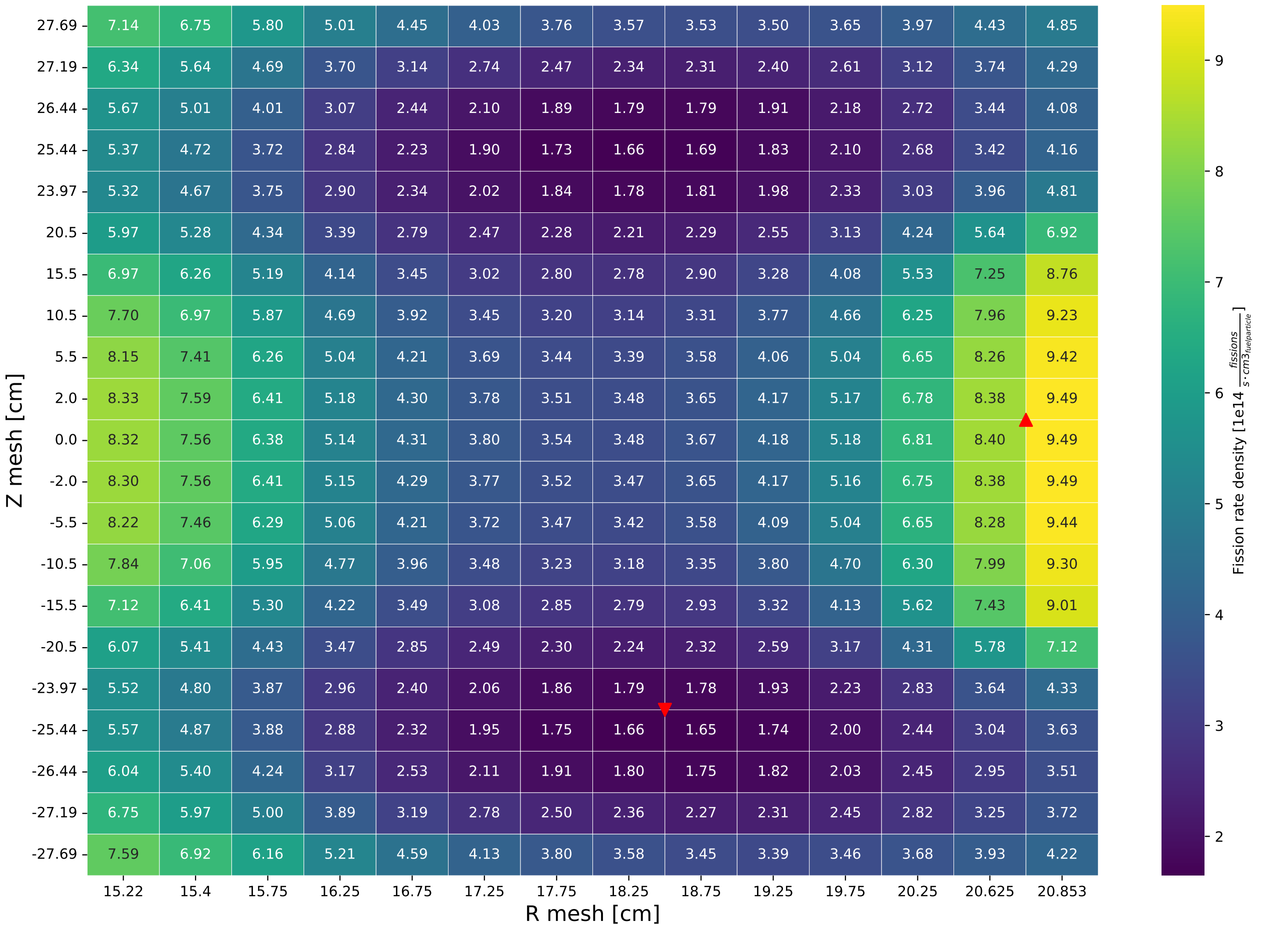

Figure 40. Fission rate density distribution for 22-inch design OFE region on day 31 (see Section 7.1.2).

APPENDIX A-2. CUMULATIVE FISSION DENSITY DISTRIBUTIONS FOR 22-INCH DESIGN

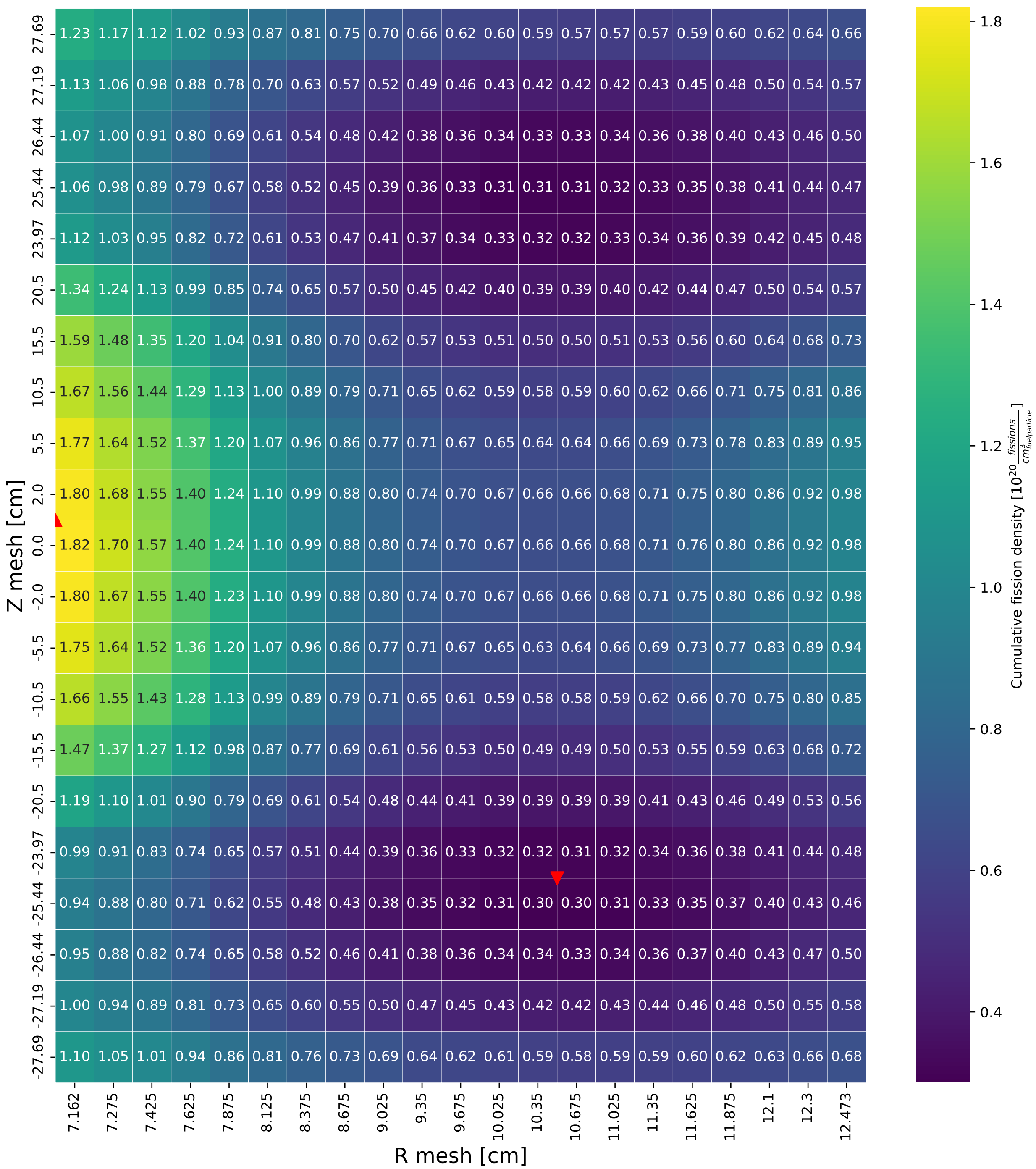

Figure 41. Cumulative fission density distribution for 22-inch design IFE region on day 1 (see Section 7.1.5).

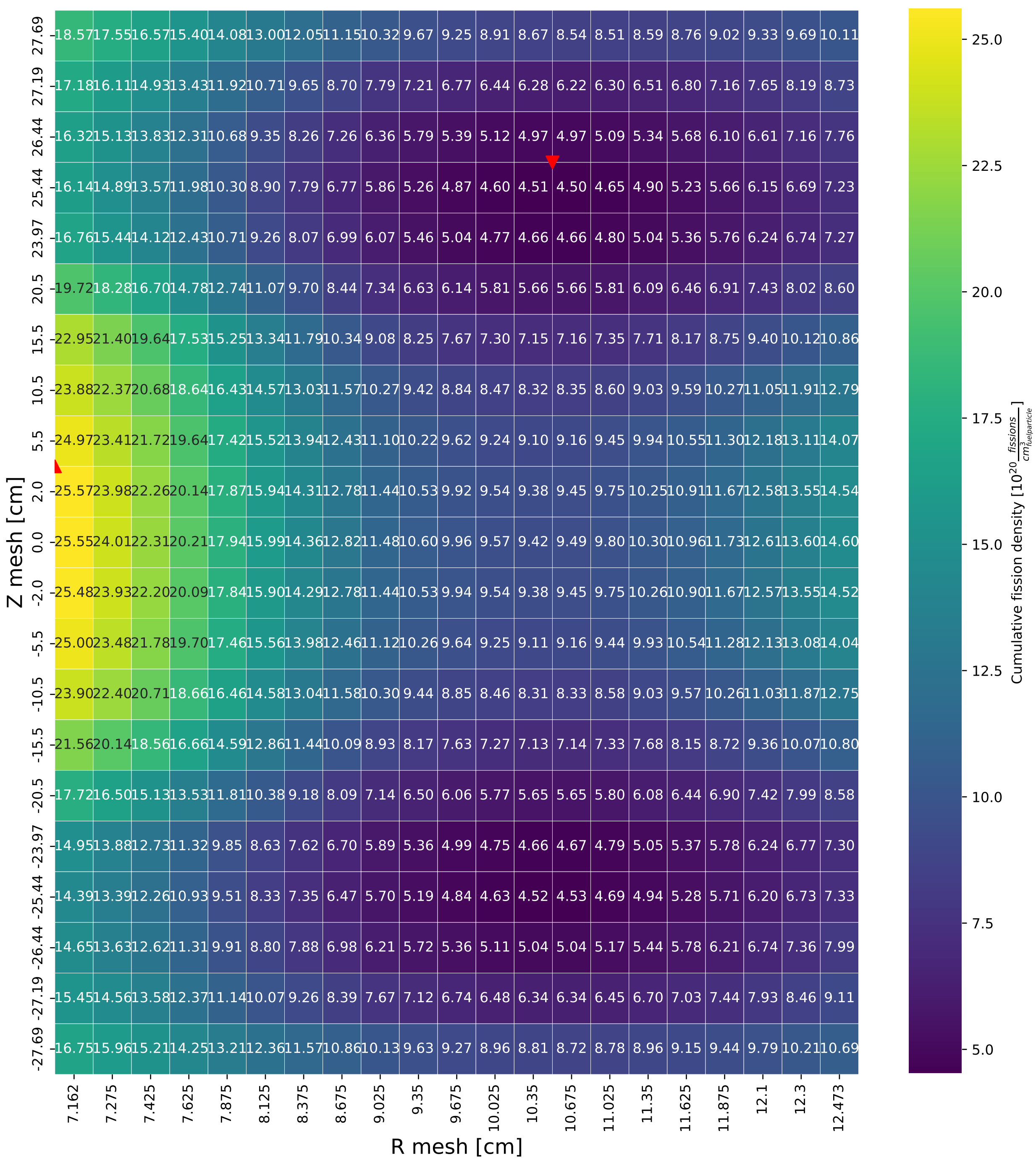

Figure 42. Cumulative fission density distribution for 22-inch design IFE region on day 15 (see Section 7.1.5).

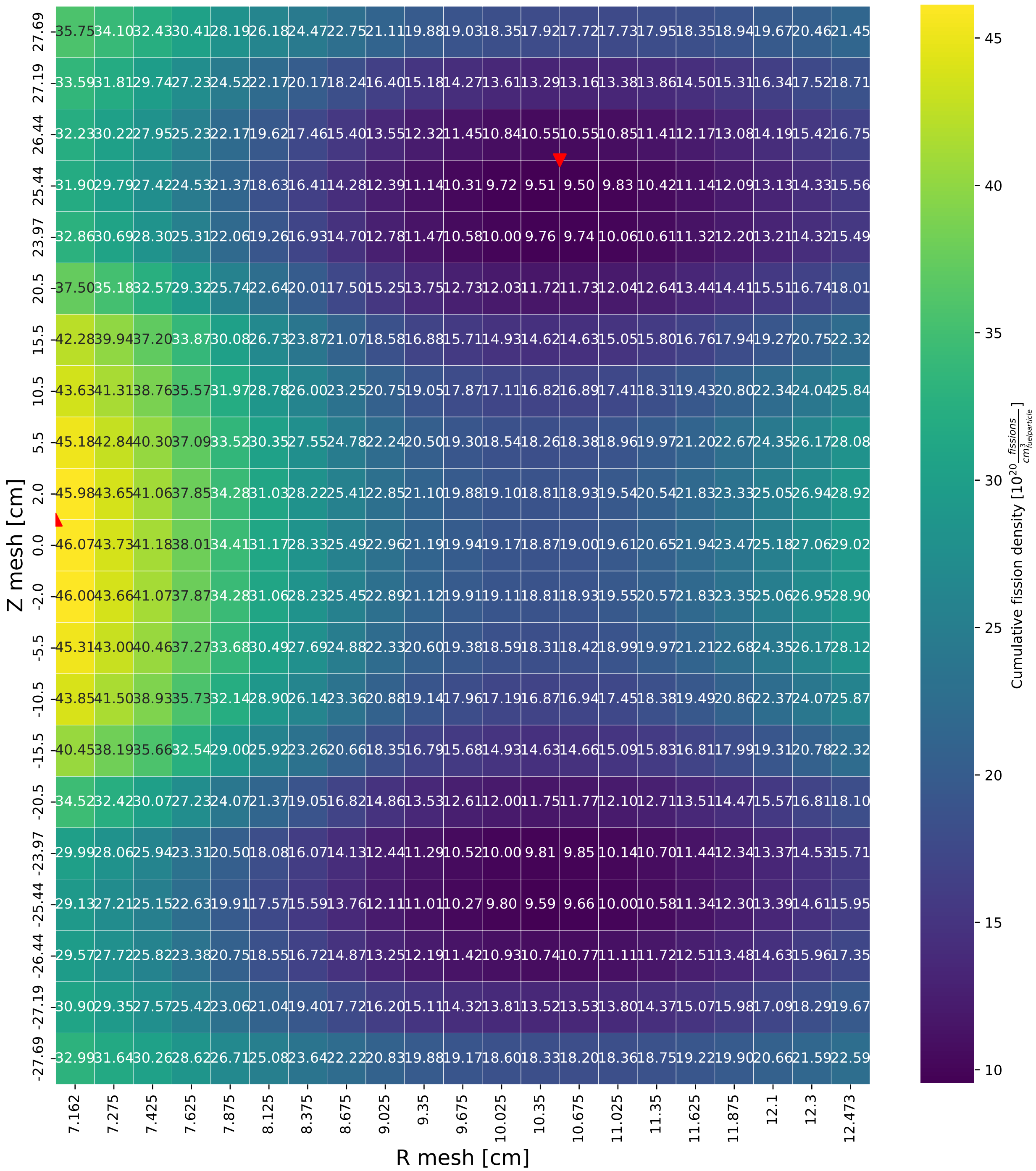

Figure 43. Cumulative fission density distribution for 22-inch design IFE region on day 31 (see Section 7.1.5).

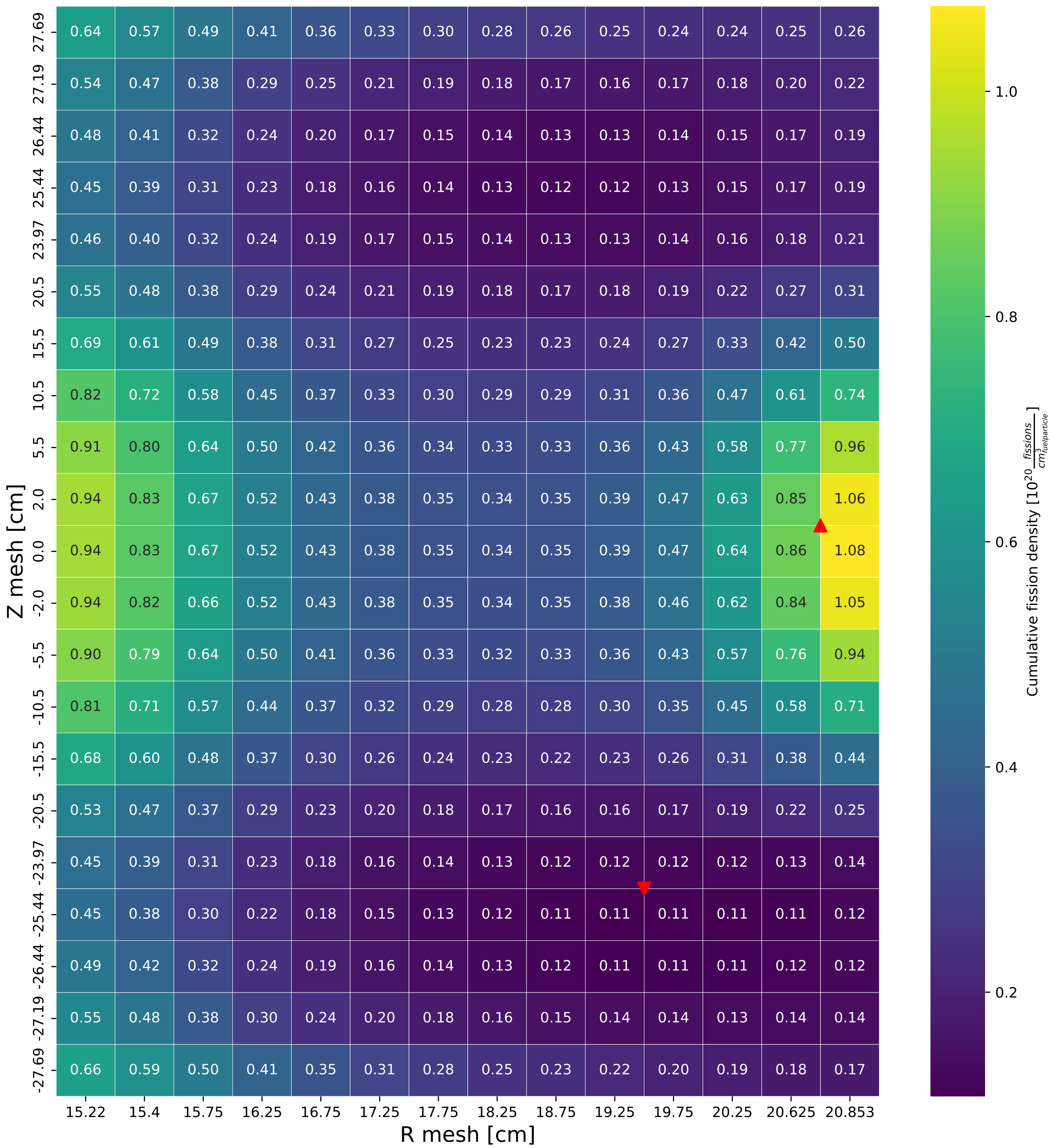

Figure 44. Cumulative fission density distribution for 22-inch design OFE region on day 1 (see Section 7.1.5).

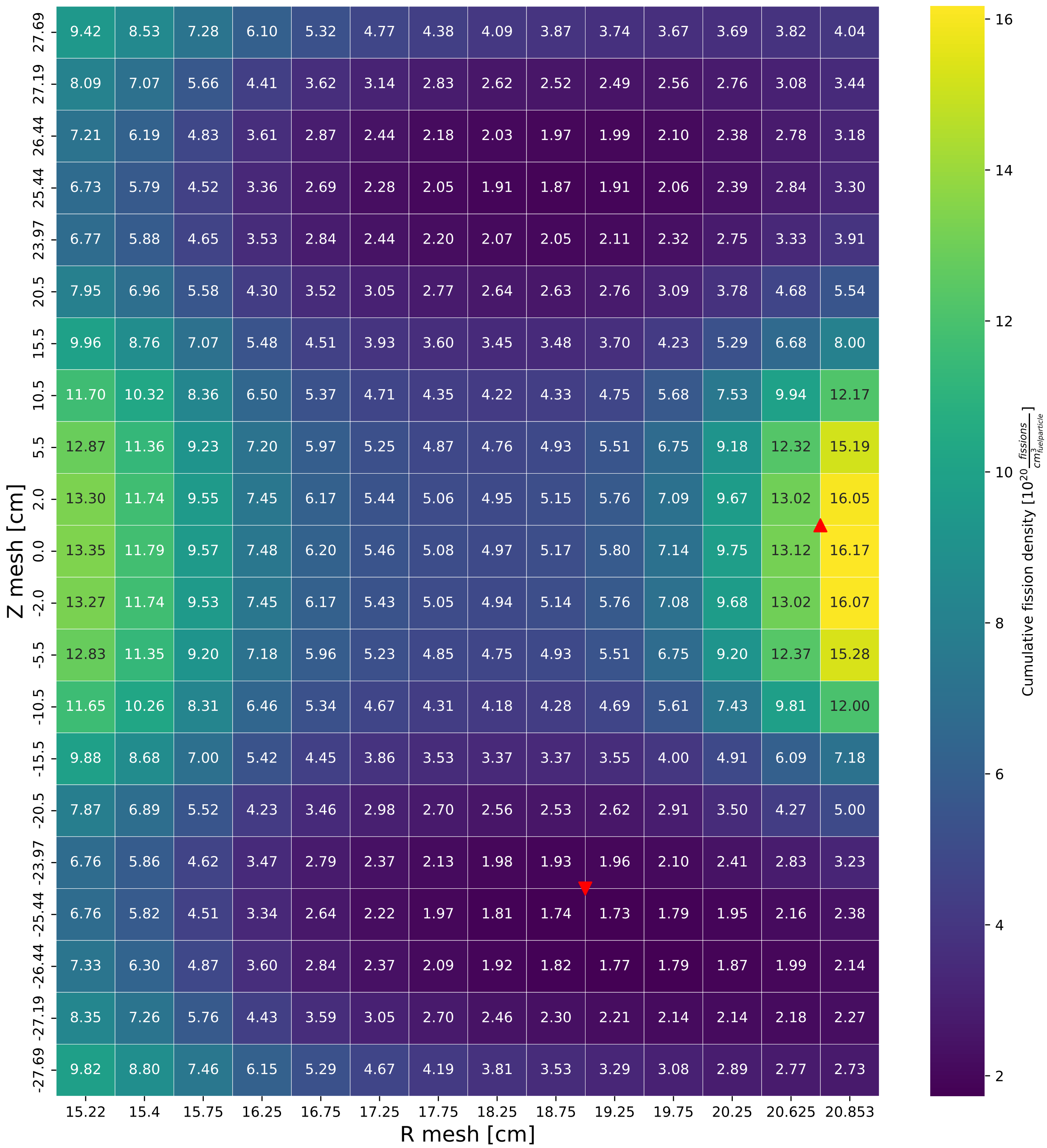

Figure 45. Cumulative fission density distribution for 22-inch design OFE region on day 15 (see Section 7.1.5).

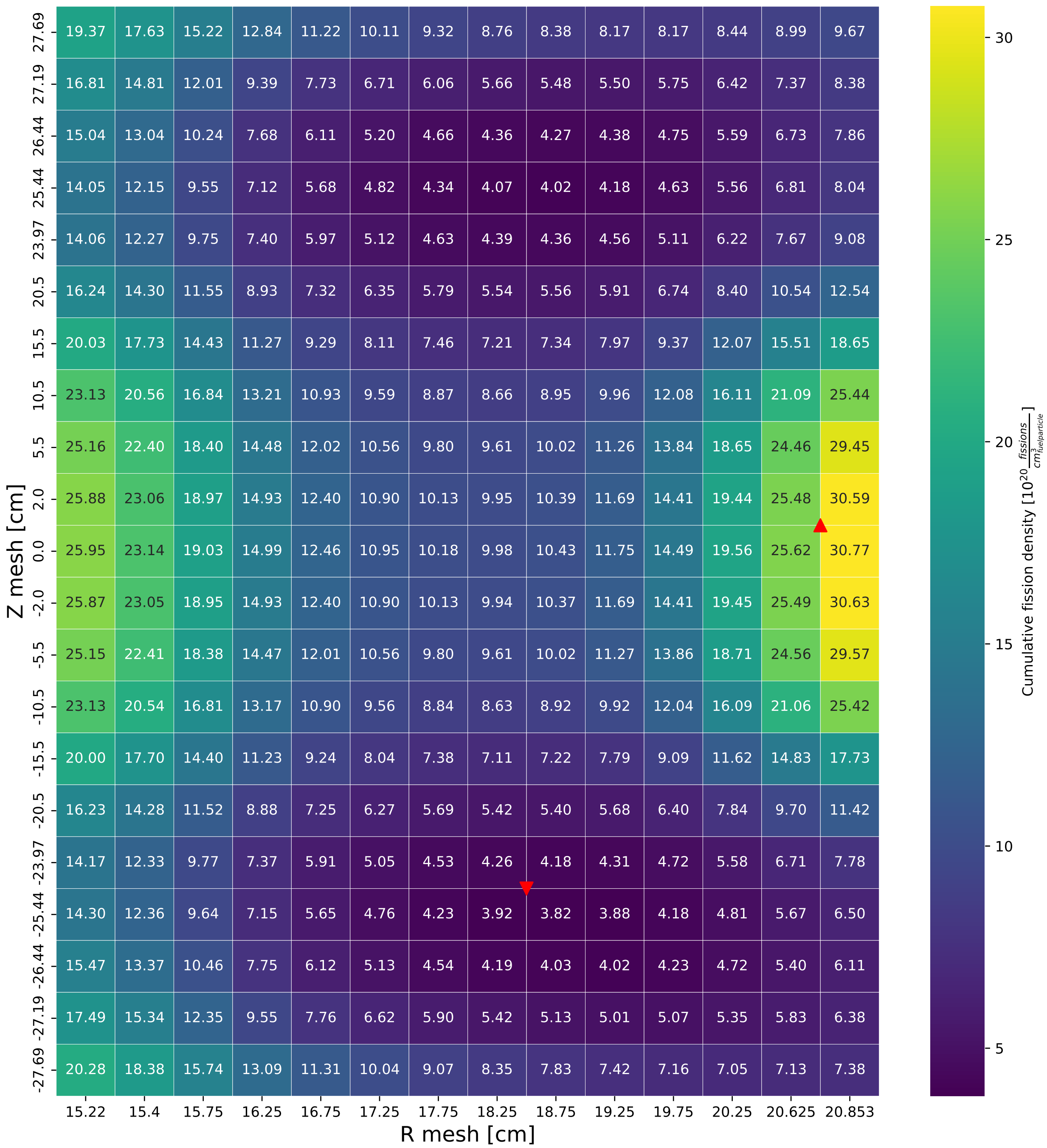

Figure 46. Cumulative fission density distribution for 22-inch design OFE region on day 31 (see Section 7.1.5).

APPENDIX A-3. POWER DENSITY DISTRIBUTIONS FOR 22-INCH DESIGN

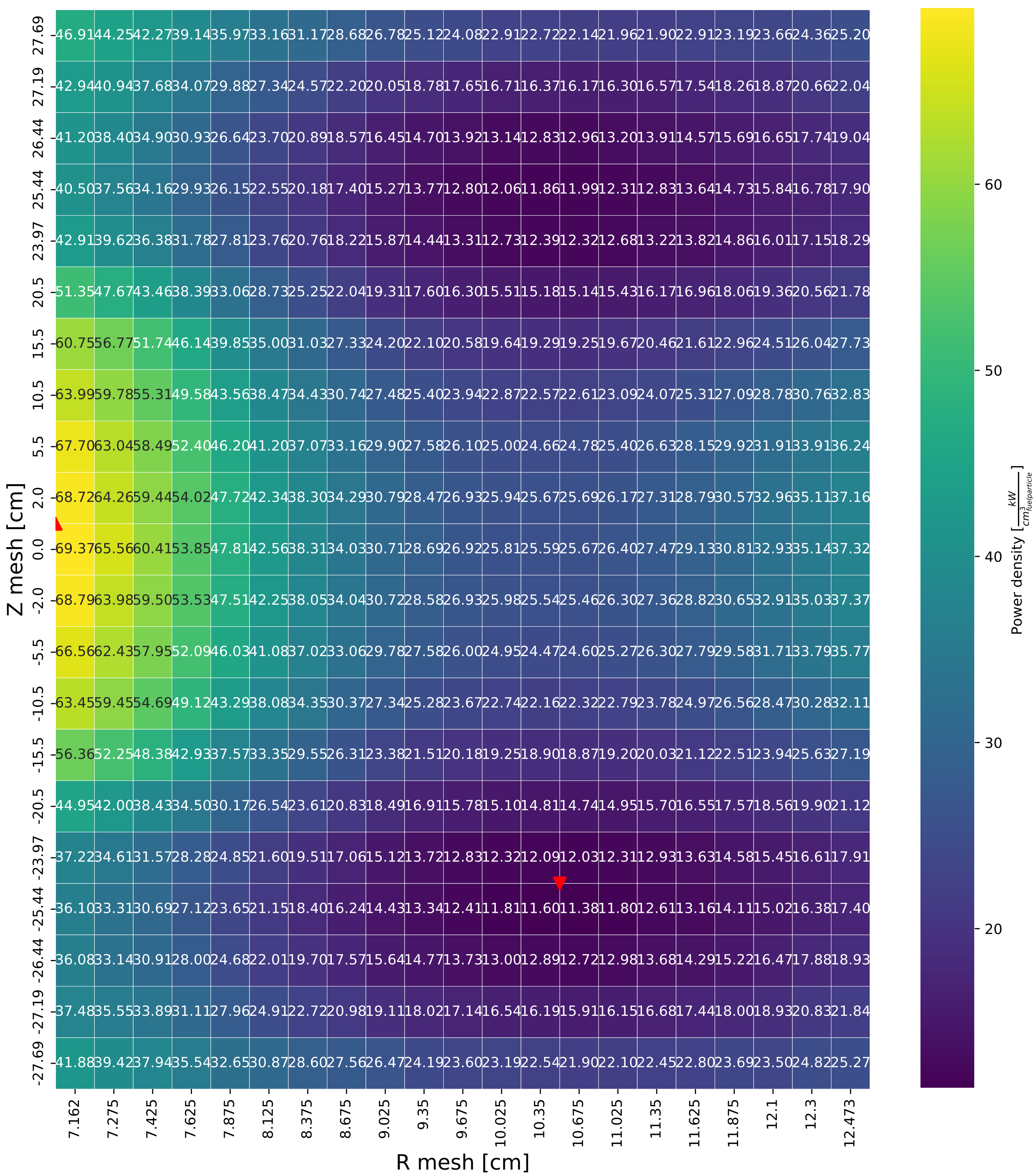

Figure 47. Power density distribution for 22-inch design IFE region on day 0 (see Section 7.1.3).

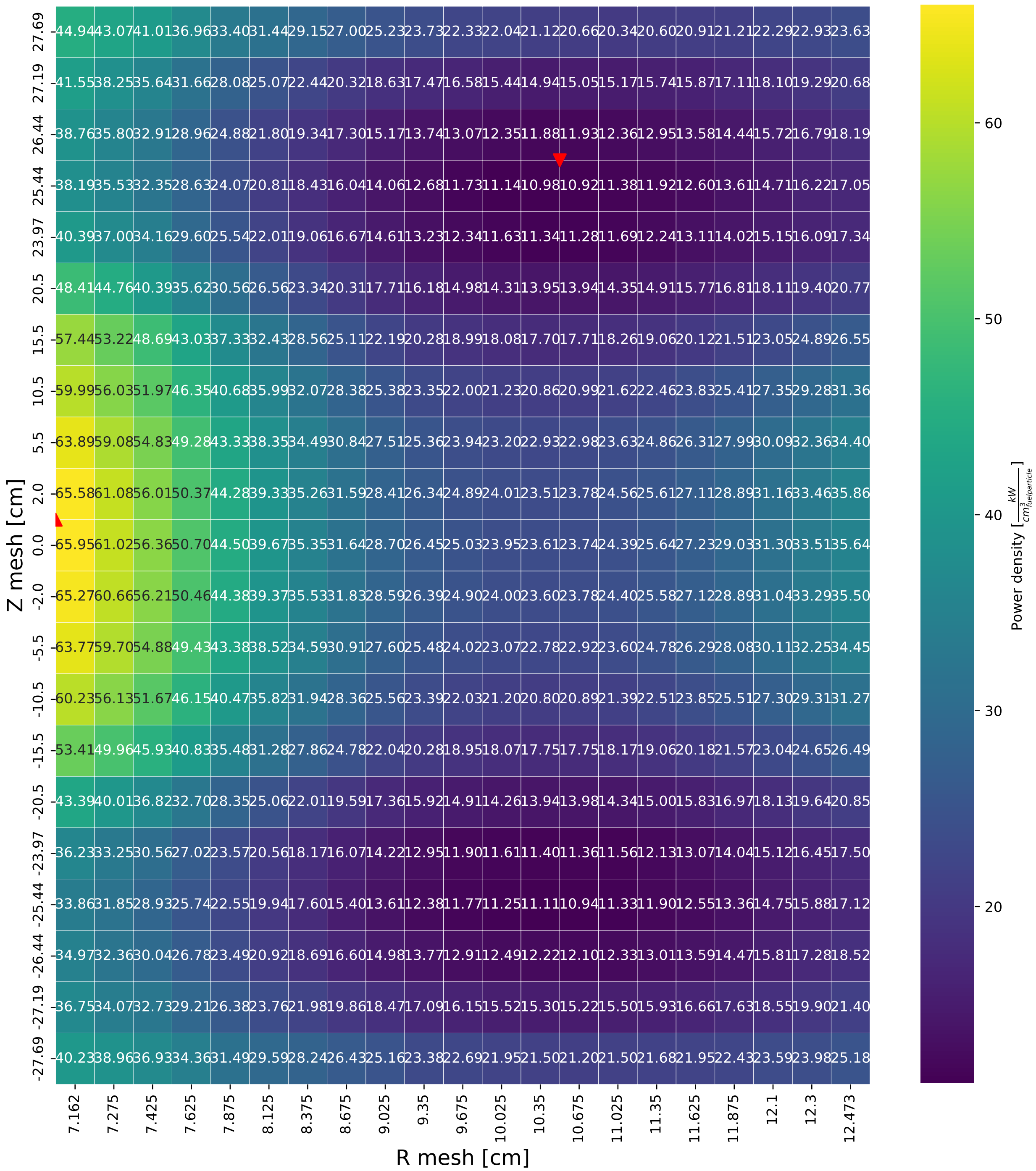

Figure 48. Power density distribution for 22-inch design IFE region on day 1 (see Section 7.1.3).

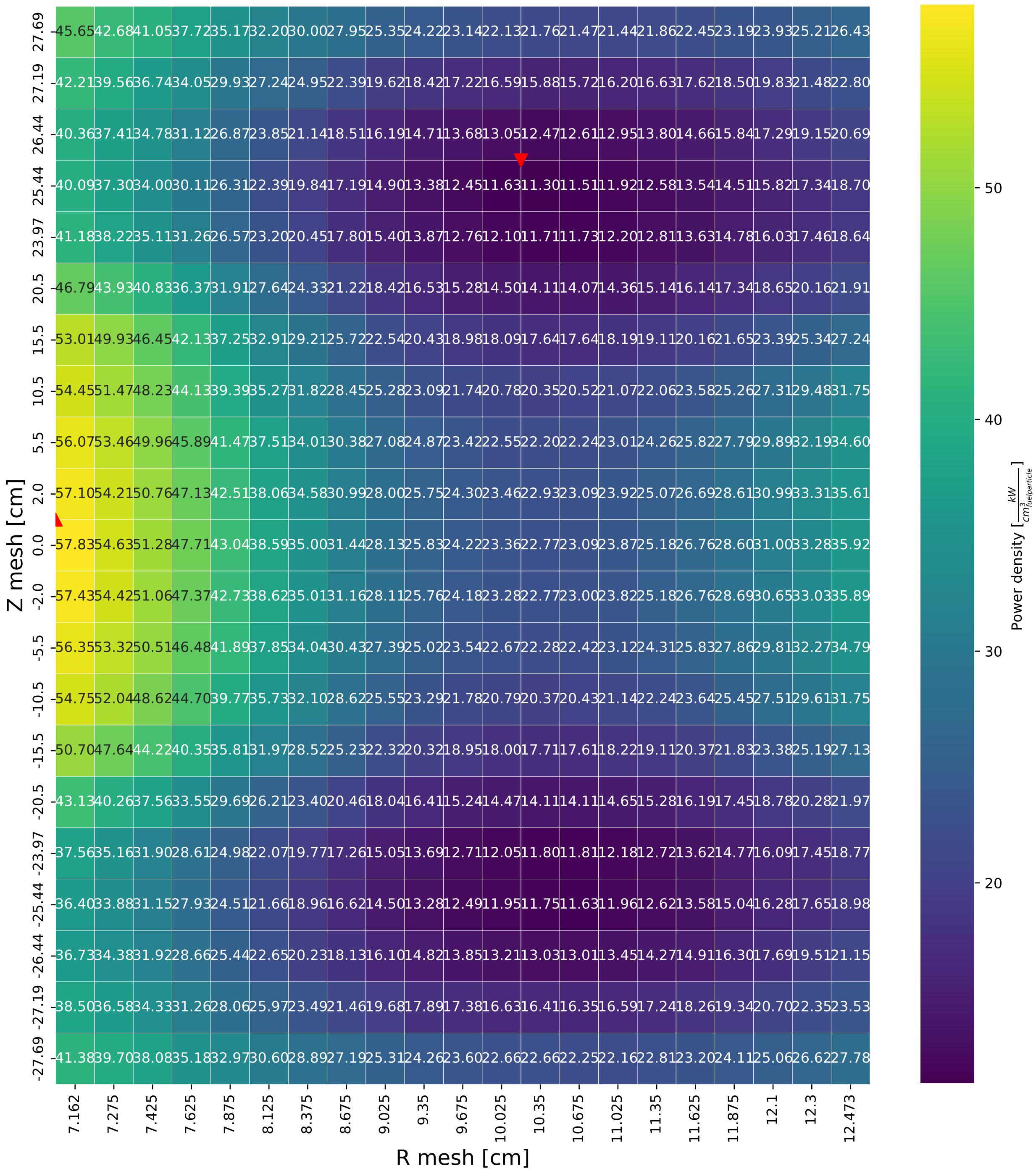

Figure 49. Power density distribution for 22-inch design IFE region on day 15 (see Section 7.1.3).

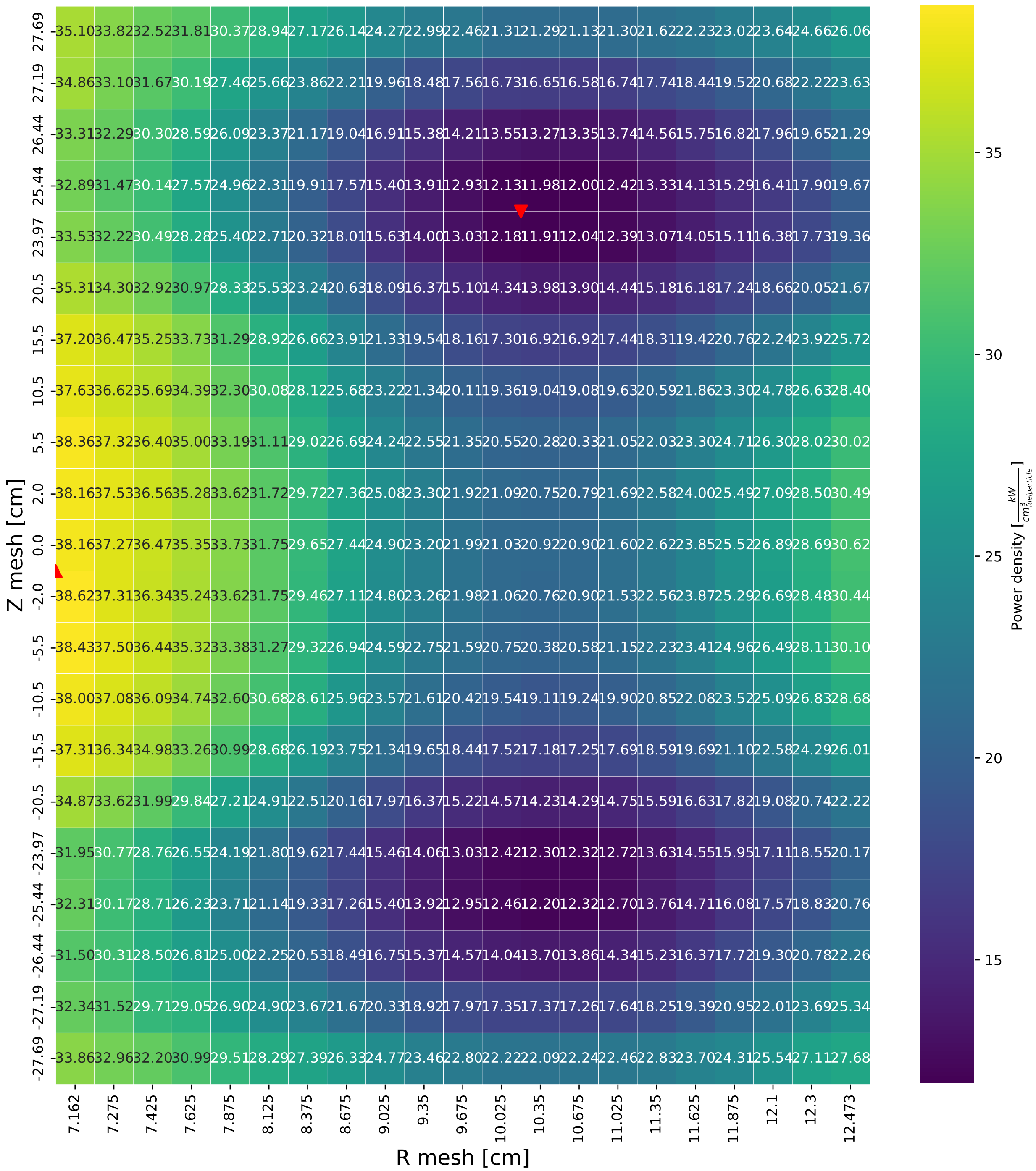

Figure 50. Power density distribution for 22-inch design IFE region on day 31 (see Section 7.1.3).

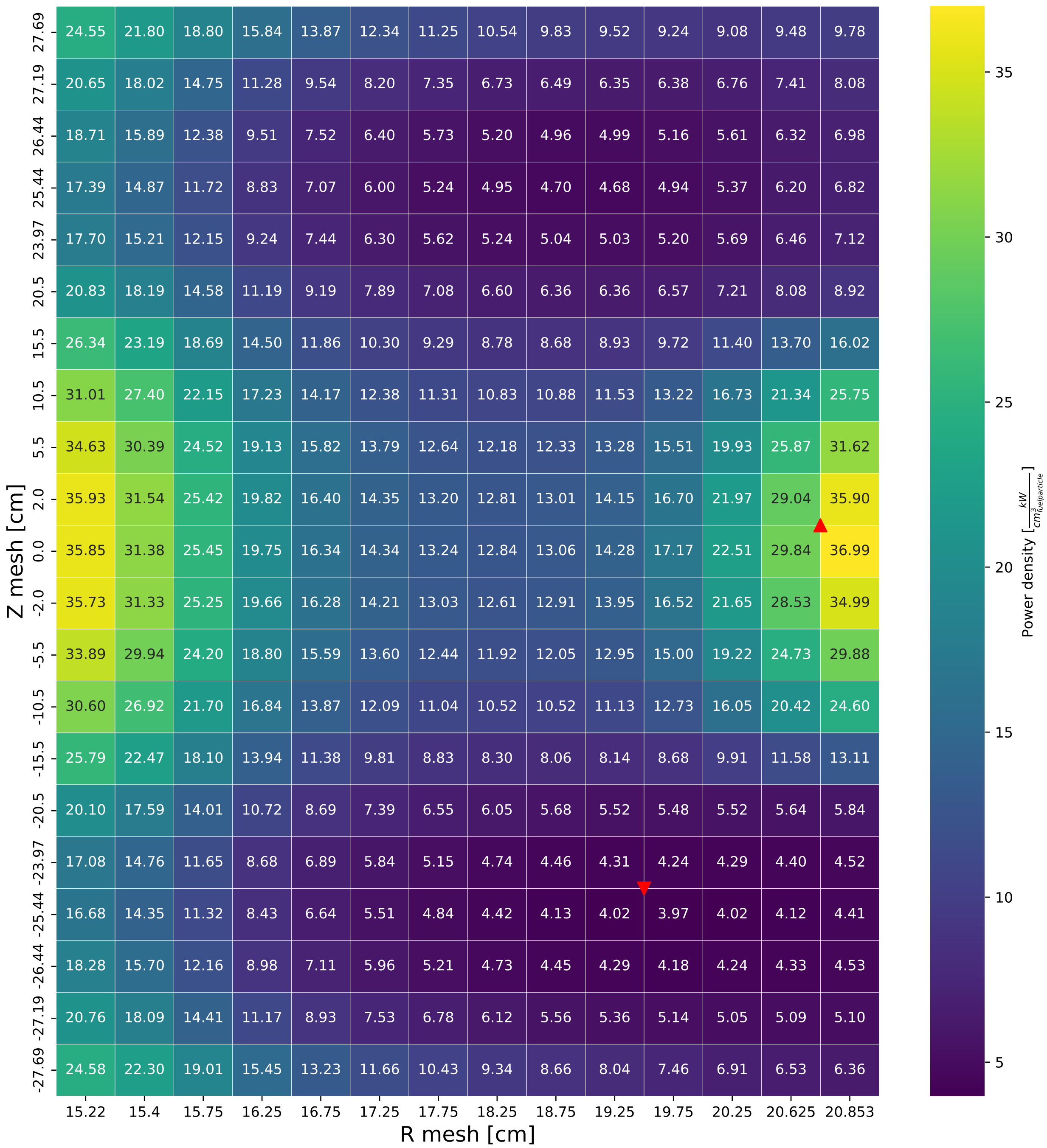

Figure 51. Power density distribution for 22-inch design OFE region on day 0 (see Section 7.1.3).

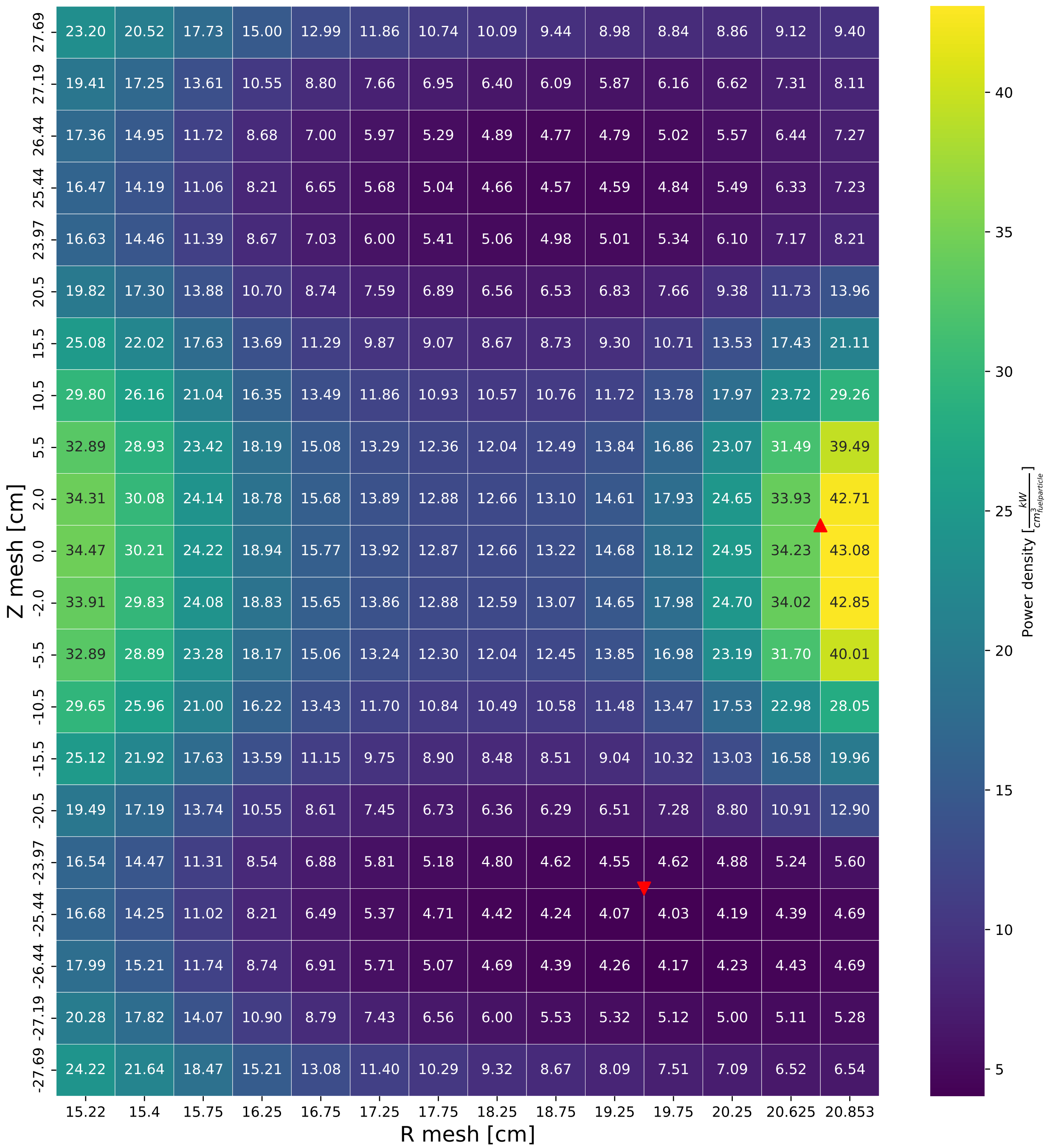

Figure 52. Power density distribution for 22-inch design OFE region on day 1 (see Section 7.1.3).

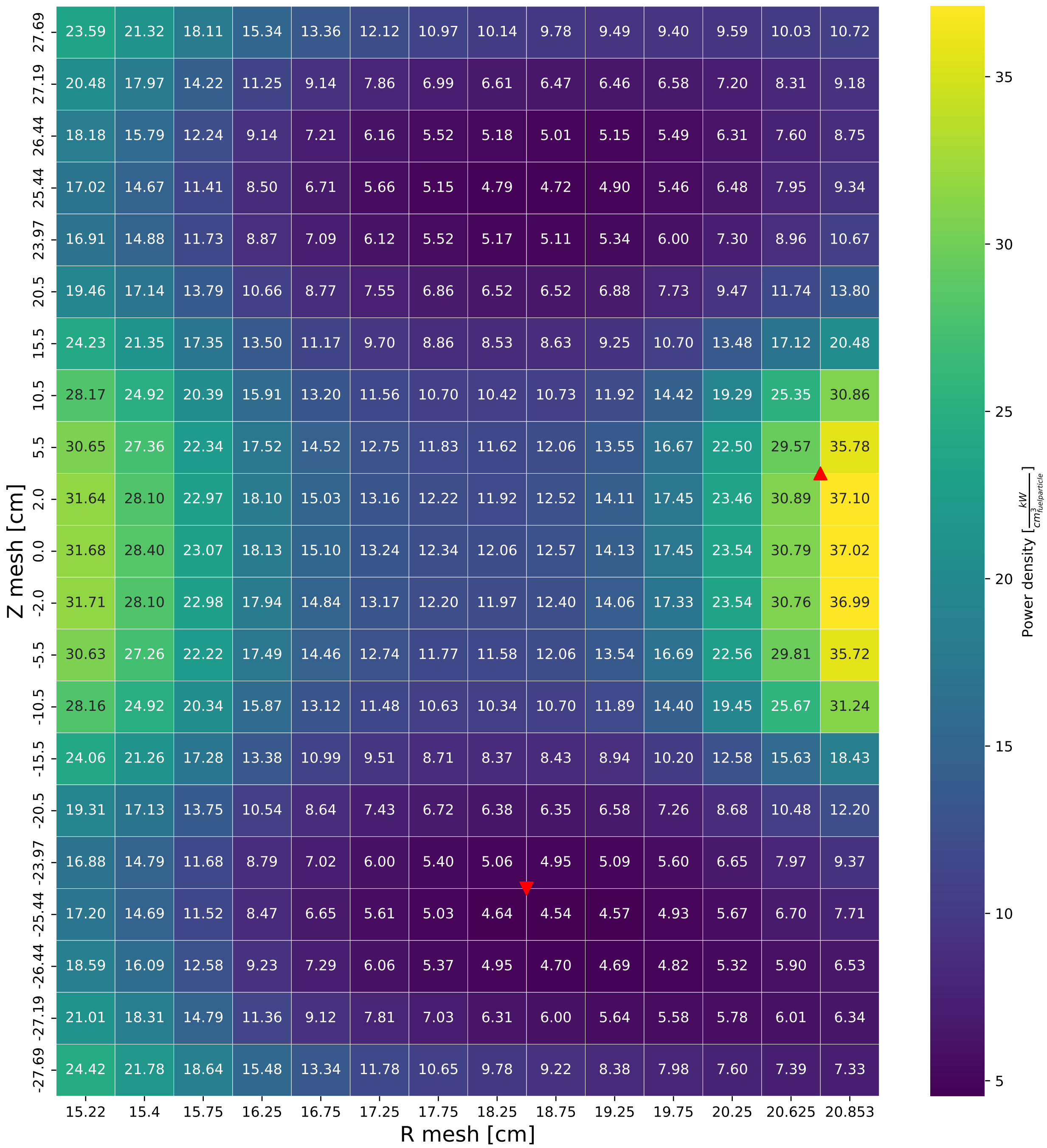

Figure 53. Power density distribution for 22-inch design OFE region on day 15 (see Section 7.1.3).

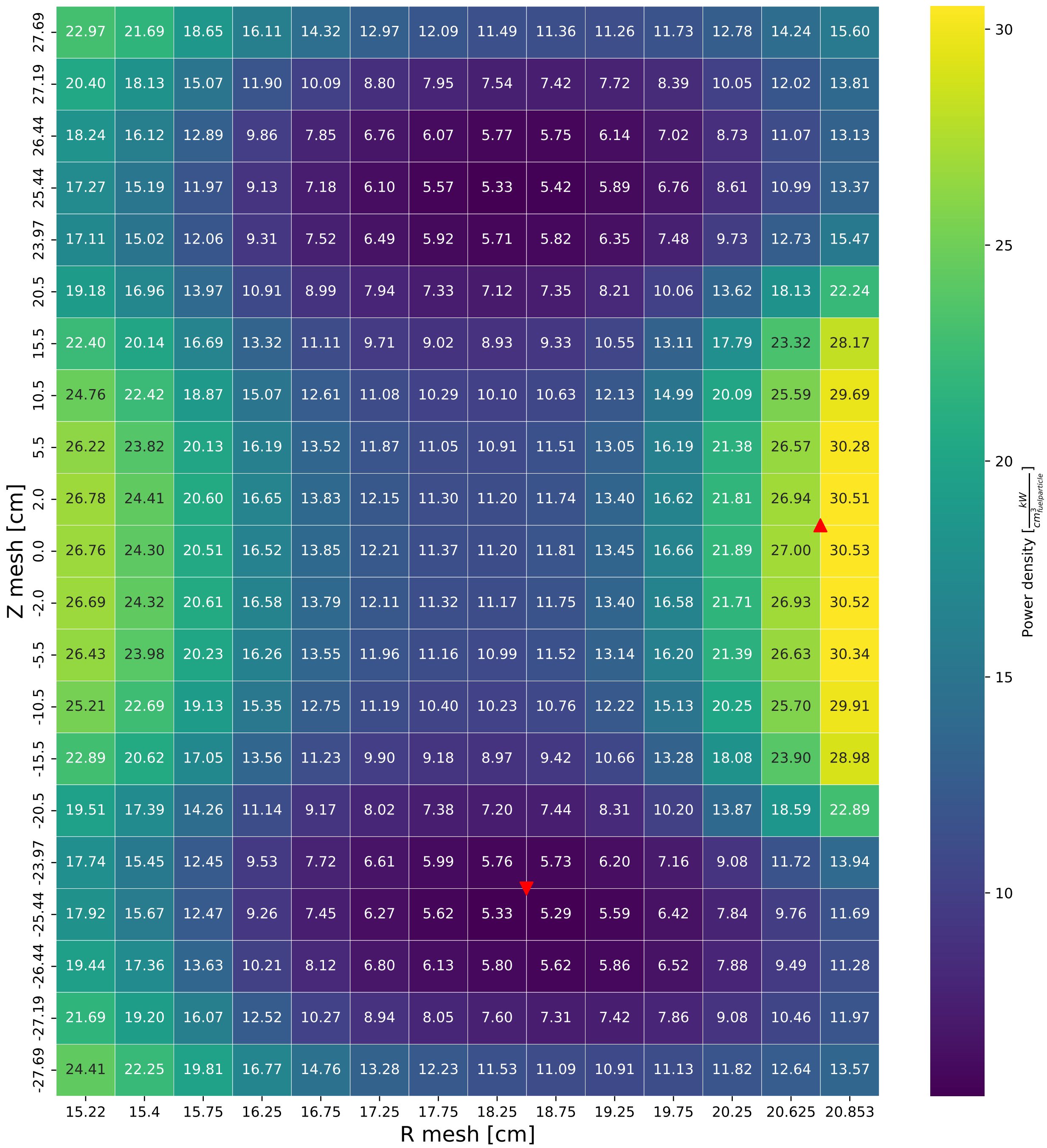

Figure 54. Power density distribution for 22-inch design OFE region on day 31 (see Section 7.1.3).

APPENDIX A-4. HEAT FLUX DISTRIBUTIONS FOR 22-INCH DESIGN

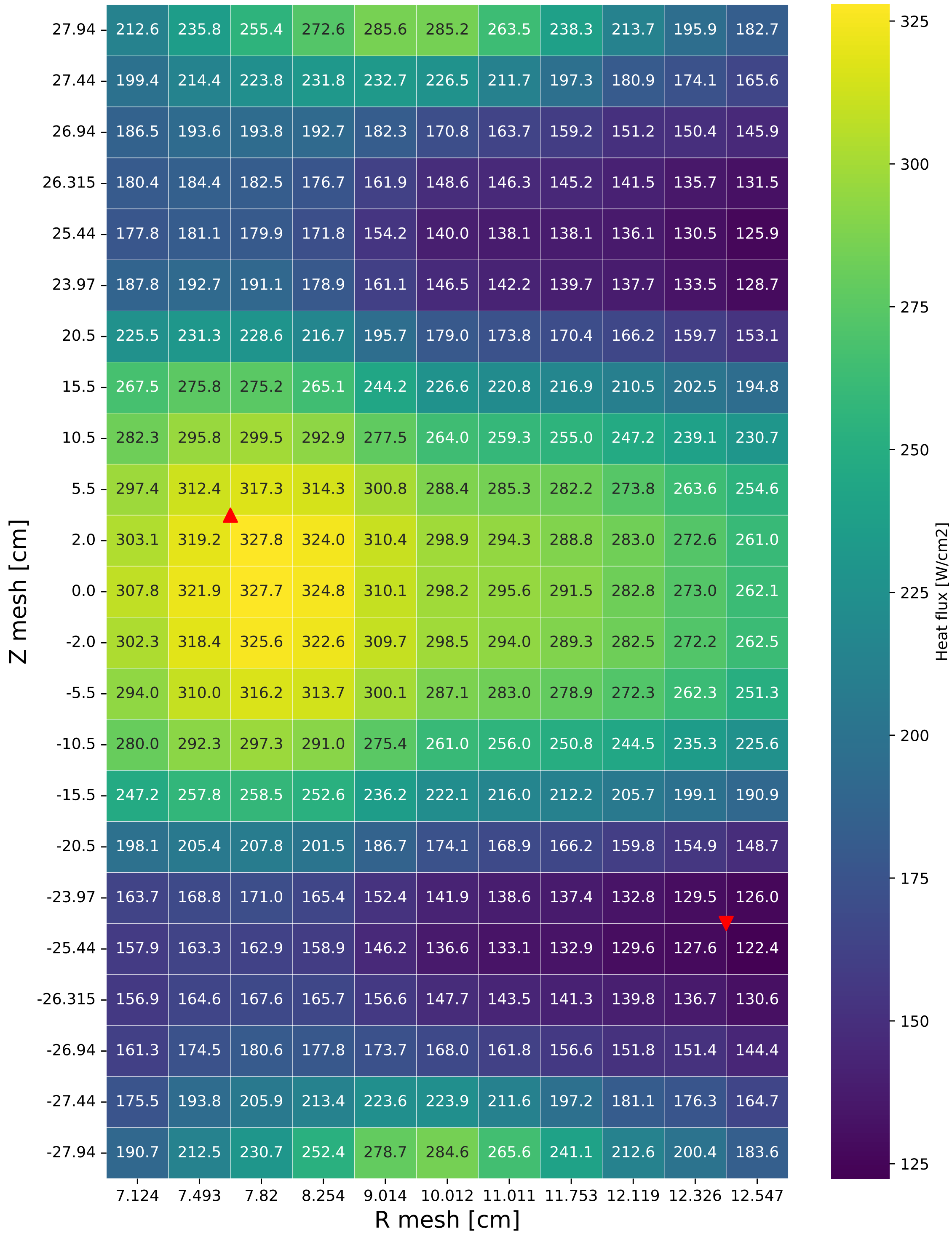

Figure 55. Heat flux distribution for 22-inch design IFE region on day 0 (see Section 7.1.4).

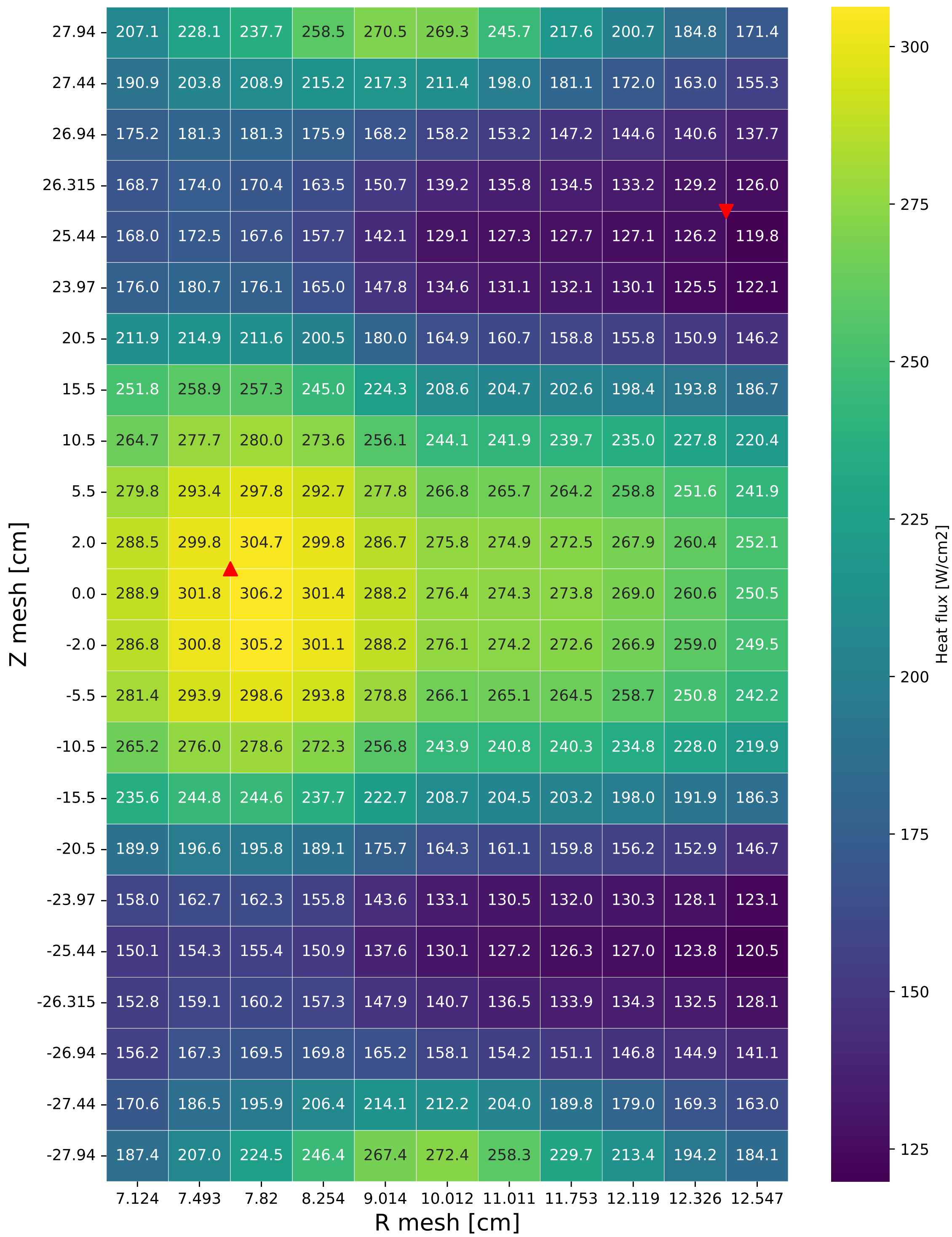

Figure 56. Heat flux distribution for 22-inch design IFE region on day 1 (see Section 7.1.4).

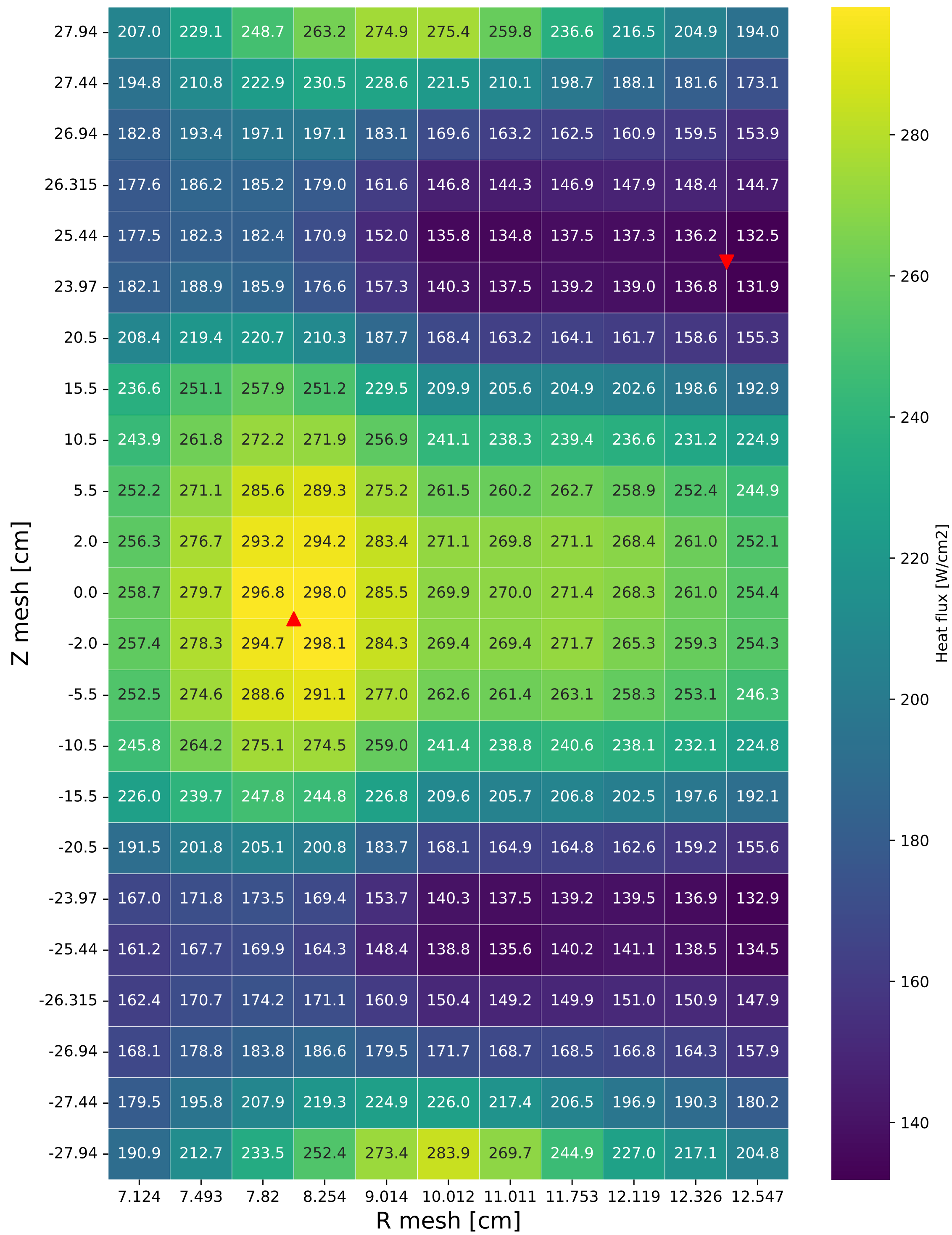

Figure 57. Heat flux distribution for 22-inch design IFE region on day 15 (see Section 7.1.4).

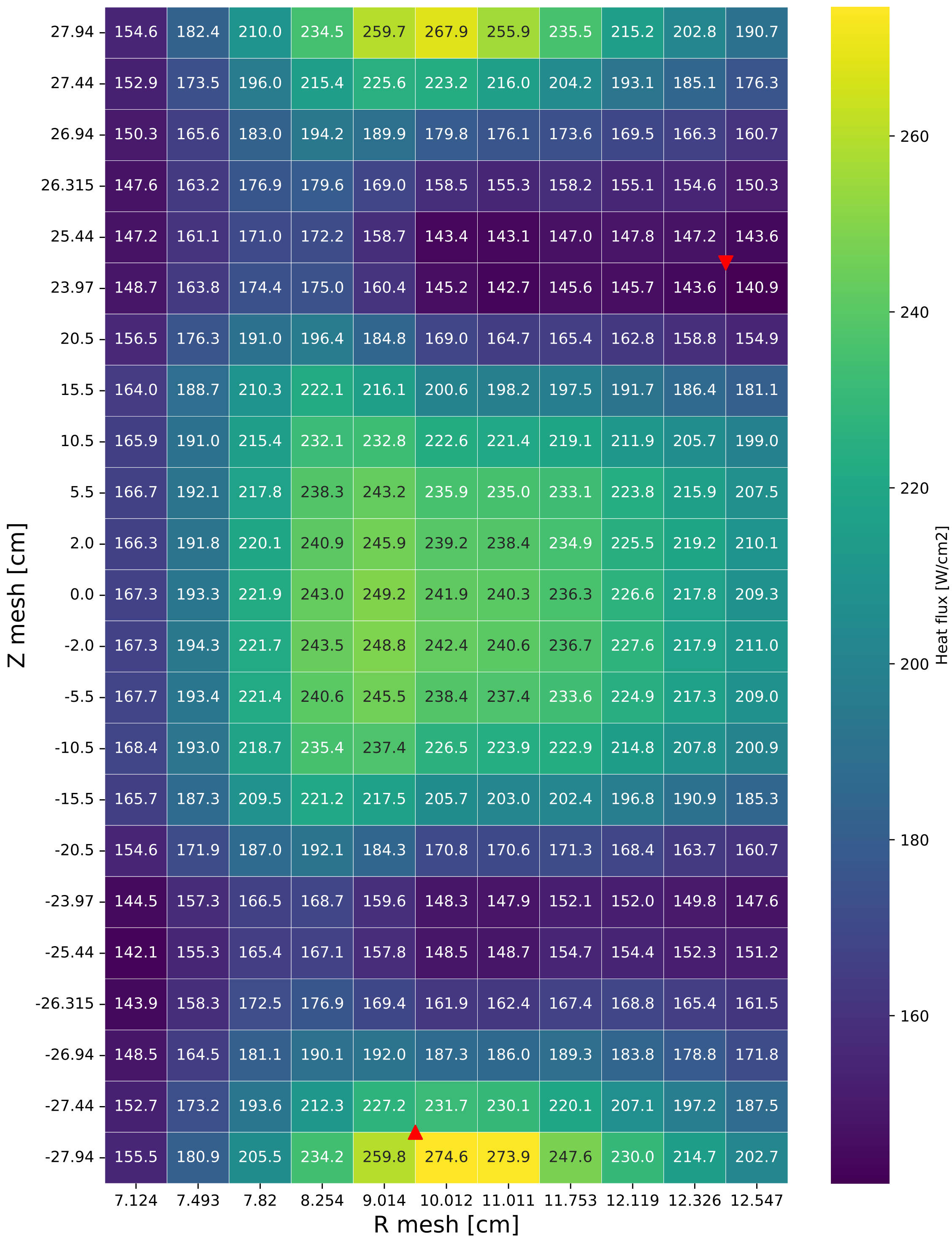

Figure 58. Heat flux distribution for 22-inch design IFE region on day 33 (see Section 7.1.4).

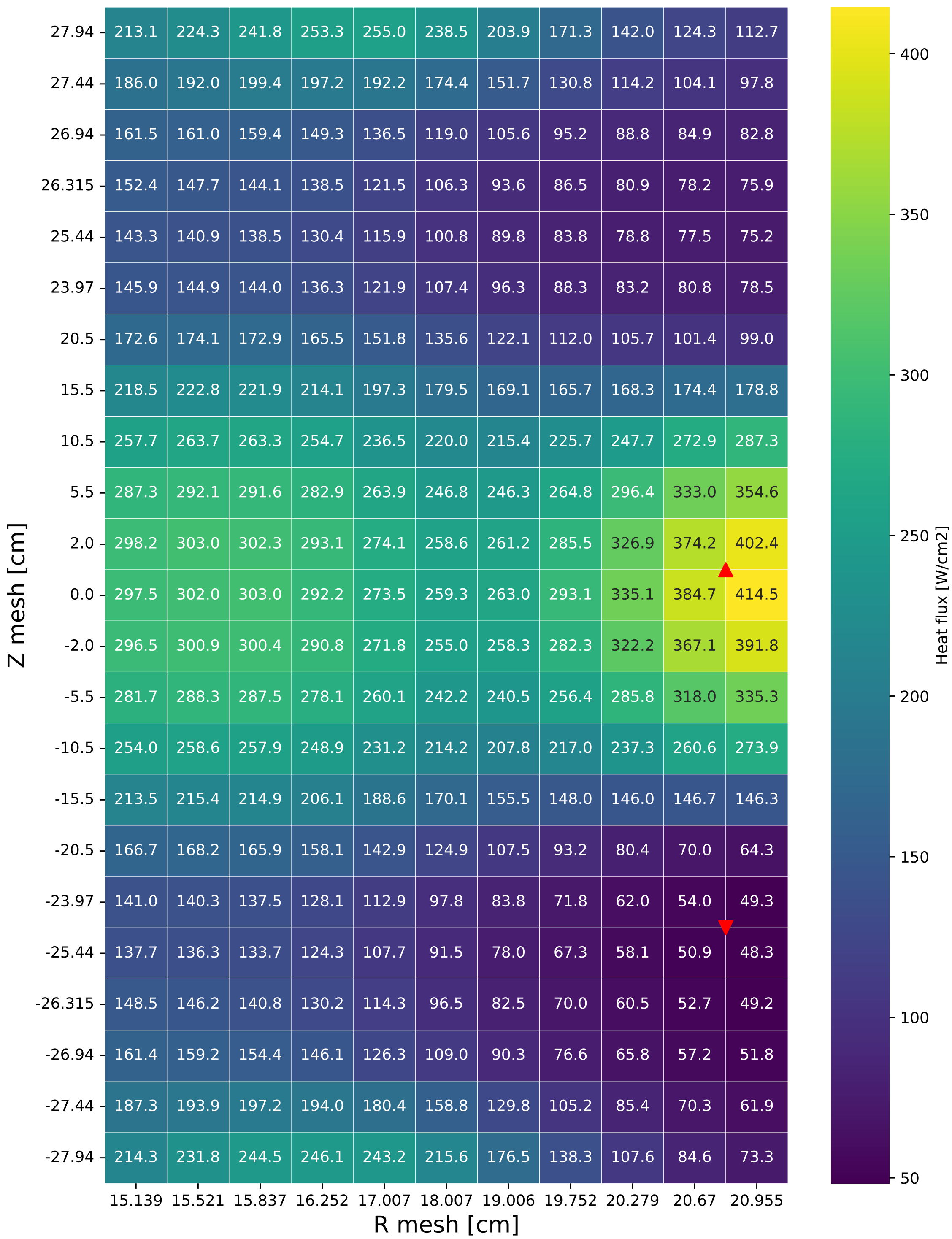

Figure 59. Heat flux distribution for 22-inch design OFE region on day 0 (see Section 7.1.4).

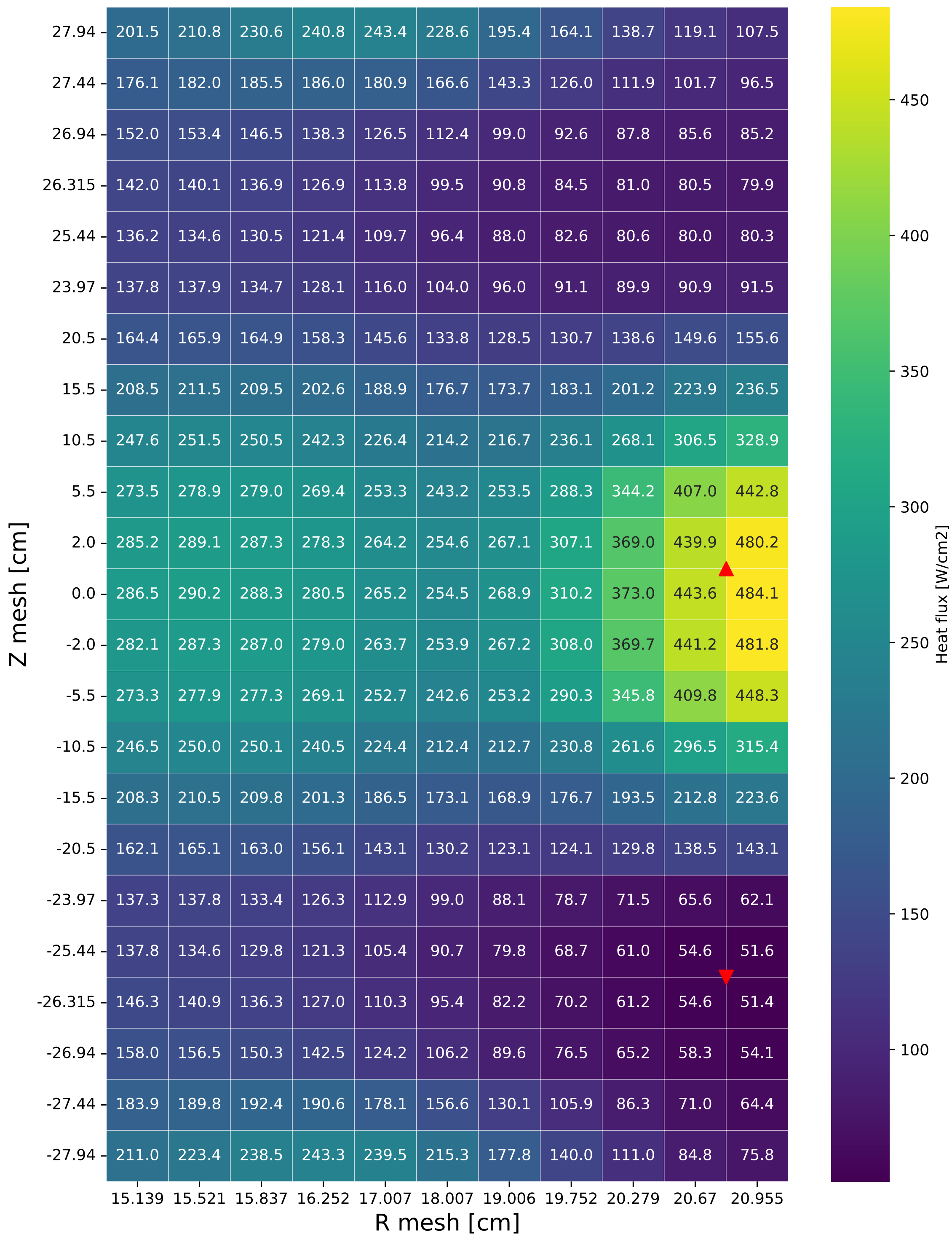

Figure 60. Heat flux distribution for 22-inch design OFE region on day 1 (see Section 7.1.4).

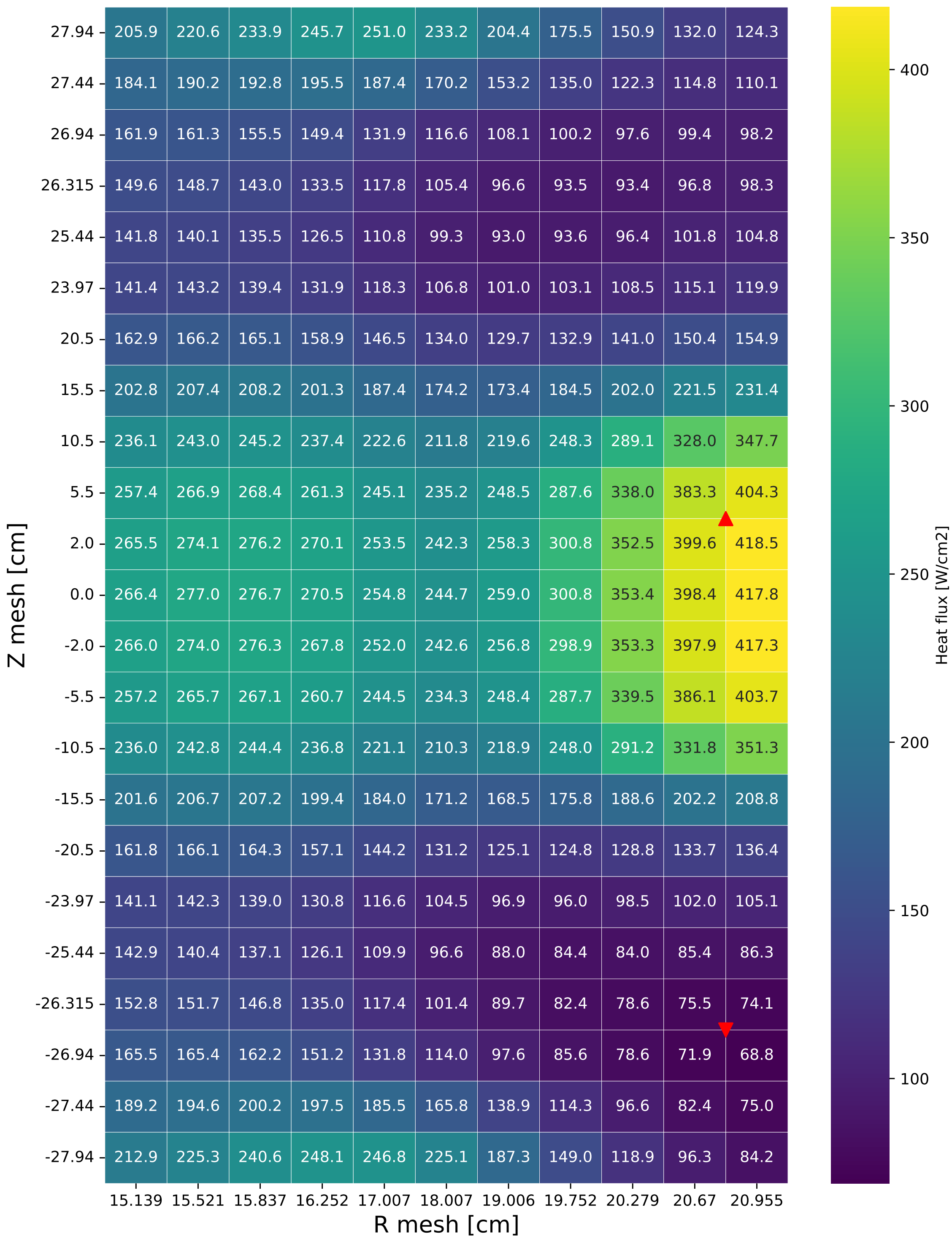

Figure 61. Heat flux distribution for 22-inch design OFE region on day 15 (see Section 7.1.4).

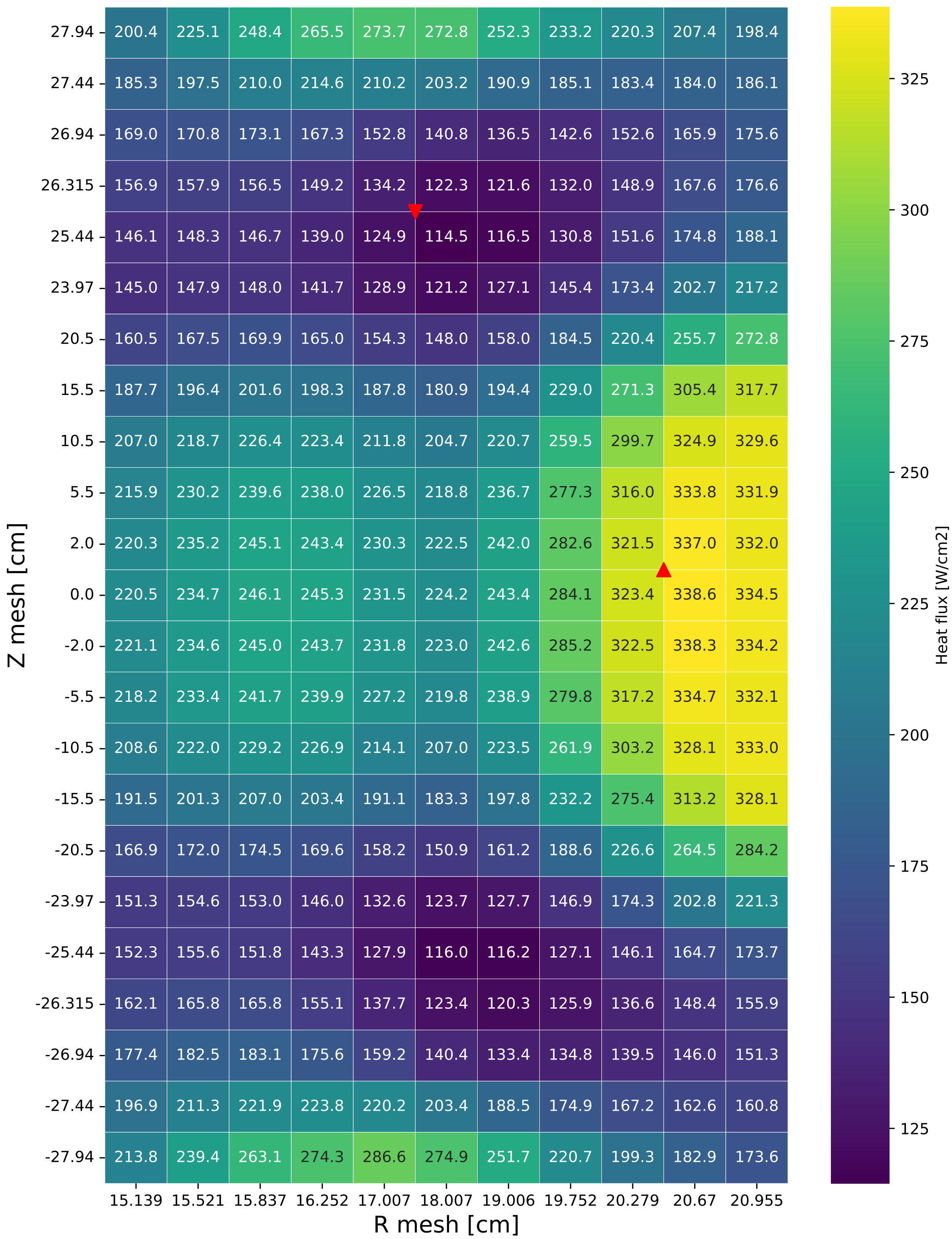

Figure 62. Heat flux distribution for 22-inch design OFE region on day 33 (see Section 7.1.4).

APPENDIX B. DISTRIBUTIONS FOR UTILIZATION DESIGN

APPENDIX B-1. FISSION RATE DENSITY DISTRIBUTIONS FOR UTILIZATION DESIGN

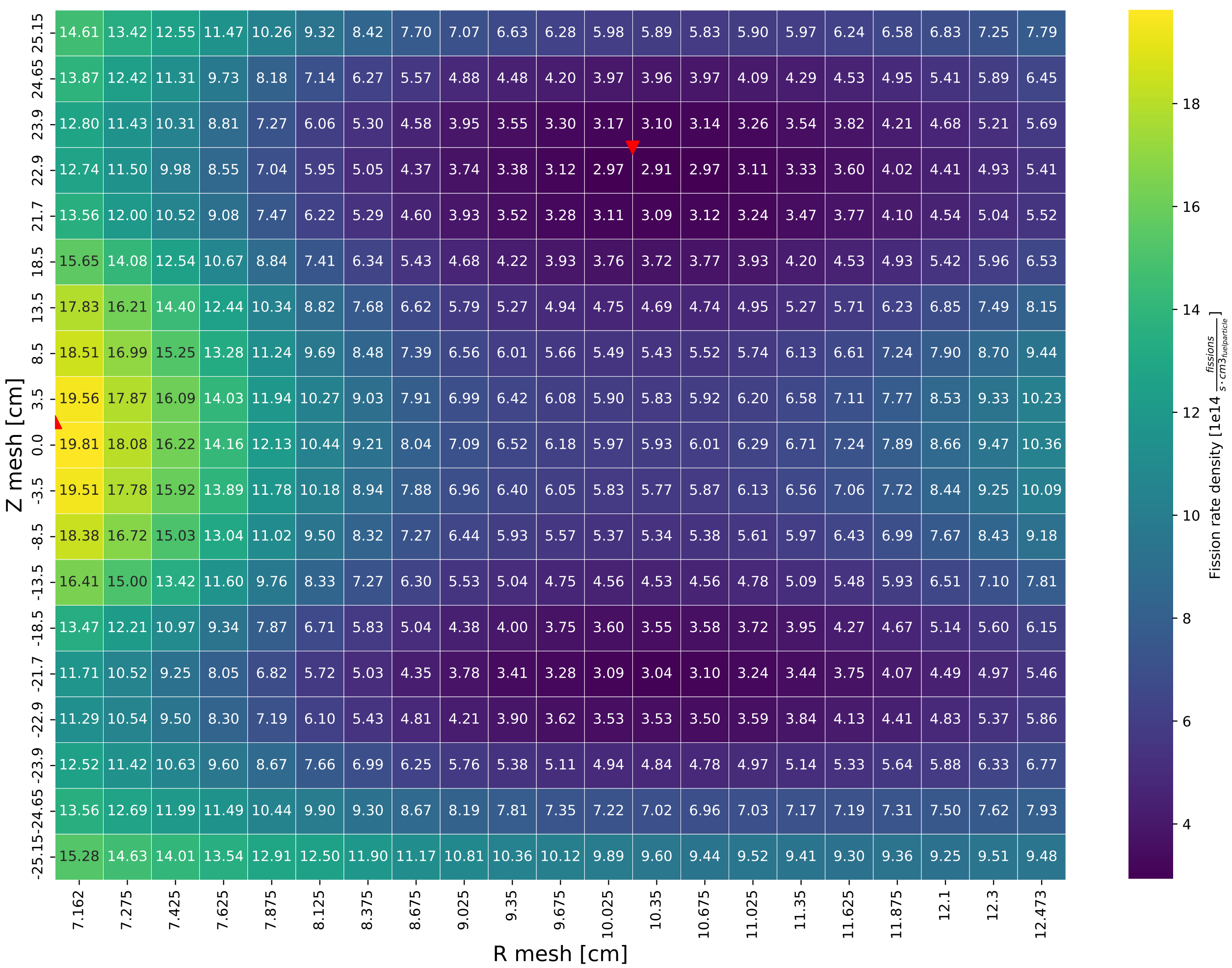

Figure 63. Fission rate density distribution for utilization design IFE region on day 0 (see Section 7.2.2).

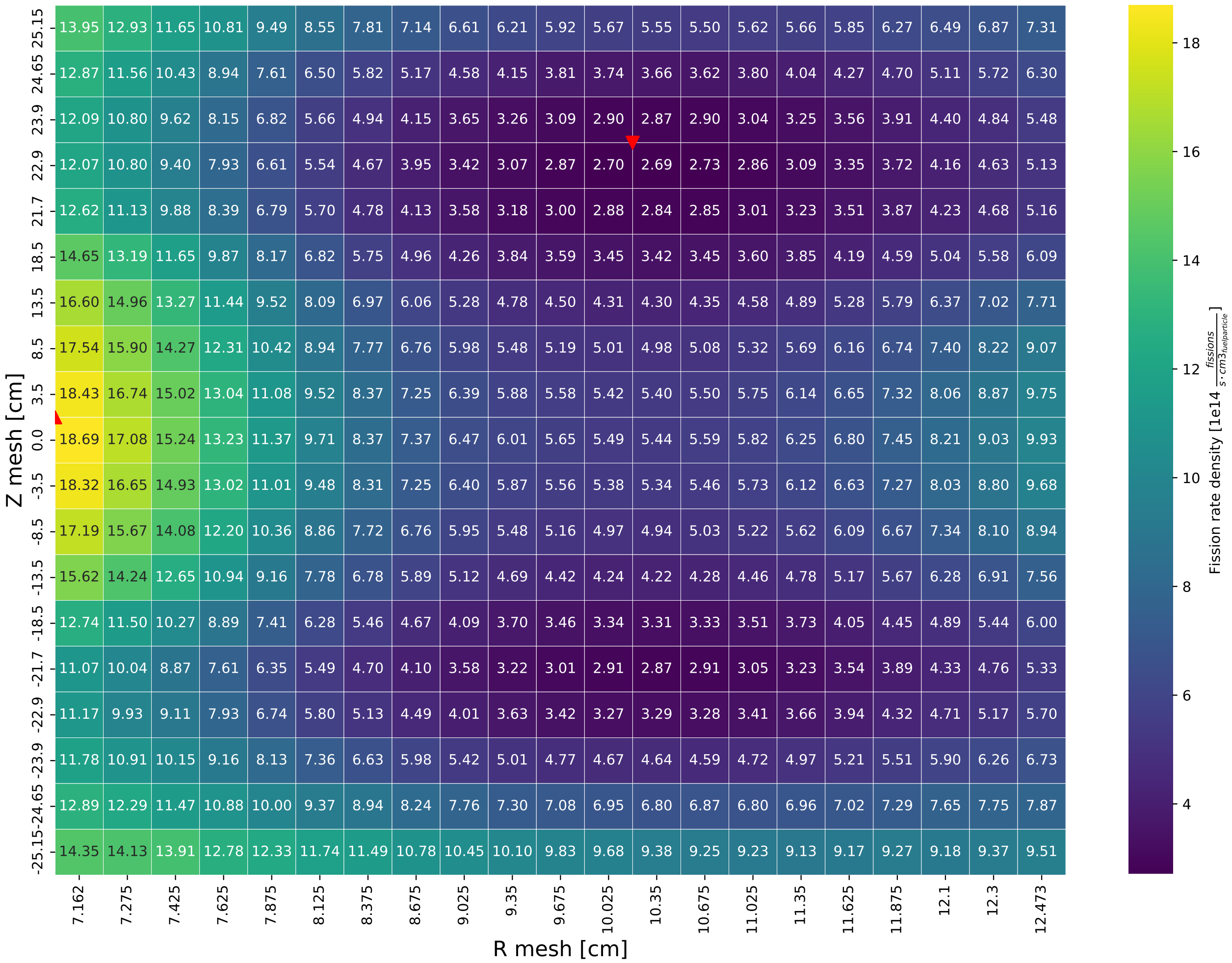

Figure 64. Fission rate density distribution for utilization design IFE region on day 1 (see Section 7.2.2).

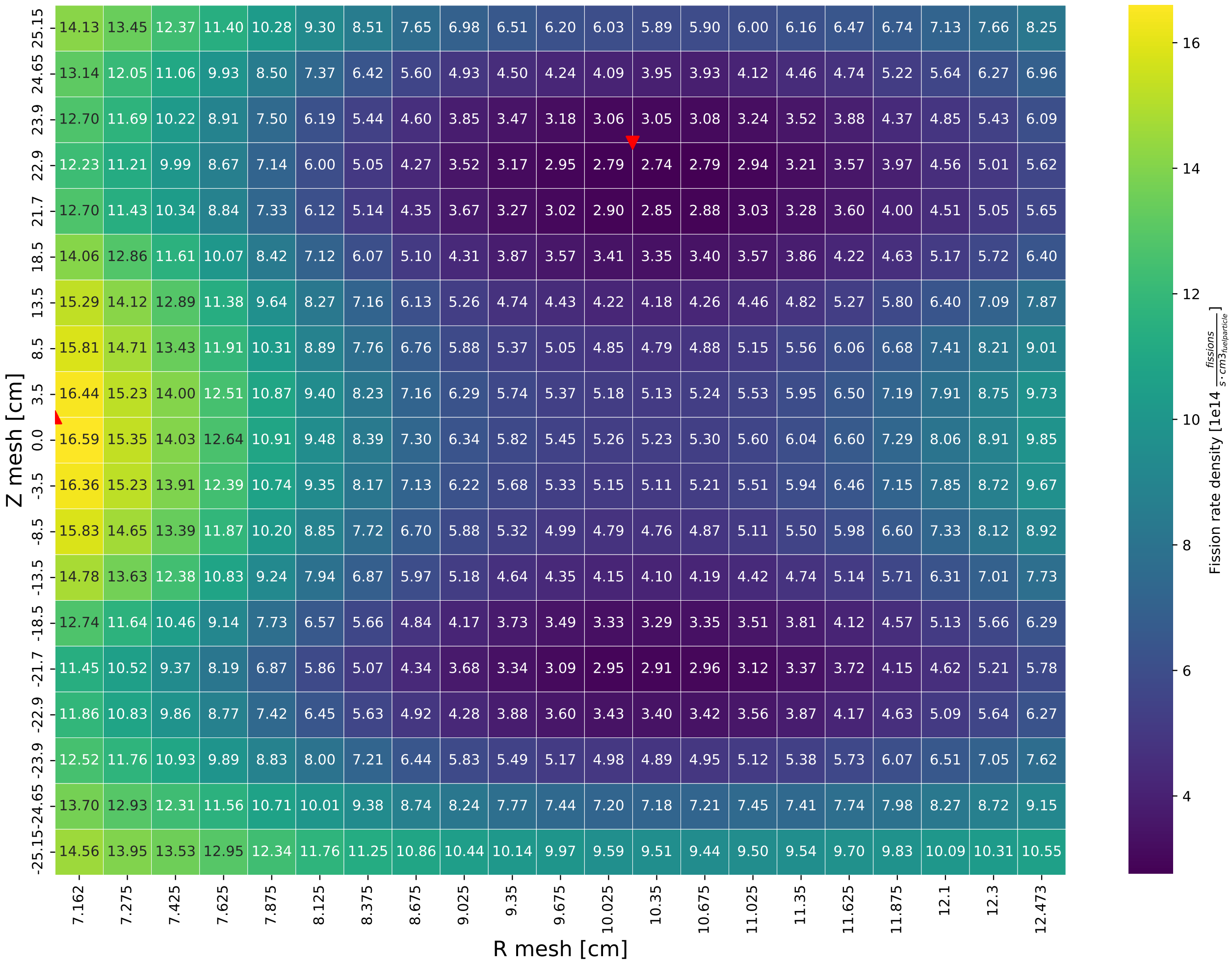

Figure 65. Fission rate density distribution for utilization design IFE region on day 15 (see Section 7.2.2).

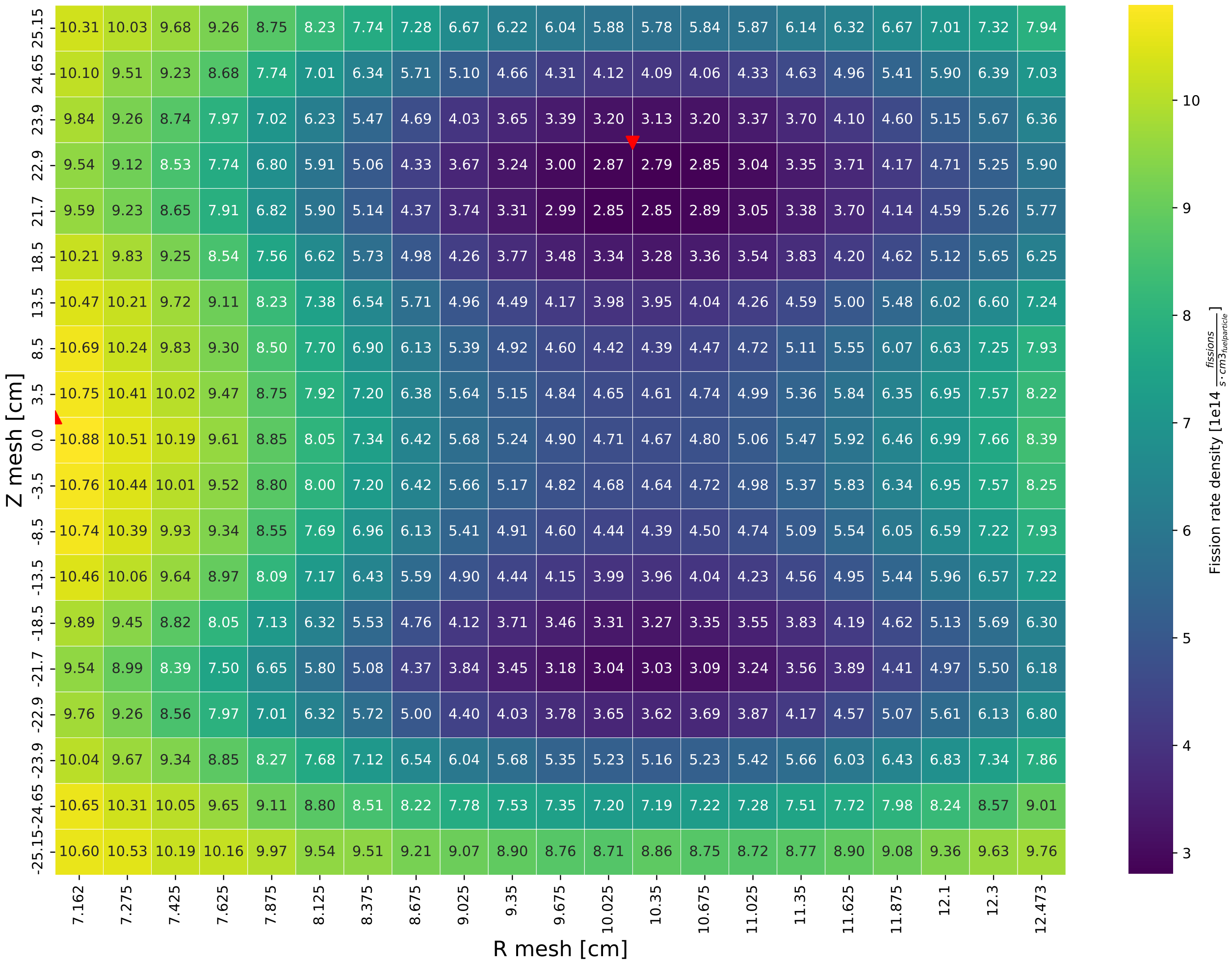

Figure 66. Fission rate density distribution for utilization design IFE region on day 34 (see Section 7.2.2).

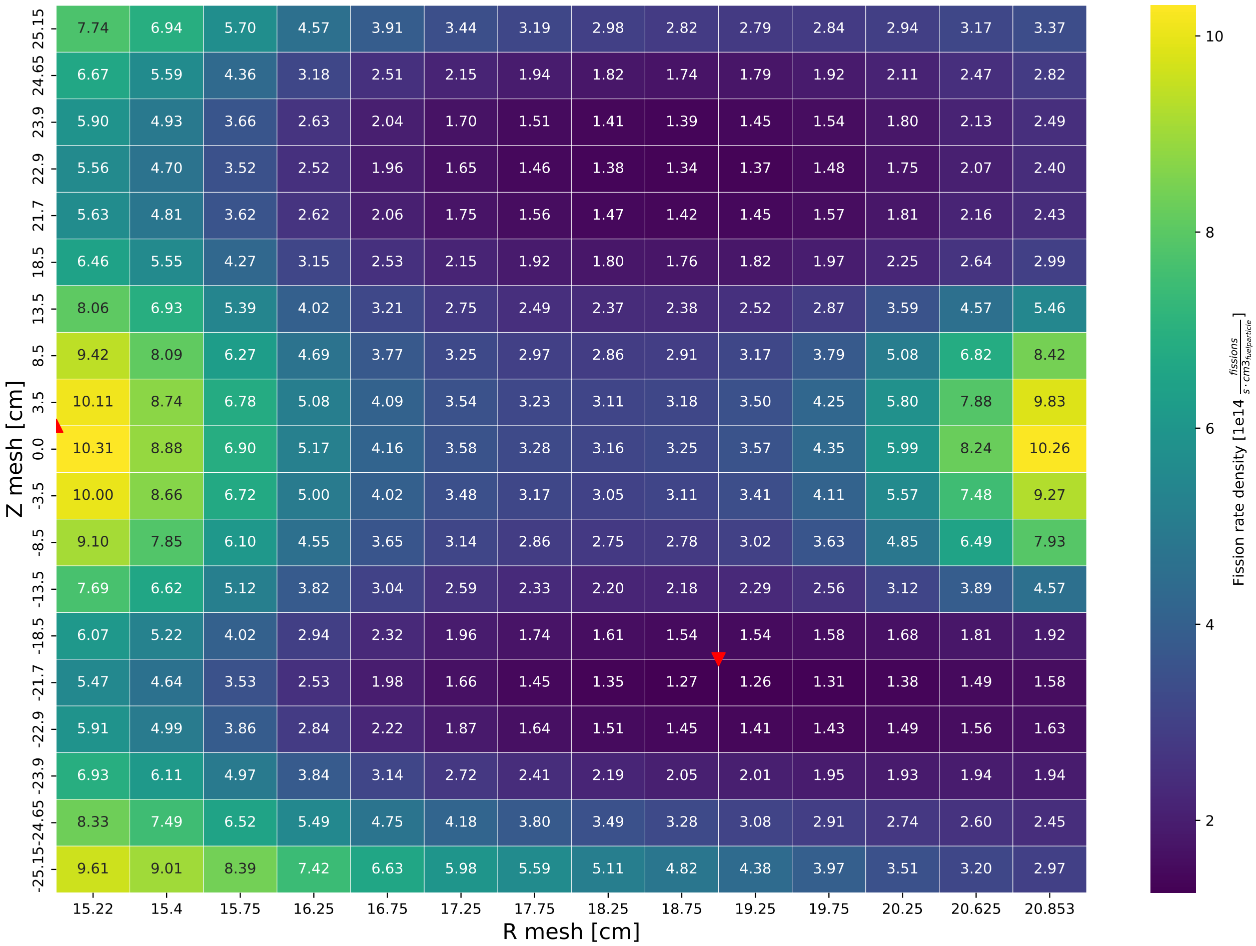

Figure 67. Fission rate density distribution for utilization design OFE region on day 0 (see Section 7.2.2).

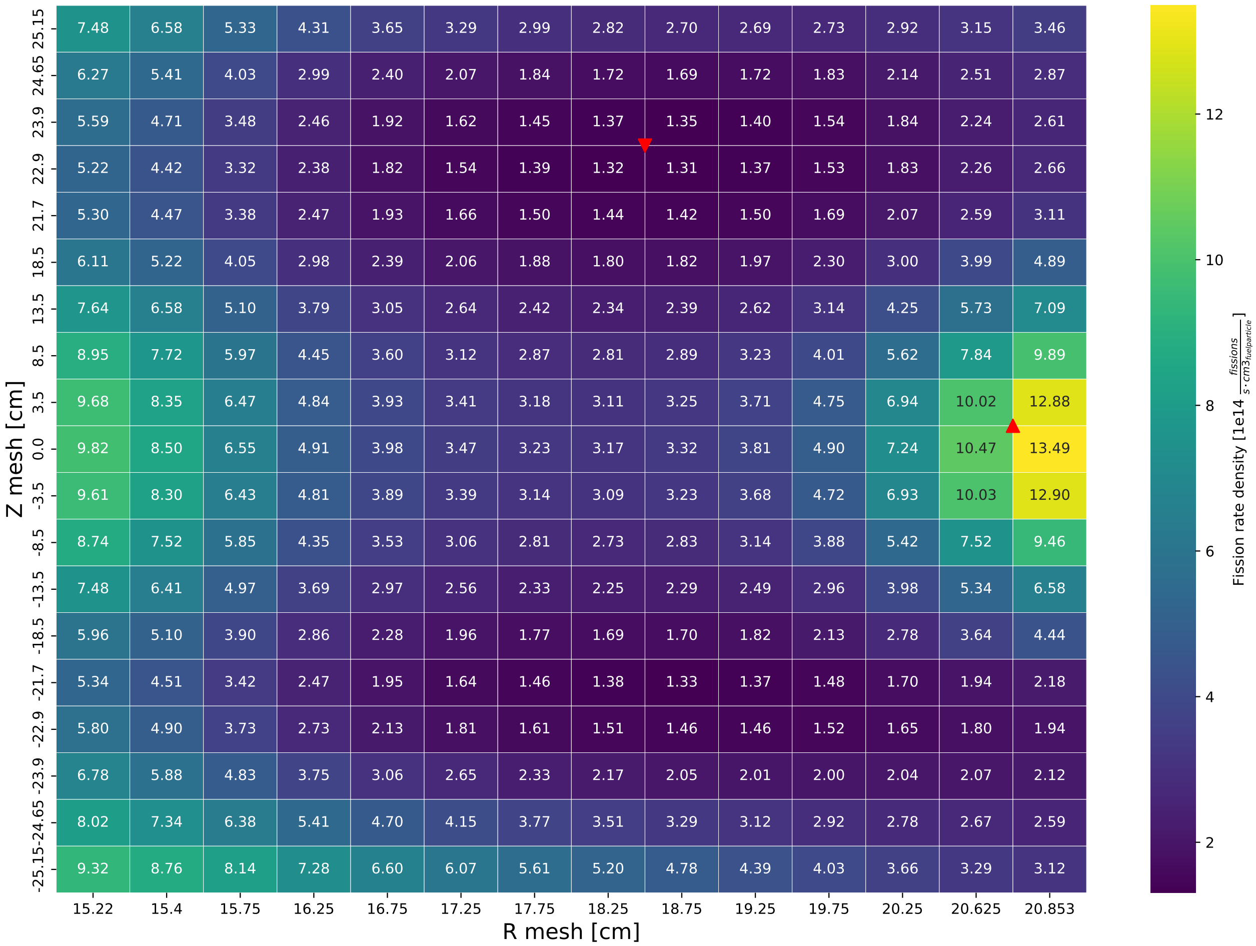

Figure 68. Fission rate density distribution for utilization design OFE region on day 1 (see Section 7.2.2).

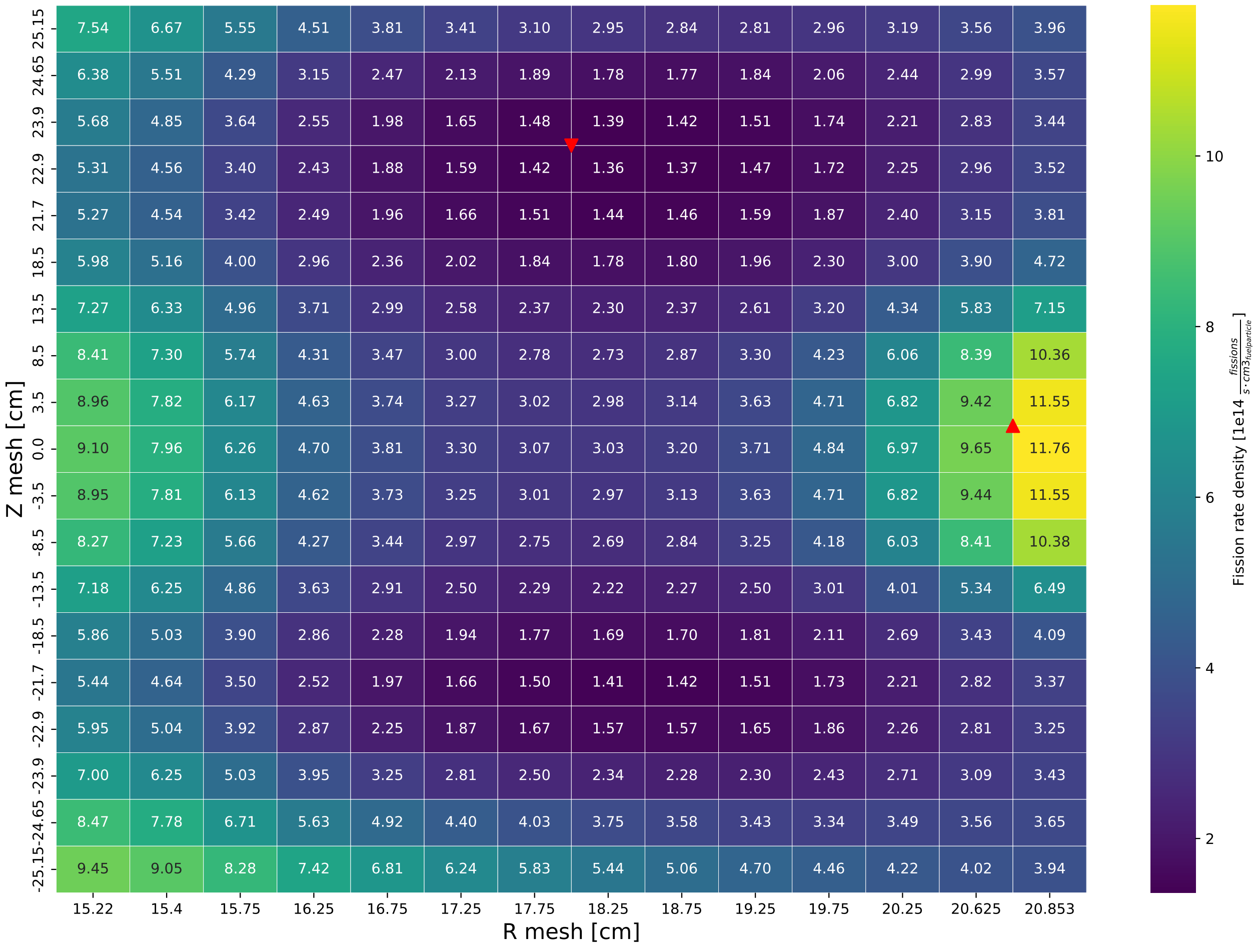

Figure 69. Fission rate density distribution for utilization design OFE region on day 15 (see Section 7.2.2).

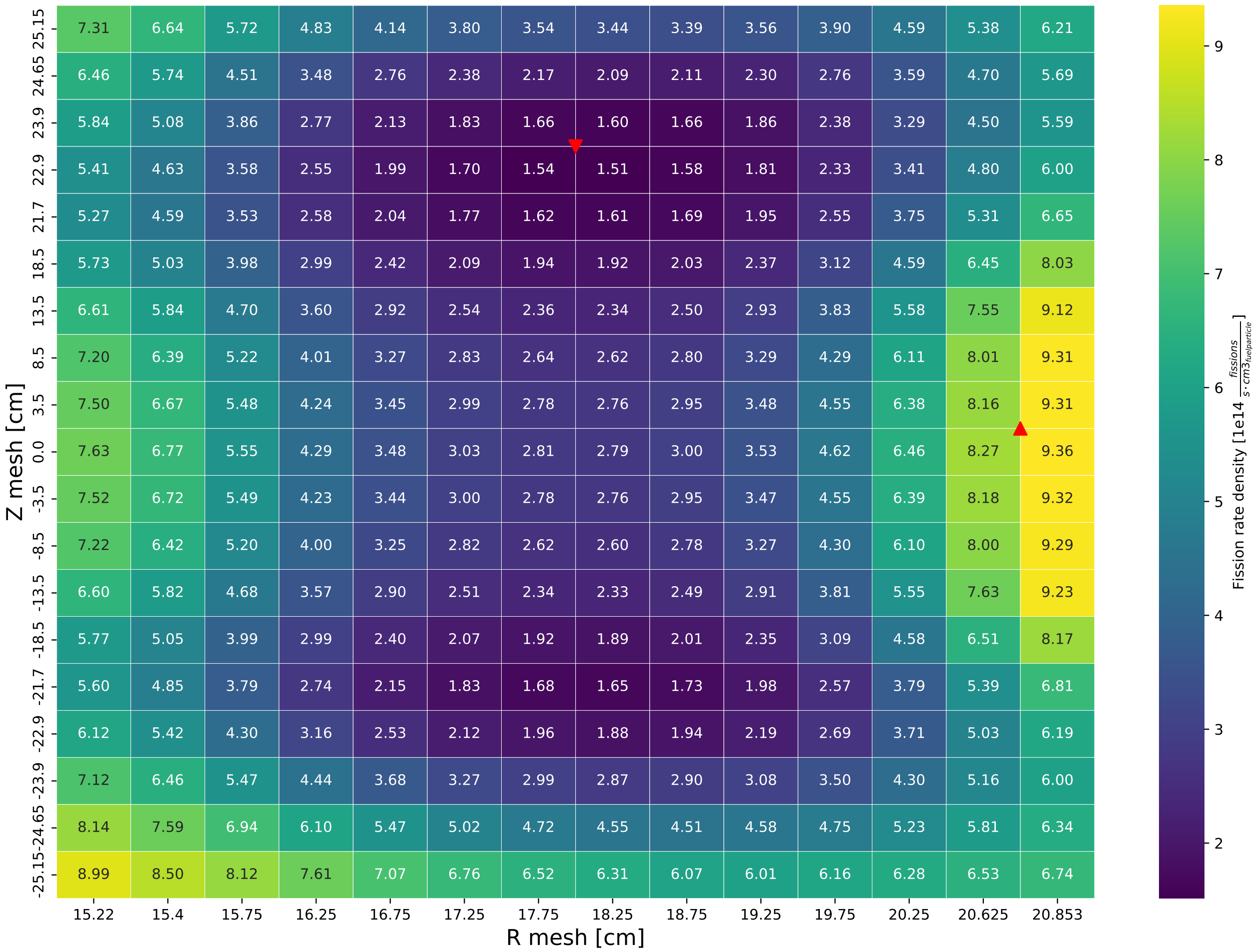

Figure 70. Fission rate density distribution for utilization design OFE region on day 34 (see Section 7.2.2).

APPENDIX B-2. CUMULATIVE FISSION DENSITY DISTRIBUTIONS FOR UTILIZATION DESIGN

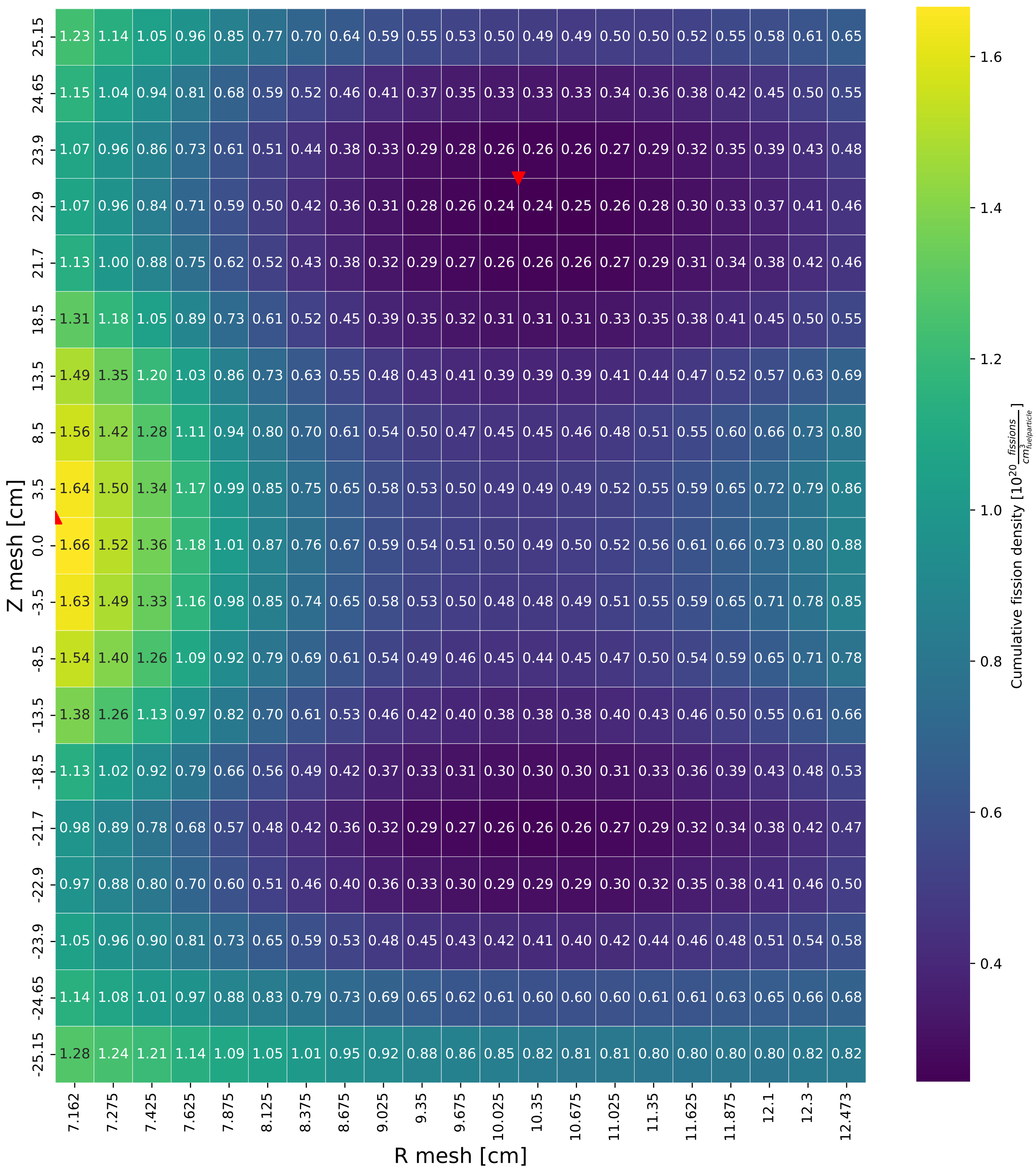

Figure 71. Cumulative fission density distribution for utilization design IFE region on day 1 (see Section 7.2.5).

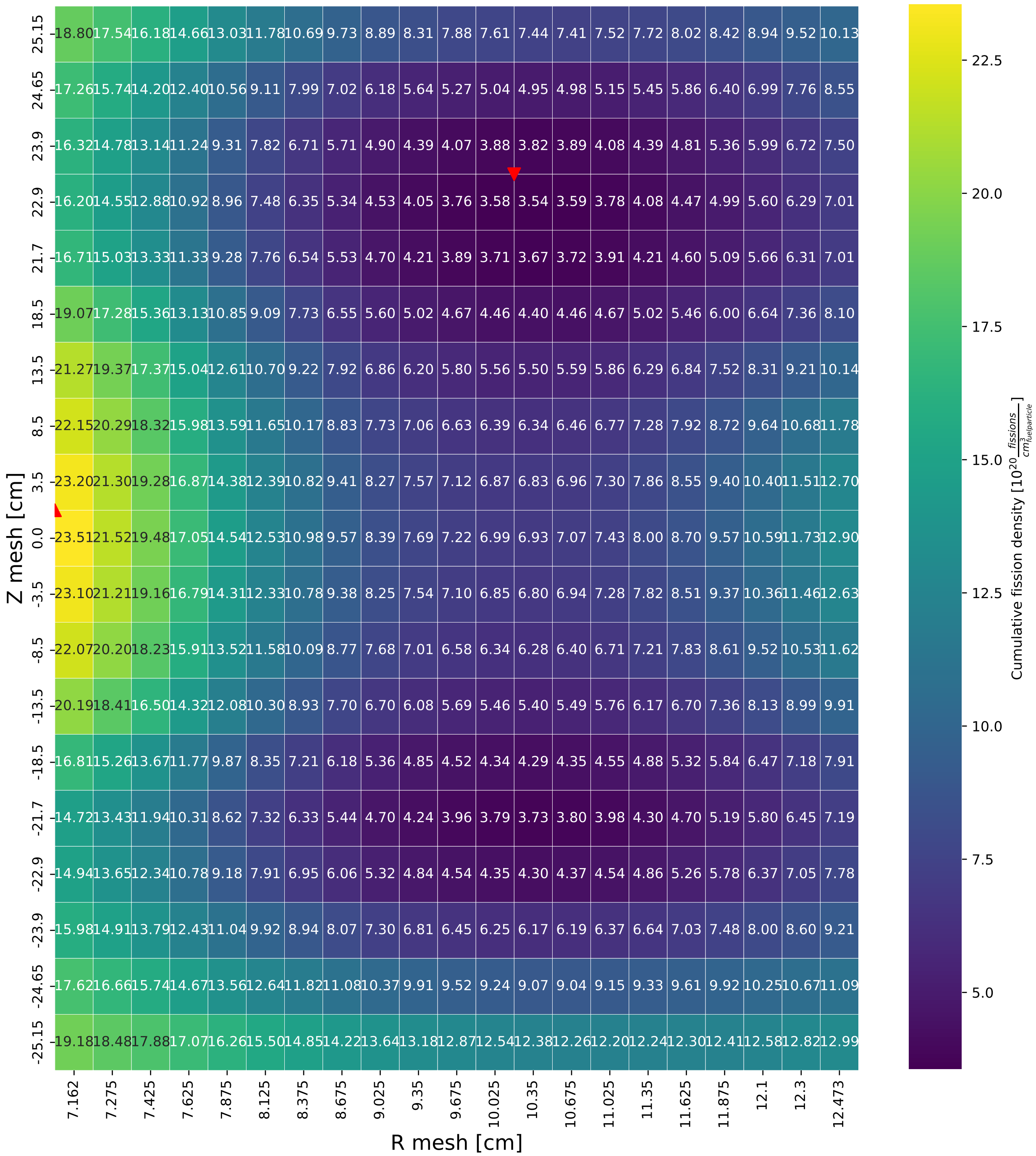

Figure 72. Cumulative fission density distribution for utilization design IFE region on day 15 (see Section 7.2.5).

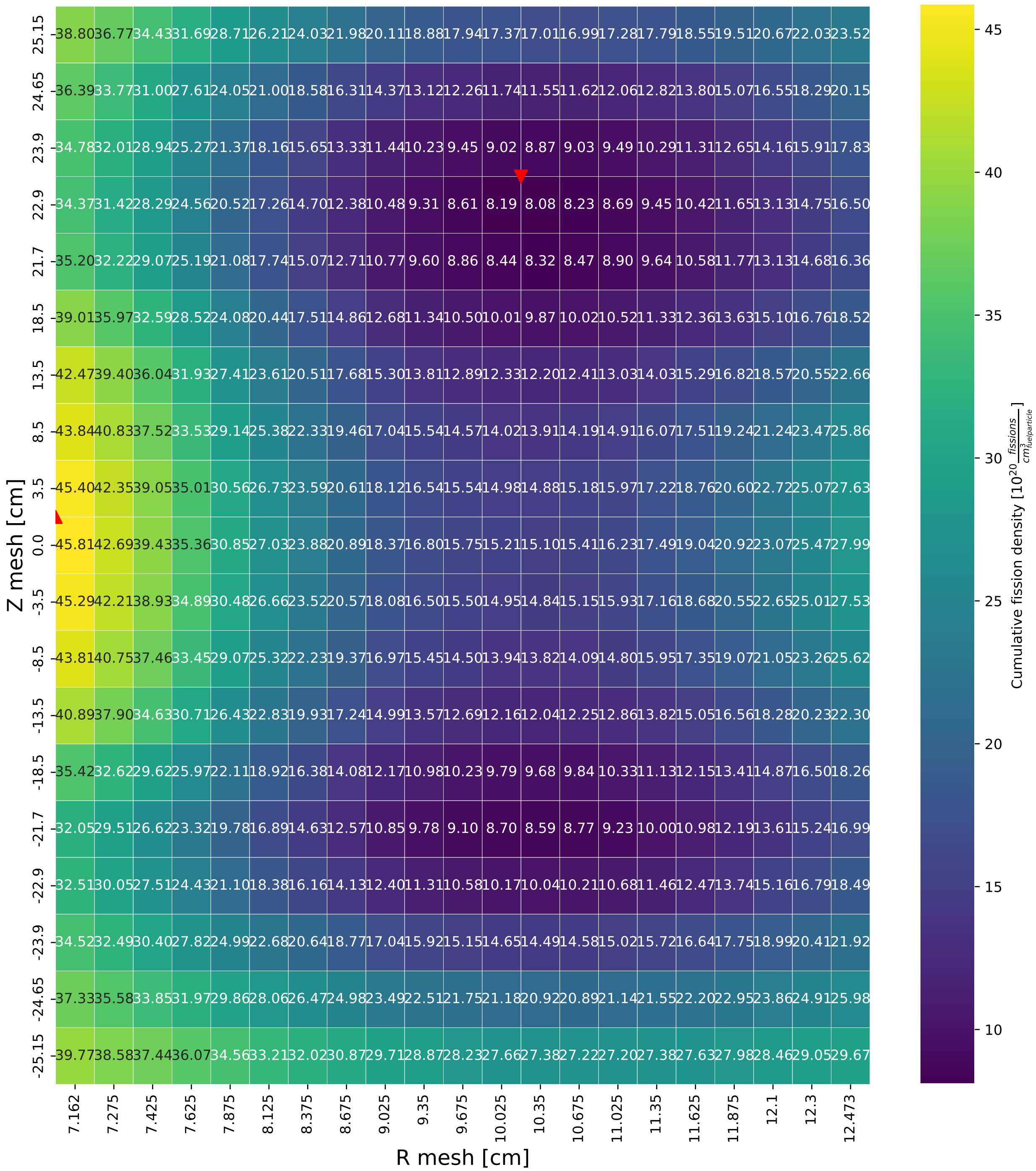

Figure 73. Cumulative fission density distribution for utilization design IFE region on day 34 (see Section 7.2.5).

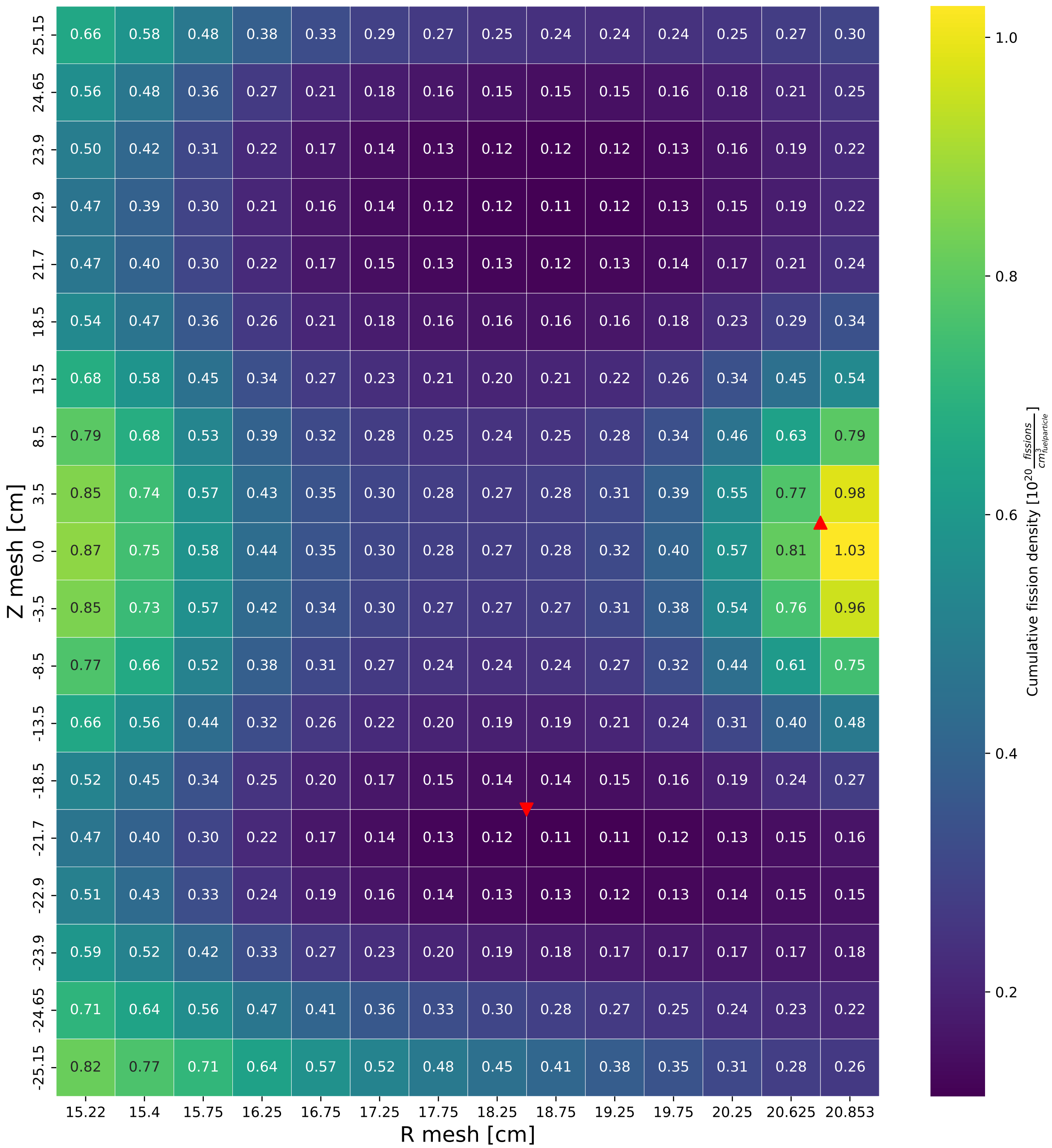

Figure 74. Cumulative fission density distribution for utilization design OFE region on day 1 (see Section 7.2.5).

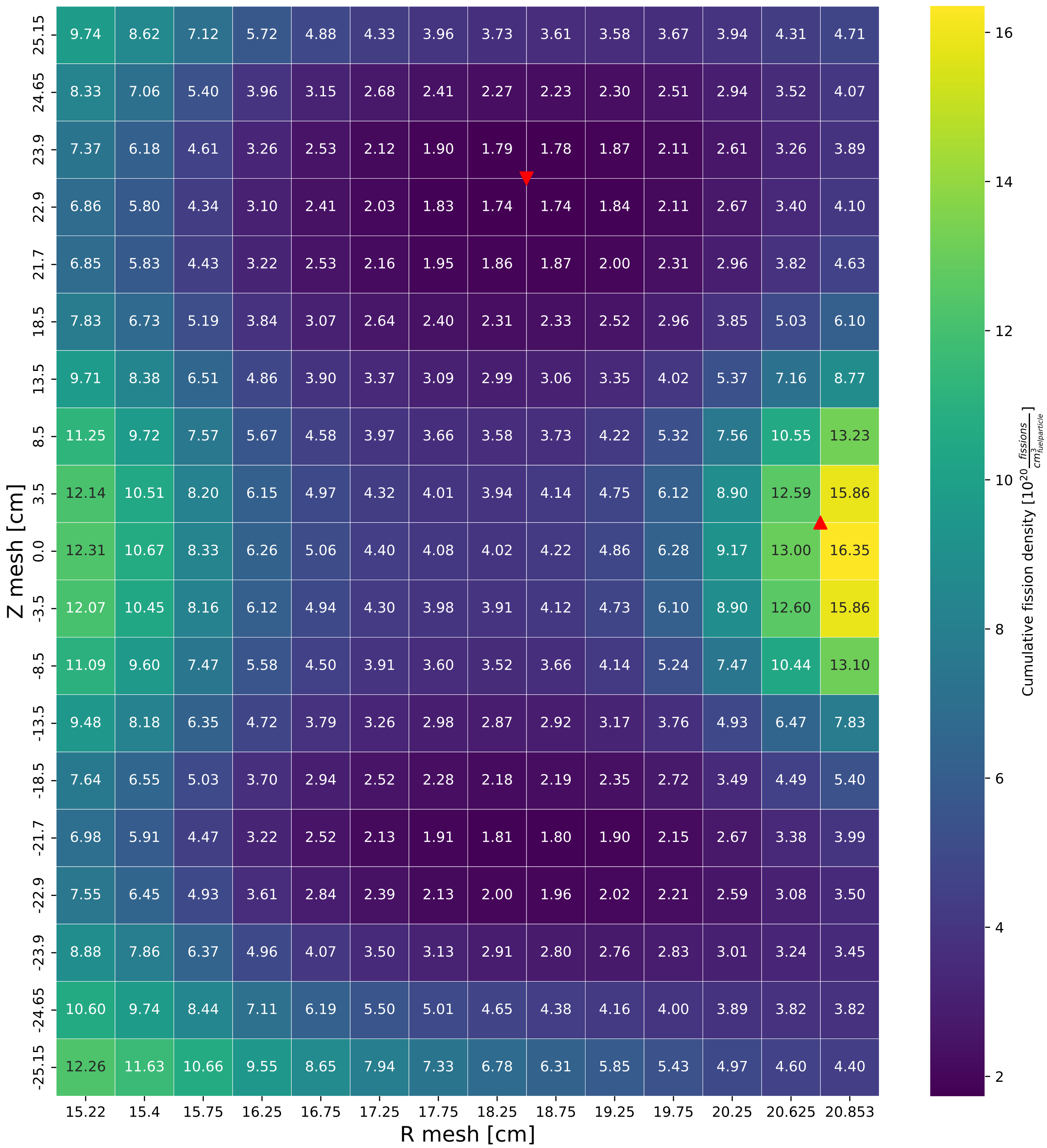

Figure 75. Cumulative fission density distribution for utilization design OFE region on day 15 (see Section 7.2.5).

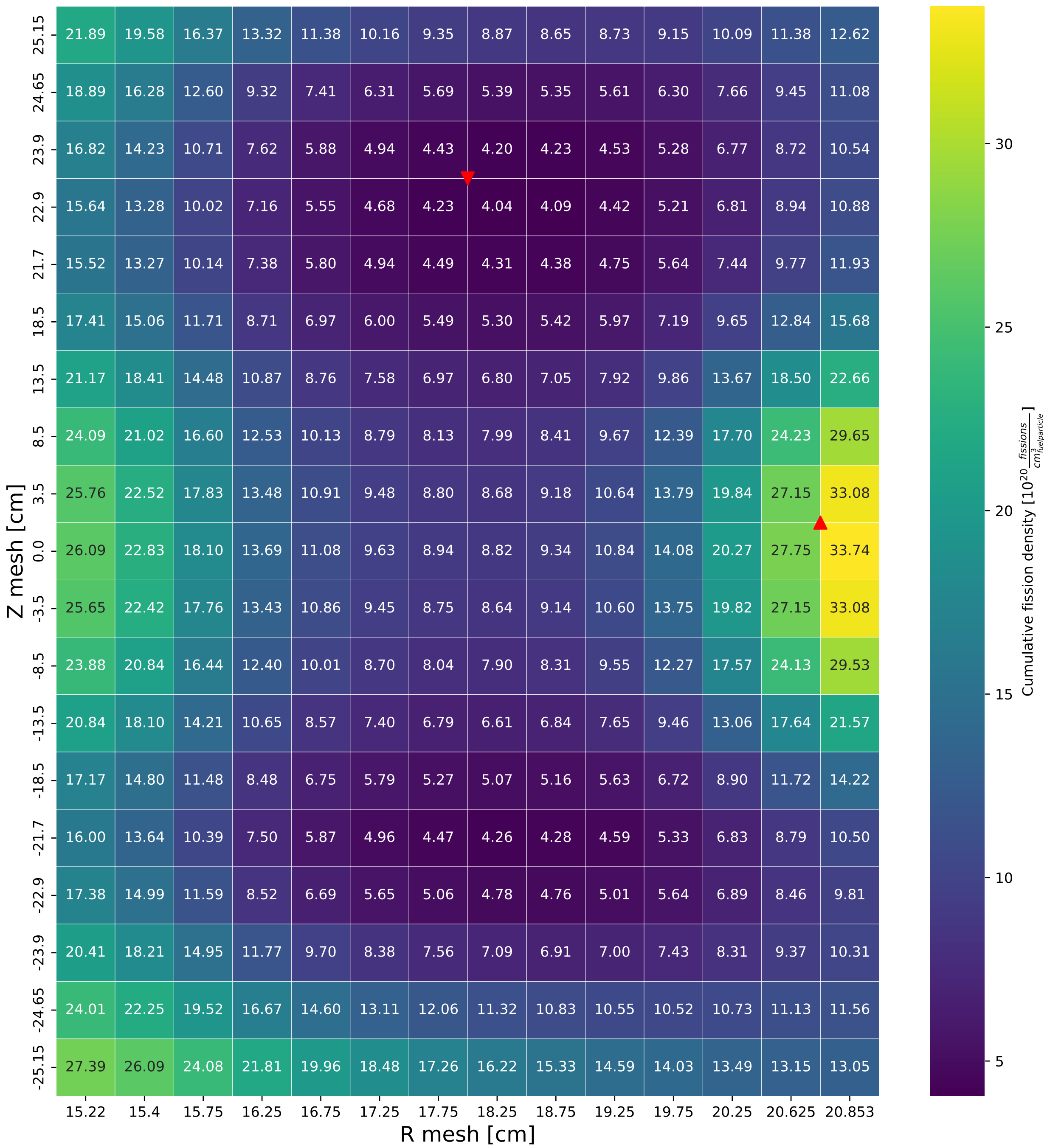

Figure 76. Cumulative fission density distribution for utilization design OFE region on day 34 (see Section 7.2.5).

APPENDIX B-3. POWER DENSITY DISTRIBUTIONS FOR UTILIZATION DESIGN

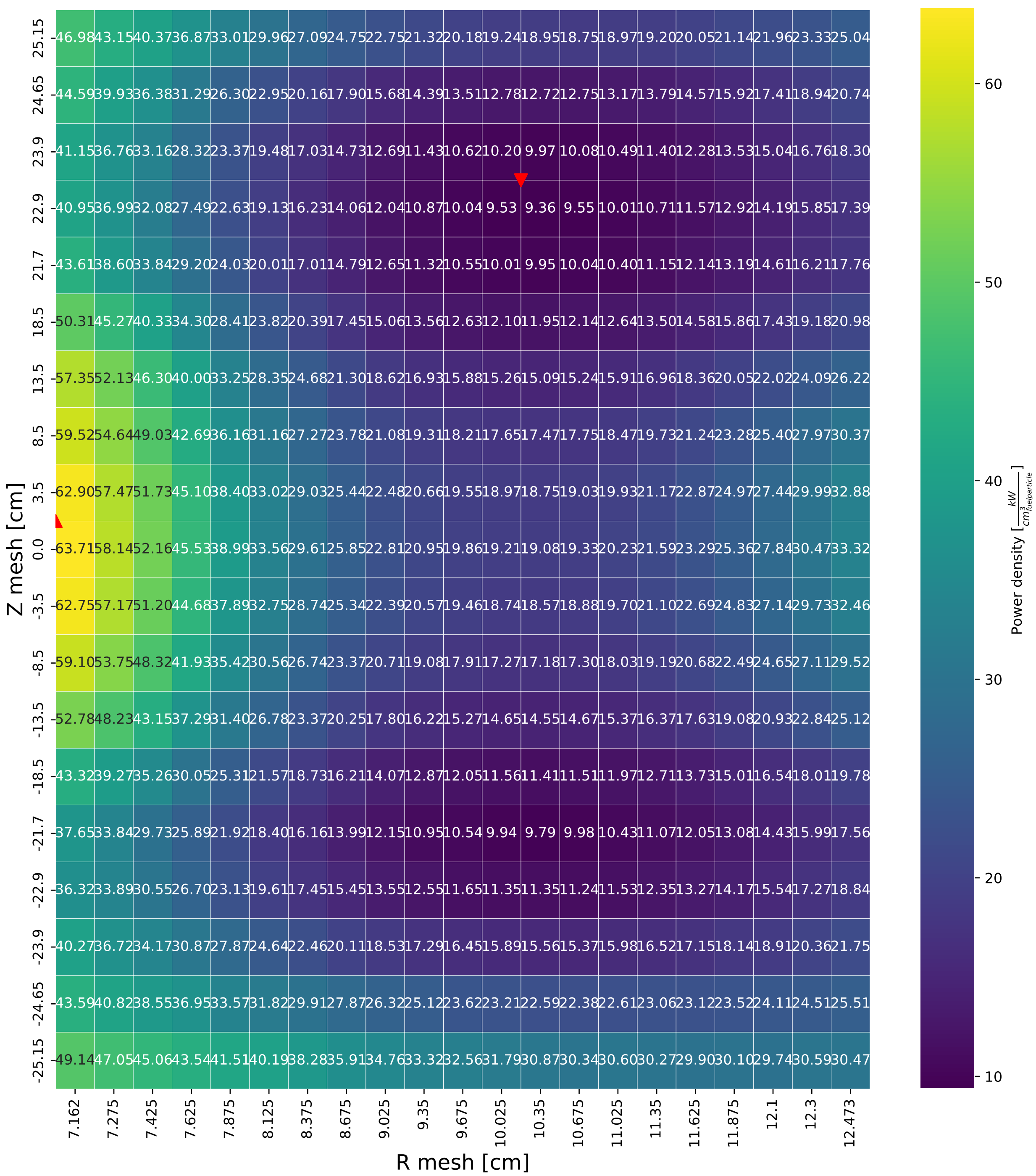

Figure 77. Power density distribution for utilization design IFE region on day 0 (see Section 7.2.3).

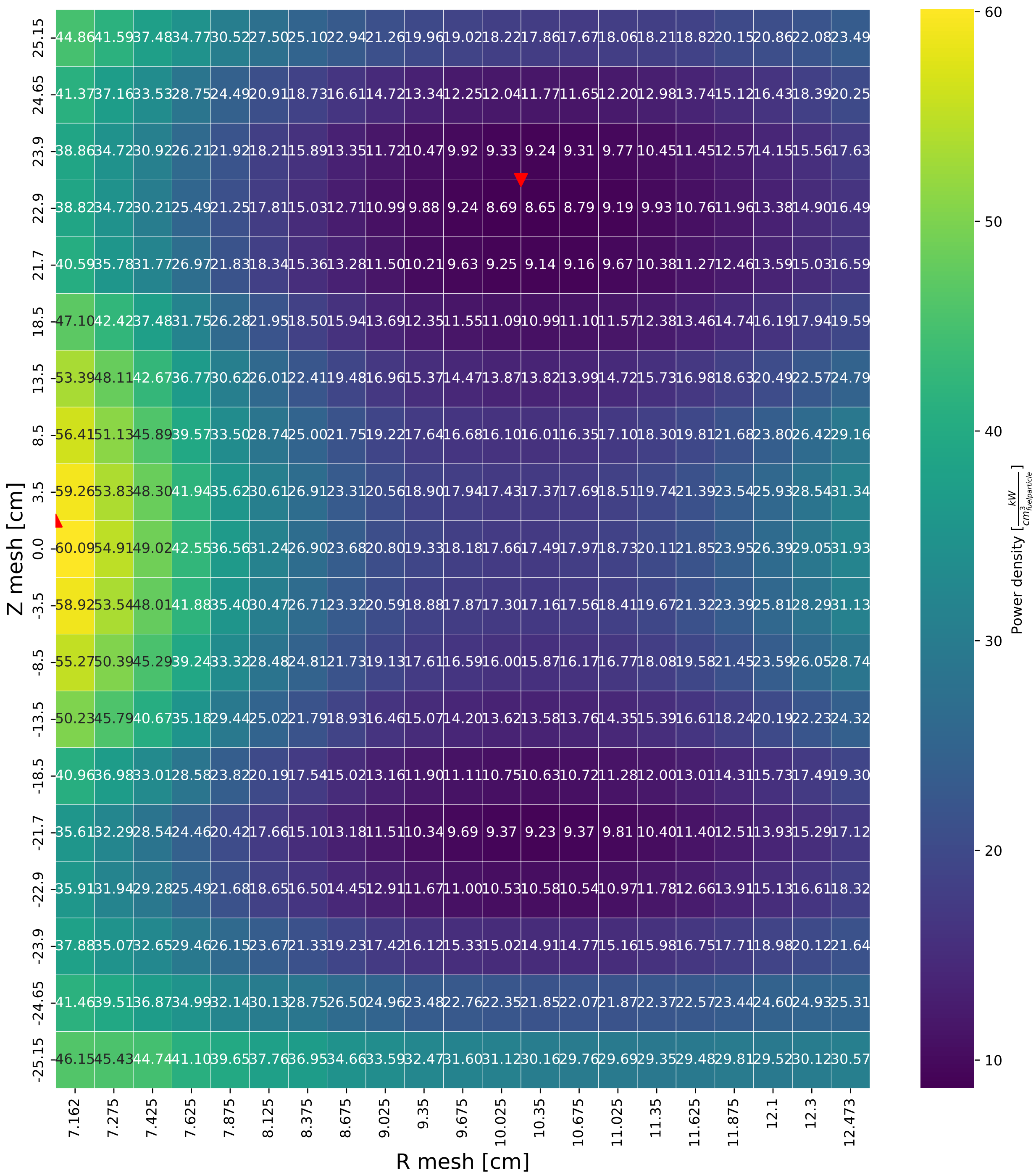

Figure 78. Power density distribution for utilization design IFE region on day 1 (see Section 7.2.3).

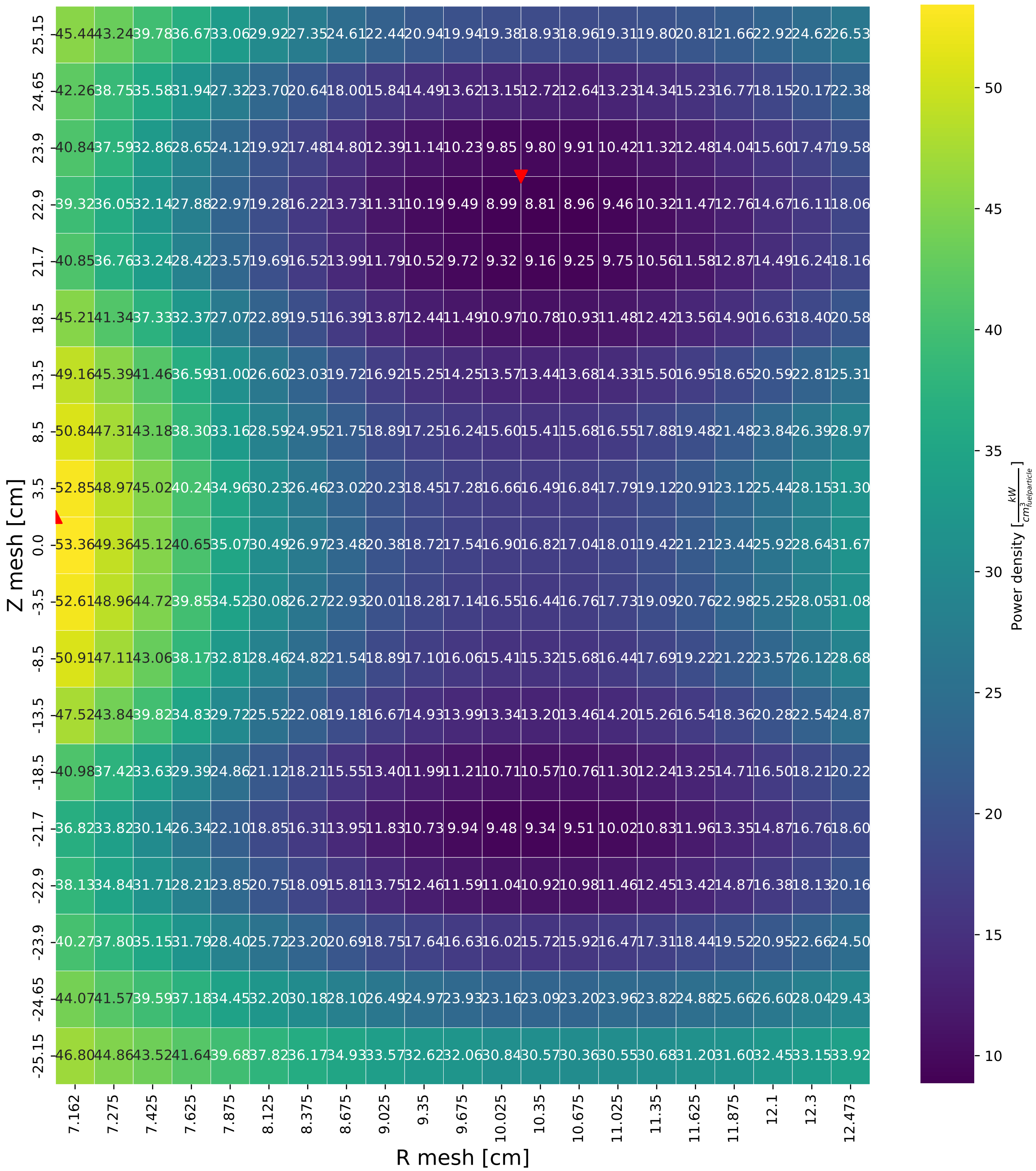

Figure 79. Power density distribution for utilization design IFE region on day 15 (see Section 7.2.3).

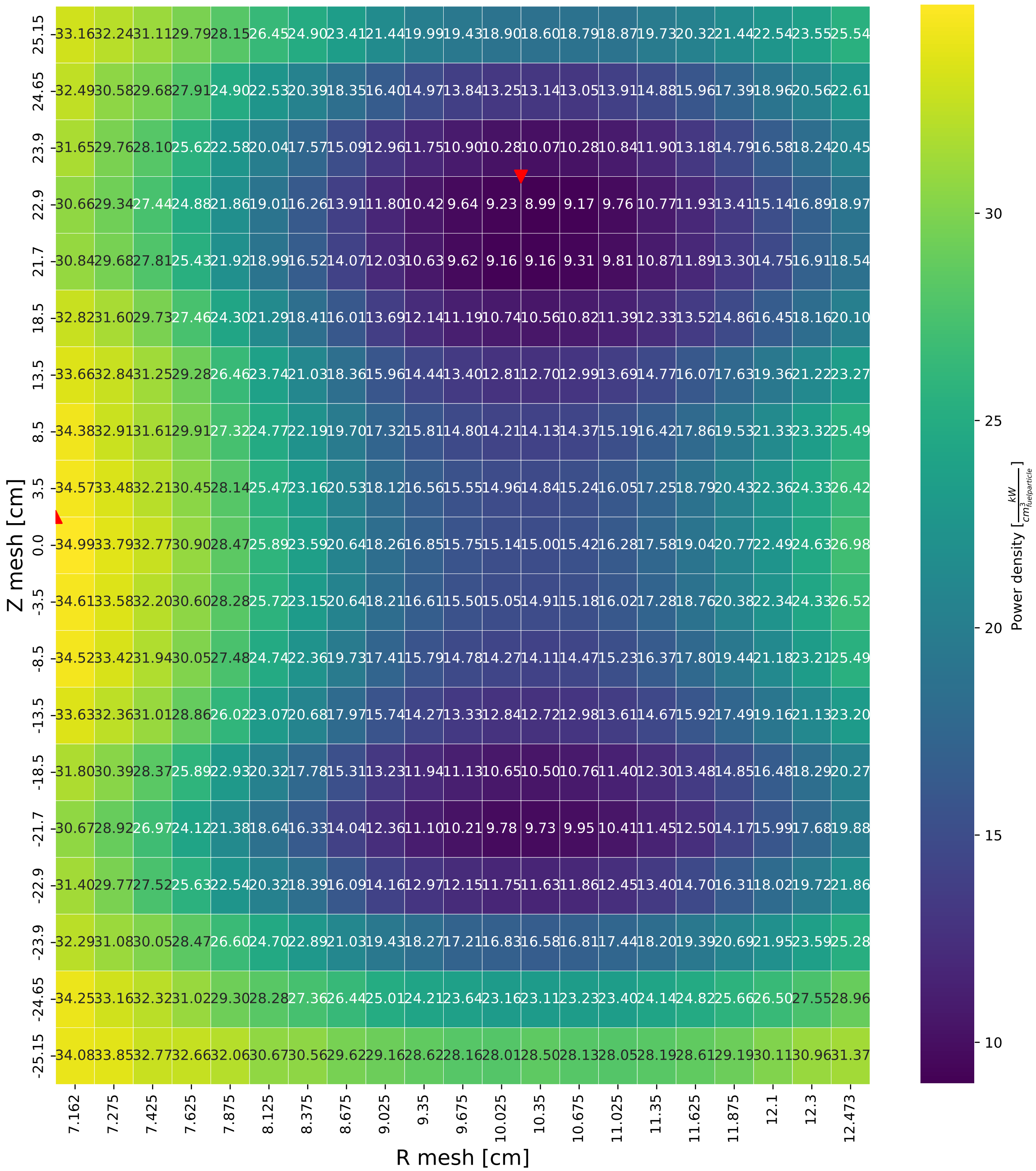

Figure 80. Power density distribution for utilization design IFE region on day 34 (see Section 7.2.3).

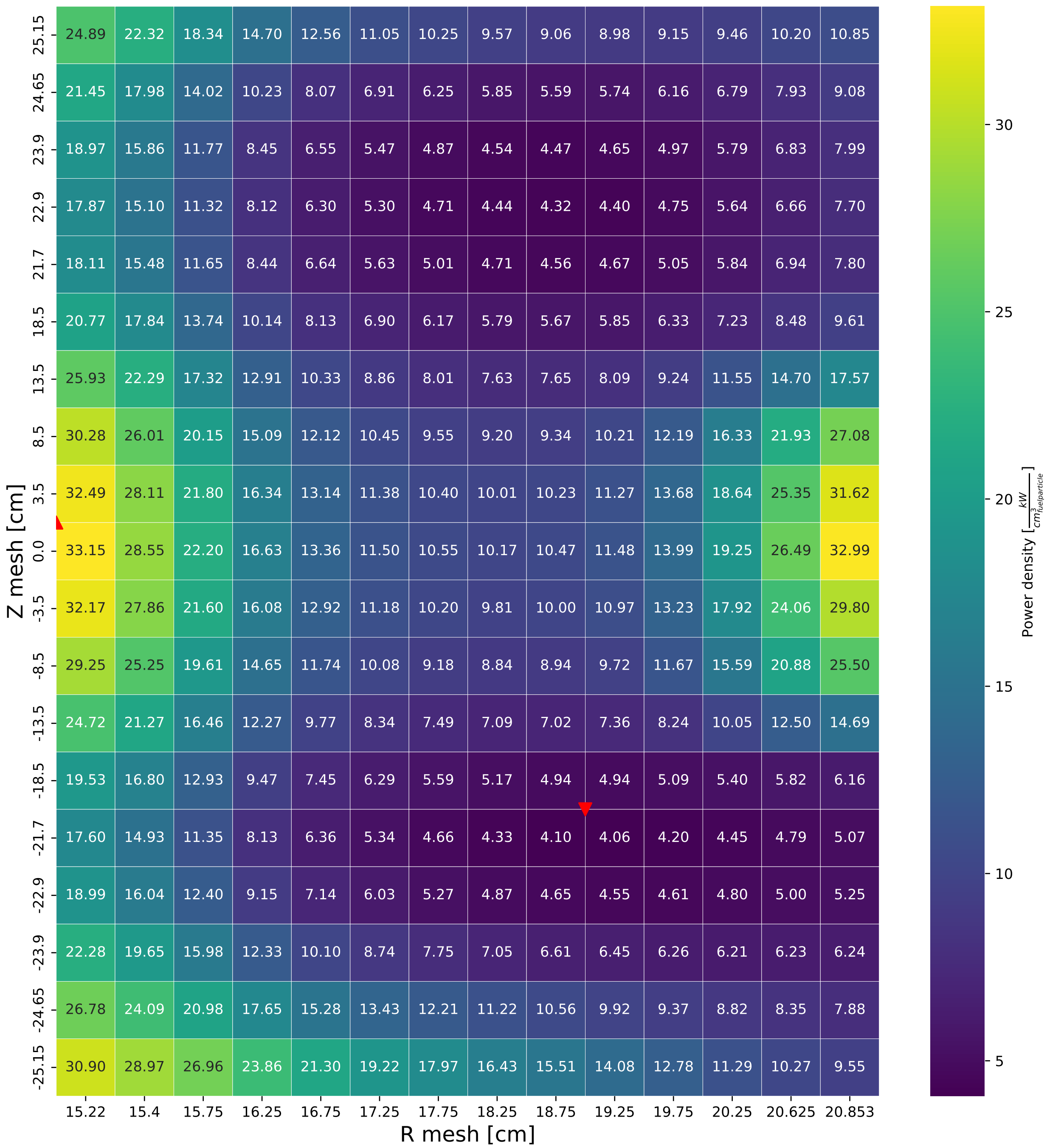

Figure 81. Power density distribution for utilization design OFE region on day 0 (see Section 7.2.3).

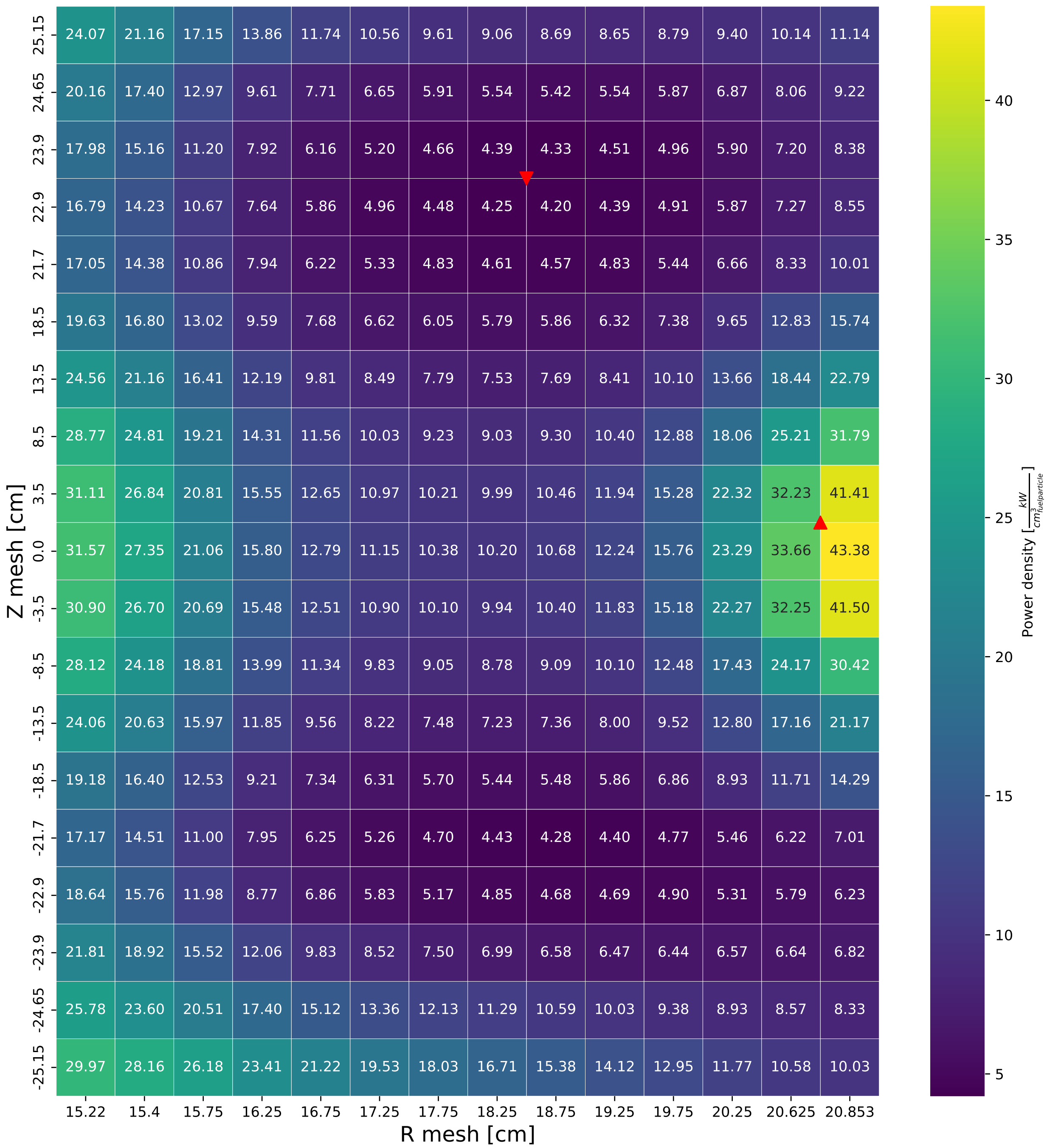

Figure 82. Power density distribution for utilization design OFE region on day 1 (see Section 7.2.3).

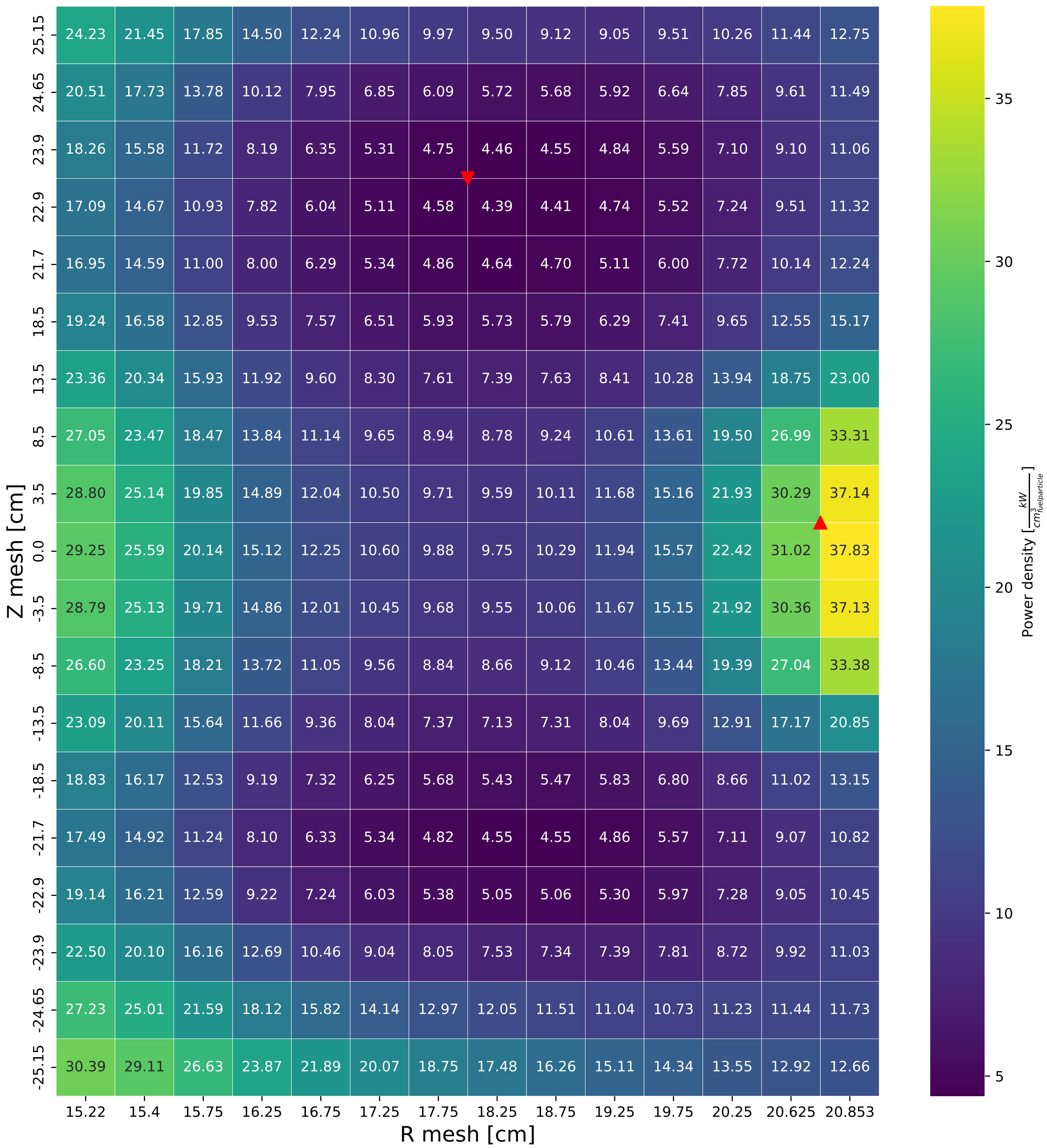

Figure 83. Power density distribution for utilization design OFE region on day 15 (see Section 7.2.3).

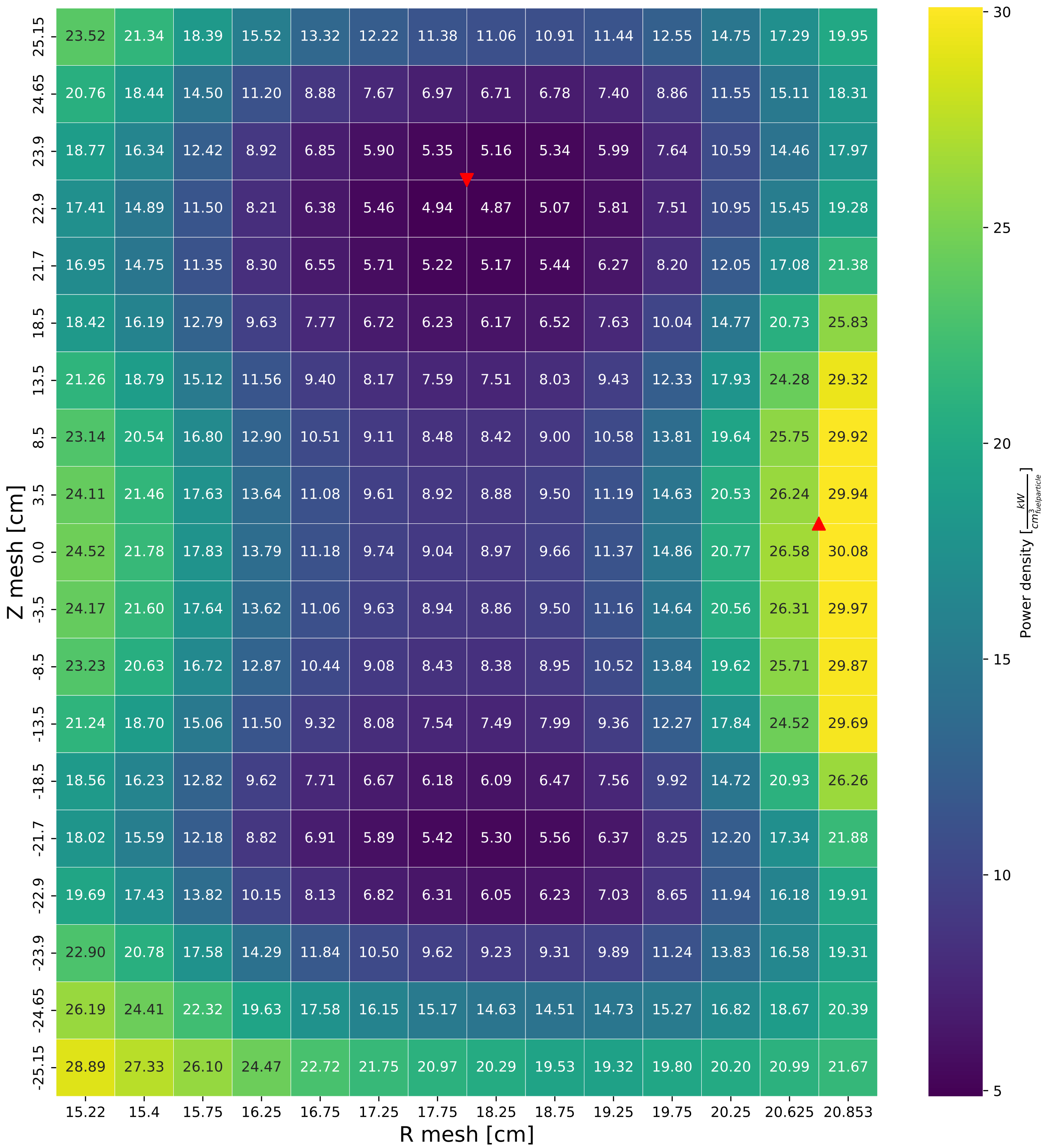

Figure 84. Power density distribution for utilization design OFE region on day 34 (see Section 7.2.3).

APPENDIX B-4. HEAT FLUX DISTRIBUTIONS FOR UTILIZATION DESIGN

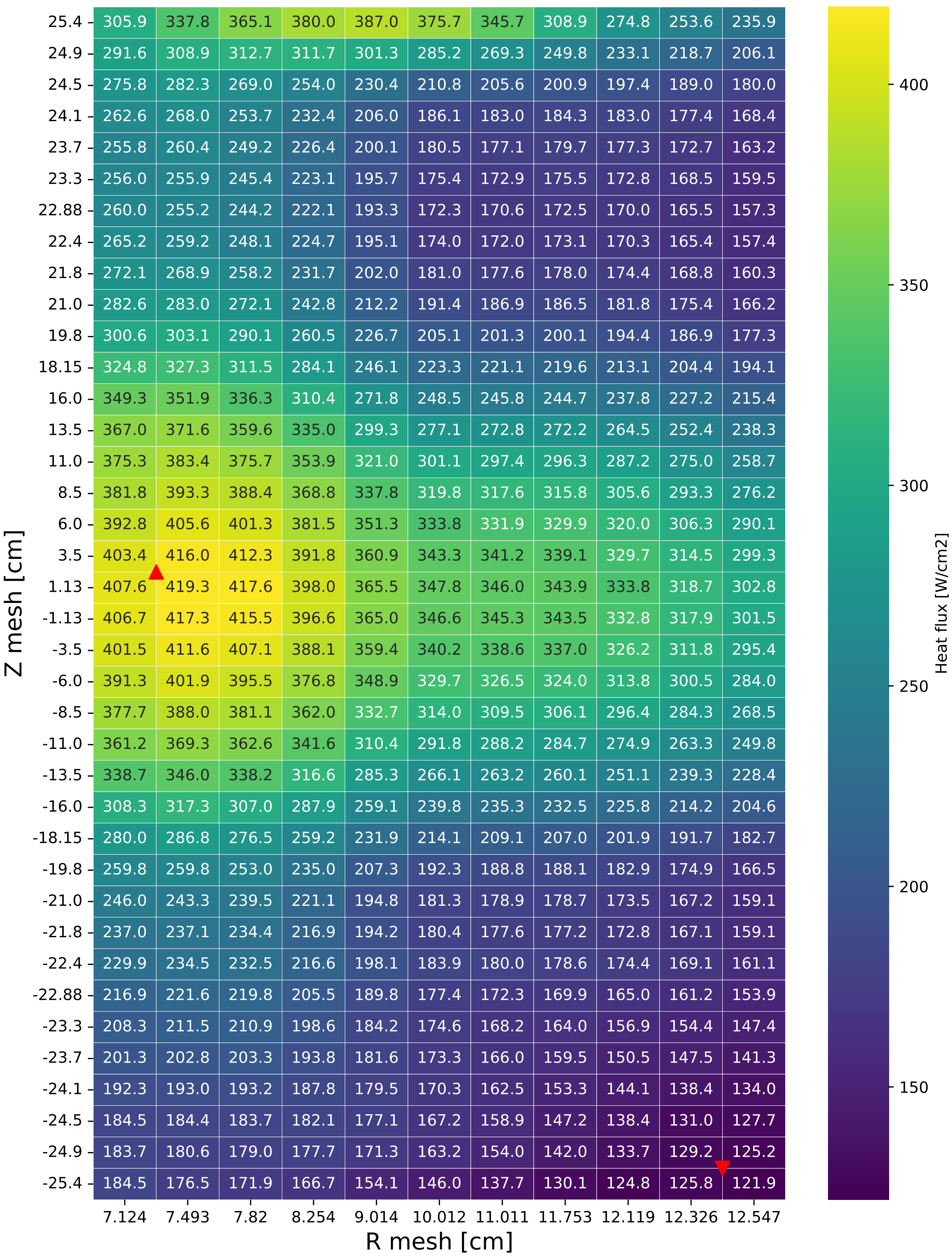

Figure 85. Heat flux distribution for utilization design IFE region on day 0 (see Section 7.2.4).

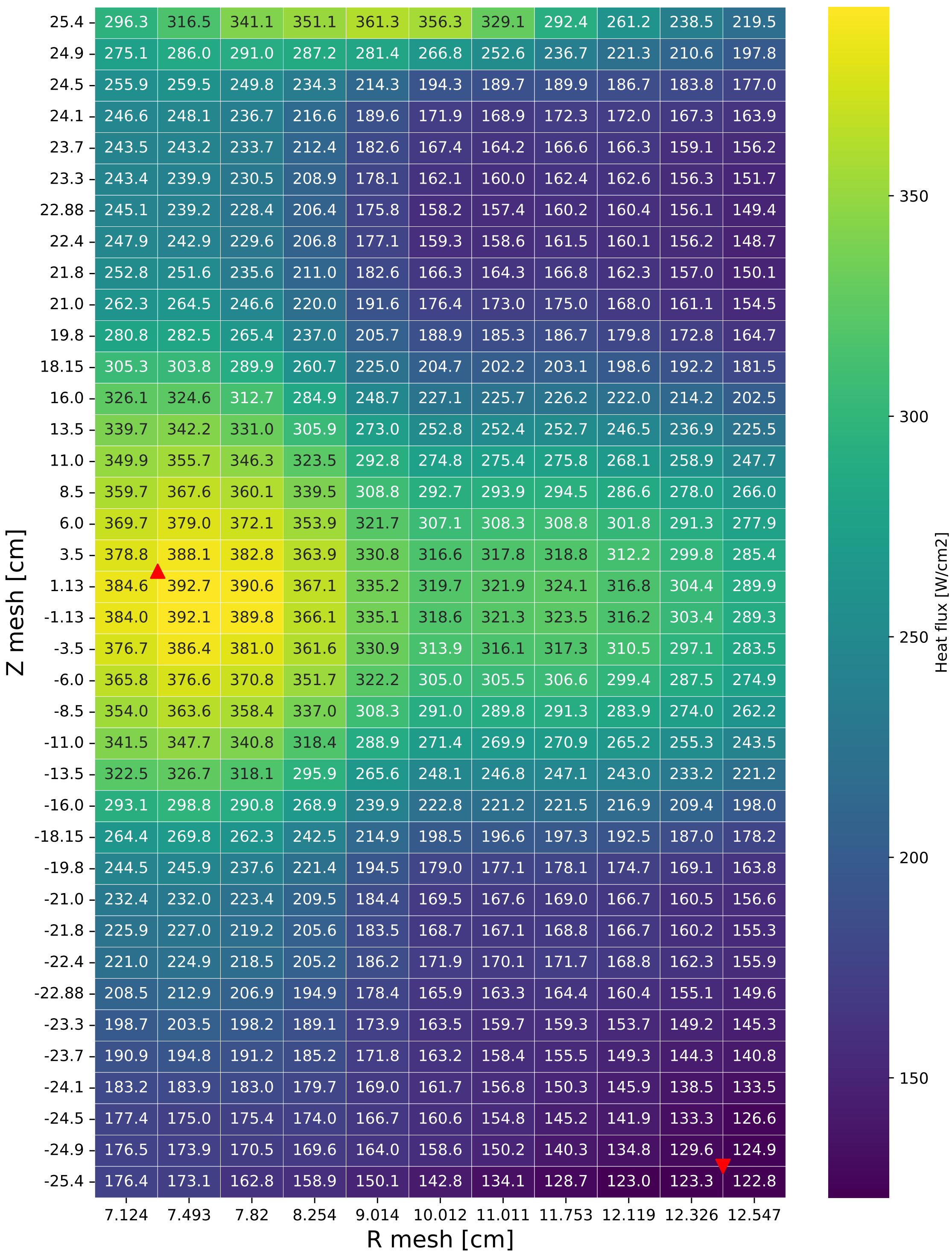

Figure 86. Heat flux distribution for utilization design IFE region on day 1 (see Section 7.2.4).

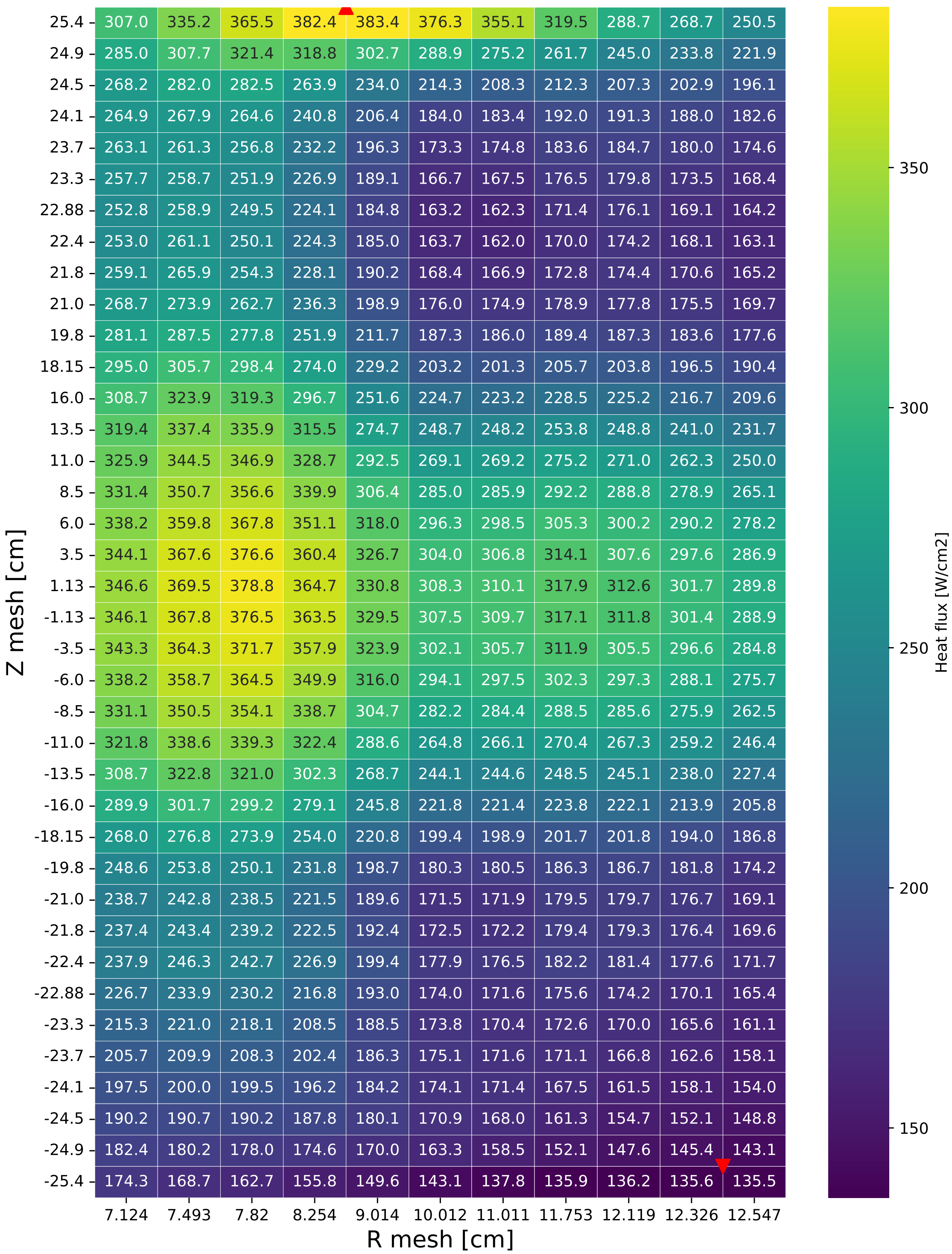

Figure 87. Heat flux distribution for utilization design IFE region on day 15 (see Section 7.2.4).

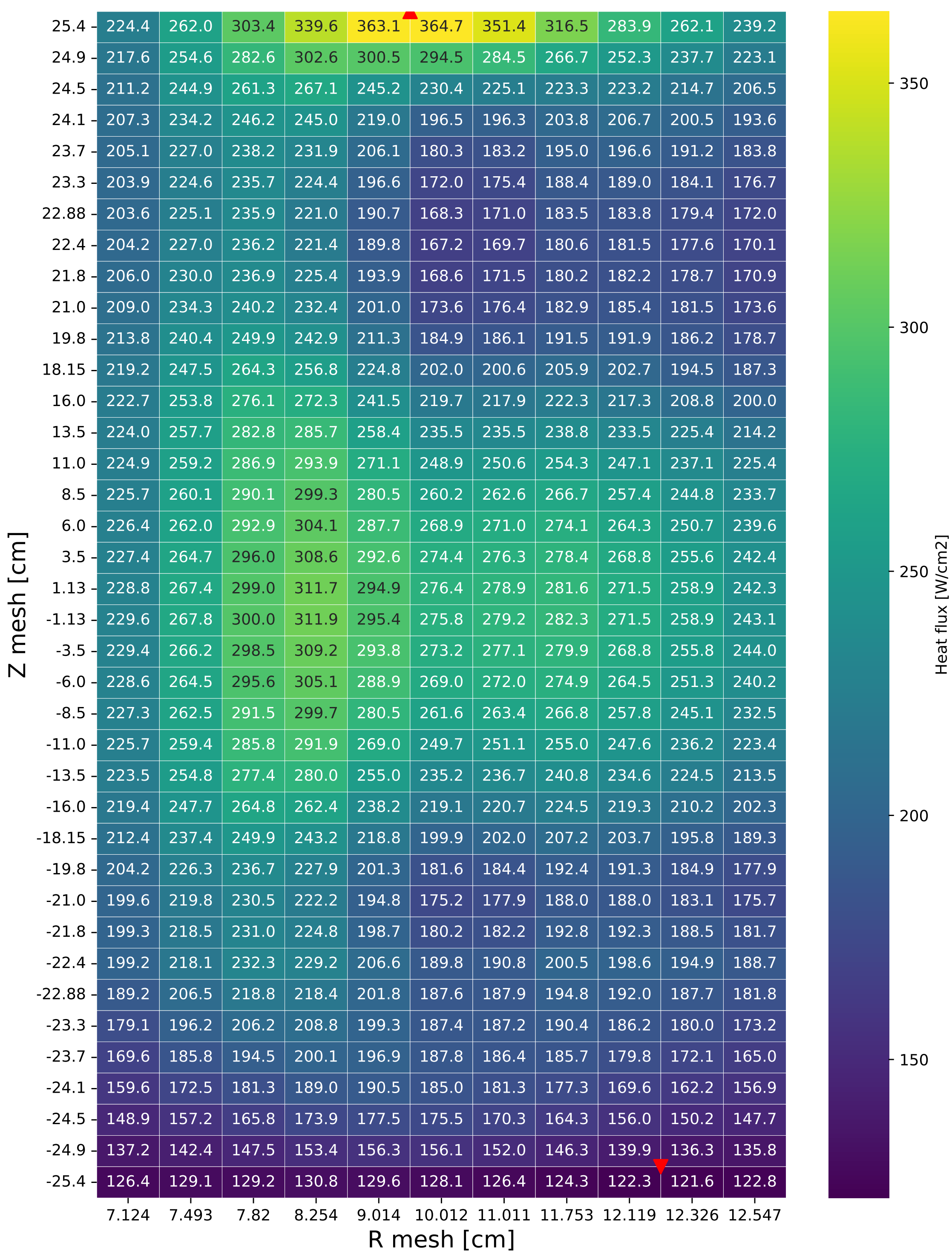

Figure 88. Heat flux distribution for utilization design IFE region on day 35 (see Section 7.2.4).

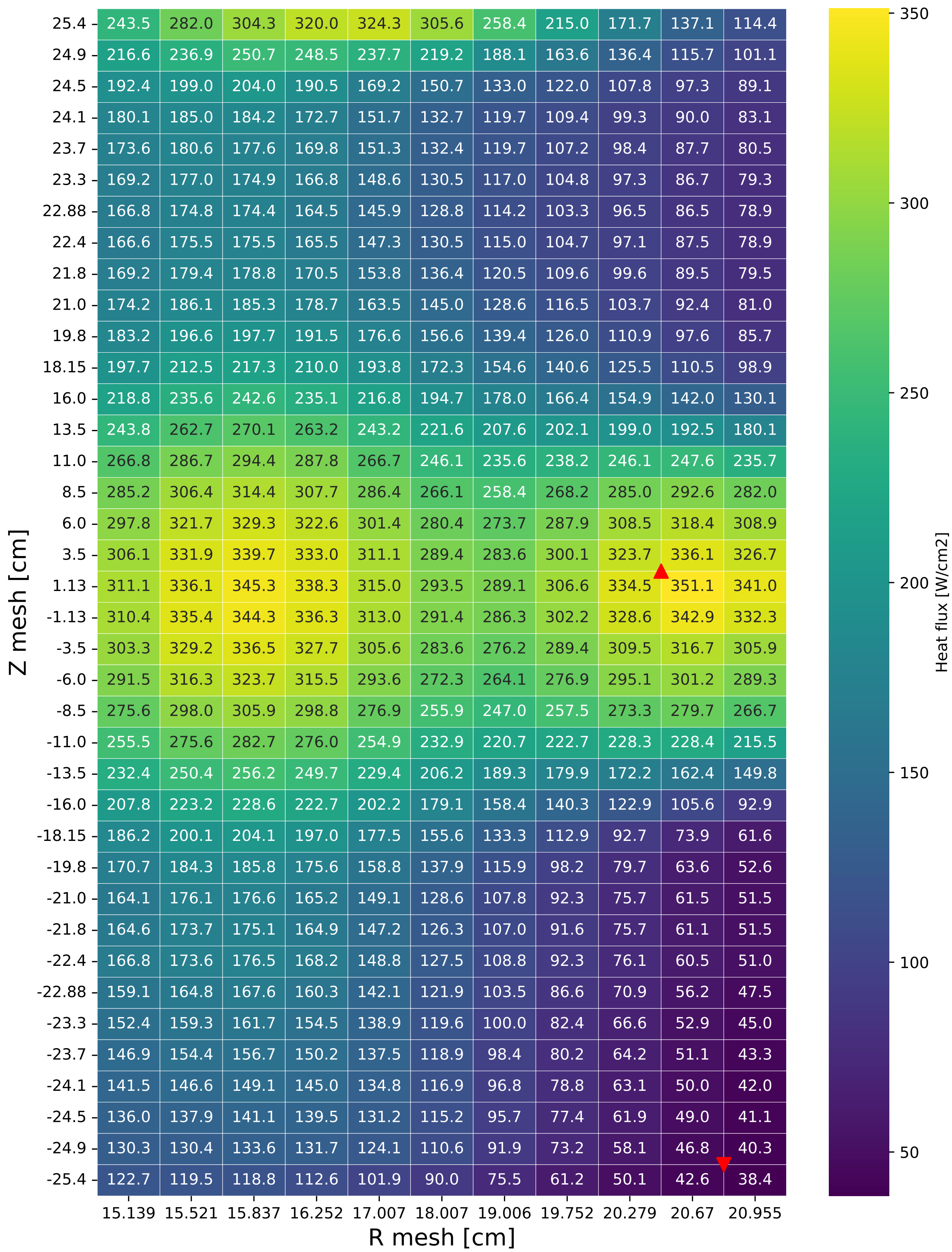

Figure 89. Heat flux distribution for utilization design OFE region on day 0 (see Section 7.2.4).

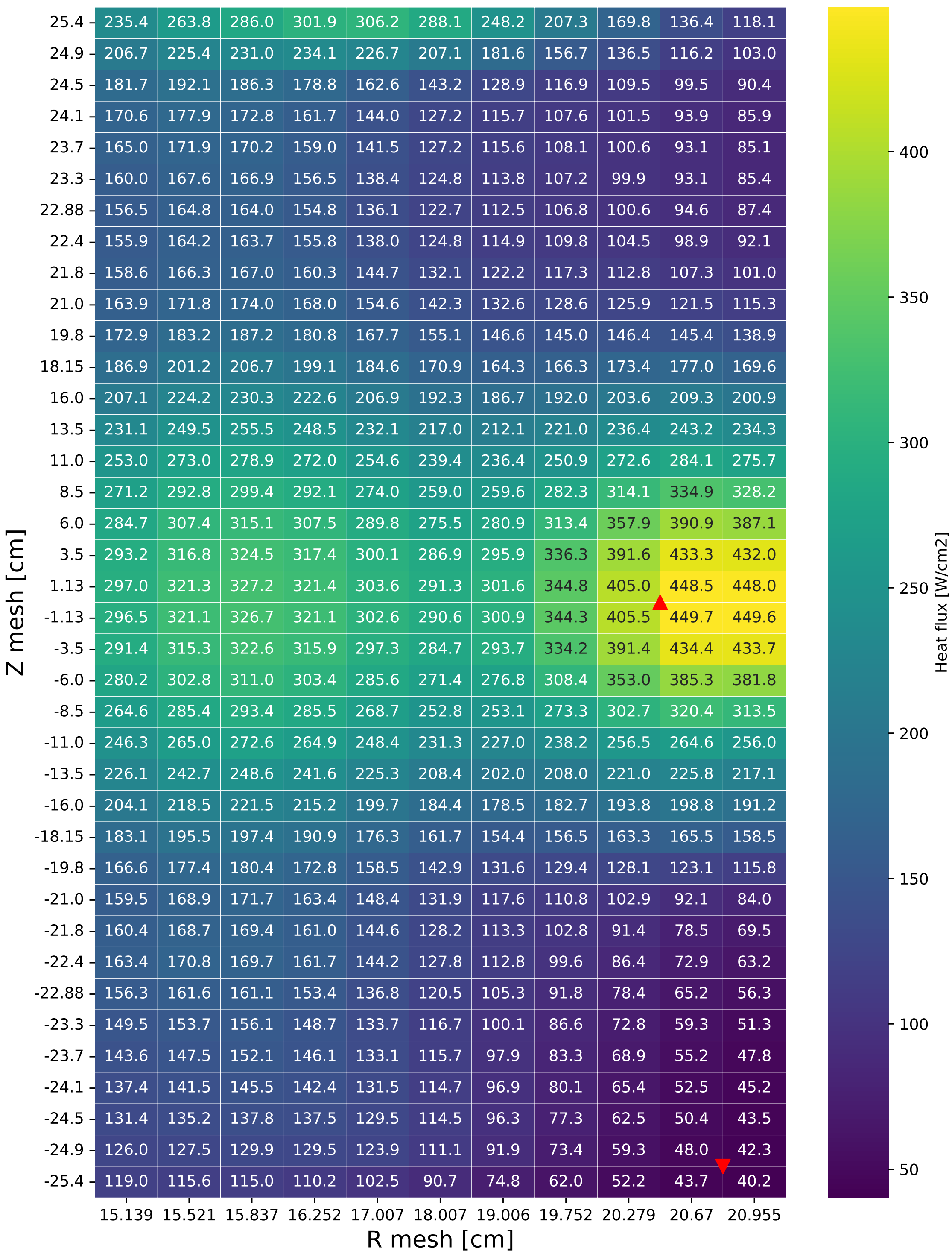

Figure 90. Heat flux distribution for utilization design OFE region on day 1 (see Section 7.2.4).

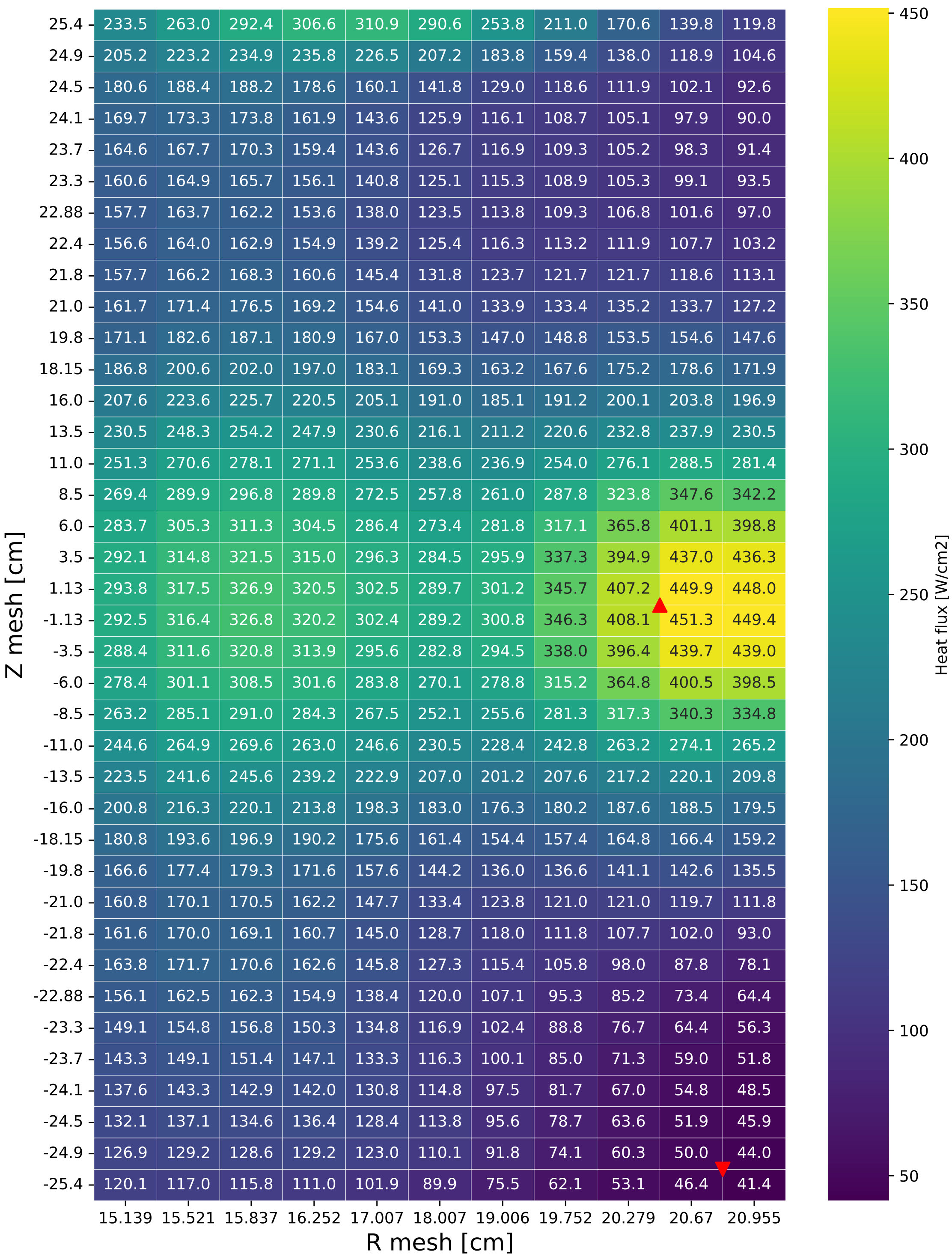

Figure 91. Heat flux distribution for utilization design OFE region on day 2 (see Section 7.2.4).

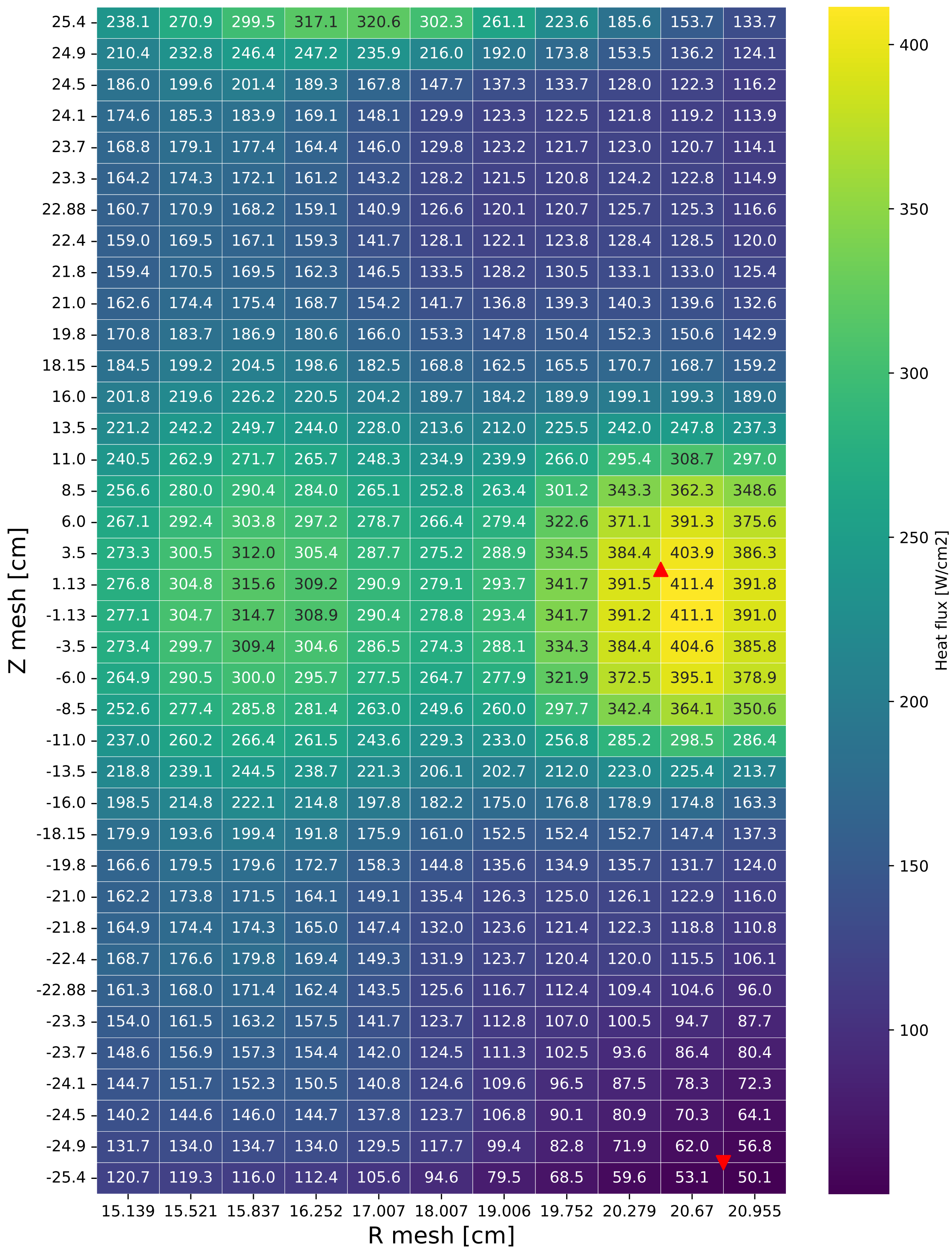

Figure 92. Heat flux distribution for utilization design OFE region on day 15 (see Section 7.2.4).

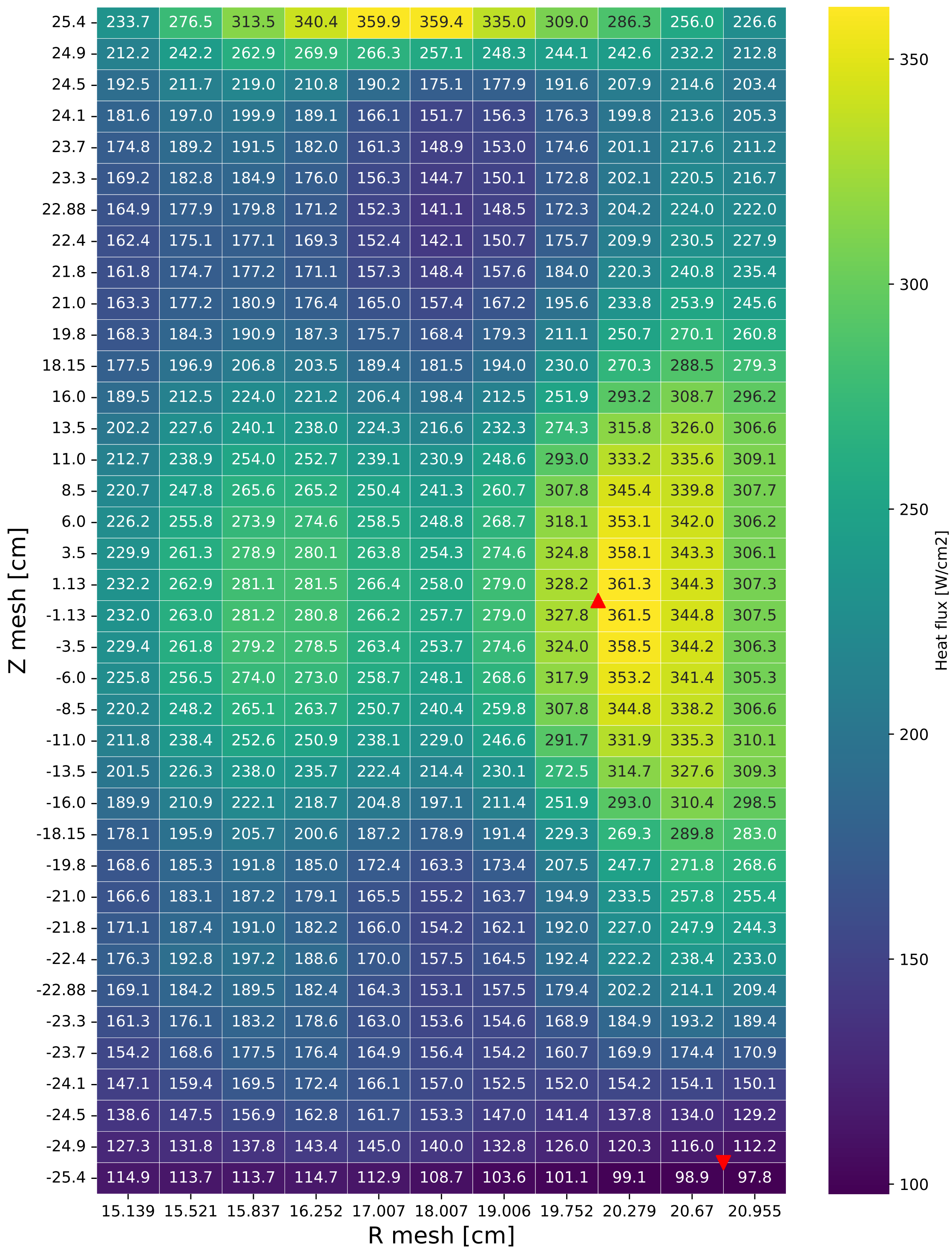

Figure 93. Heat flux distribution for utilization design OFE region on day 35 (see Section 7.2.4).

APPENDIX C. DISTRIBUTIONS FOR COLD DESIGN

APPENDIX C-1. FISSION RATE DENSITY DISTRIBUTIONS FOR COLD DESIGN

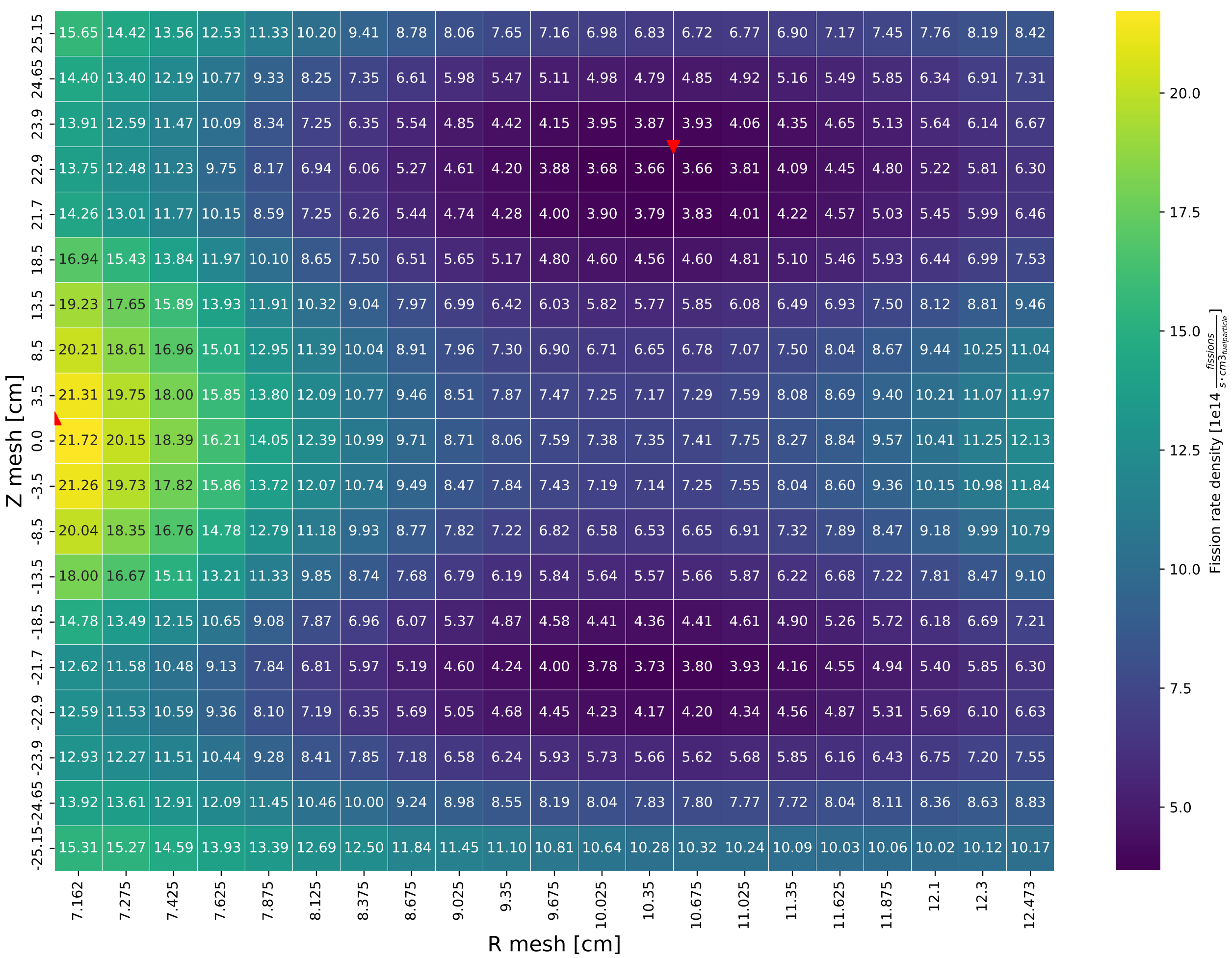

Figure 94. Fission rate density distribution for cold design IFE region on day 0 (see Section 7.3.2).

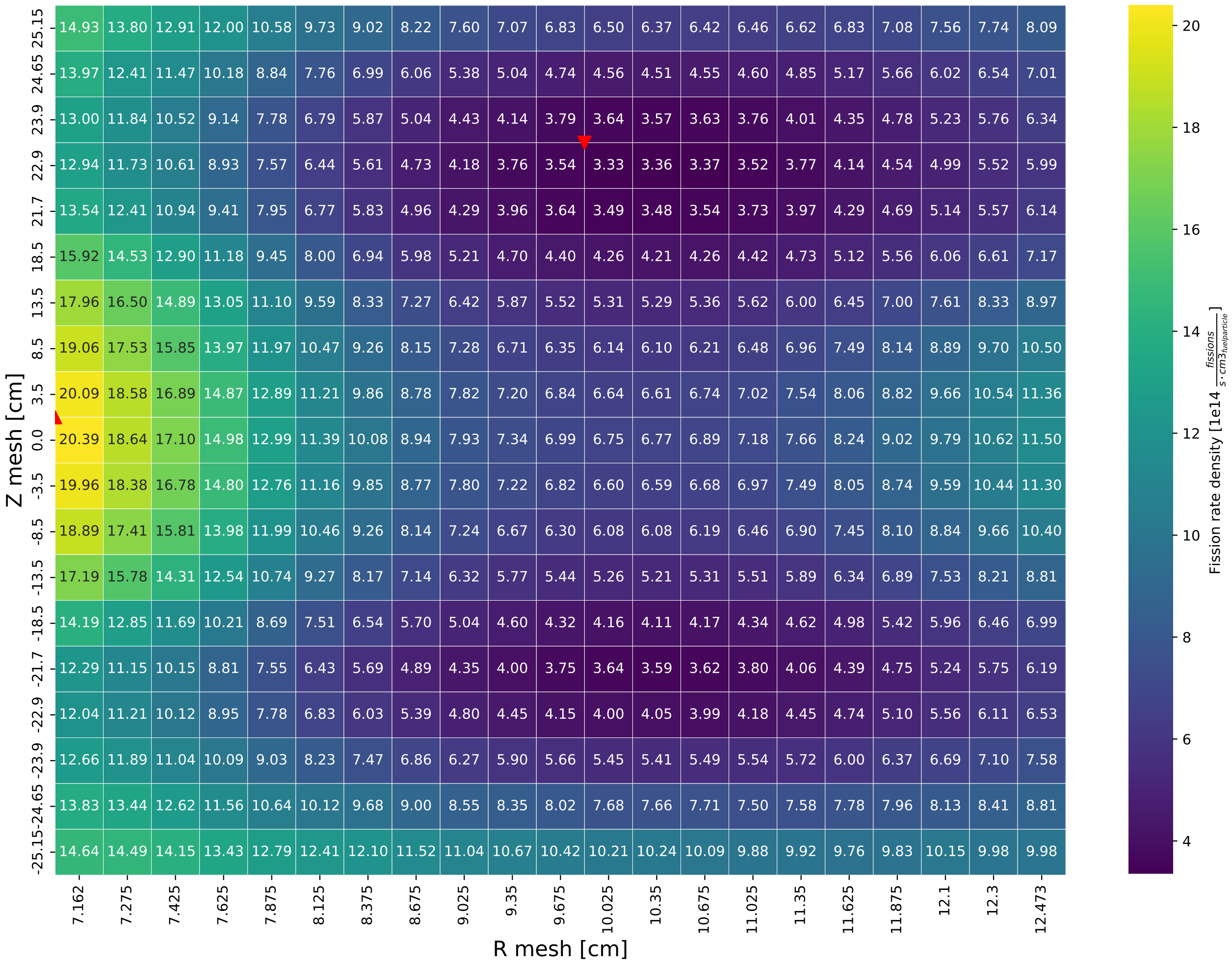

Figure 95. Fission rate density distribution for cold design IFE region on day 1 (see Section 7.3.2).

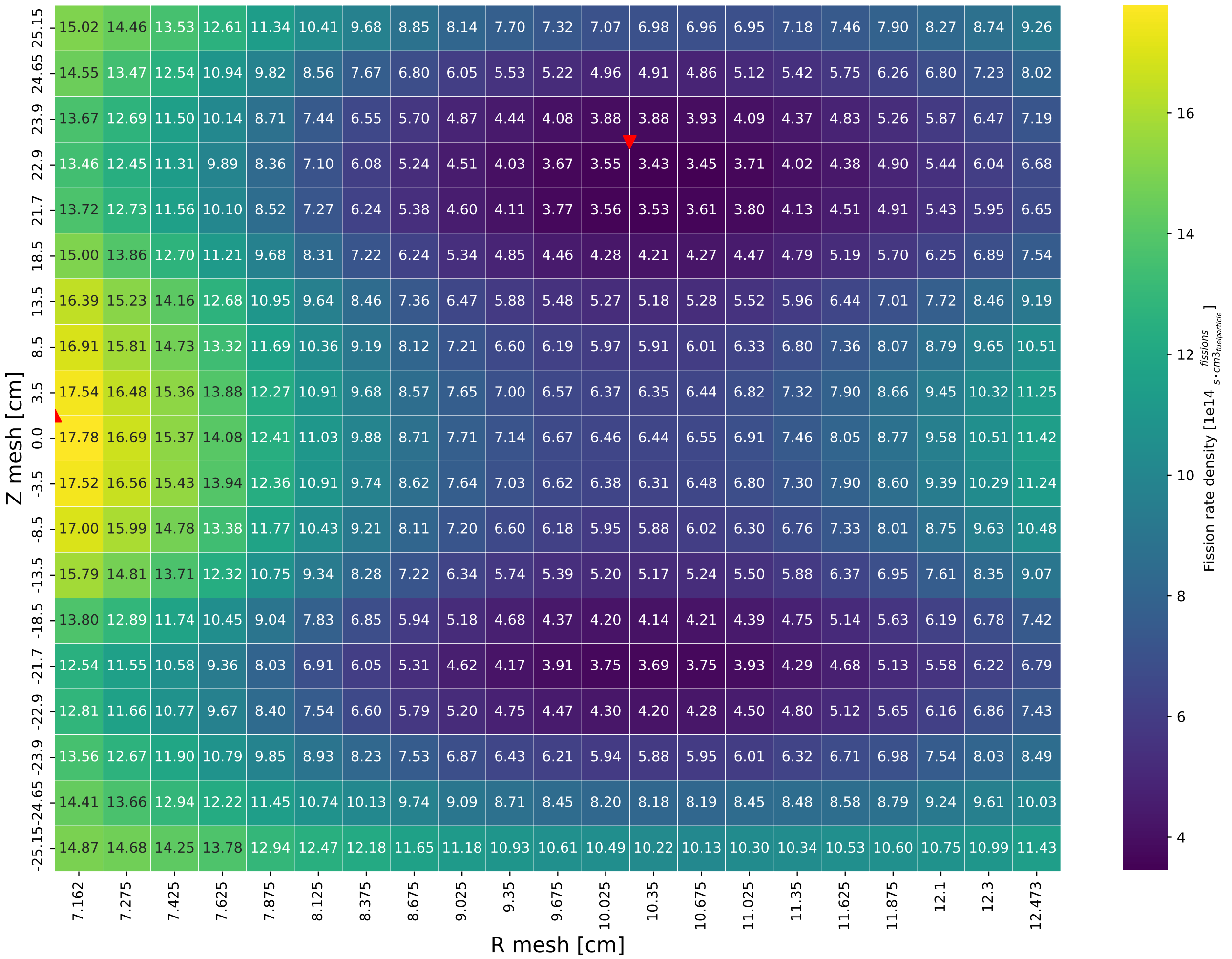

Figure 96. Fission rate density distribution for cold design IFE region on day 15 (see Section 7.3.2).

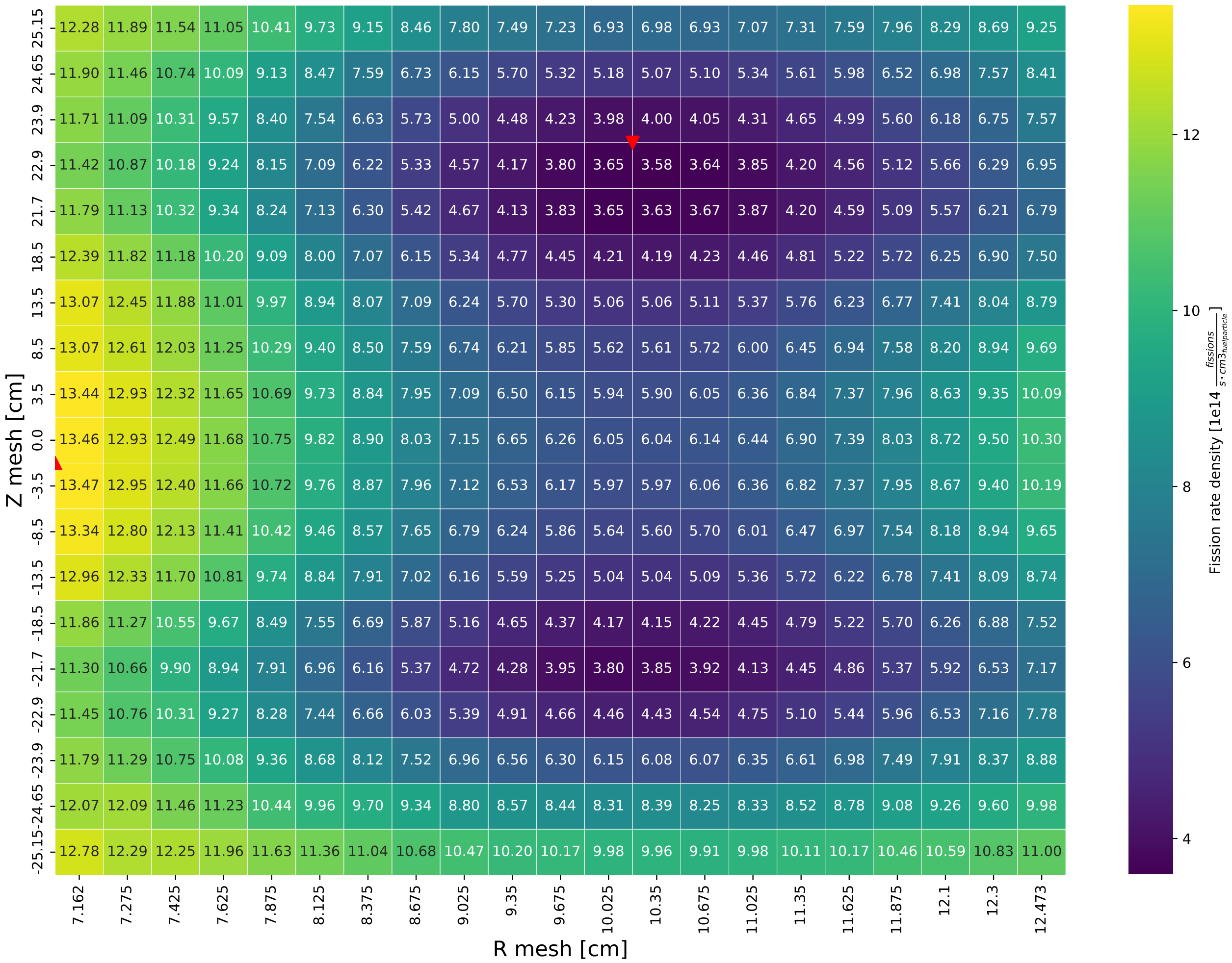

Figure 97. Fission rate density distribution for cold design IFE region on day 26 (see Section 7.3.2).

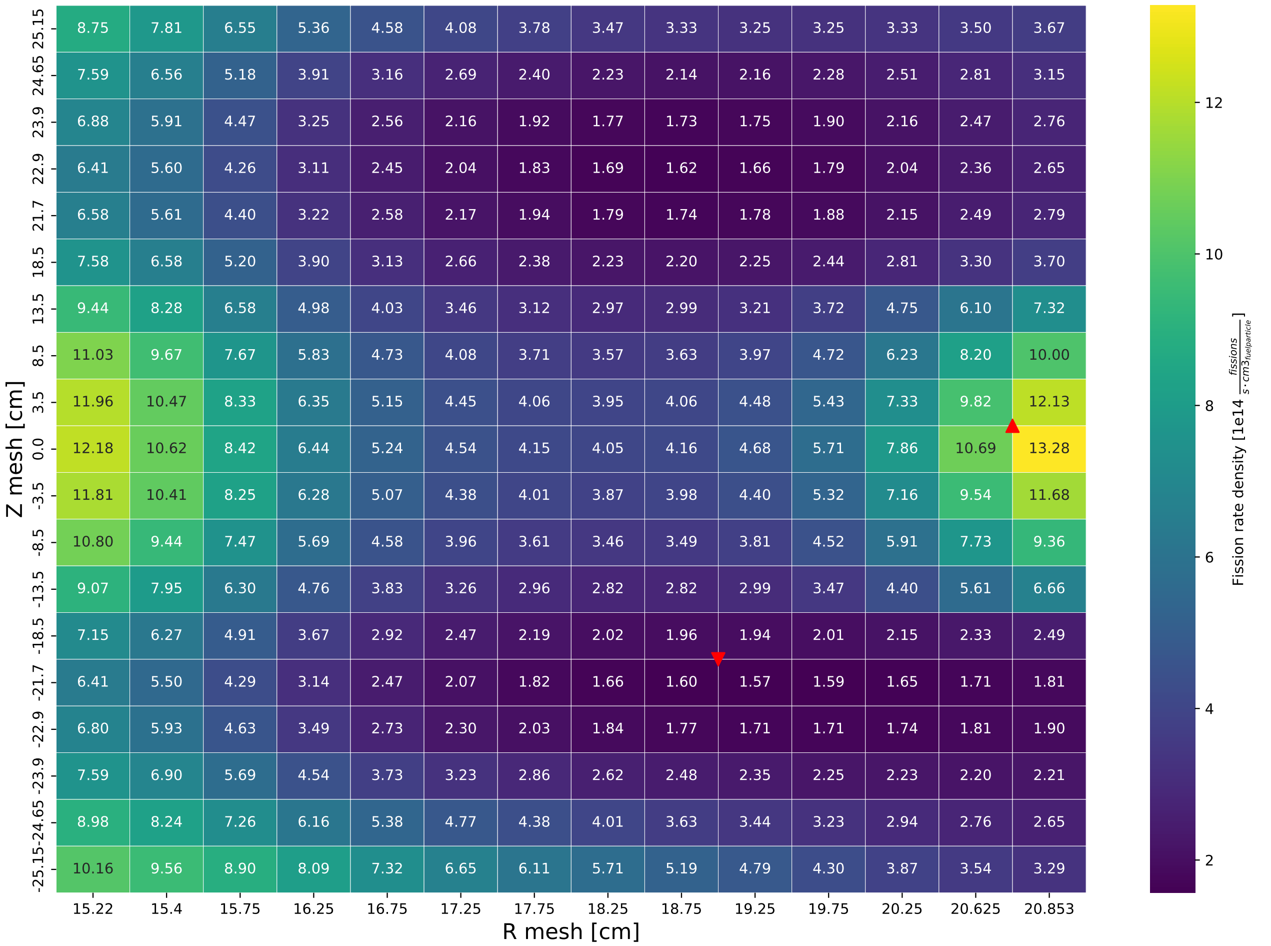

Figure 98. Fission rate density distribution for cold design OFE region on day 0 (see Section 7.3.2).

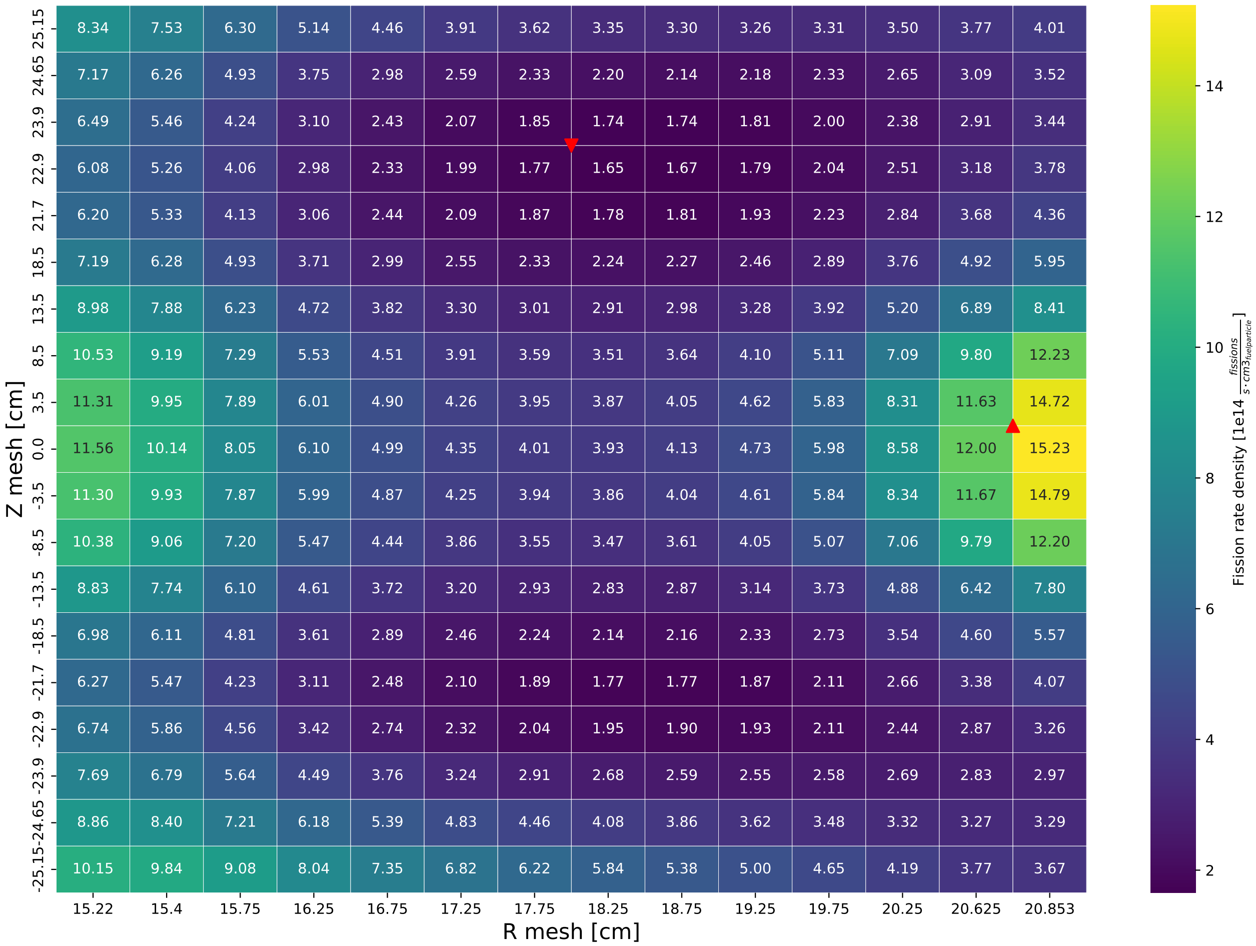

Figure 99. Fission rate density distribution for cold design OFE region on day 1 (see Section 7.3.2).

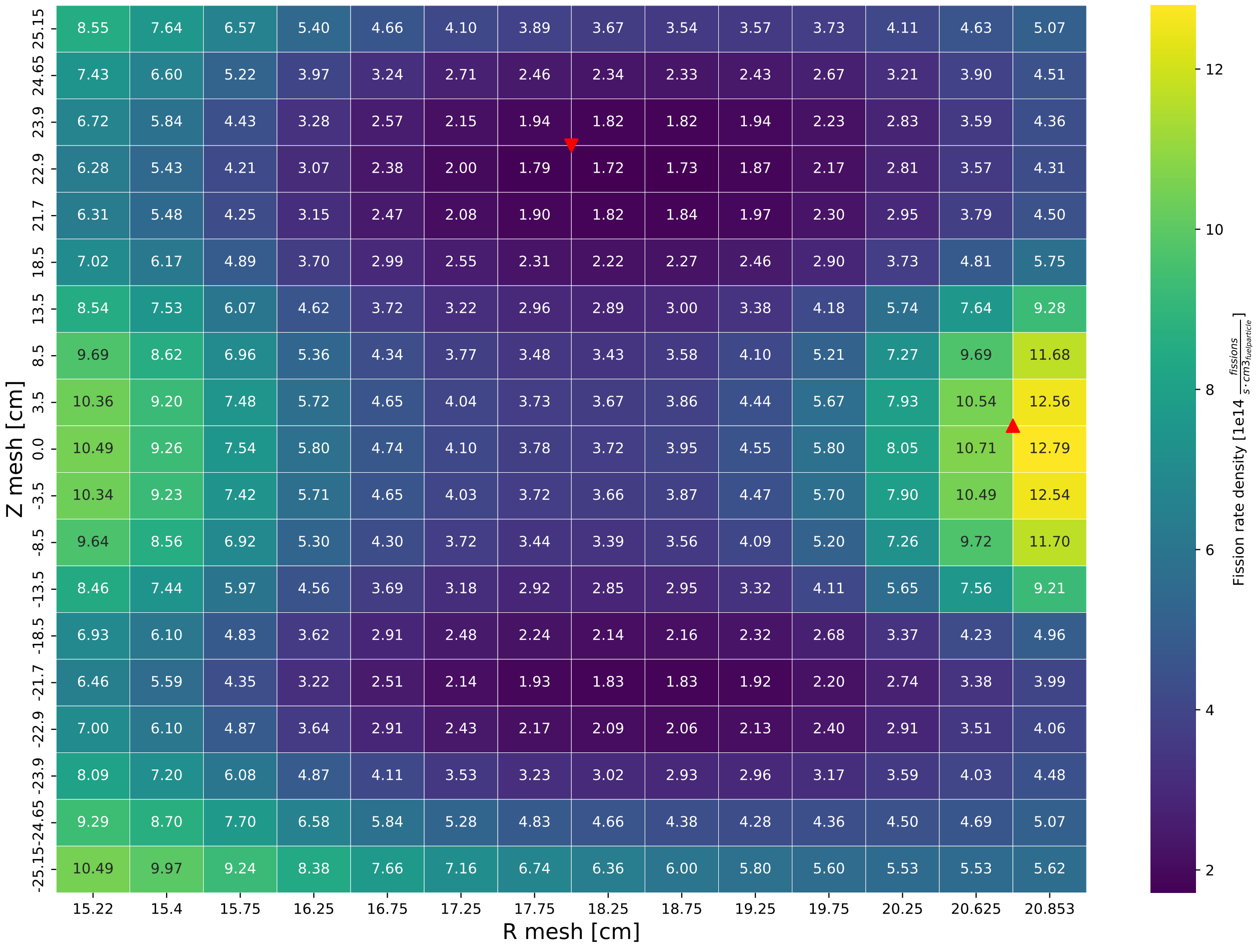

Figure 100. Fission rate density distribution for cold design OFE region on day 15 (see Section 7.3.2).

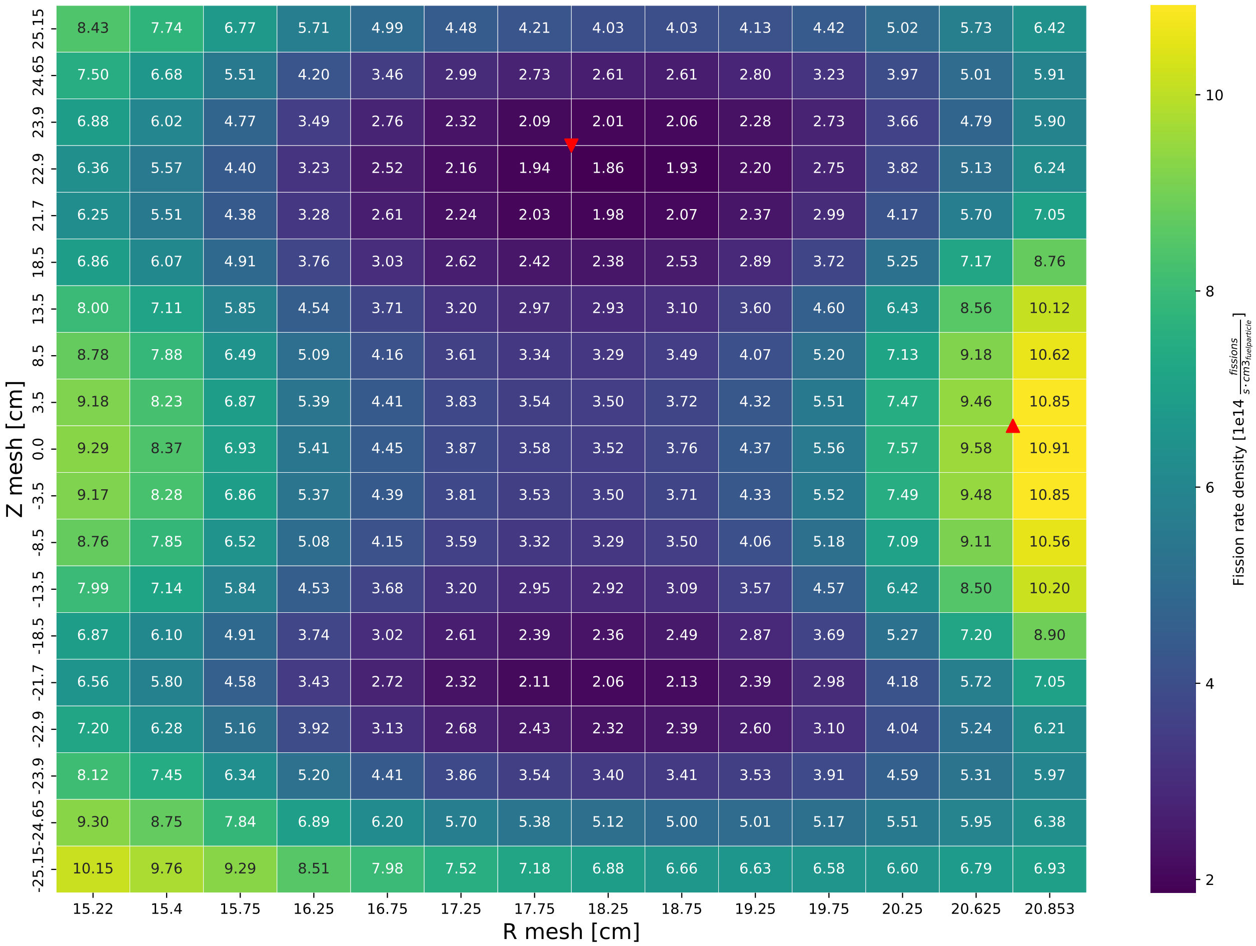

Figure 101. Fission rate density distribution for cold design OFE region on day 26 (see Section 7.3.2).

APPENDIX C-2. CUMULATIVE FISSION DENSITY DISTRIBUTIONS FOR COLD DESIGN

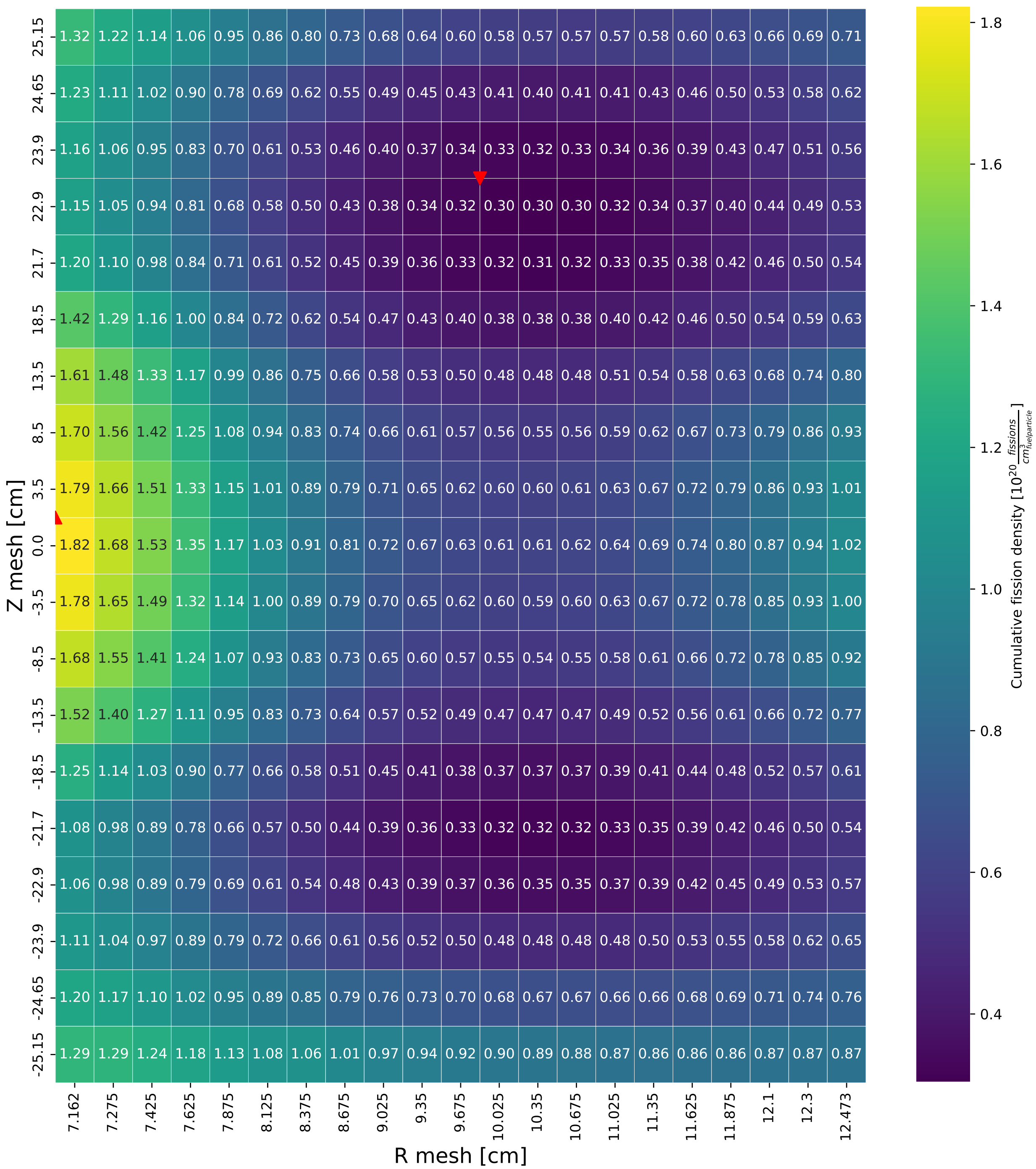

Figure 102. Cumulative fission density distribution for cold design IFE region on day 1 (see Section 7.3.5).

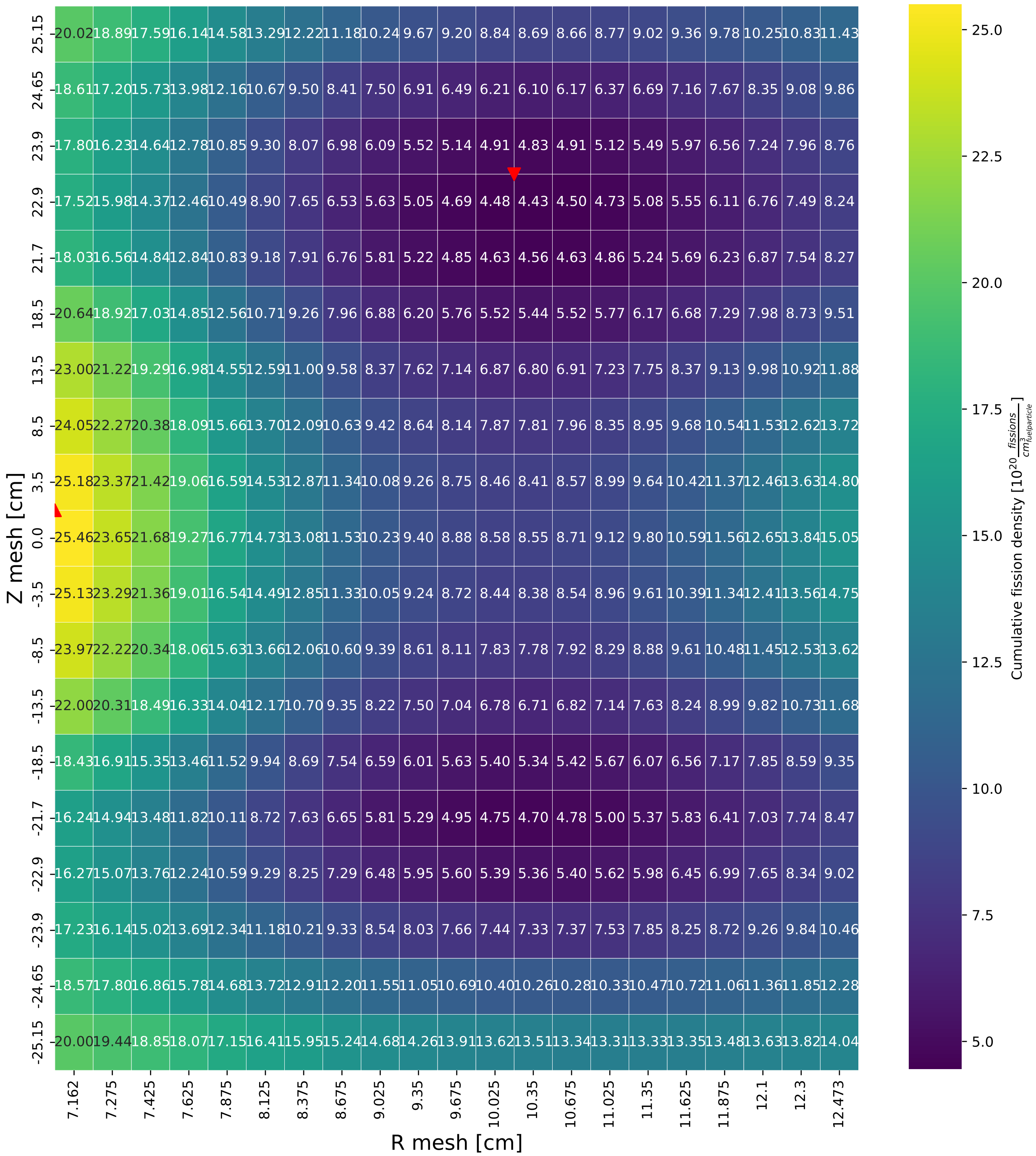

Figure 103. Cumulative fission density distribution for cold design IFE region on day 15 (see Section 7.3.5).

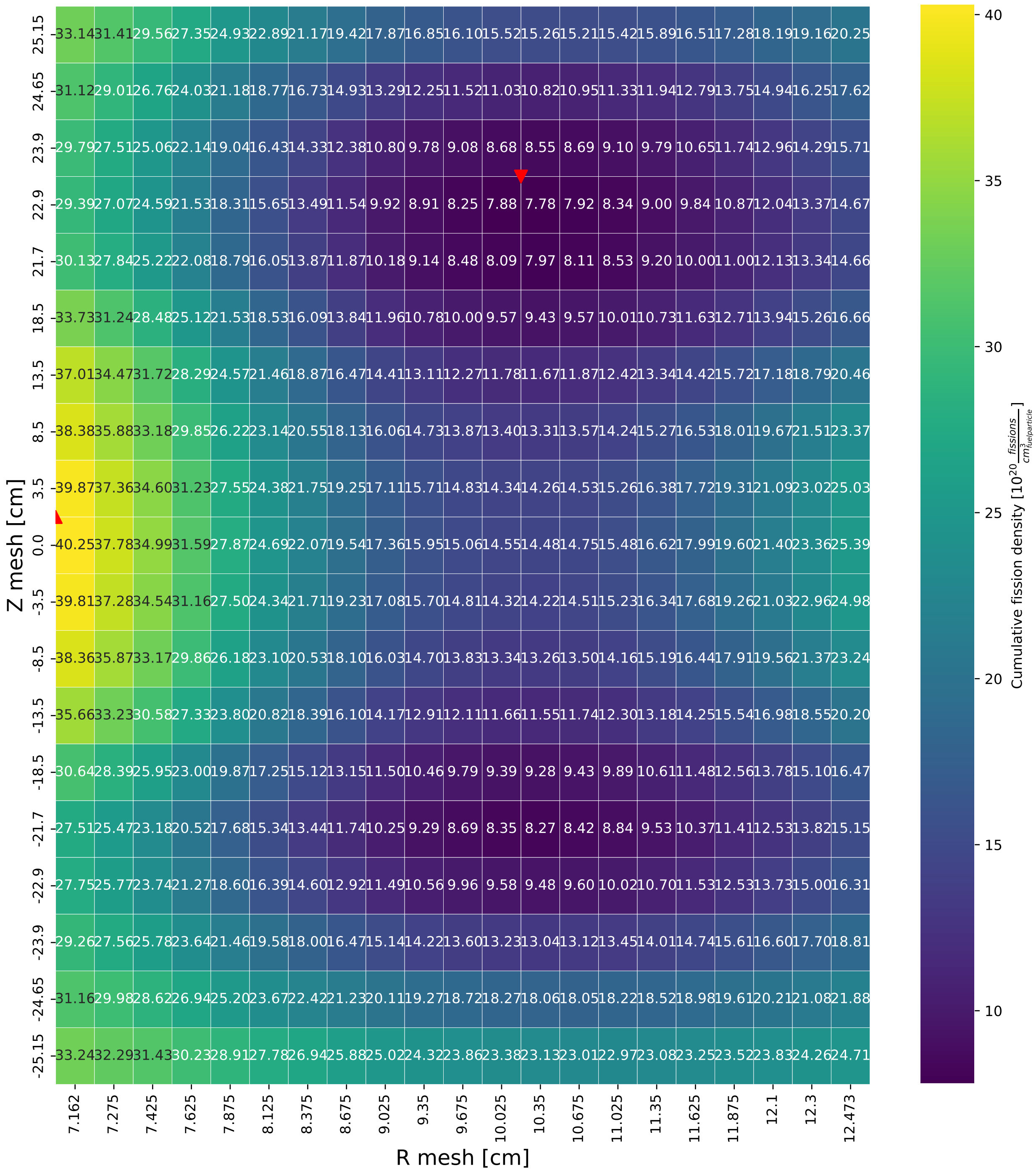

Figure 104. Cumulative fission density distribution for cold design IFE region on day 26 (see Section 7.3.5).

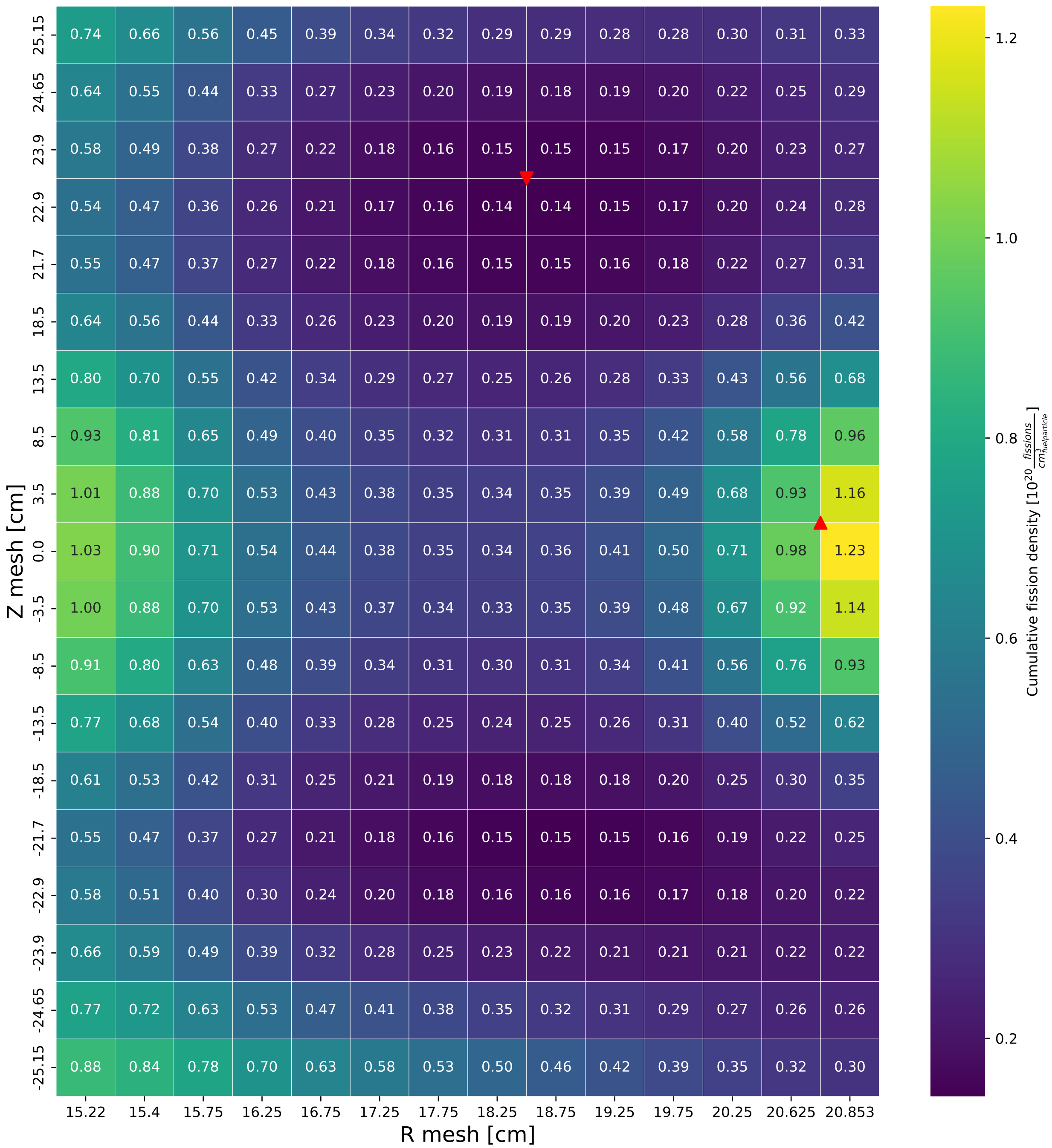

Figure 105. Cumulative fission density distribution for cold design OFE region on day 1 (see Section 7.3.5).

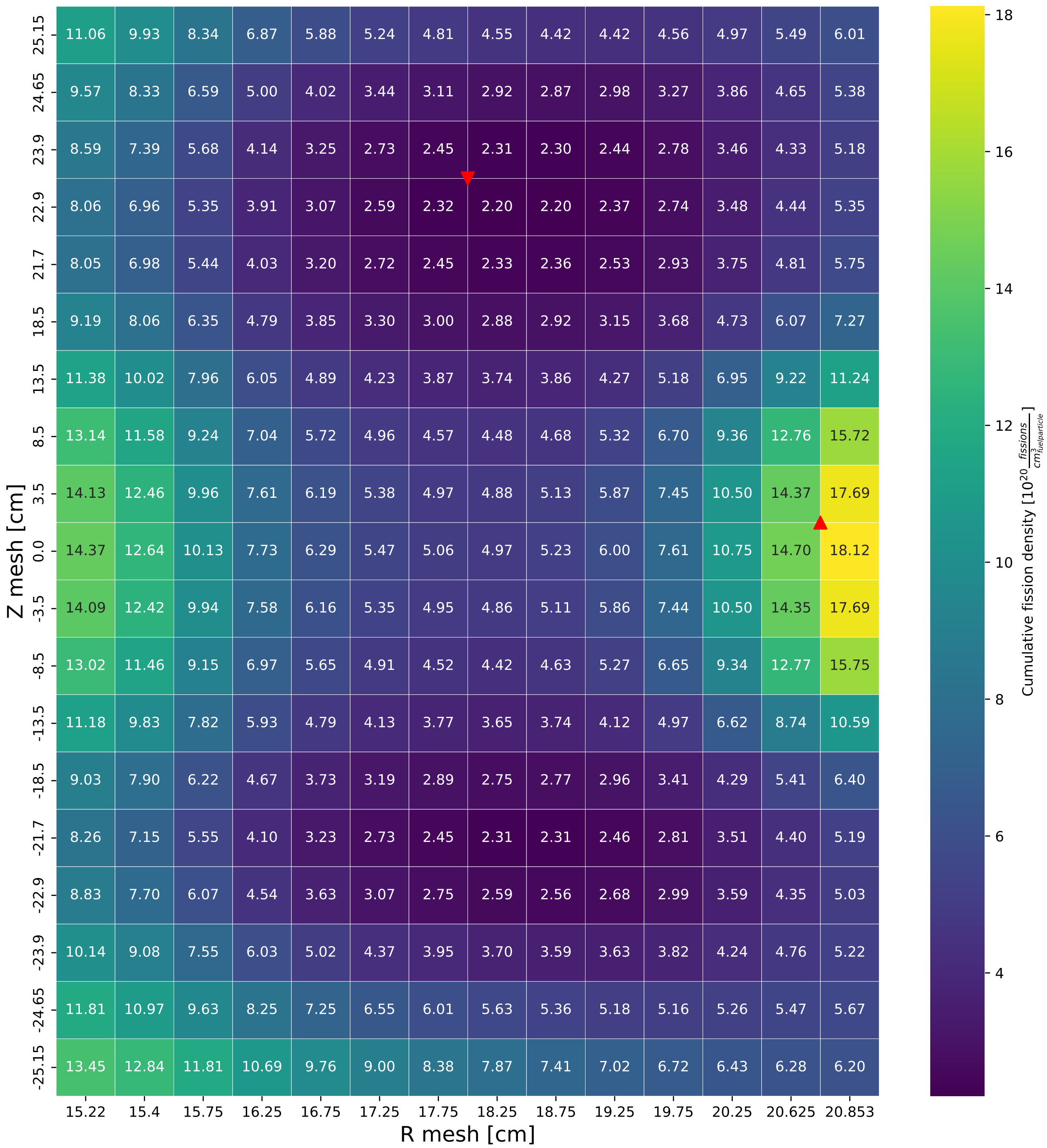

Figure 106. Cumulative fission density distribution for cold design OFE region on day 15 (see Section 7.3.5).

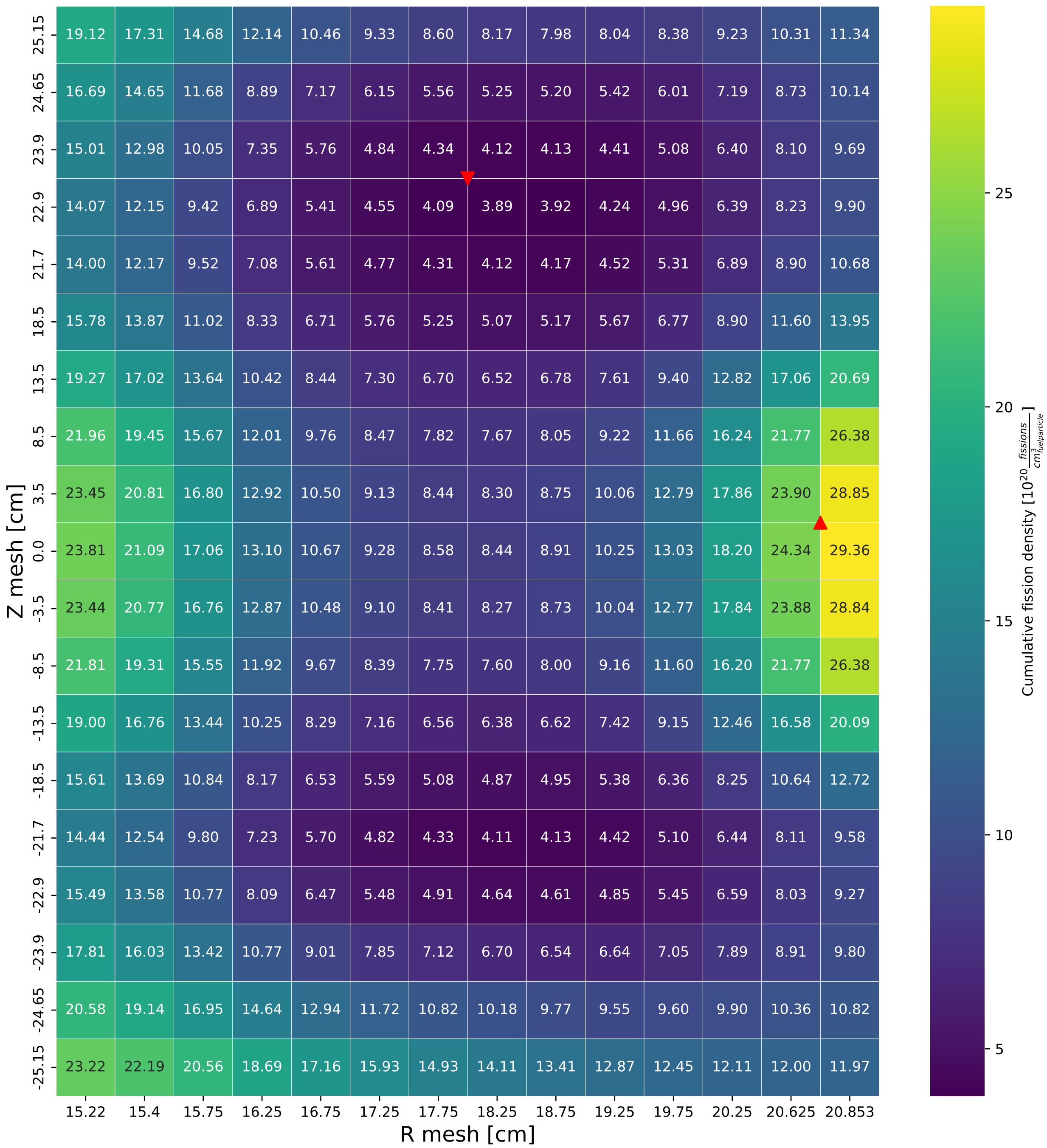

Figure 107. Cumulative fission density distribution for cold design OFE region on day 26 (see Section 7.3.5).

APPENDIX C-3. POWER DENSITY DISTRIBUTIONS FOR COLD DESIGN

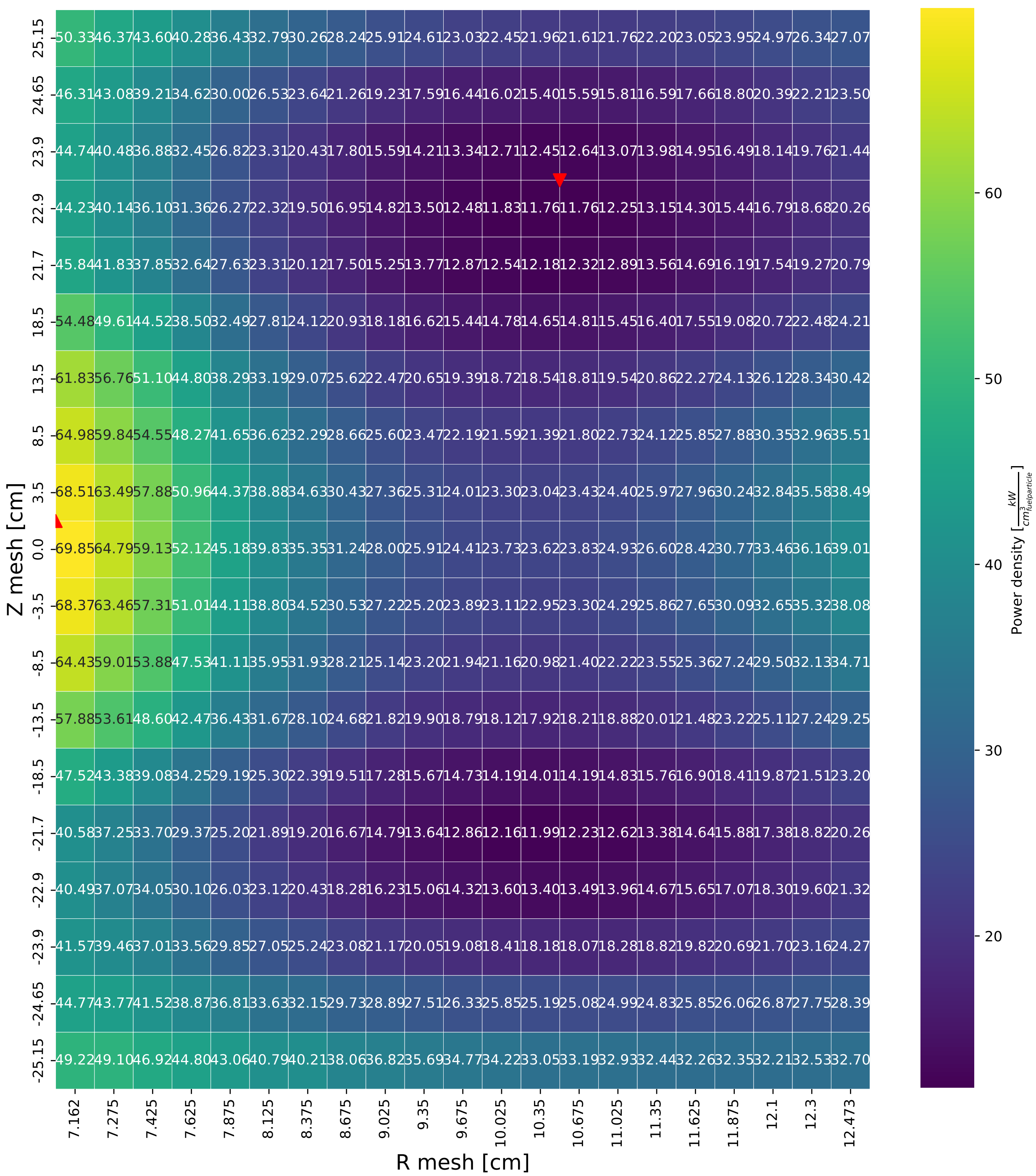

Figure 108. Power density distribution for cold design IFE region on day 0 (see Section 7.3.3).

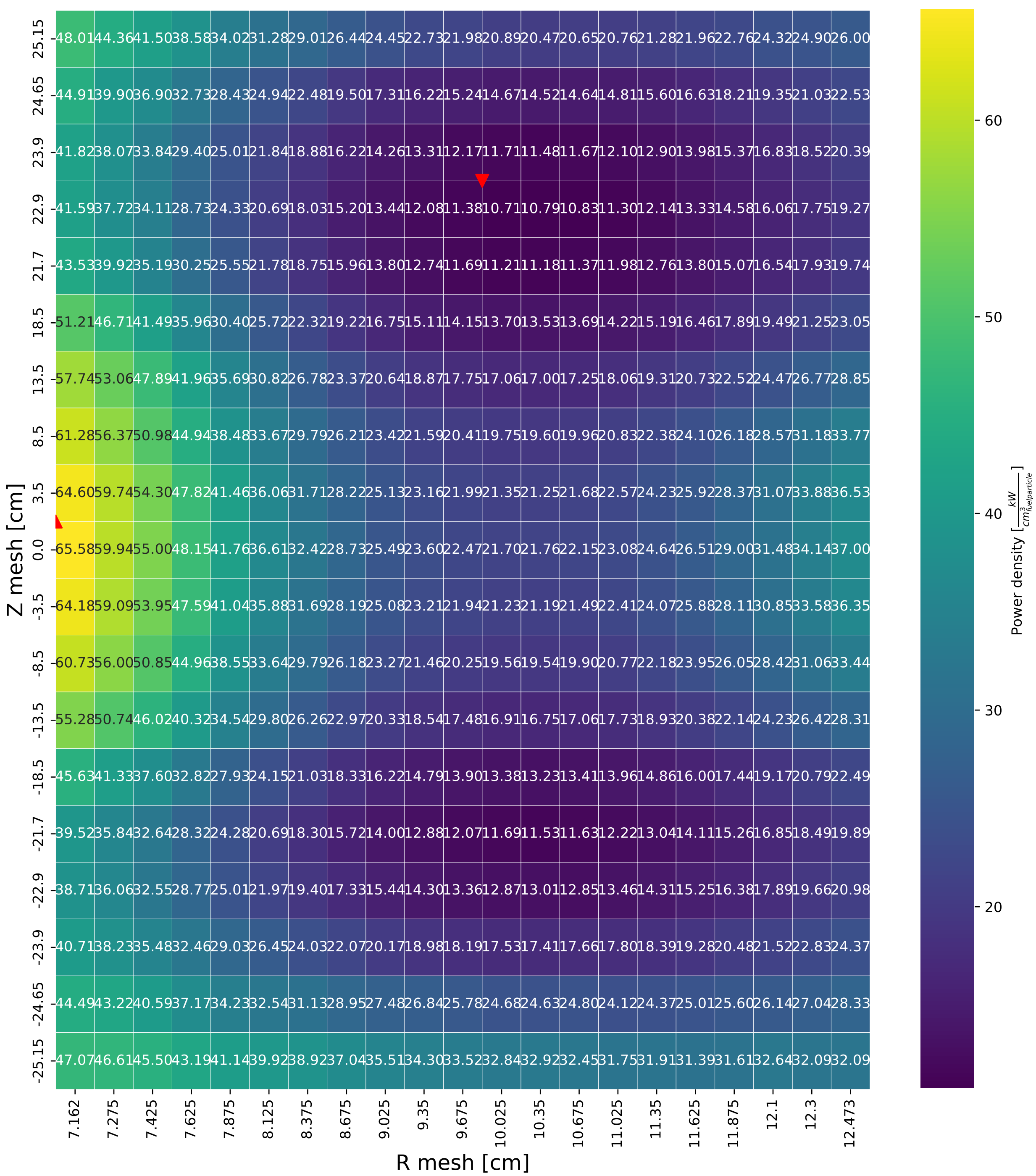

Figure 109. Power density distribution for cold design IFE region on day 1 (see Section 7.3.3).

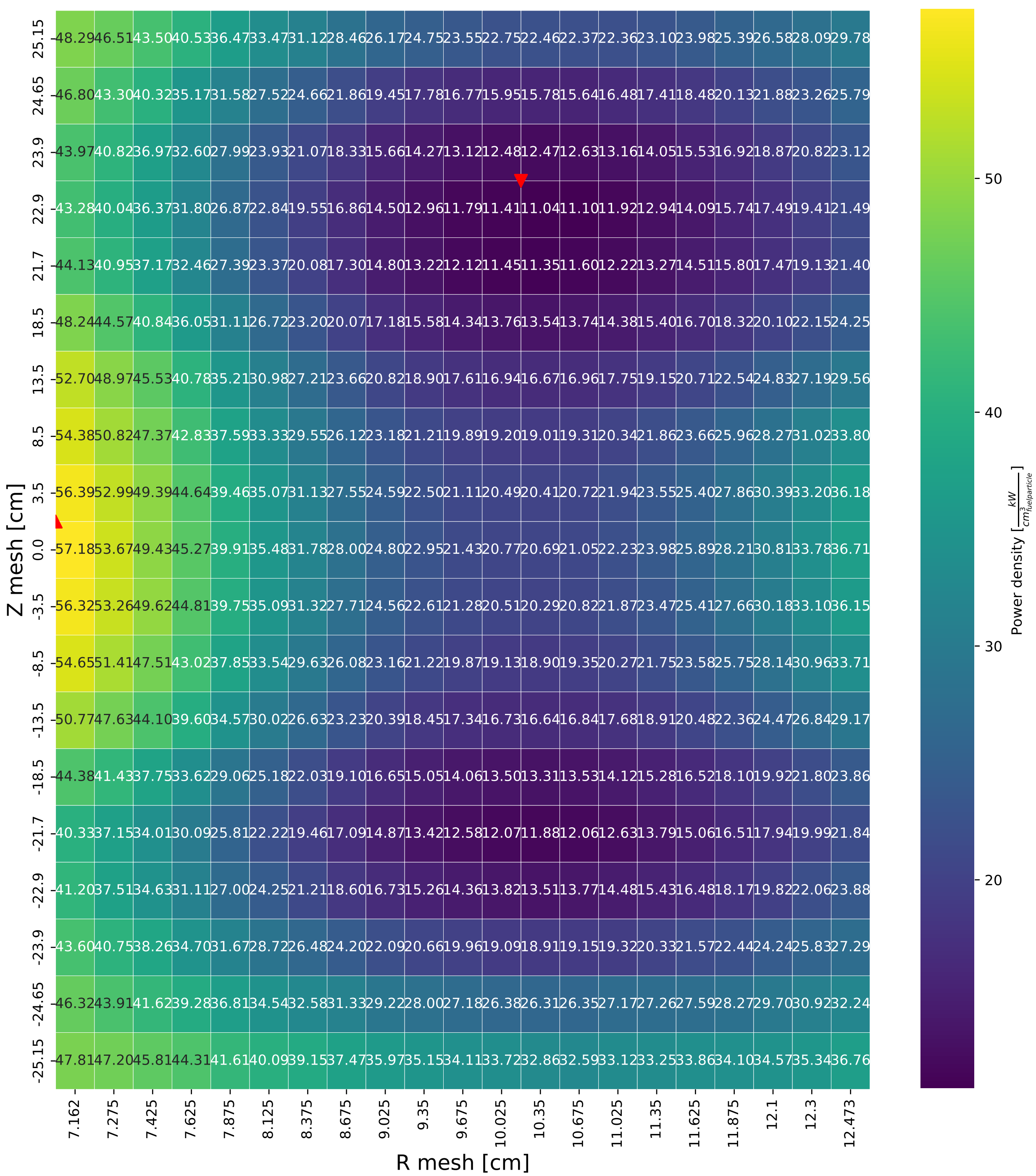

Figure 110. Power density distribution for cold design IFE region on day 15 (see Section 7.3.3).

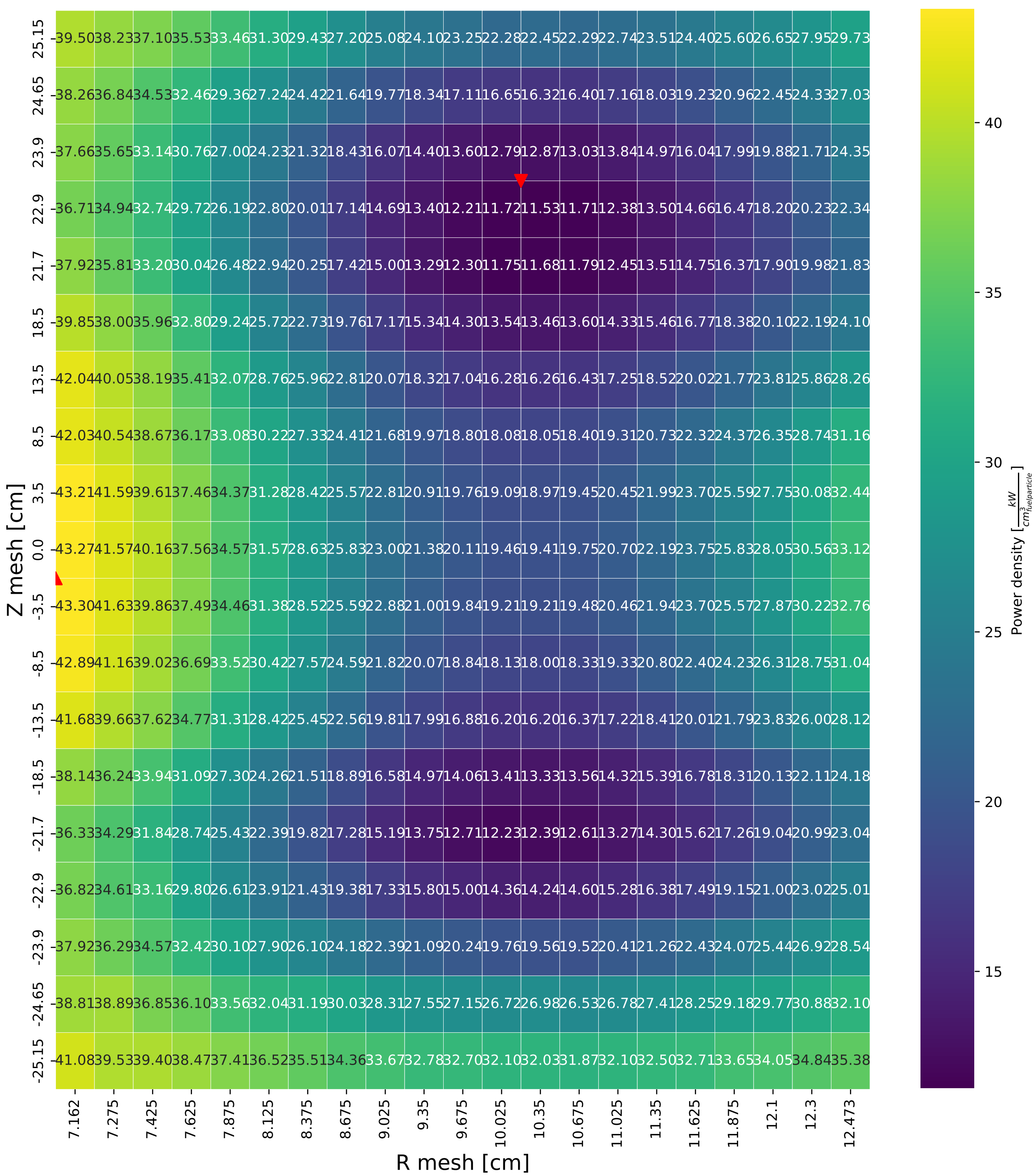

Figure 111. Power density distribution for cold design IFE region on day 26 (see Section 7.3.3).

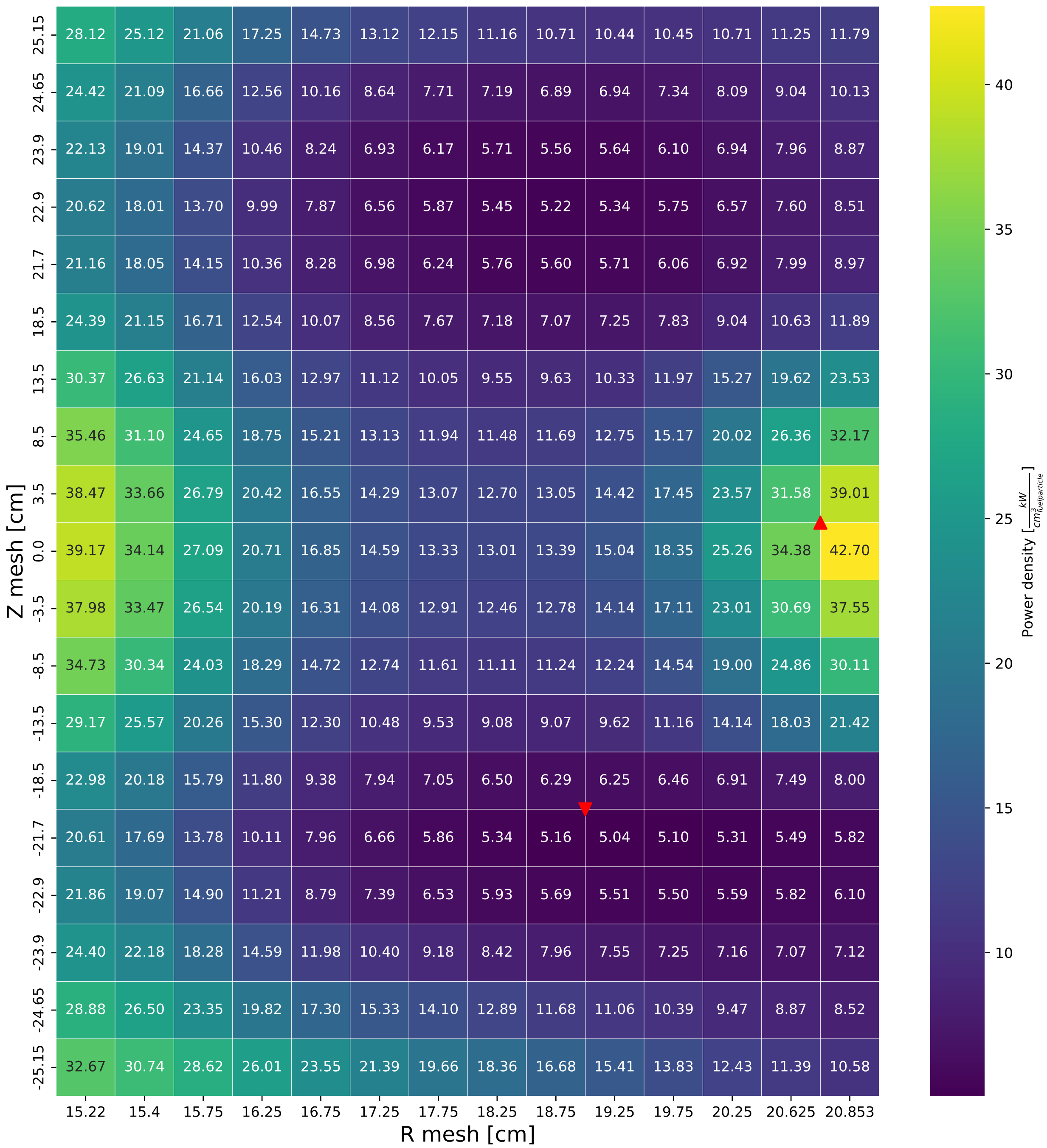

Figure 112. Power density distribution for cold design OFE region on day 0 (see Section 7.3.3).

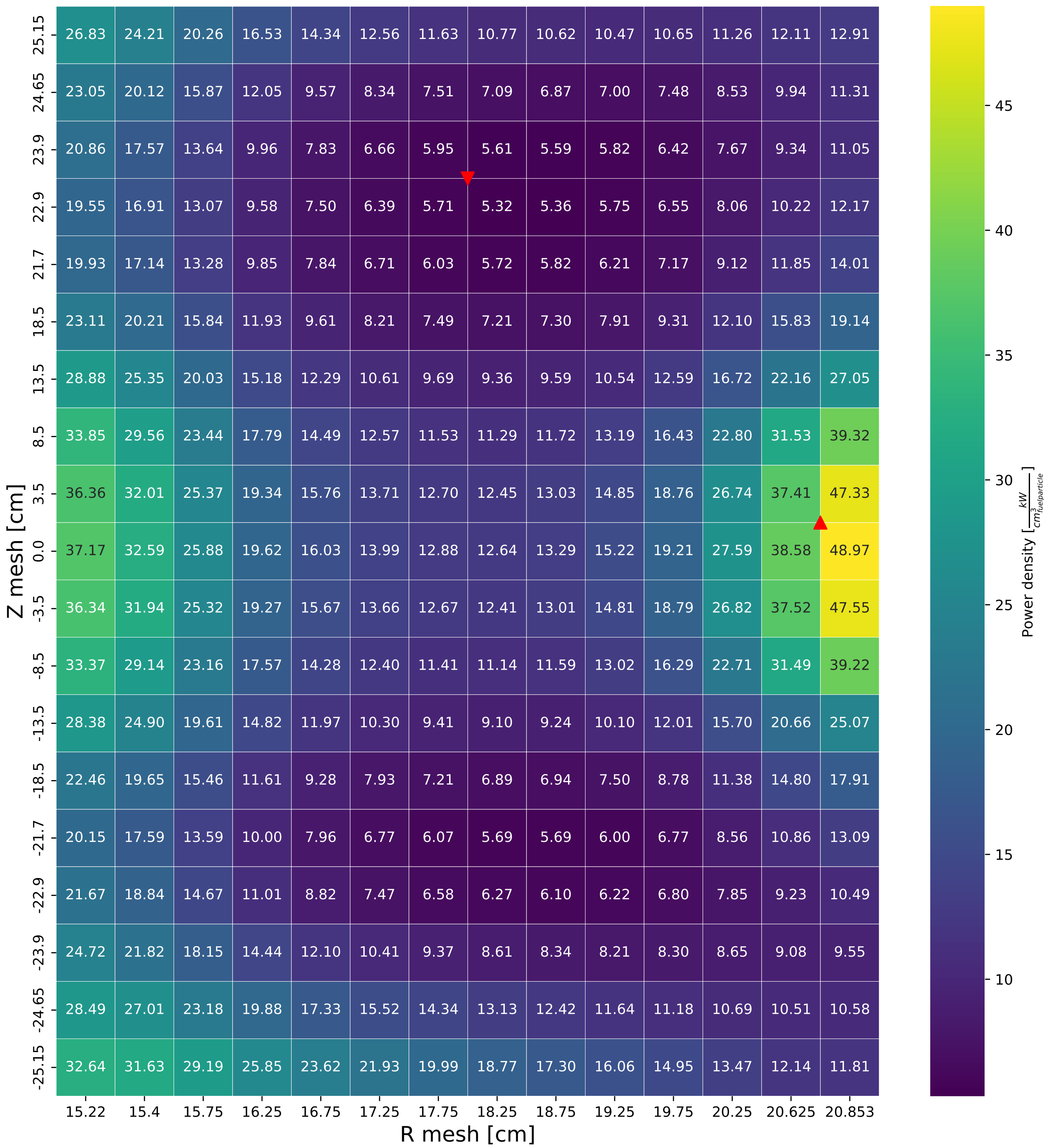

Figure 113. Power density distribution for cold design OFE region on day 1 (see Section 7.3.3).

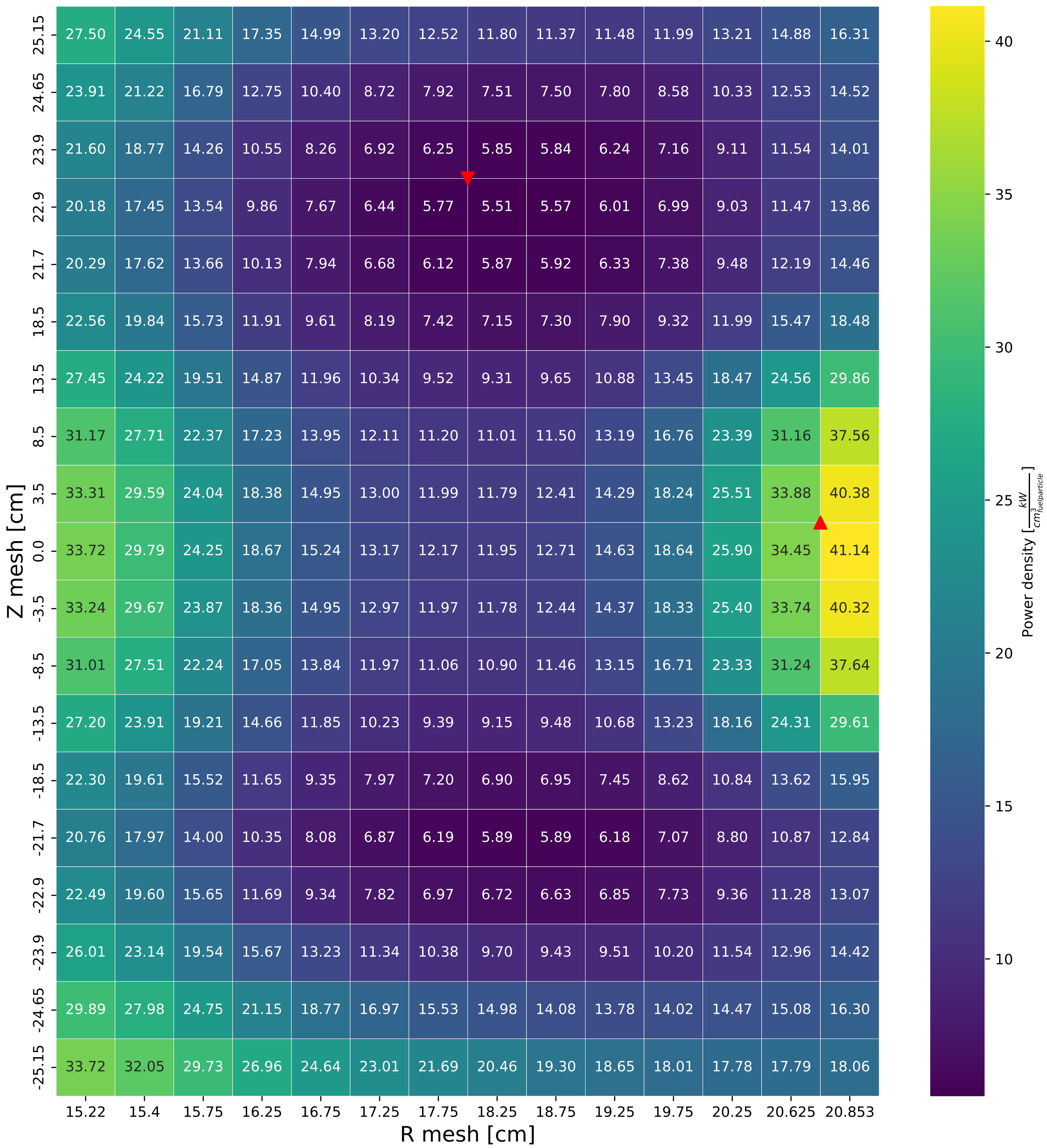

Figure 114. Power density distribution for cold design OFE region on day 15 (see Section 7.3.3).

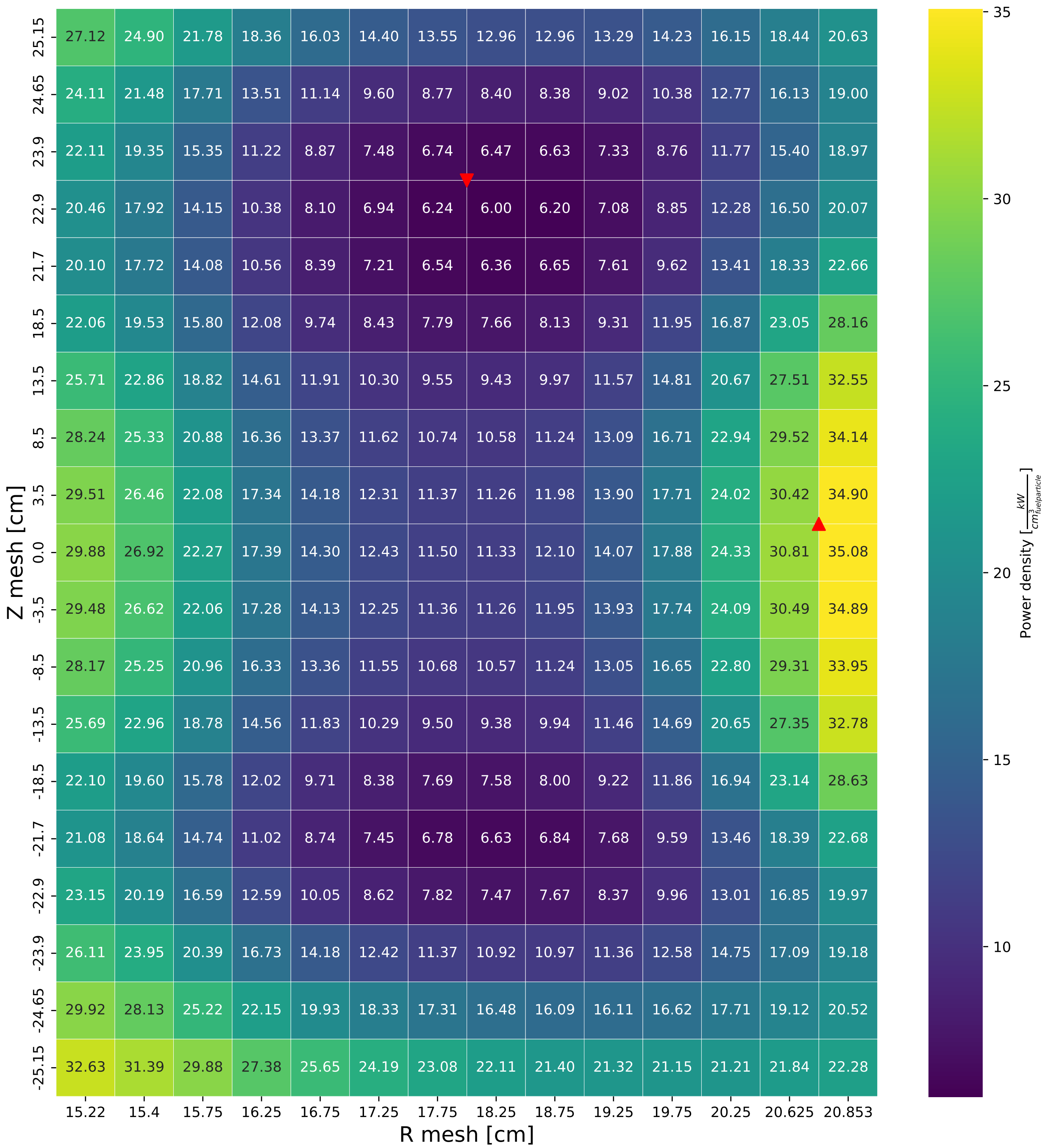

Figure 115. Power density distribution for cold design OFE region on day 26 (see Section 7.3.3).

APPENDIX C-4. HEAT FLUX DISTRIBUTIONS FOR COLD DESIGN

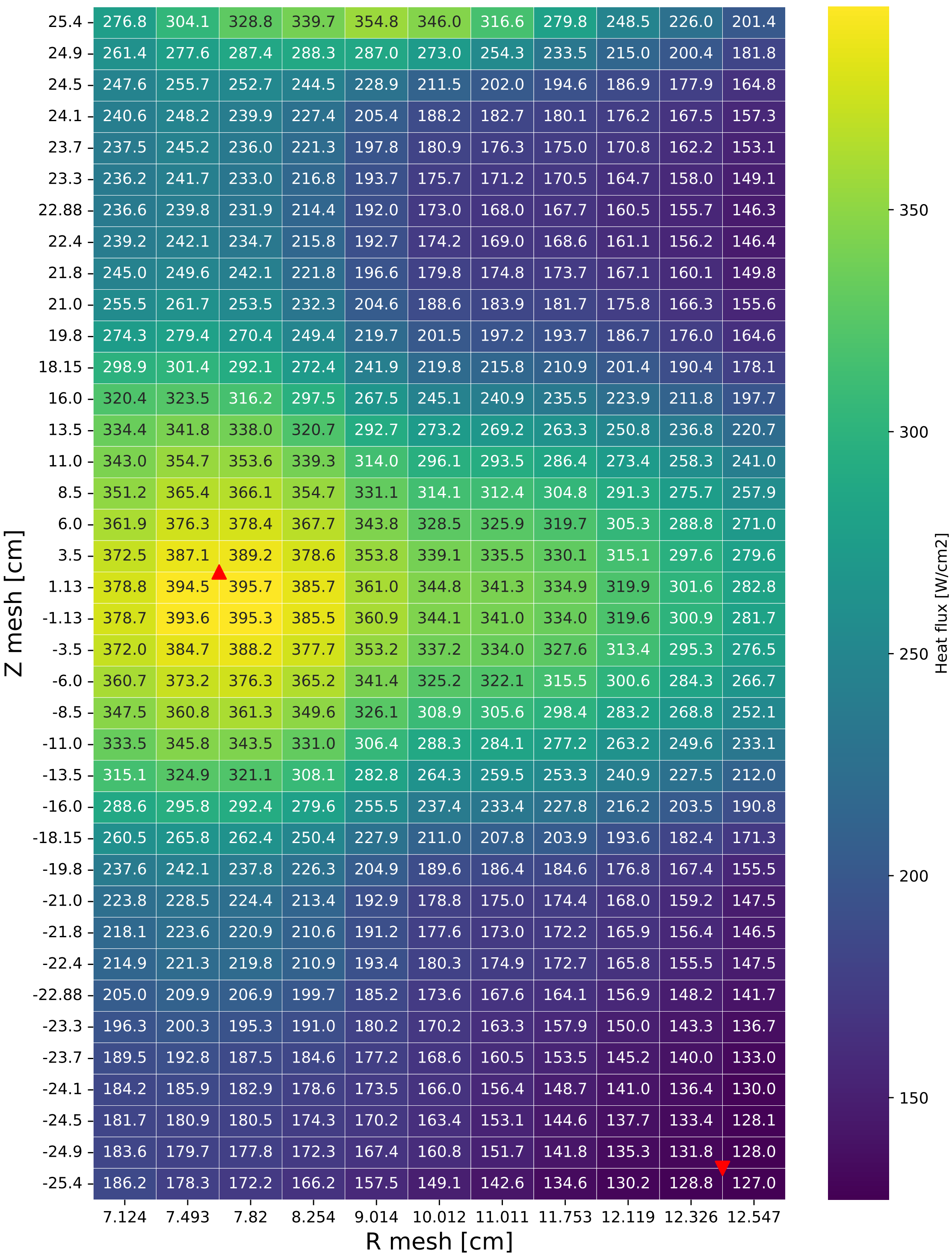

Figure 116. Heat flux distribution for cold design IFE region on day 0 (see Section 7.3.4).

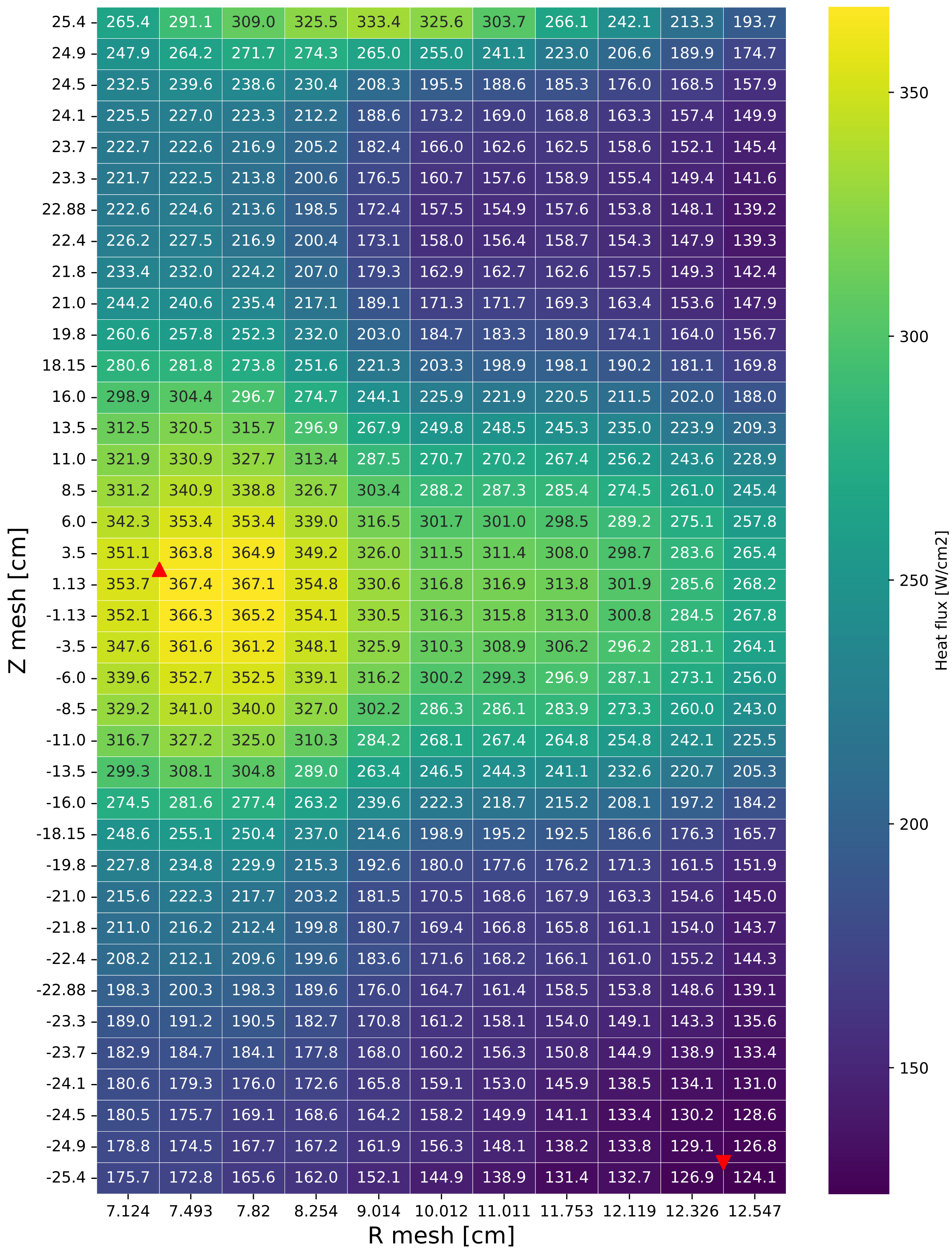

Figure 117. Heat flux distribution for cold design IFE region on day 1 (see Section 7.3.4).

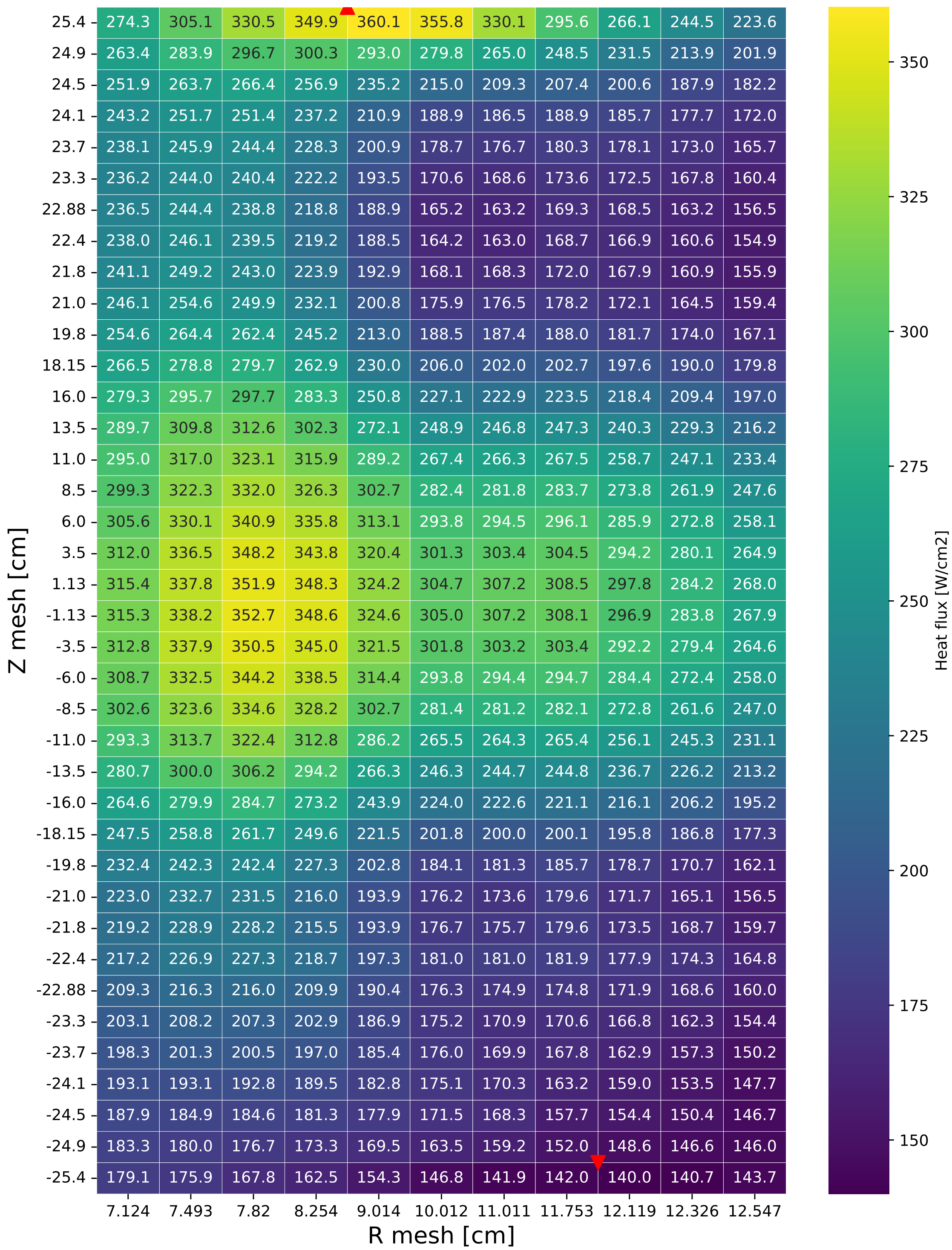

Figure 118. Heat flux distribution for cold design IFE region on day 15 (see Section 7.3.4).

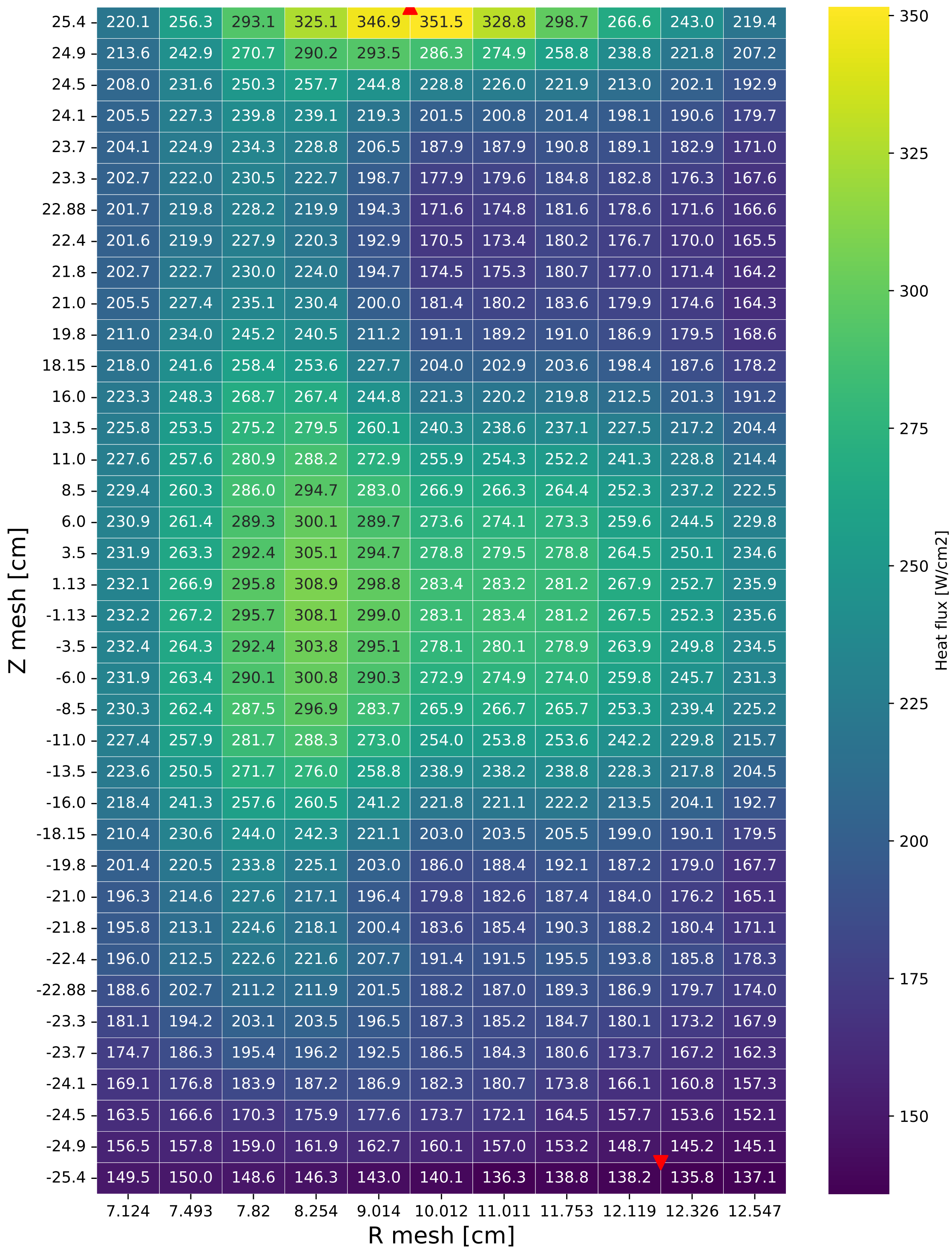

Figure 119. Heat flux distribution for cold design IFE region on day 28 (see Section 7.3.4).

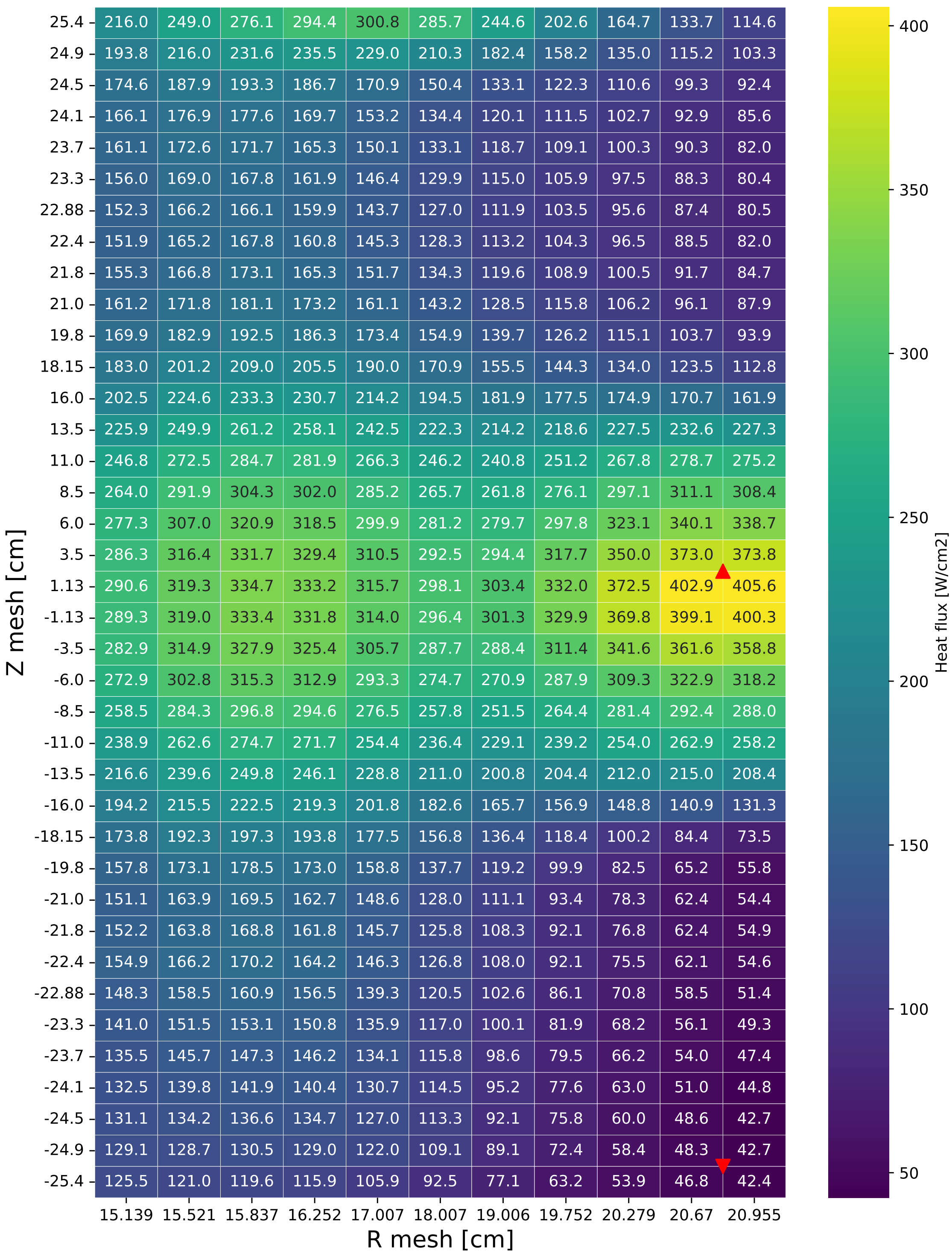

Figure 120. Heat flux distribution for cold design OFE region on day 0 (see Section 7.3.4).

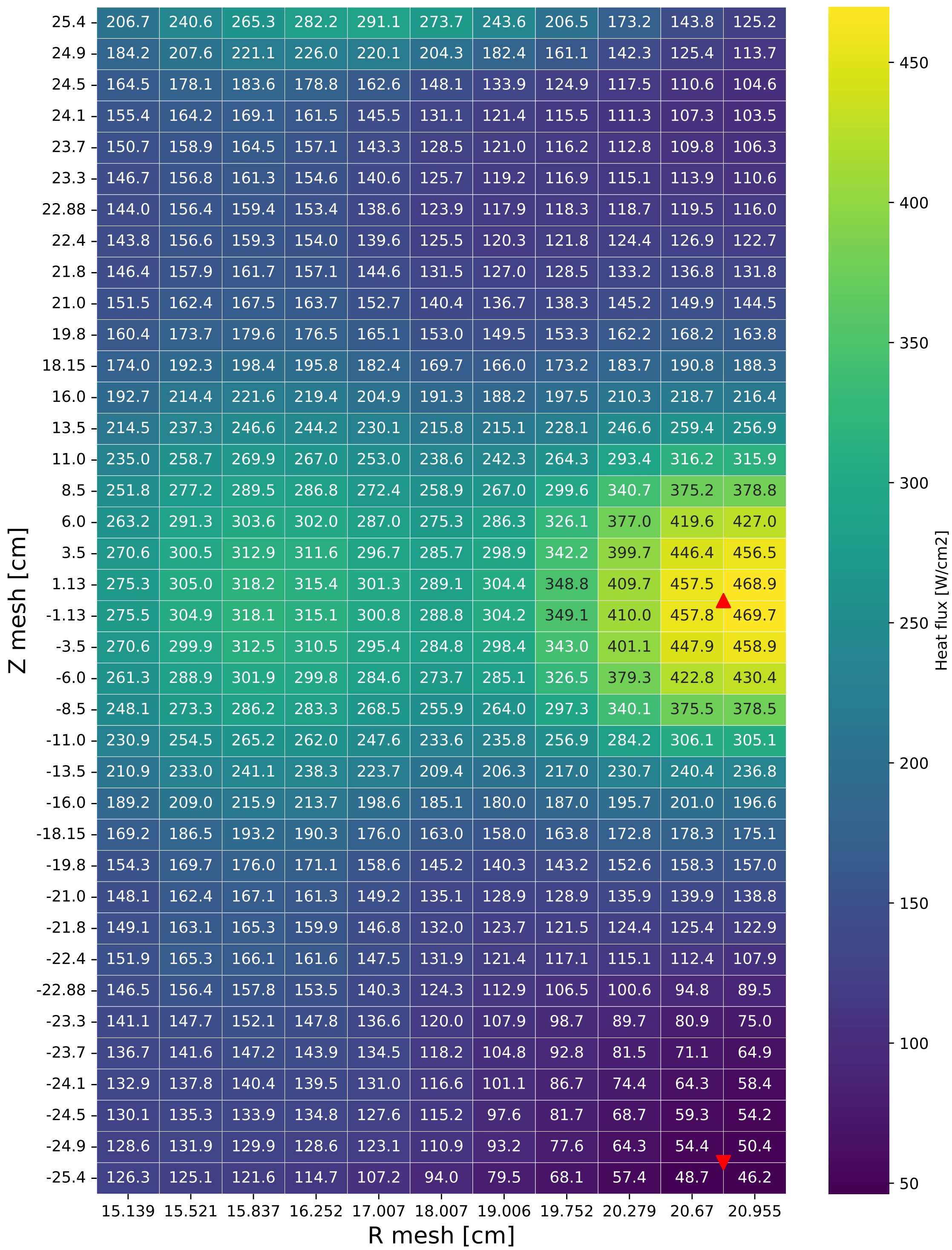

Figure 121. Heat flux distribution for cold design OFE region on day 1 (see Section 7.3.4).

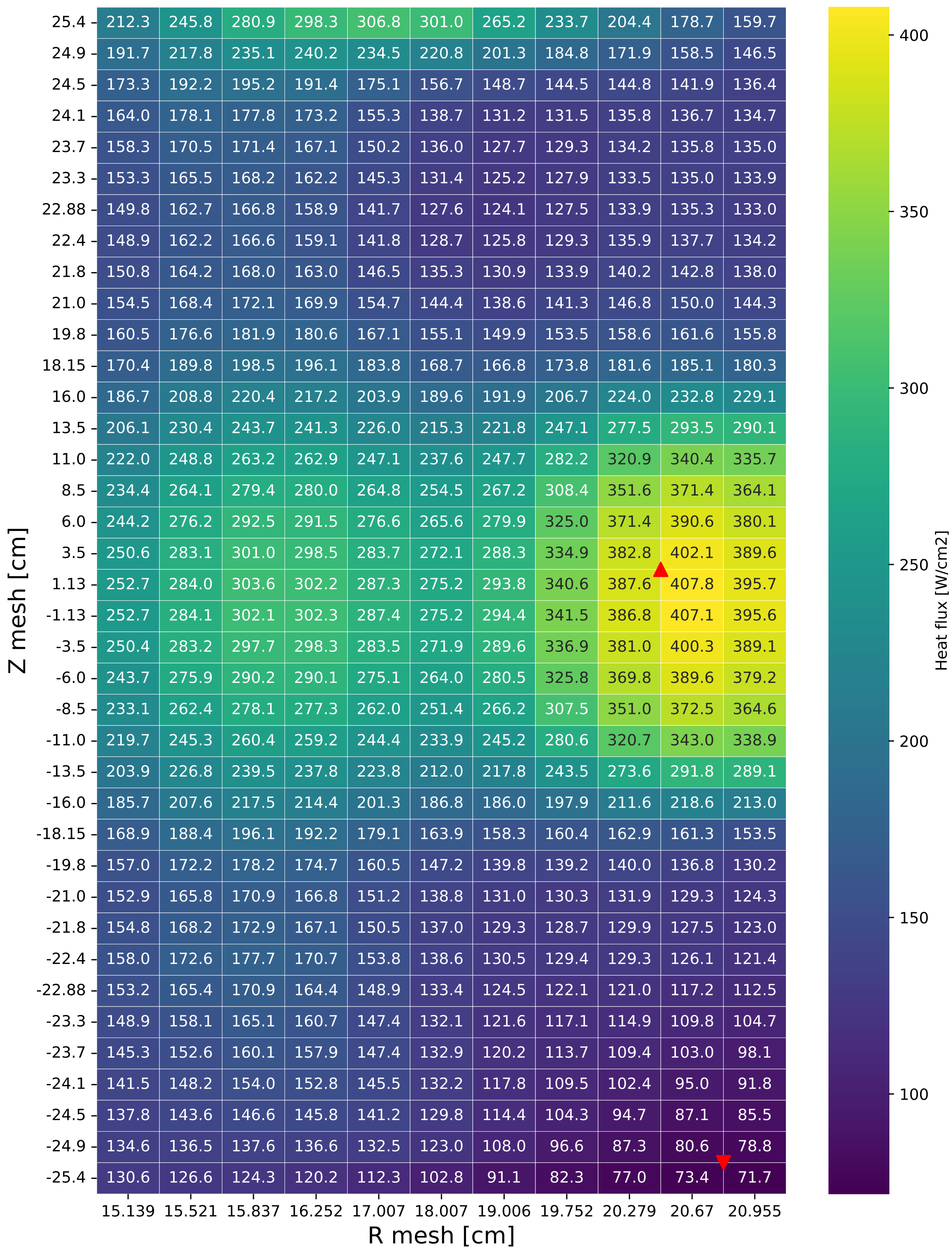

Figure 122. Heat flux distribution for cold design OFE region on day 15 (see Section 7.3.4).

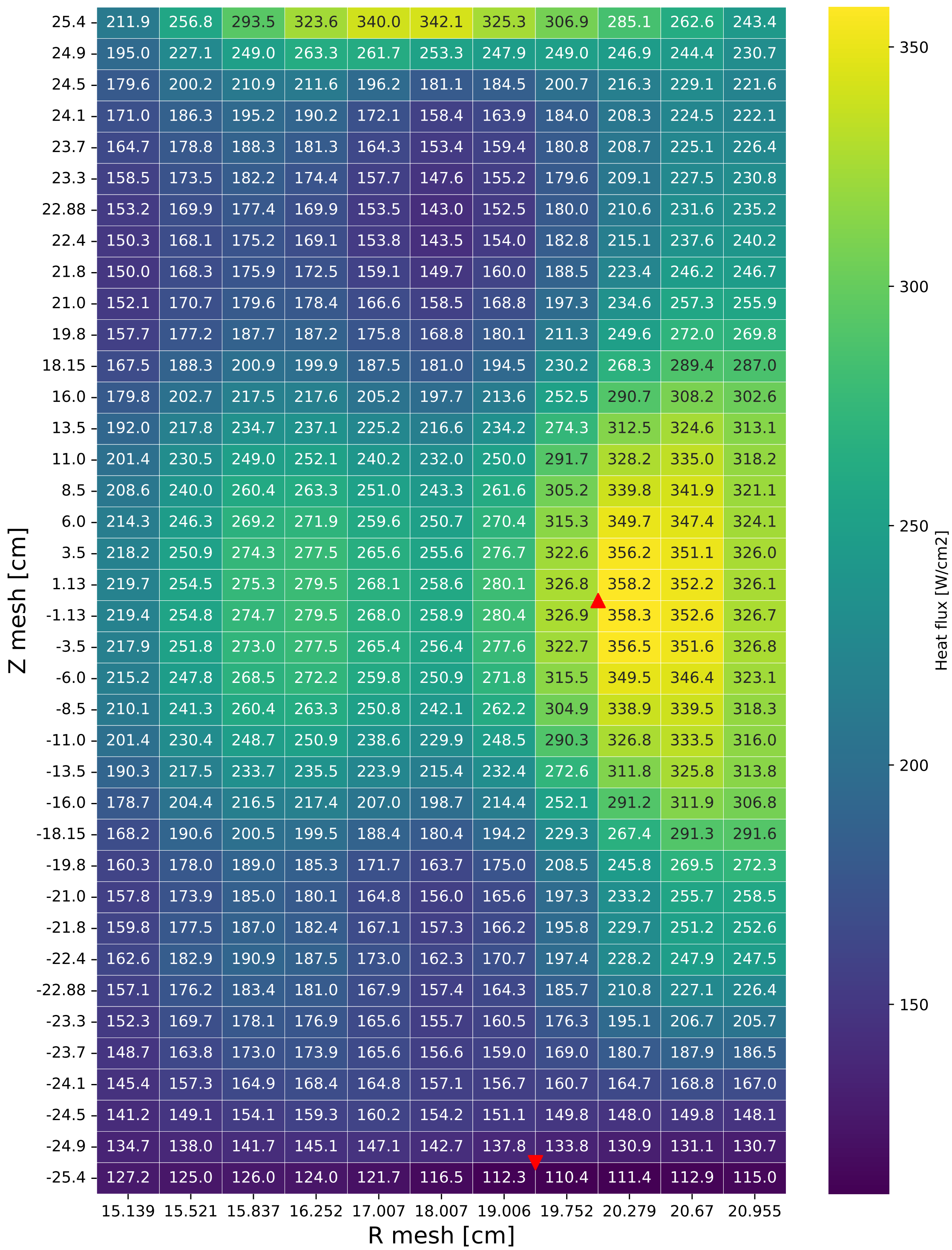

Figure 123. Heat flux distribution for cold design OFE region on day 28 (see Section 7.3.4).

APPENDIX D. DISTRIBUTIONS FOR BORON-CLAD DESIGN

APPENDIX D-1. FISSION RATE DENSITY DISTRIBUTIONS FOR BORON-CLAD DESIGN

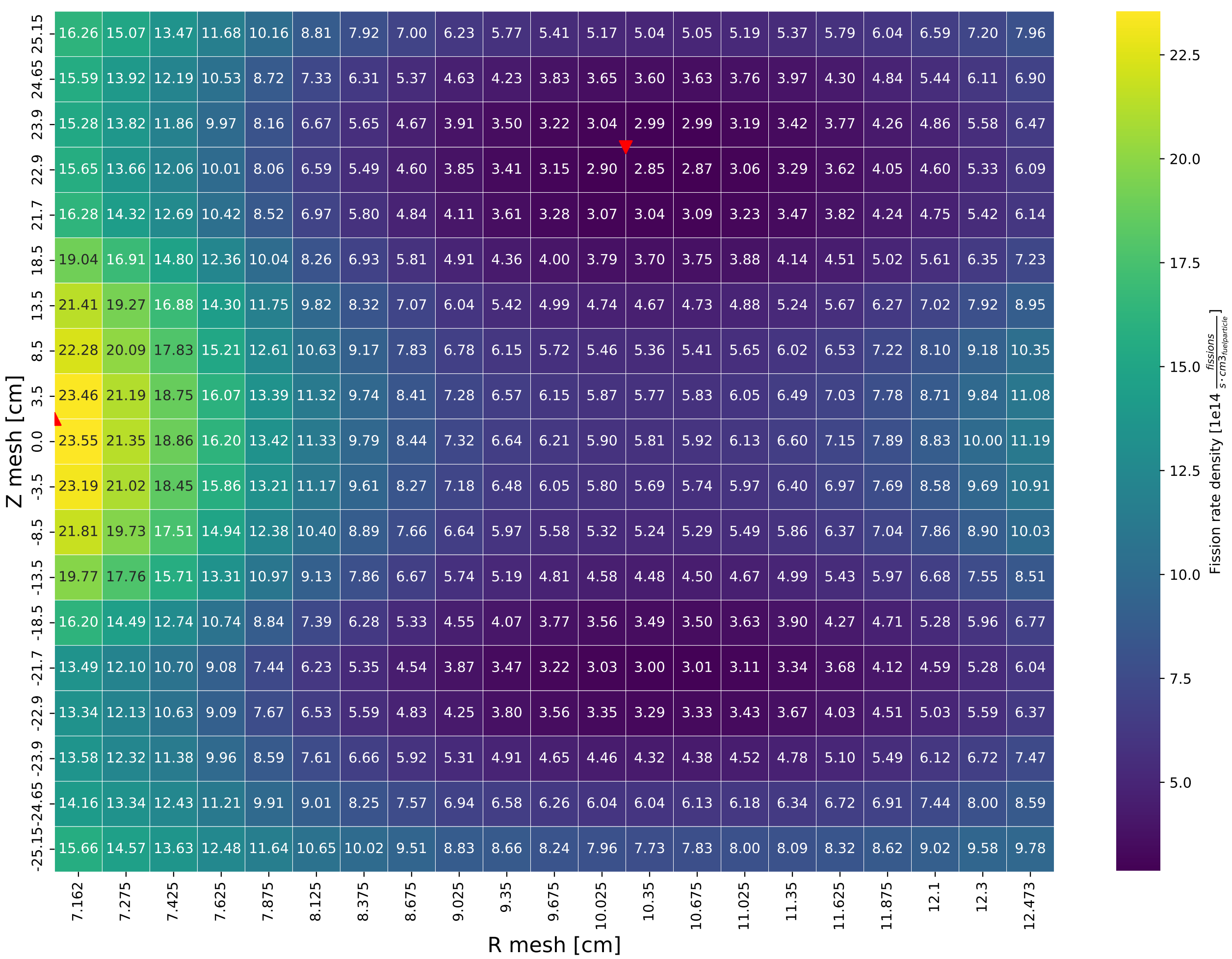

Figure 124. Fission rate density distribution for boron-clad design IFE region on day 0 (see Section 7.4.2).

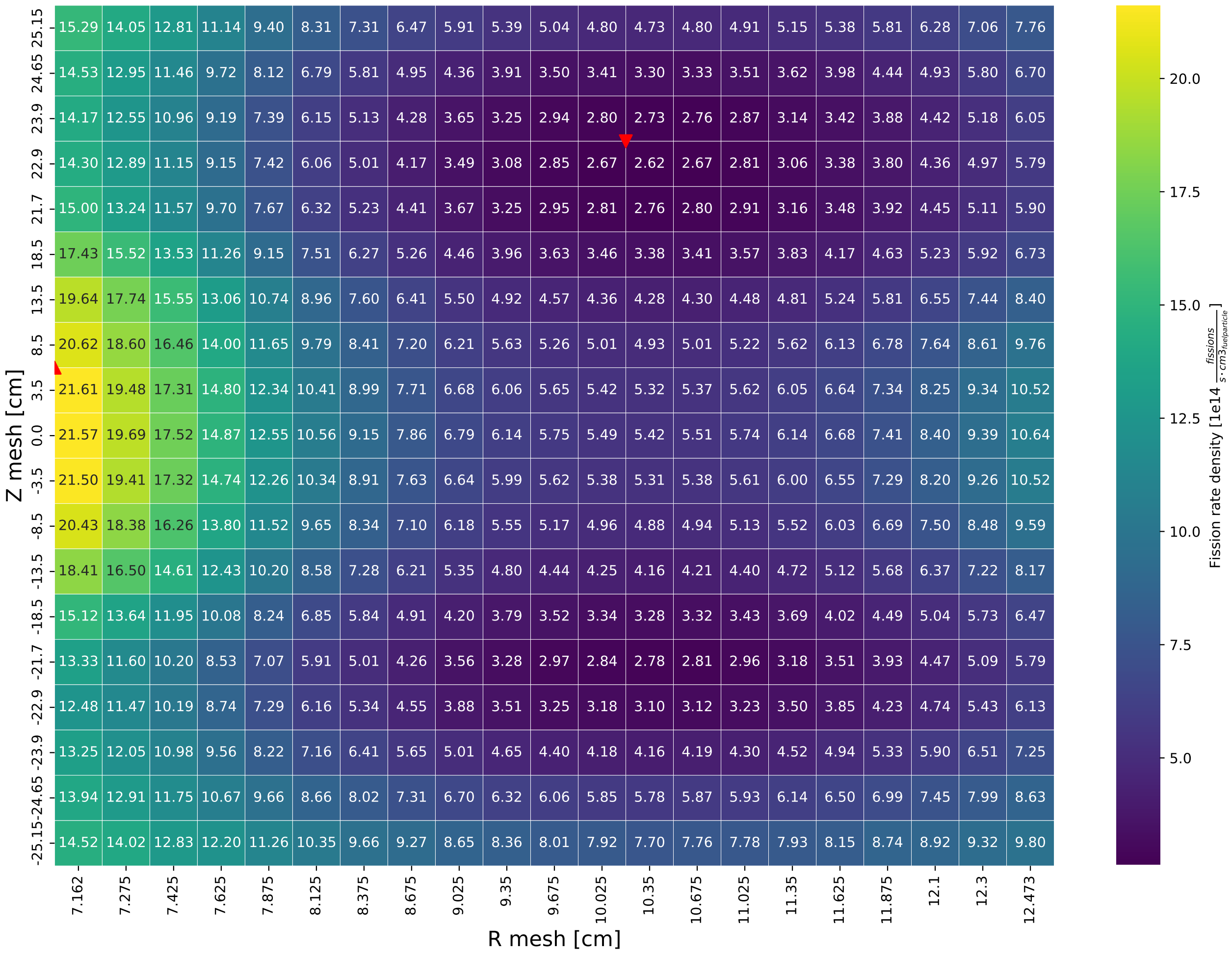

Figure 125. Fission rate density distribution for boron-clad design IFE region on day 1 (see Section 7.4.2).

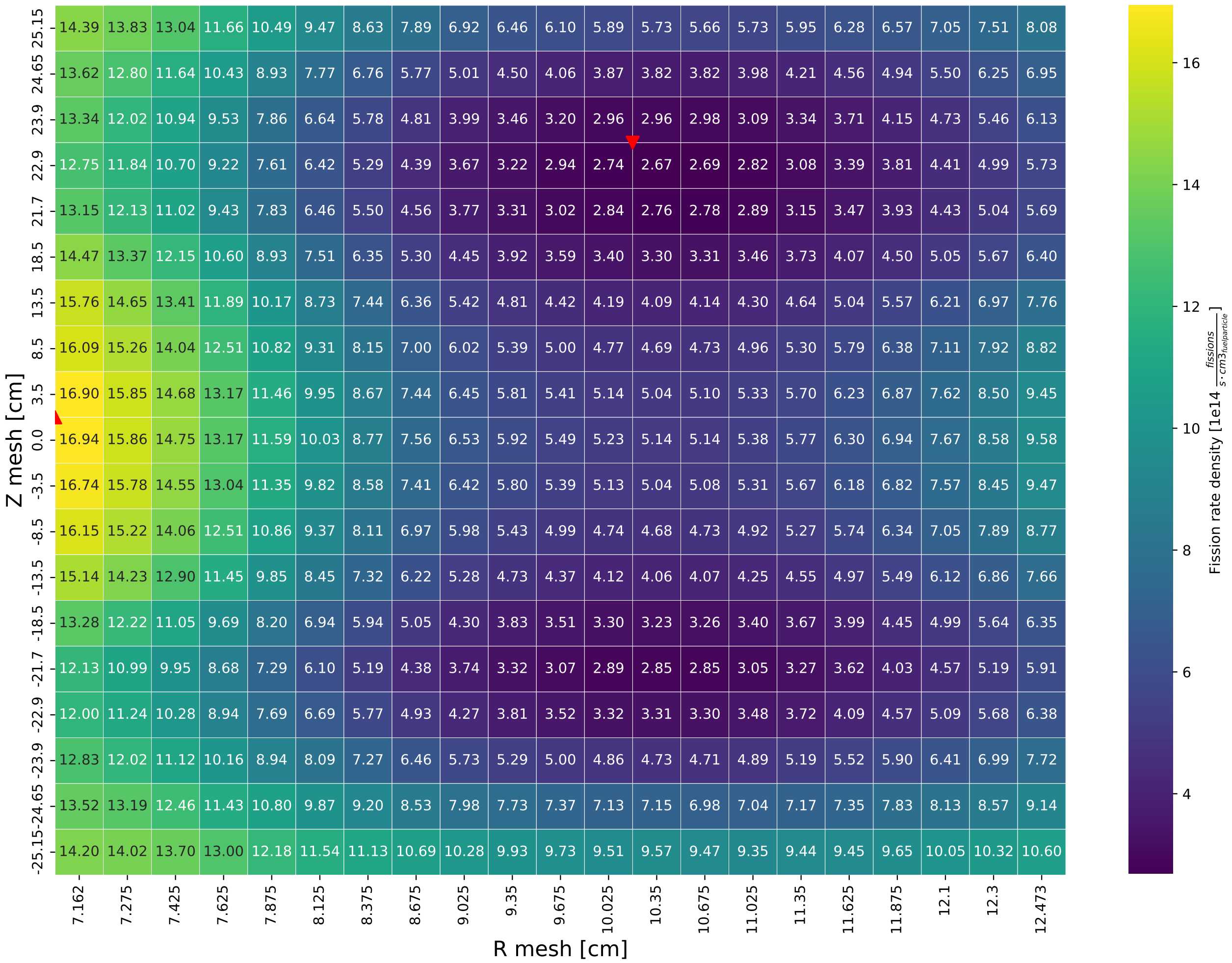

Figure 126. Fission rate density distribution for boron-clad design IFE region on day 15 (see Section 7.4.2).

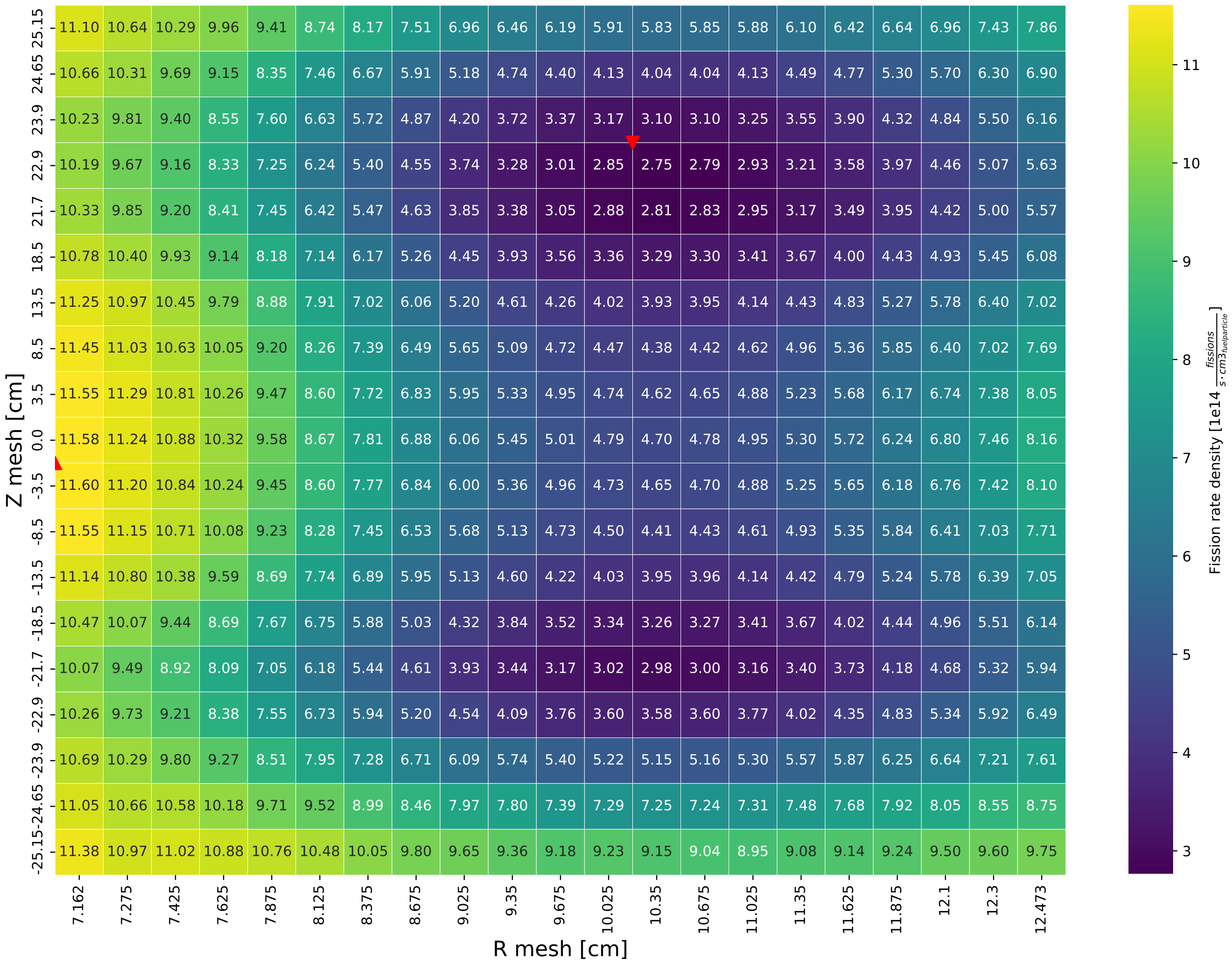

Figure 127. Fission rate density distribution for boron-clad design IFE region on day 31 (see Section 7.4.2).

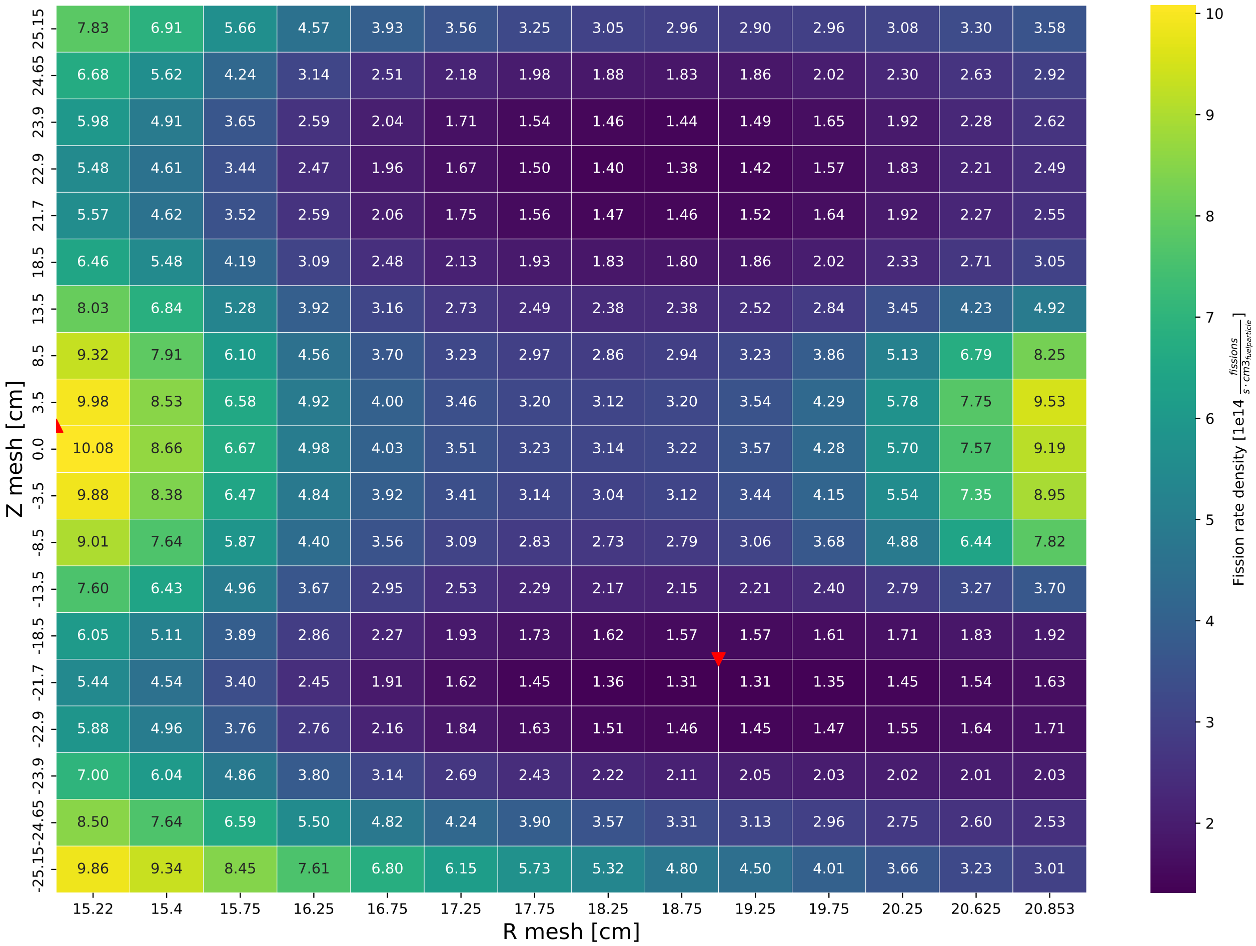

Figure 128. Fission rate density distribution for boron-clad design OFE region on day 0 (see Section 7.4.2).

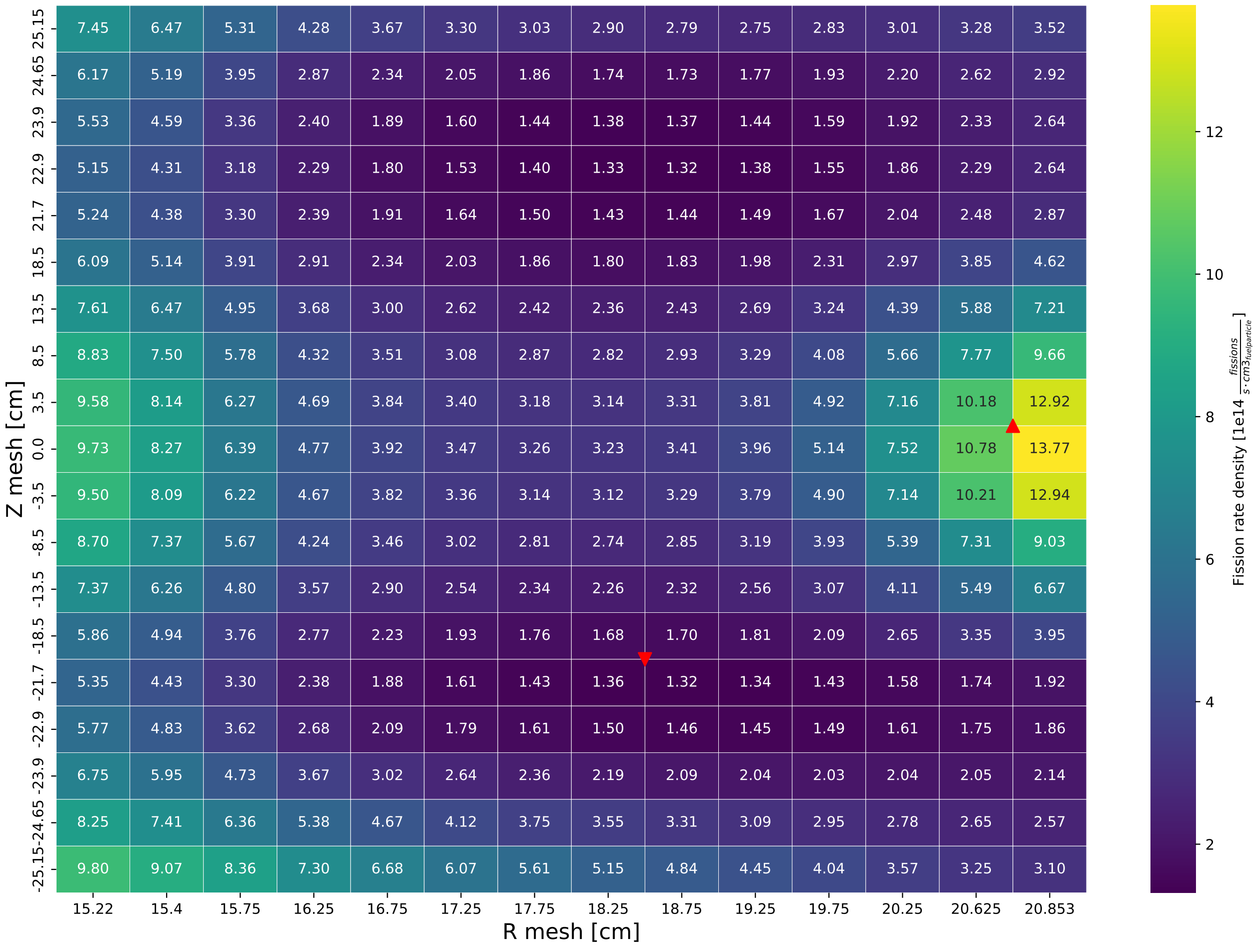

Figure 129. Fission rate density distribution for boron-clad design OFE region on day 1 (see Section 7.4.2).

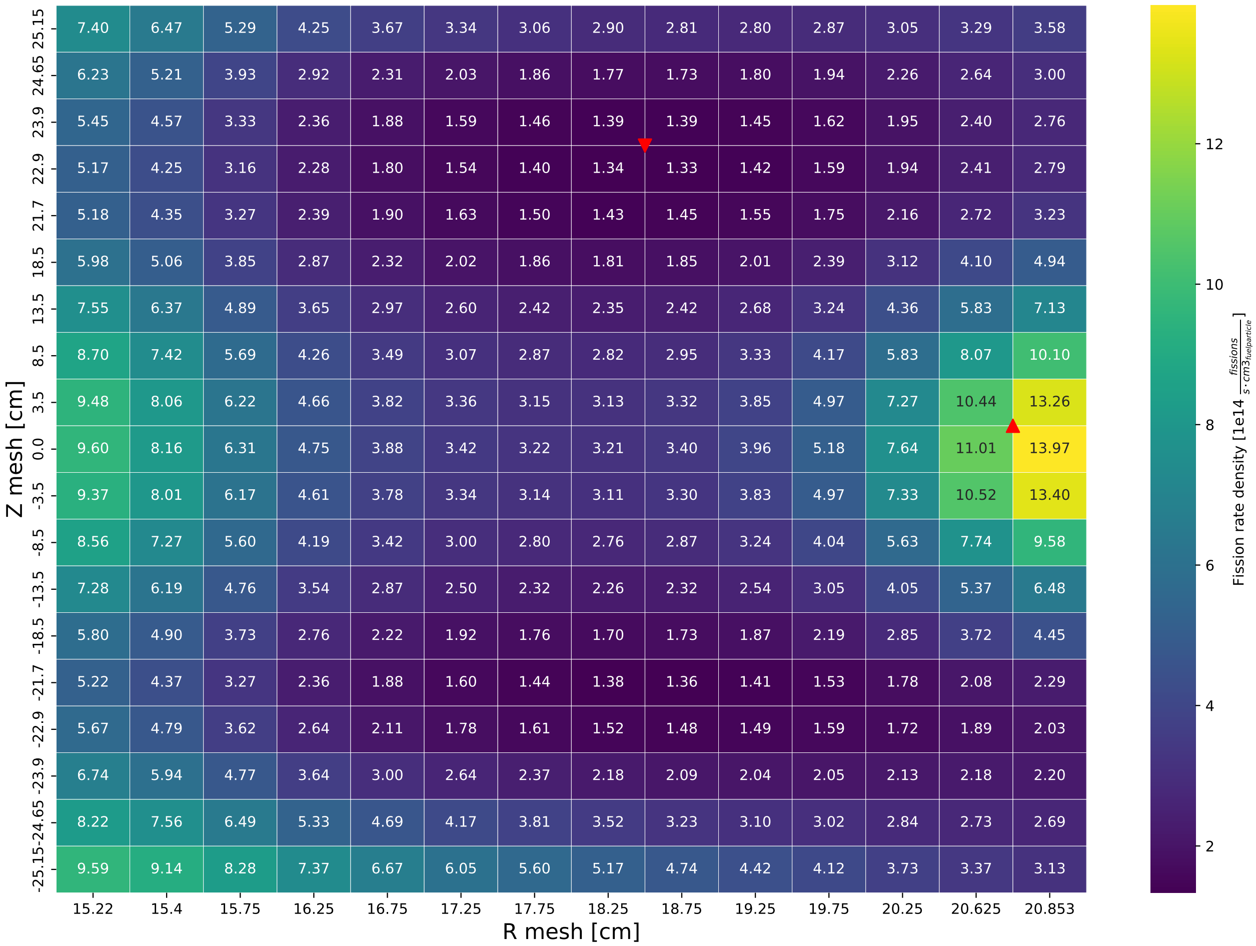

Figure 130. Fission rate density distribution for boron-clad design OFE region on day 2 (see Section 7.4.2).

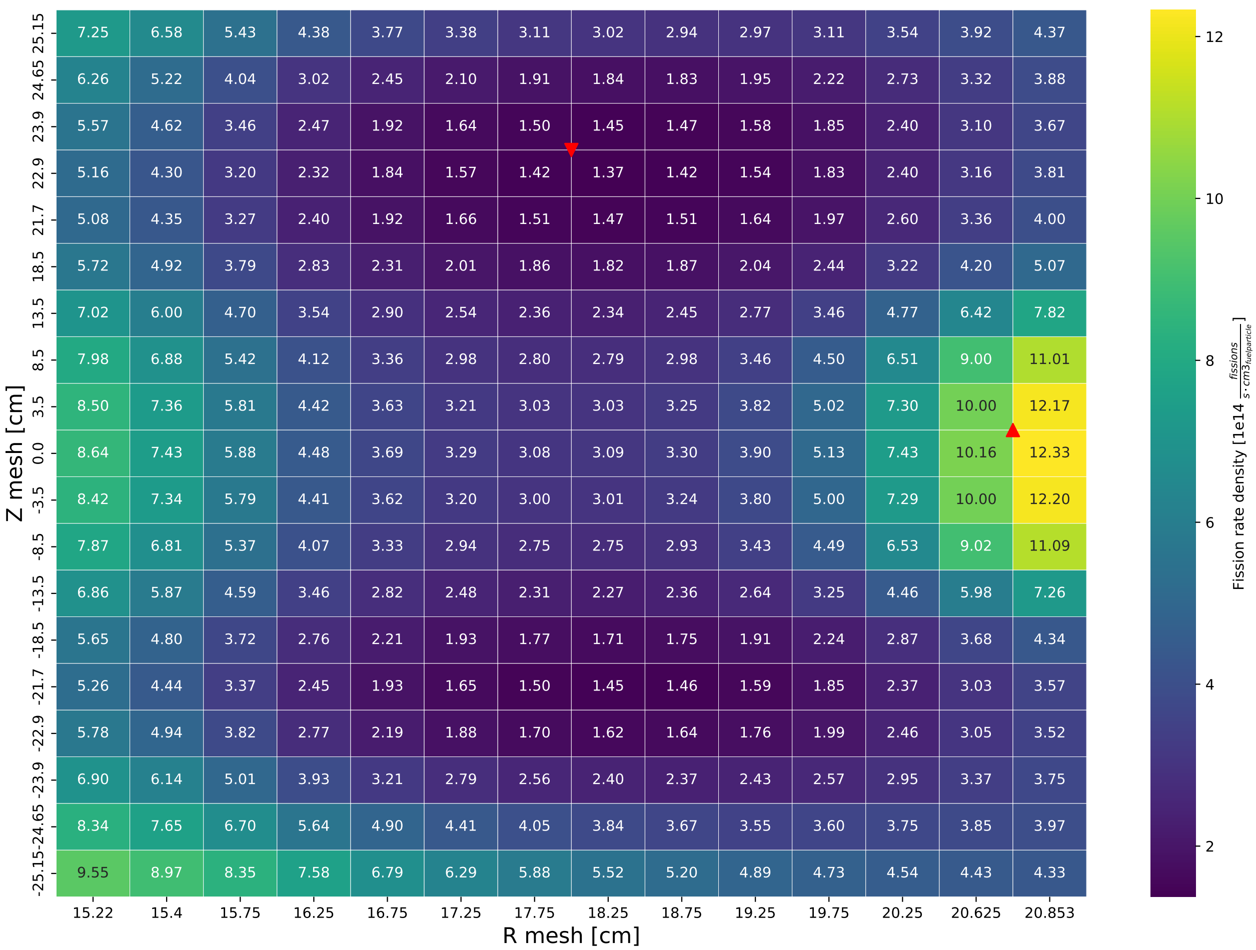

Figure 131. Fission rate density distribution for boron-clad design OFE region on day 15 (see Section 7.4.2).

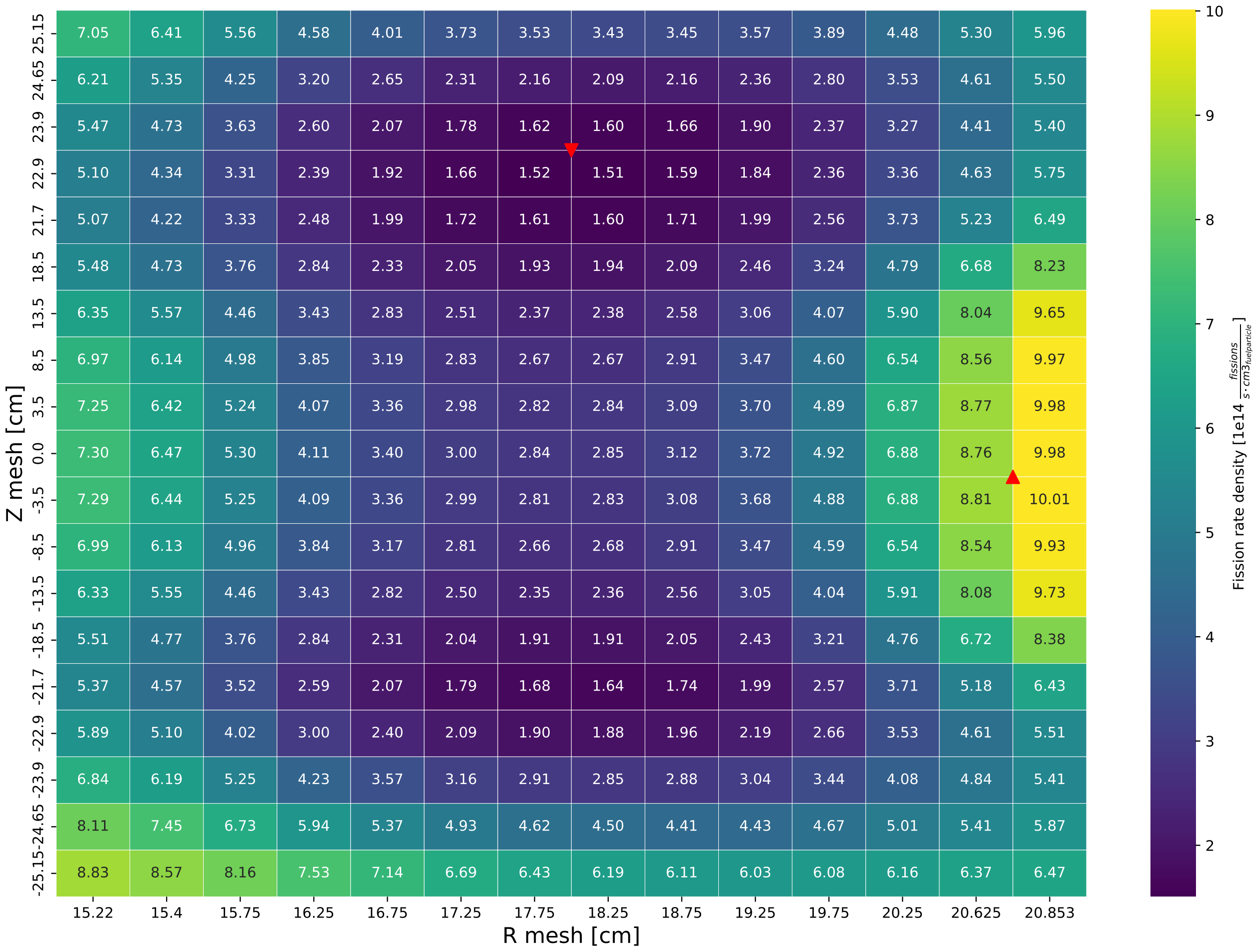

Figure 132. Fission rate density distribution for boron-clad design OFE region on day 31 (see Section 7.4.2).

APPENDIX D-2. CUMULATIVE FISSION DENSITY DISTRIBUTIONS FOR BORON-CLAD DESIGN

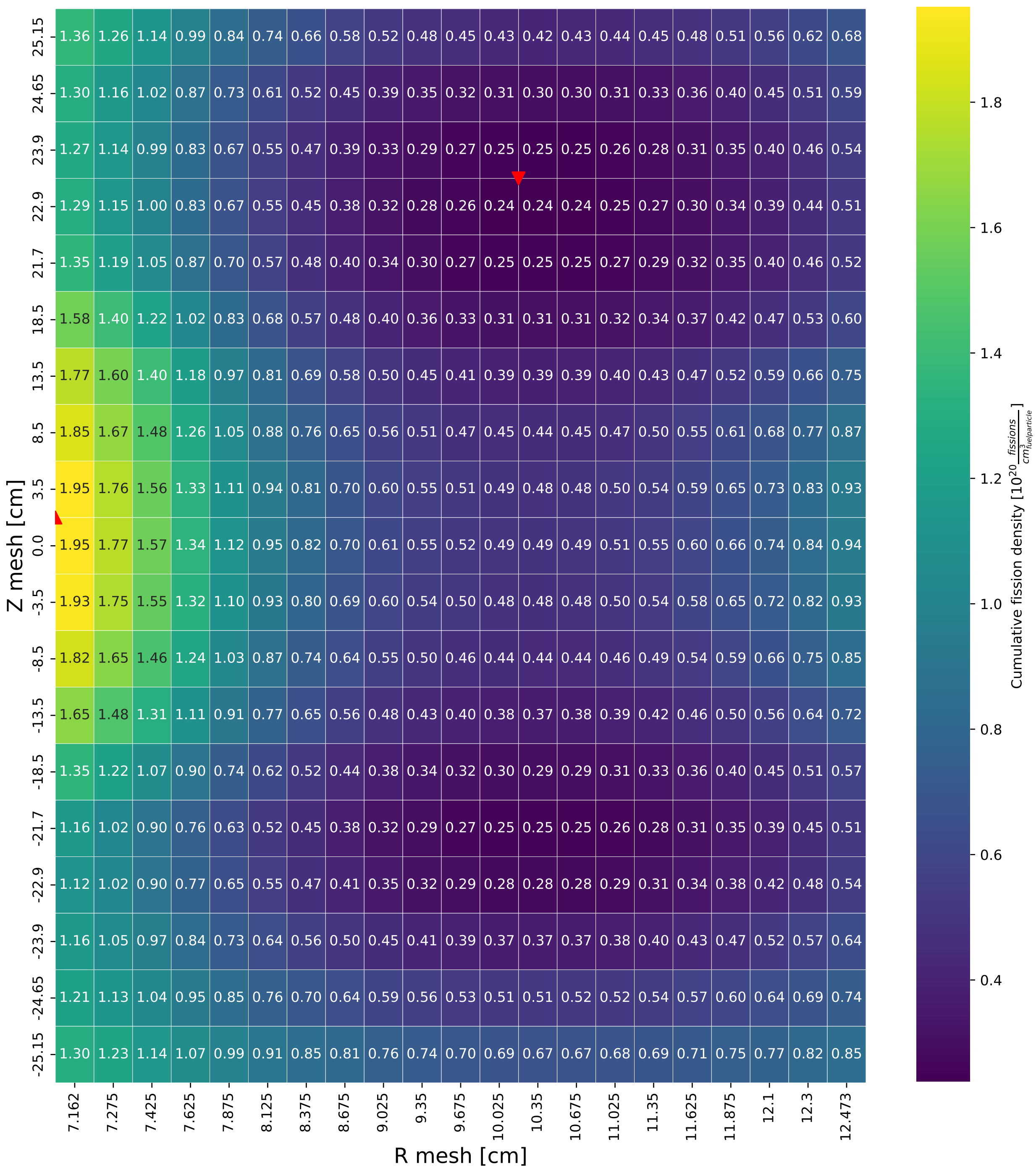

Figure 133. Cumulative fission density distribution for boron-clad design IFE region on day 1 (see Section 7.4.5).

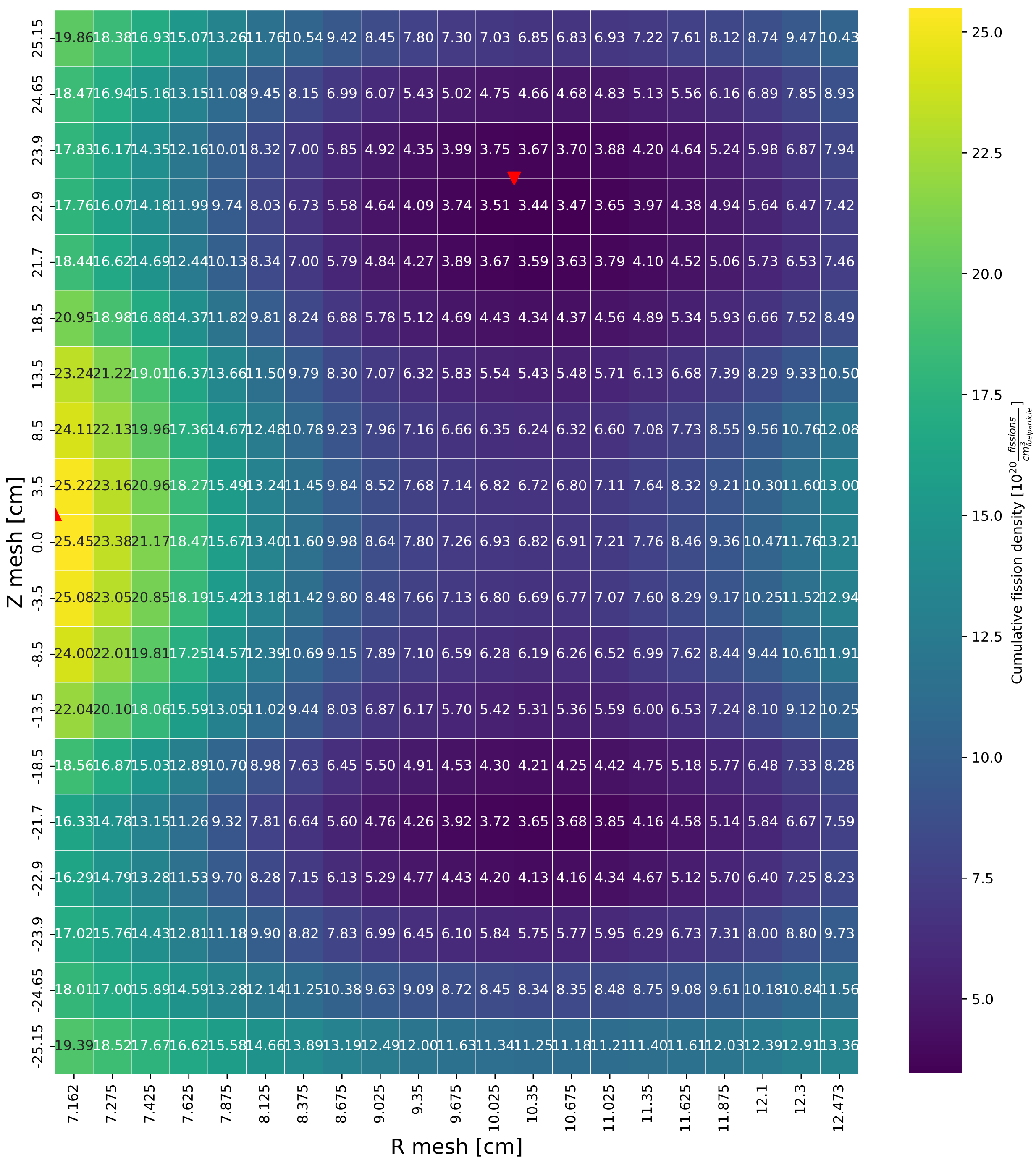

Figure 134. Cumulative fission density distribution for boron-clad design IFE region on day 15 (see Section 7.4.5).

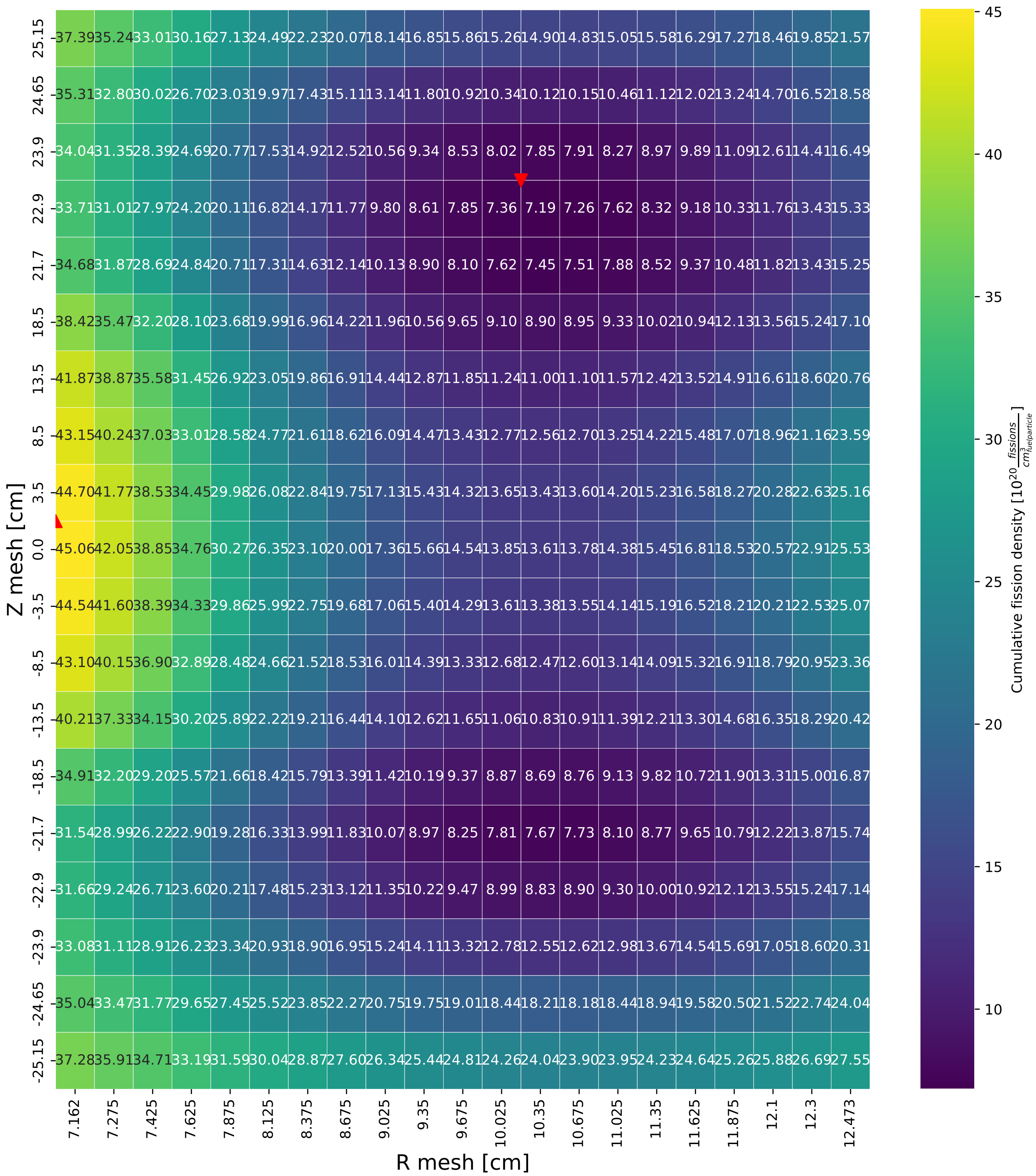

Figure 135. Cumulative fission density distribution for boron-clad design IFE region on day 31 (see Section 7.4.5).

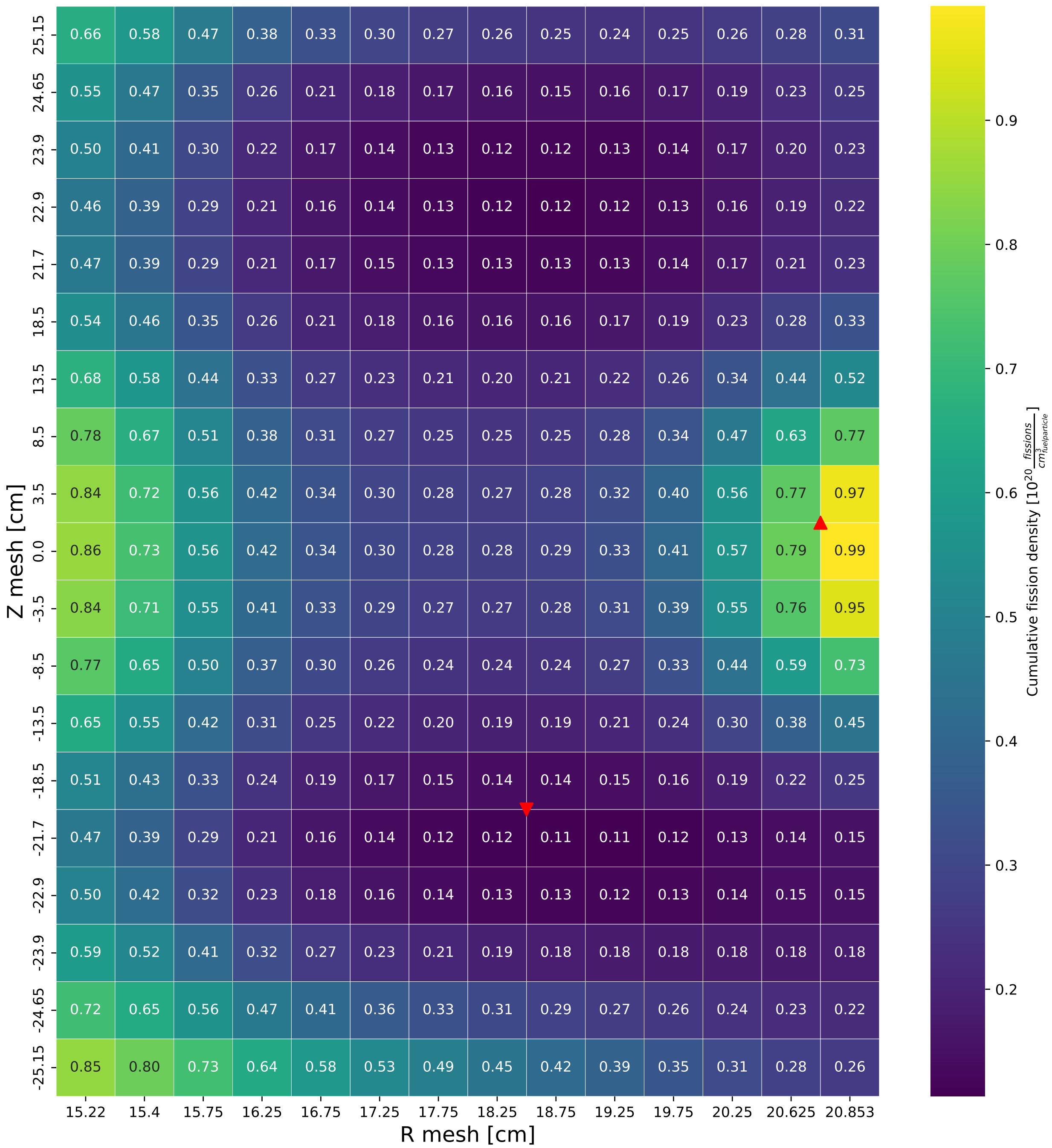

Figure 136. Cumulative fission density distribution for boron-clad design OFE region on day 1 (see Section 7.4.5).

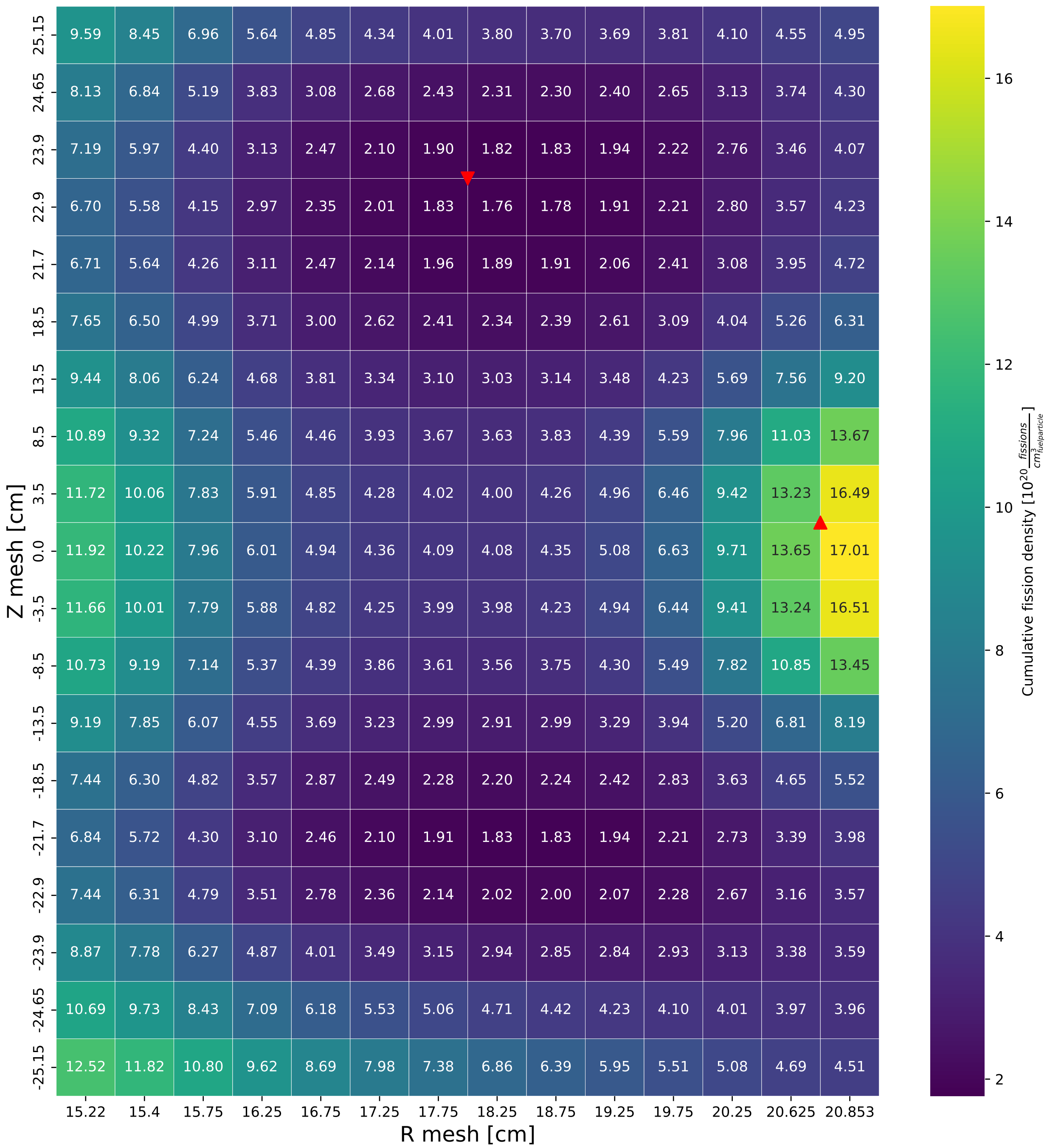

Figure 137. Cumulative fission density distribution for boron-clad design OFE region on day 15 (see Section 7.4.5).

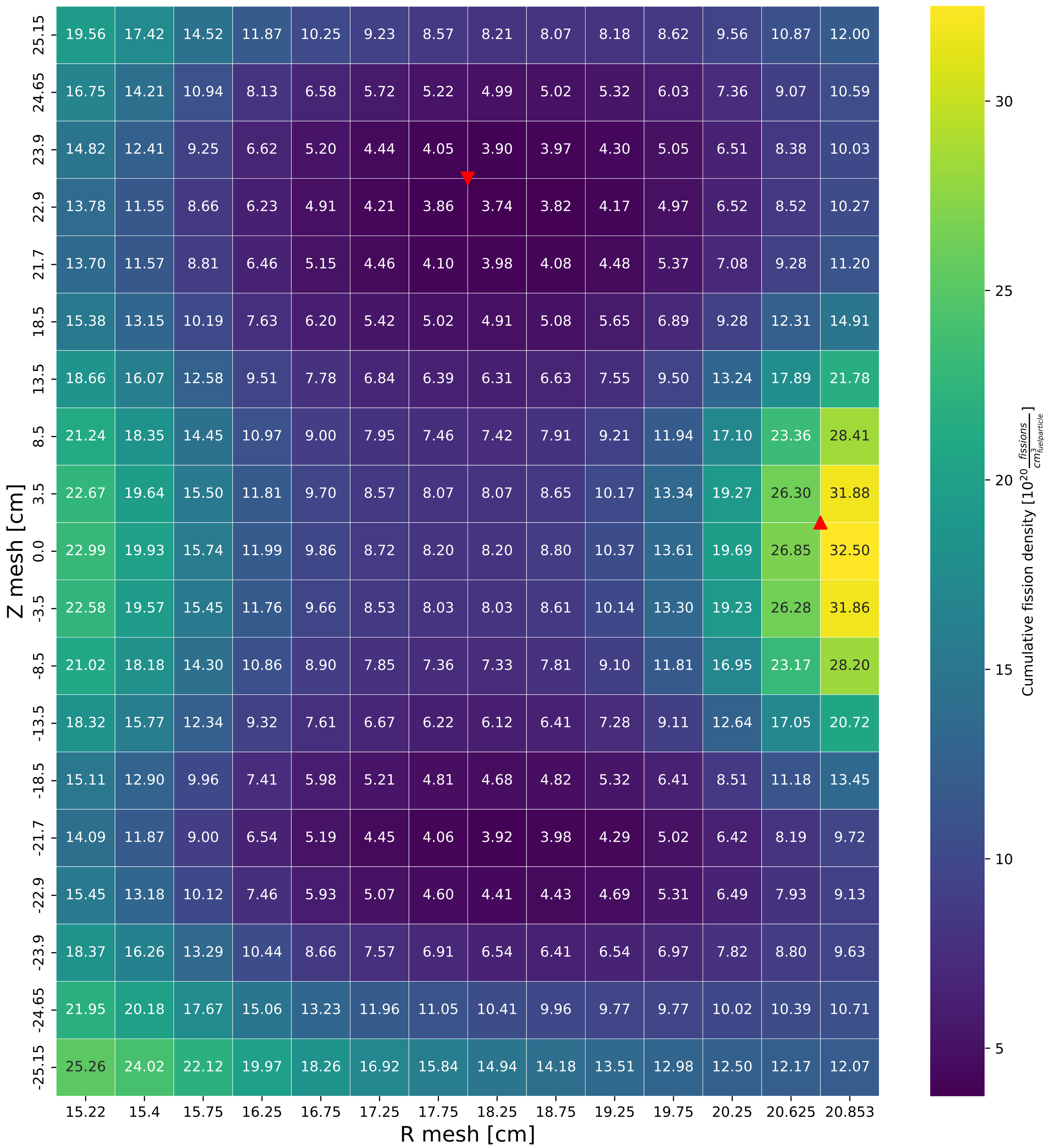

Figure 138. Cumulative fission density distribution for boron-clad design OFE region on day 31 (see Section 7.4.5).

APPENDIX D-3. POWER DENSITY DISTRIBUTIONS FOR BORON-CLAD DESIGN

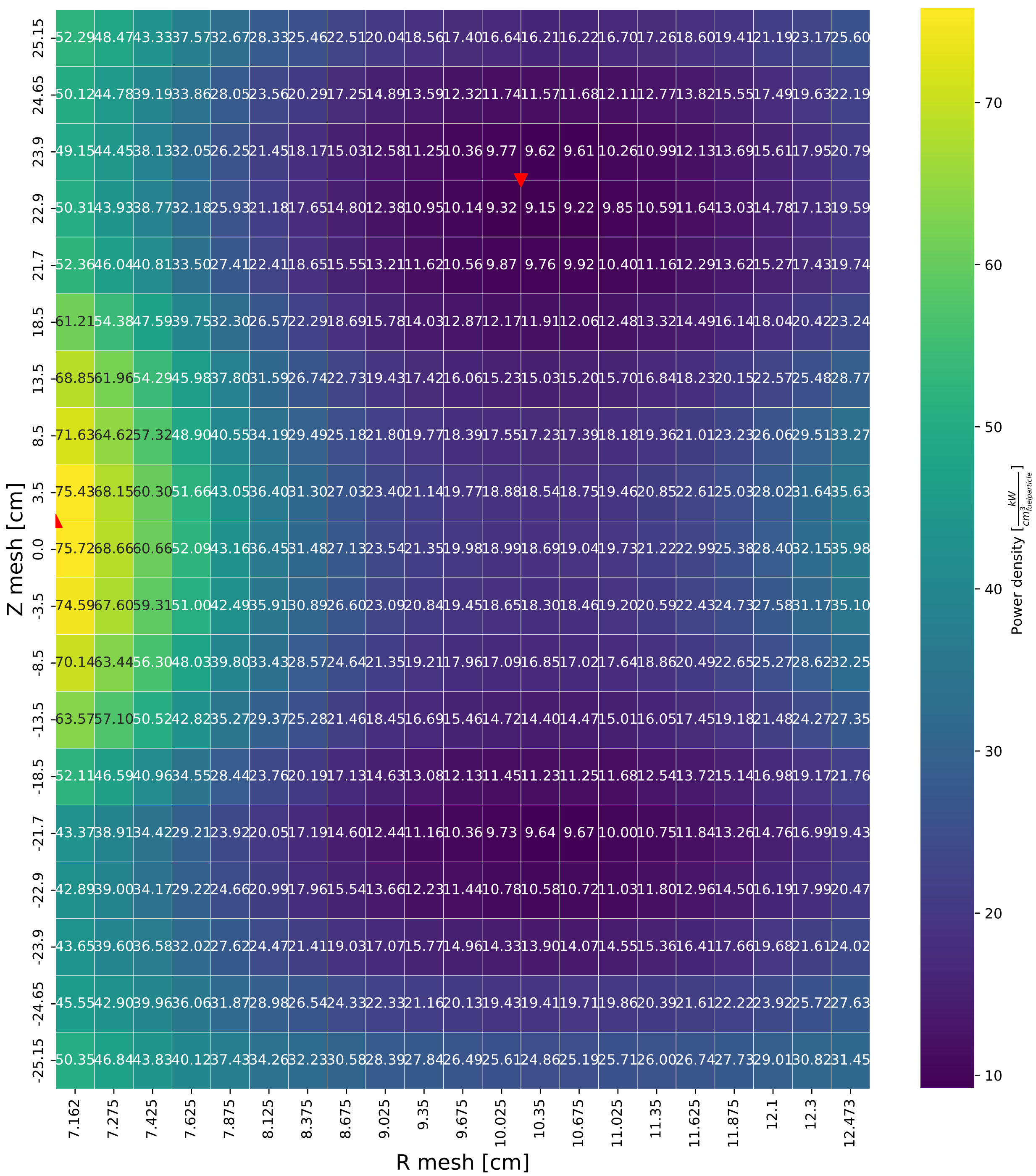

Figure 139. Power density distribution for boron-clad design IFE region on day 0 (see Section 7.4.3).

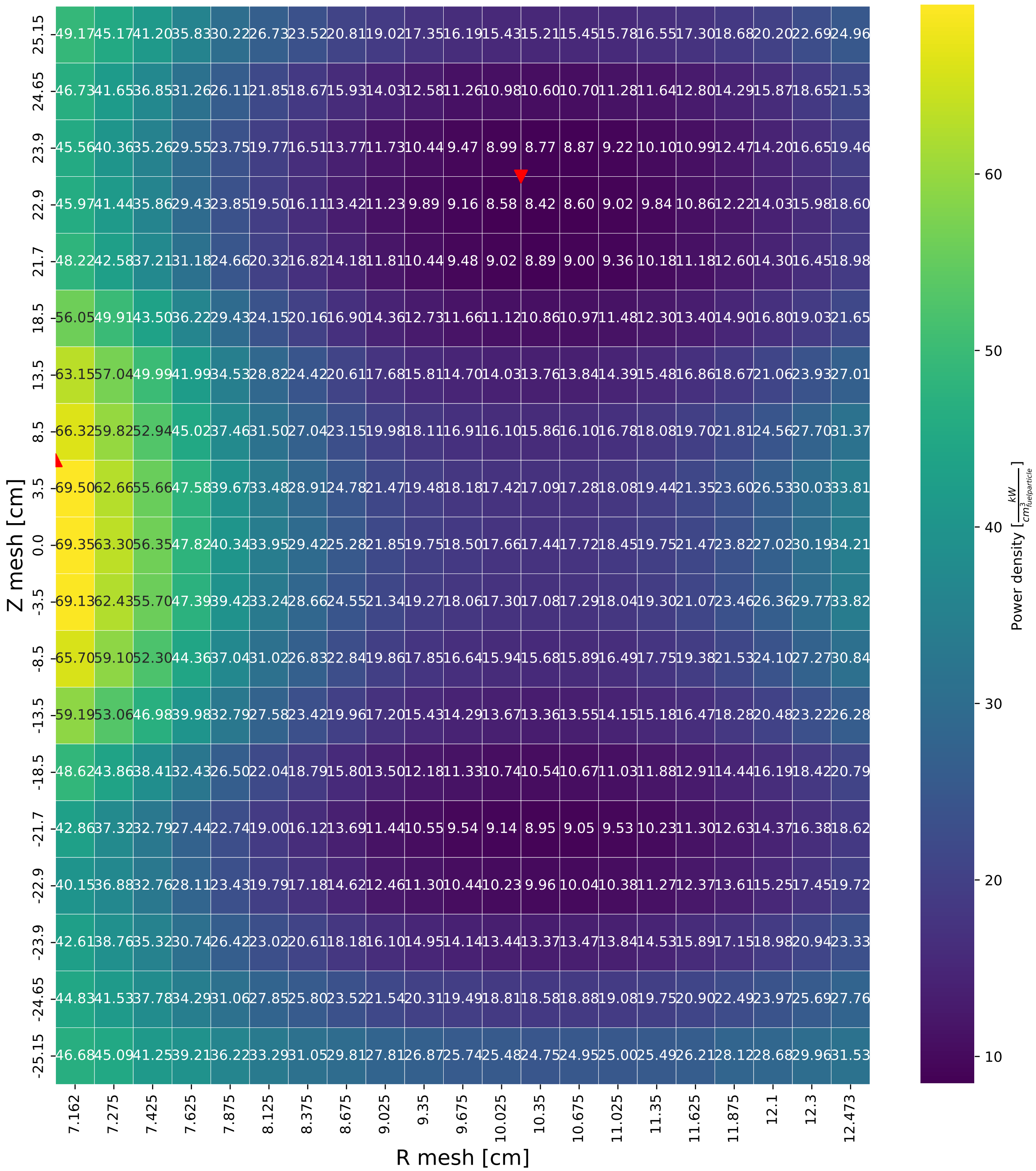

Figure 140. Power density distribution for boron-clad design IFE region on day 1 (see Section 7.4.3).

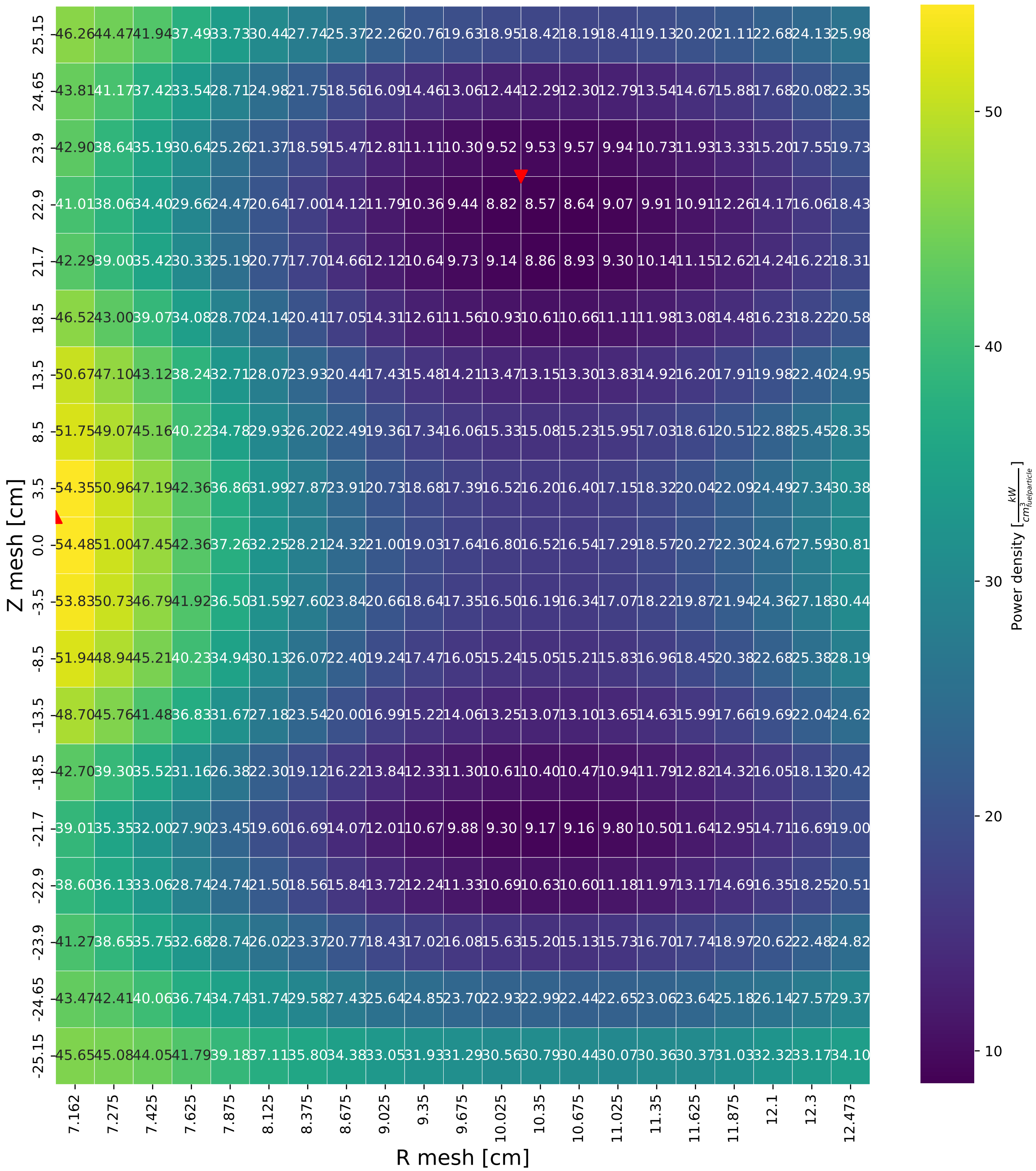

Figure 141. Power density distribution for boron-clad design IFE region on day 15 (see Section 7.4.3).

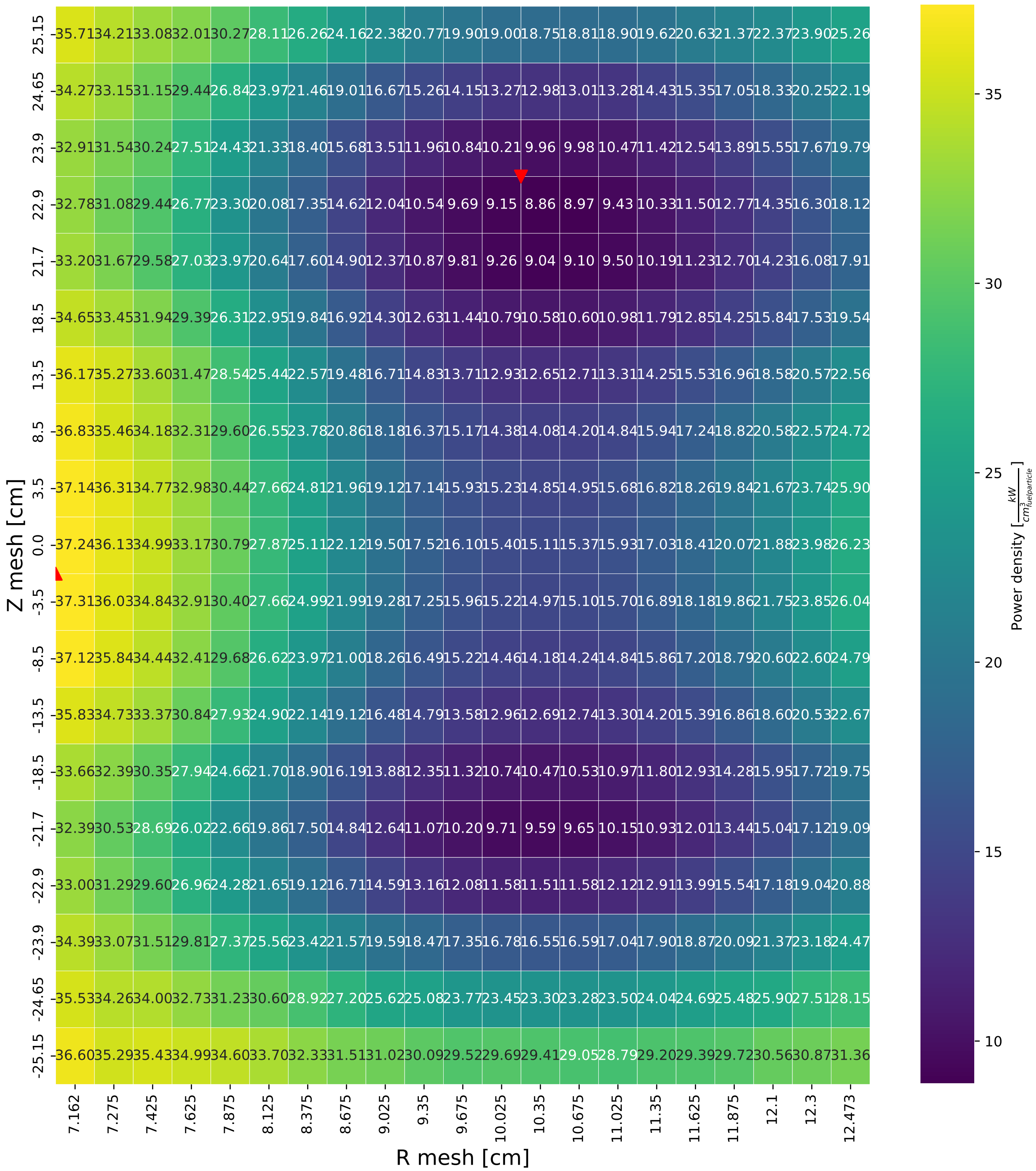

Figure 142. Power density distribution for boron-clad design IFE region on day 31 (see Section 7.4.3).

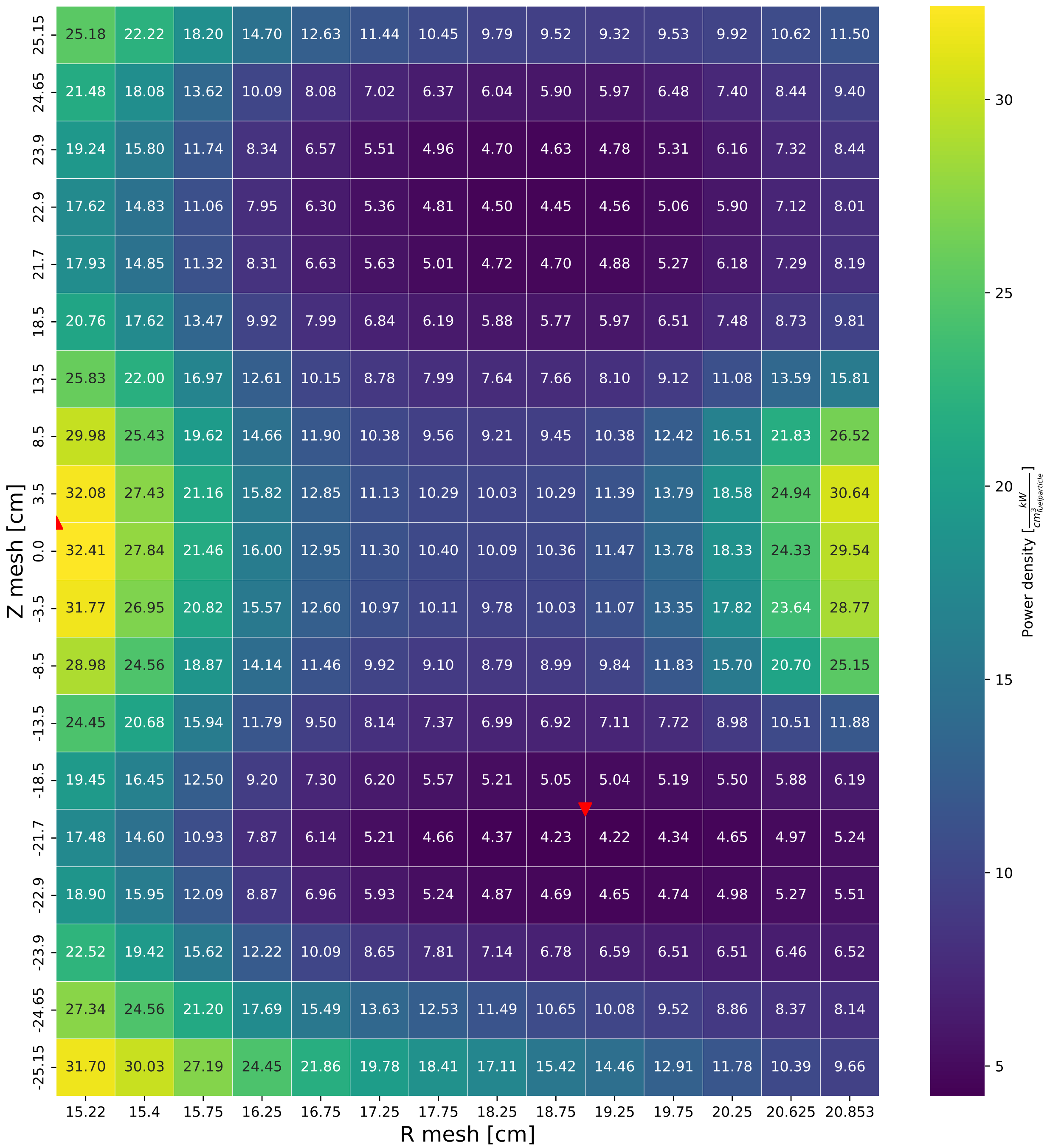

Figure 143. Power density distribution for boron-clad design OFE region on day 0 (see Section 7.4.3).

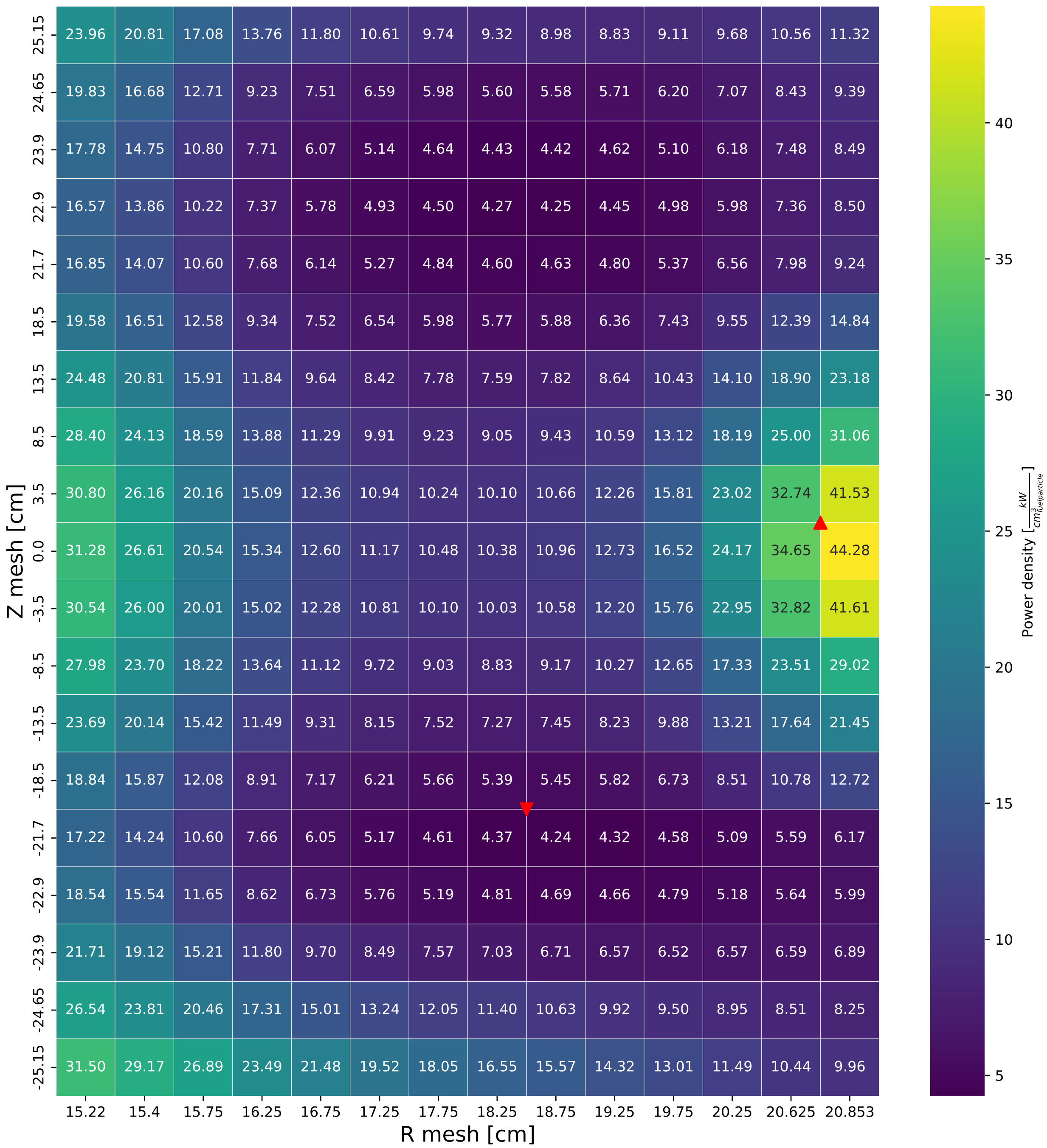

Figure 144. Power density distribution for boron-clad design OFE region on day 1 (see Section 7.4.3).

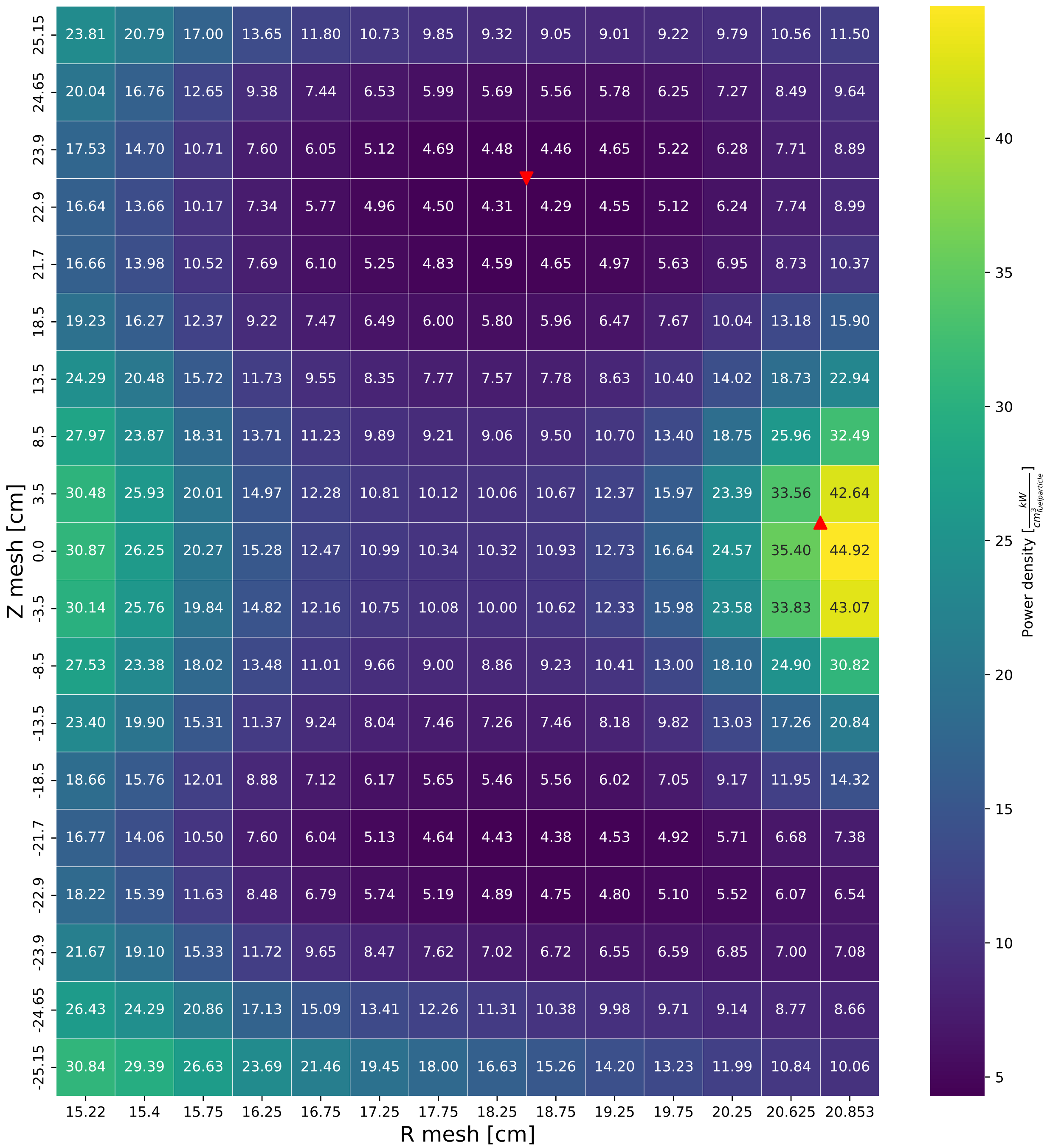

Figure 145. Power density distribution for boron-clad design OFE region on day 2 (see Section 7.4.3).

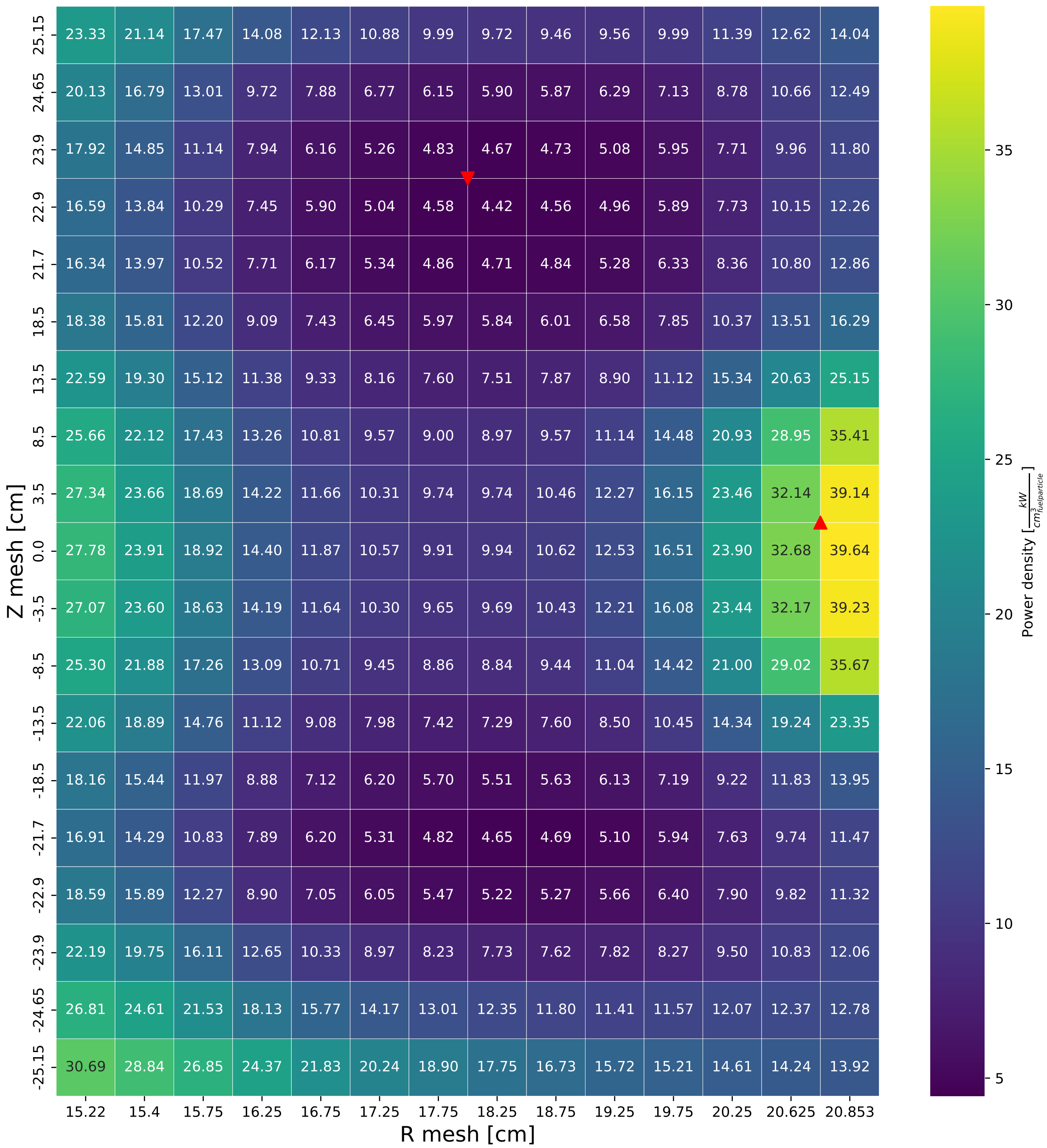

Figure 146. Power density distribution for boron-clad design OFE region on day 15 (see Section 7.4.3).

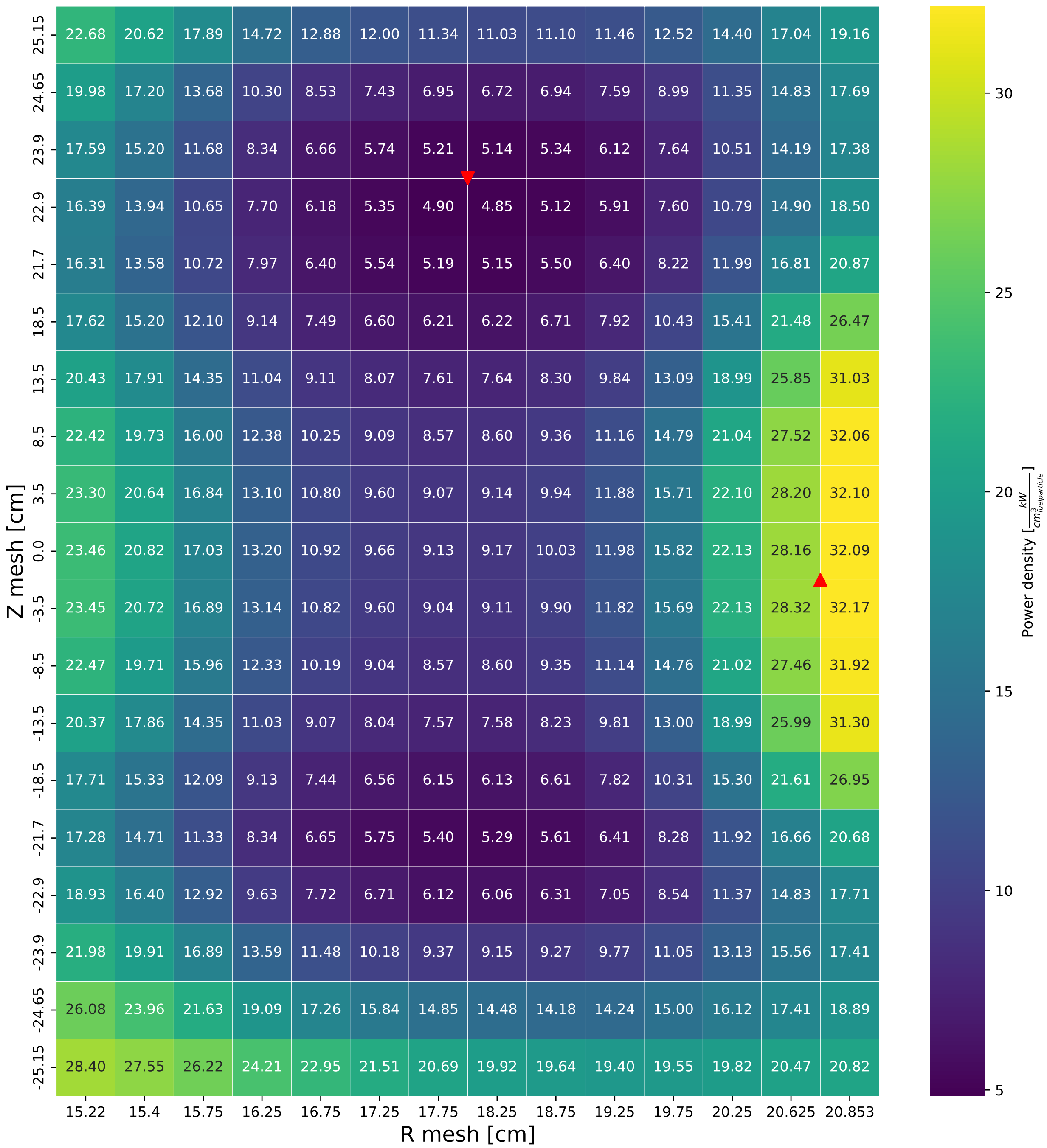

Figure 147. Power density distribution for boron-clad design OFE region on day 31 (see Section 7.4.3).

APPENDIX D-4. HEAT FLUX DISTRIBUTIONS FOR BORON-CLAD DESIGN

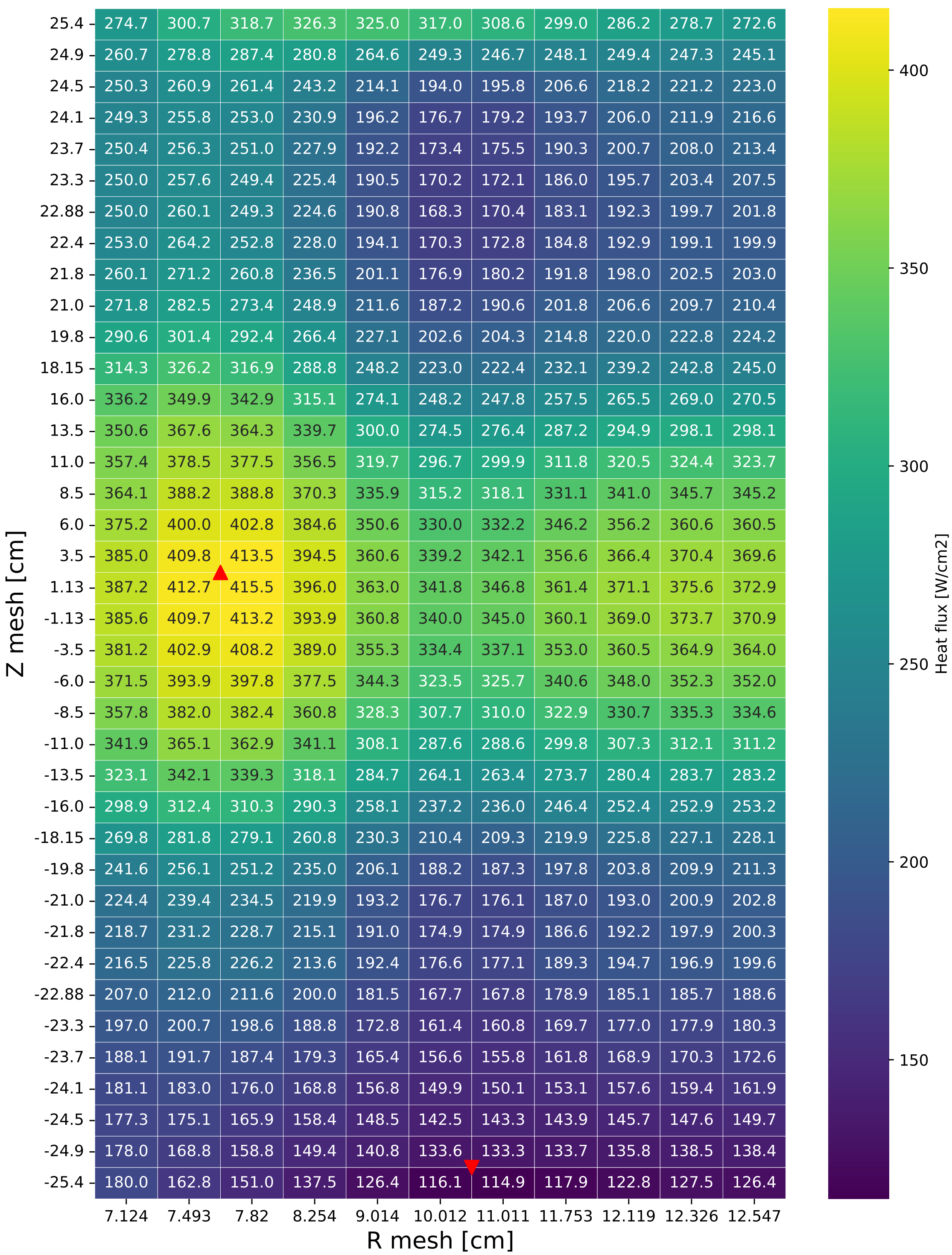

Figure 148. Heat flux distribution for boron-clad design IFE region on day 0 (see Section 7.4.4).

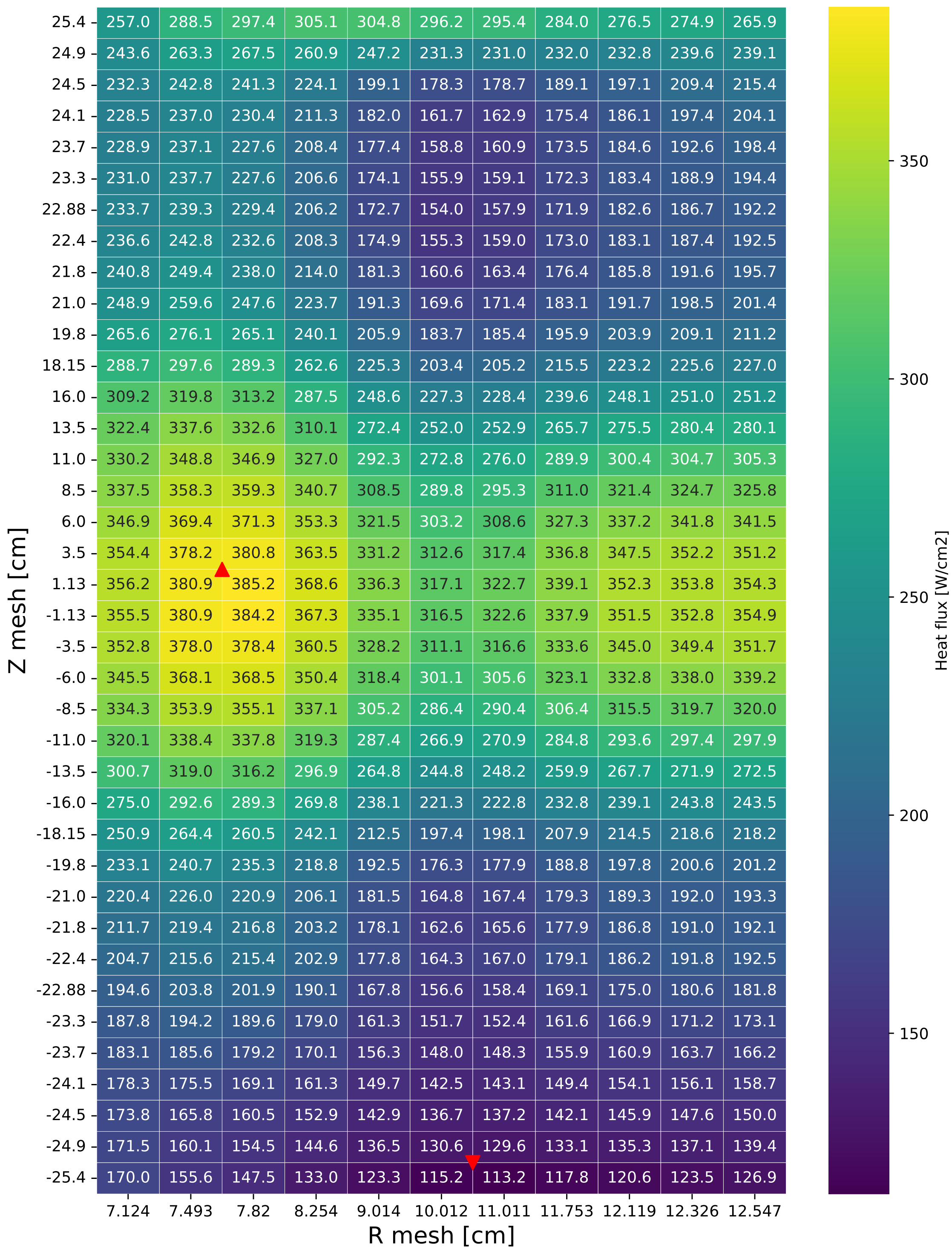

Figure 149. Heat flux distribution for boron-clad design IFE region on day 1 (see Section 7.4.4).

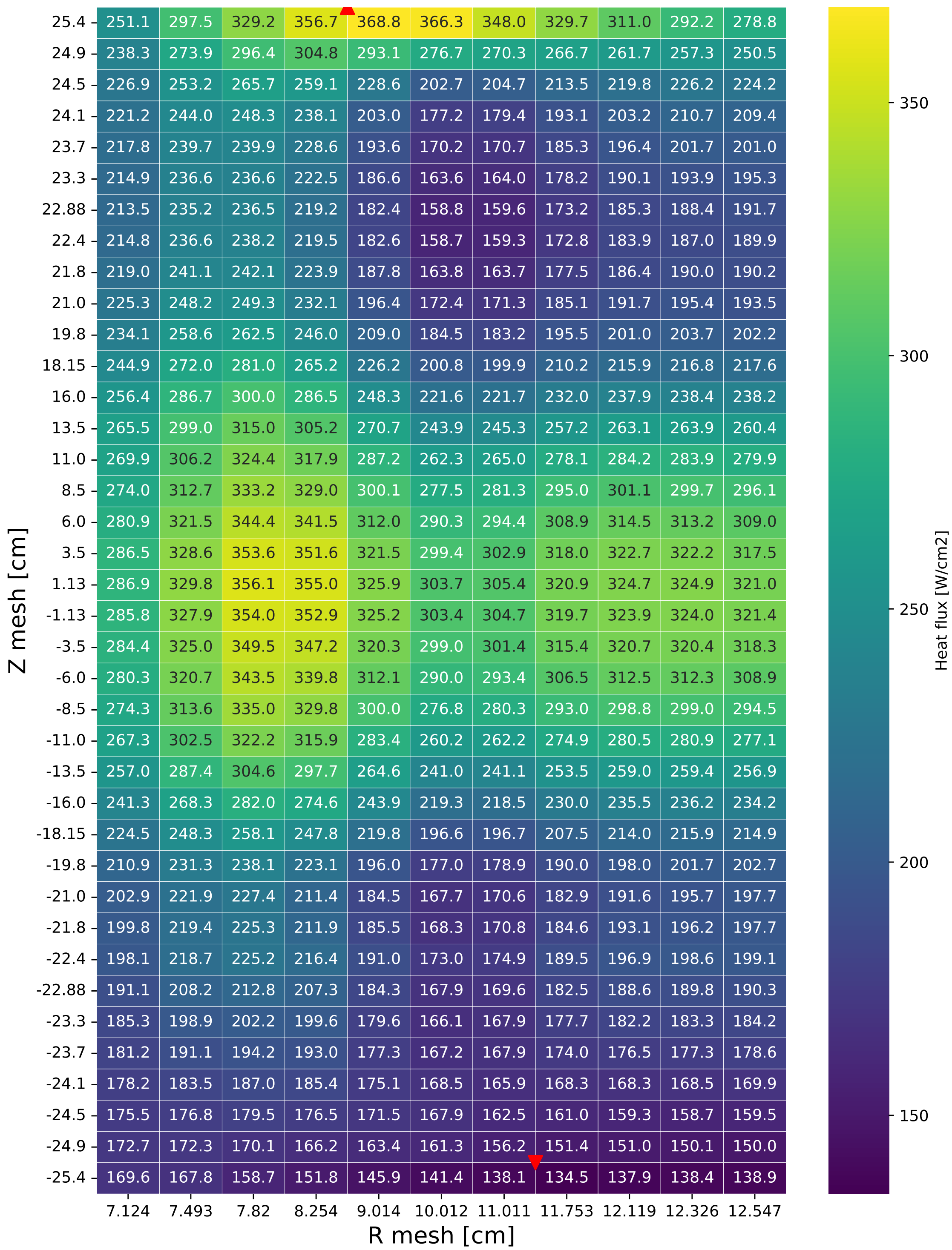

Figure 150. Heat flux distribution for boron-clad design IFE region on day 15 (see Section 7.4.4).

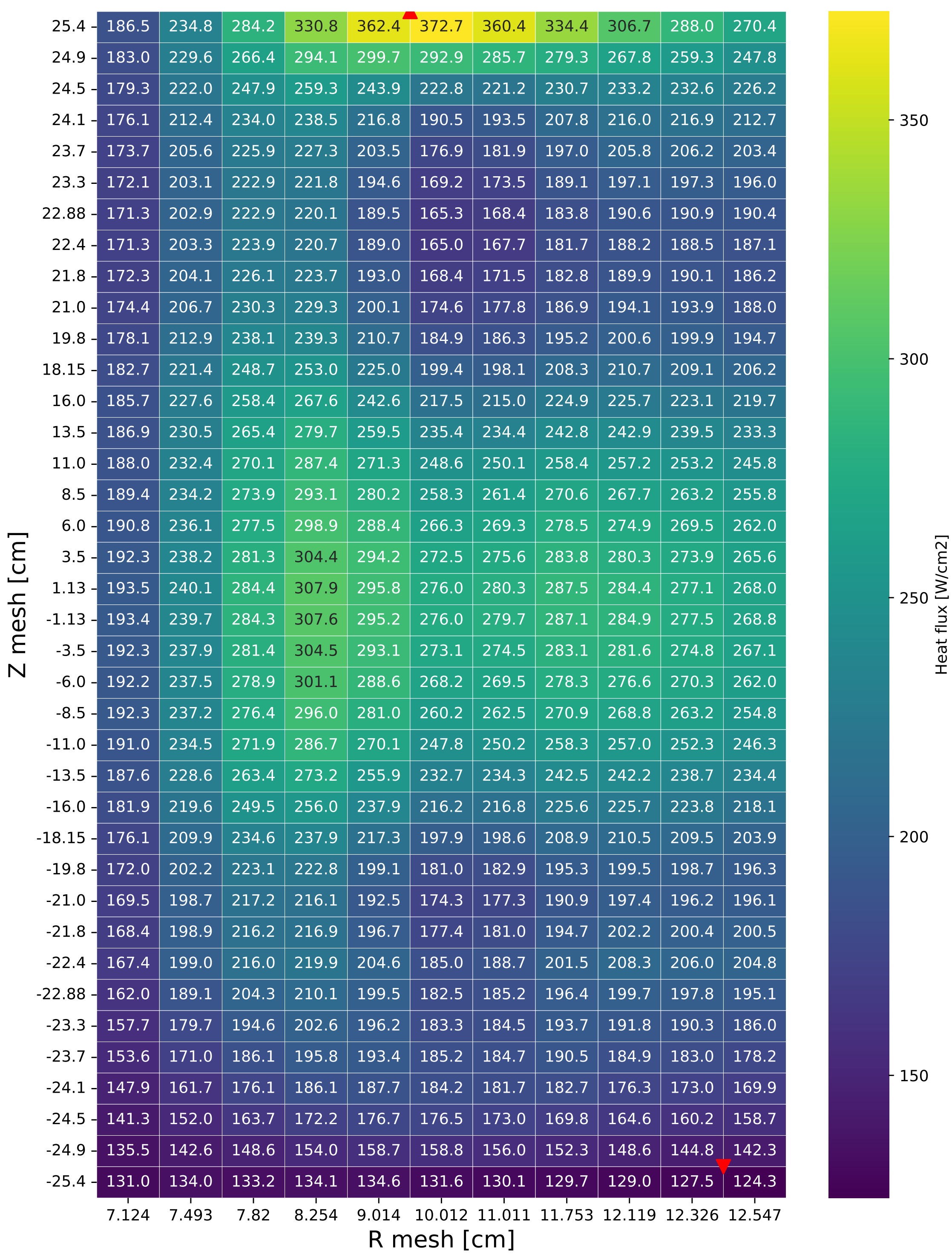

Figure 151. Heat flux distribution for boron-clad design IFE region on day 33 (see Section 7.4.4).

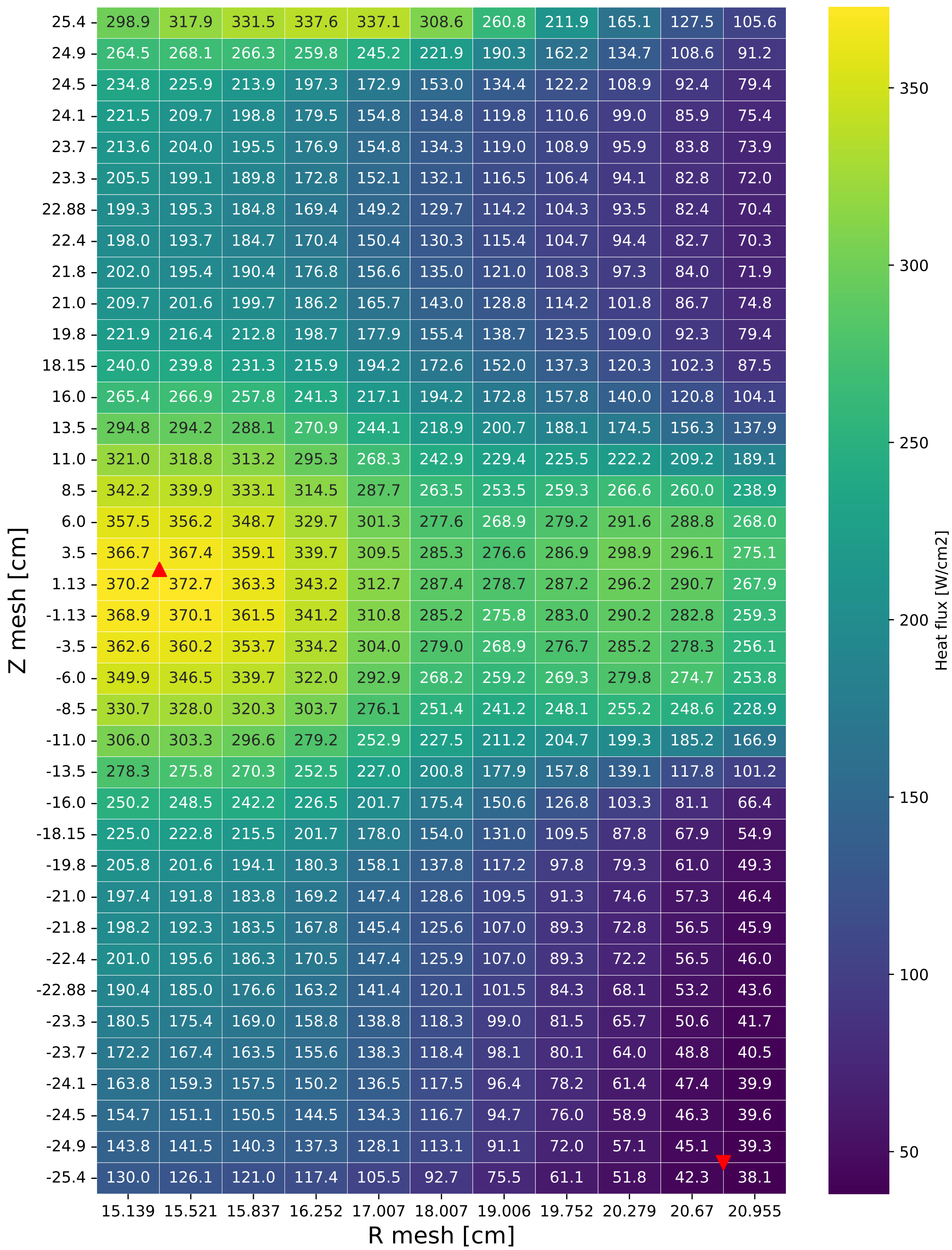

Figure 152. Heat flux distribution for boron-clad design OFE region on day 0 (see Section 7.4.4).

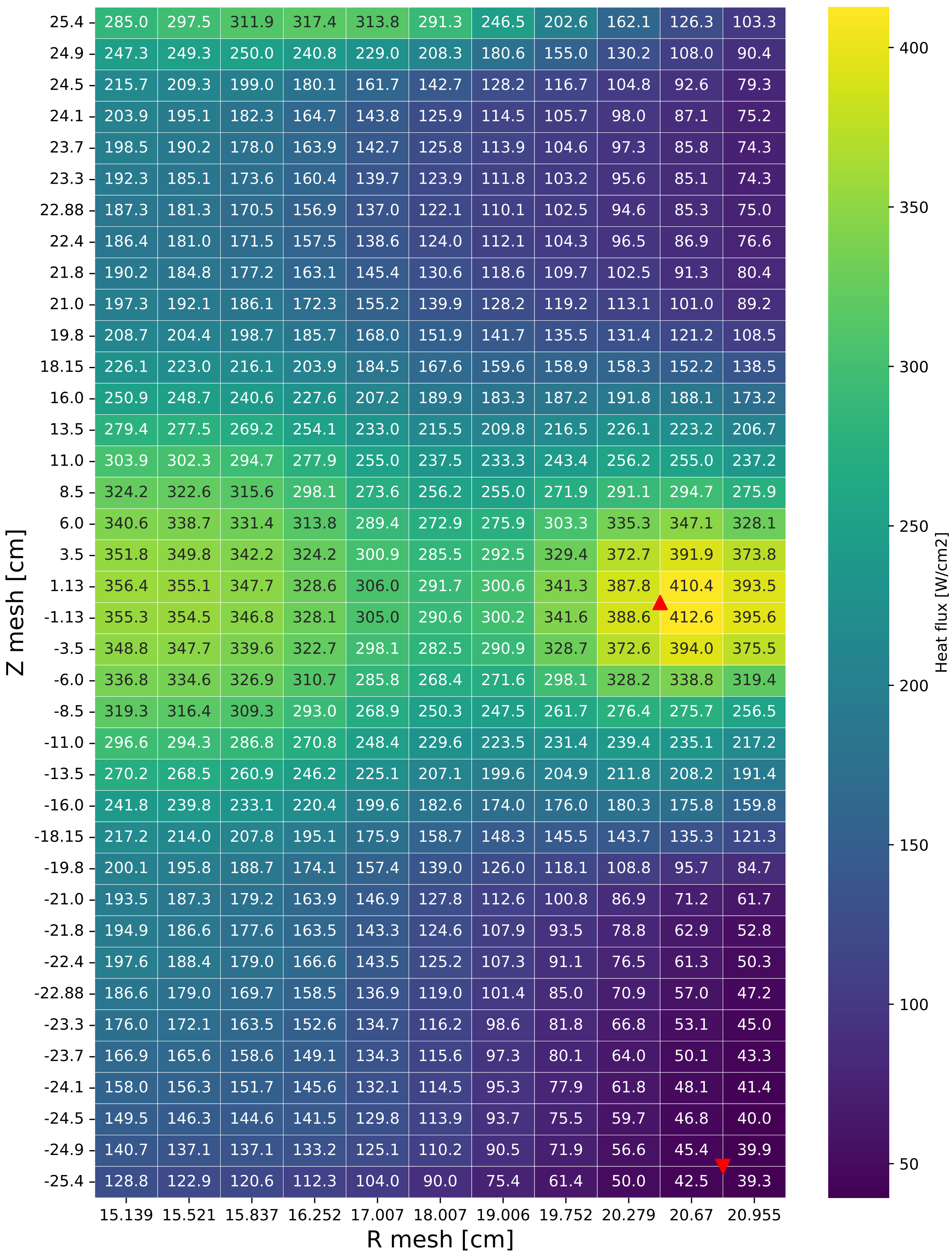

Figure 153. Heat flux distribution for boron-clad design OFE region on day 1 (see Section 7.4.4).

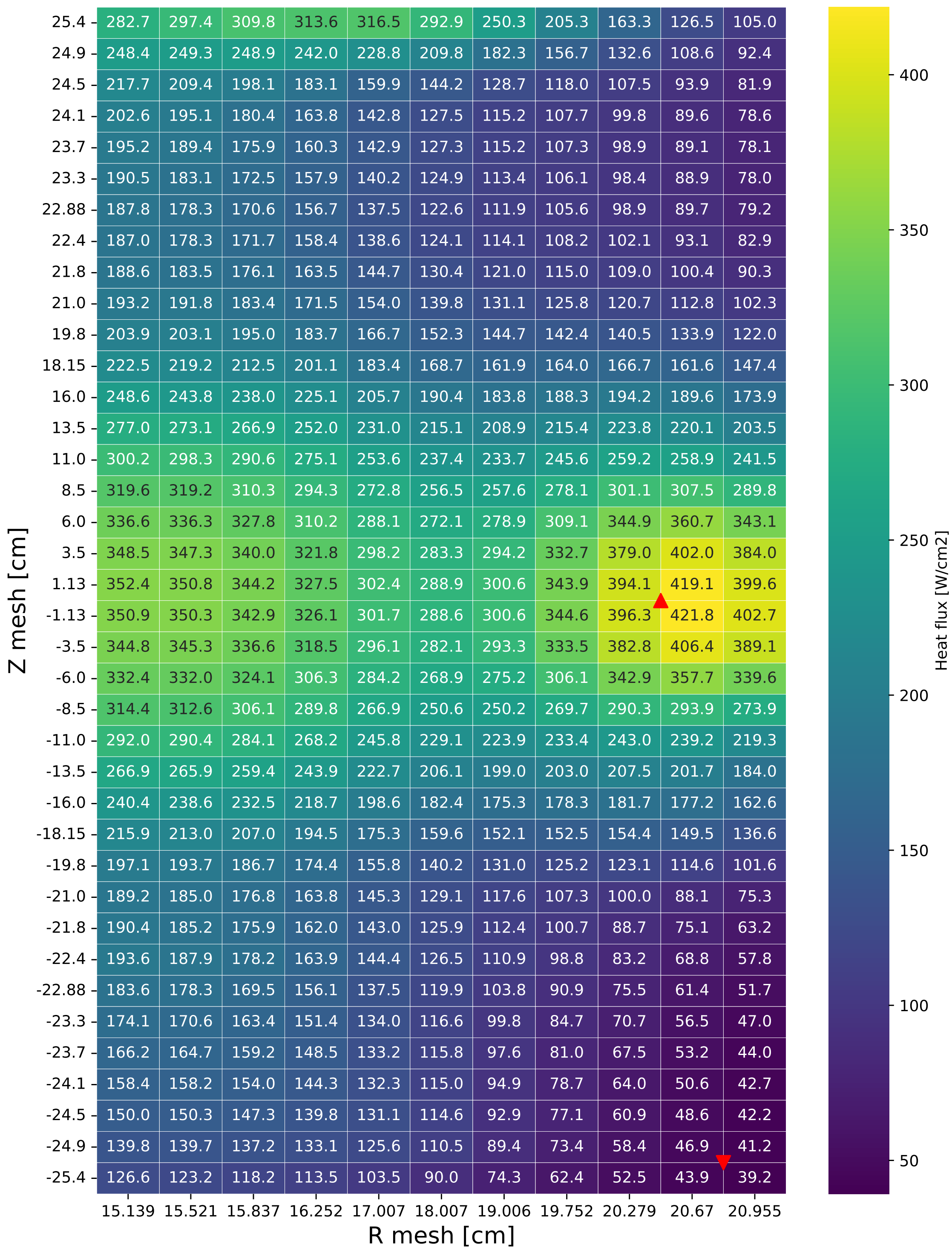

Figure 154. Heat flux distribution for boron-clad design OFE region on day 2 (see Section 7.4.4).

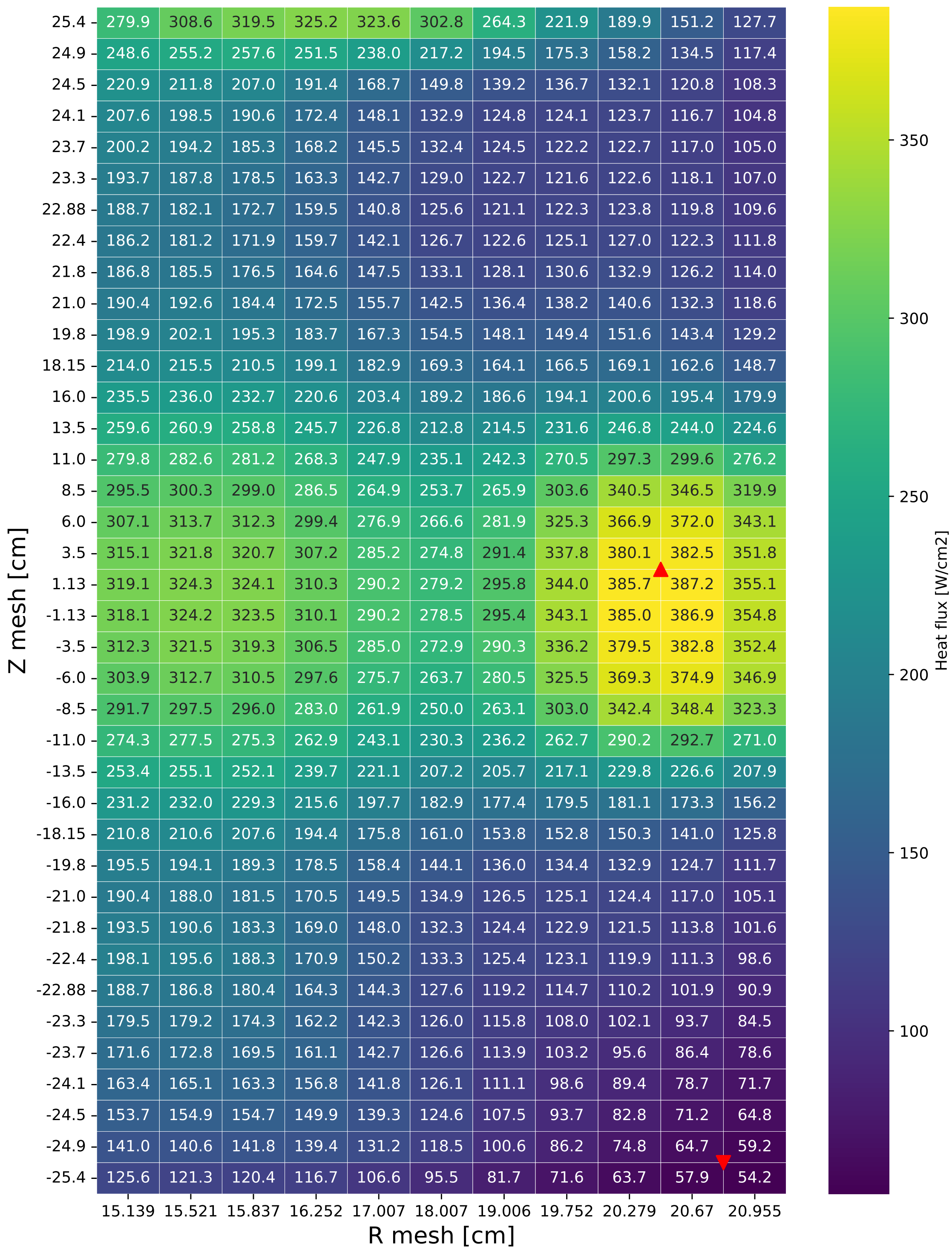

Figure 155. Heat flux distribution for boron-clad design OFE region on day 15 (see Section 7.4.4).

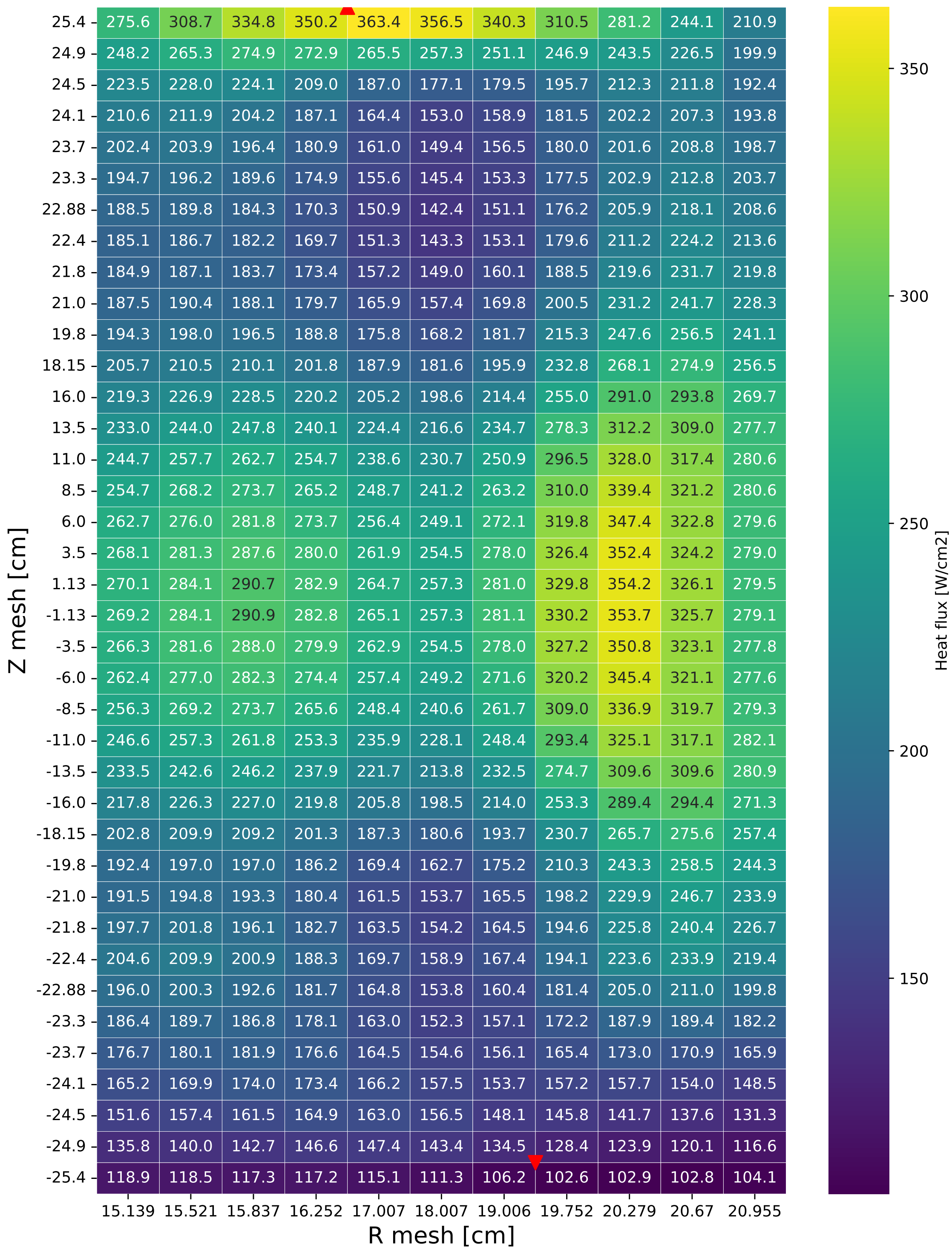

Figure 156. Heat flux distribution for boron-clad design OFE region on day 33 (see Section 7.4.4).